Multiphoton Quantum State Engineering using Time Multiplexing

A Single Source but Many Entangled Photons

Der Naturwissenschaftlichen Fakultät
der Universität Paderborn
zur
Erlangung des Doktorgrades Dr. rer. nat.
vorgelegt von

NIDHIN PRASANNAN

Contents

Chapter 1

Summary

The advancement of quantum theory brings up the idea of quantum advantage over classical devices. Quantum optical technology as a resource to solve classically impossible tasks in the optical domain, desperately needs efficient quantum hardware and techniques to demonstrate its actual usefulness. Specifically bright squeezed light and entangled states of light are highly demanding in photonic quantum technology.

In this thesis, we experimentally demonstrate an efficient quantum light source that can be used for both single and multiphoton quantum optical state manipulation. The non-linear waveguide-based source is spatially and spectrally engineered to emit bright, identical quantum light states upon subsequent ultrafast-pulsed optical excitations. By changing the mode of operation we generate- heralded single-photons, squeezed light, polarization-entangled photon pairs, and mesoscopic polarization entanglement from a single, novel waveguide-bulk integrated source.

Our novel time multiplexing and feed-forward method works as a resource-efficient photonic entangler, that uses a single quantum light source and a quantum buffer to entangle multiple photons. We entangle up to eight photons from a single parametric downconversion-based Bell state emitter; both theoretically and experimentally demonstrating the advantage of the feed-forward scheme over the existing state-of-the-art experimental schemes in multi-photon state generation.

The intrinsic nature of multiphoton emission from a parametric down-conversion source is utilized to test multiphoton interference and non-linear squeezing criteria theoretically and experimentally for the first time. A Sagnac-type polarization entangled and polarization squeezed light source is realized by considering a large mean photon number per polarization mode from the parametric source. A unique non-Gaussian (photon number) measurement strategy in the form of a non-linear functional of the Stokes operator is then constructed from click counting and detector multiplexing theory. By employing such a non-linear operator, non-classical photon number correlation and non-linear polarization squeezing properties of the light source are verified with high precision.

Chapter 2

Zusammenfassung

Die Weiterentwicklung der Quantentheorie bringt die Idee eines Quantenvorteils gegenüber klassischen Geräten hervor. Quantenoptische Technologie als Ressource zur Lösung klassisch unmöglicher Aufgaben im optischen Bereich benötigt somit dringend effiziente Quantenhardware und -techniken um einen tatsächlichen Nutzen zu demonstrieren. Insbesondere helles gequetschtes Licht sowie verschränkte Lichtzustände sind sehr gefragt in photonischen Quantentechnologien.

In dieser Arbeit wird eine effiziente Quantenlichtquelle, die sowohl für die quantenoptische Zustandsmanipulation mit einzelnen als auch mit mehreren Photonen verwendet werden kann experimentell demonstriert. Die nichtlineare, wellenleiterbasierte Quelle ist räumlich und spektral so konstruiert, dass sie bei aufeinanderfolgender ultraschnell gepulster optischer Anregung helle, identische Quantenlichtzustände emittiert. Durch Ändern der Betriebsart werden vorangekündigte Einzelphotonen, gequetschtes Licht, polarisationsverschränkte Photonenpaare und mesoskopische Polarisationsverschränkung aus einer einzigen, neuartigen integrierten Wellenleiter-Freistrahlquelle erzeugt.

Die neuartige Zeitmultiplex- und Feed-Forward-Methode funktioniert als ressourceneffizienter photonischer Verschränker, der einen einzelnen Quantenemitter und einen Quantenzwischenspeicher verwendet, um mehrere Photonen zu verschränken. Es wurden bis zu acht Photonen aus einer einzigen Bell-Zustandsquelle auf Basis parametrischer Fluoreszenz verschränkt; sodass sowohl theoretisch als auch experimentell den Vorteil des Feed-Forward-Schemas gegenüber dem bestehenden Stand der Technik zur experimentellen Erzeugung von Multiphotonenzuständen demonstriert werden konnte.

Die intrinsische Multiphotonenemission aus einer parametrischen Fluoreszenz wird genutzt, um Multiphotoneninterferenz und nichtlineare Kriterien zur Bewertung von gequetschten Zuständen erstmals theoretisch und experimentell zu testen. Eine polarisationsverschränkte und polarisationsgequetschte Lichtquelle vom Sagnac-Typ wurde realisiert, indem eine große mittlere Photonenzahl pro Polarisationsmode aus der parametrischen Quelle berücksichtigt wurde. Anschließend wurde aus der Klickzählungs- und der Detektor-Multiplexing-Theorie eine einzigartige nicht-Gaußsche Messstrategie (Photonenzahl) in Form eines nichtlinearen Funktionals des Stokes-Operators konstruiert. Durch die Verwendung eines solchen nichtlinearen Operators wurden die nichtklassische Photonenzahlkorrelation und die nichtlinearen Polarisationsquetscheigenschaften der Lichtquelle mit hoher Präzision überprüft.

Chapter 3

Preface

The main theme of the research proposal is to generate and characterize genuine multiphoton quantum light, which shows its essential quantum features in the form of entanglement and squeezing. This research was carried out under Prof. Christine Silberhorn's guidance within the Integrated Quantum Optics working group at the University of Paderborn (during the $2019 - 2024$ period). Novel experimental techniques and theoretical methods are introduced to conceive our different research ideas. Exceptional experimental data quality and results are obtained in various projects, that are complemented with high-impact research publications.

For a long time, experimental quantum information research relied on parametric down-conversion-based quantum light resources, that exploited single or two-photon quantum states to demonstrate preliminary quantum advantage. An extension to higher dimensional quantum systems or larger photon numbers requires multiple resources in the form of sources and detectors. In this aspect entanglement generation between many photons and detecting squeezing in photon number regime is a real challenge. Two essential quantum elements, entanglement and squeezing with a larger number of photons have both fundamental and technological importance. With the current methods, one needs many identical single or two-photon emitters and as many linear optical elements to entangle many photons. Here I have used the idea of temporal source multiplexing to demonstrate polarization entanglement of up to six photons and the first-ever detection of non-linear squeezing with a six-fold coincidence using a time multiplexed photon number detection scheme- that contributes major experimental results for this thesis. And, I want to highlight the method of time multiplexing as a resource-efficient route to many photon quantum state generation and detection.

Moreover, I have used our efficient experimental platform to investigate many theoretical proposals with pristine experimental data sets. I have collaborated with several research groups outside our group and university. We shared our experimental expertise to implement their intriguing theoretical ideas. Finally, we jointly evaluated the theoretical and experimental results for successful scientific publications. In this section, I would like to briefly explain different research projects and contributions delivered during the thesis work.

Evan Meyer-Scott, Nidhin Prasannan *et al.* Opt. Express 26, 32475-32490 (2018).

We demonstrated a highly efficient heralded single-photon source and polarization-entangled photon pair source on hybrid buk-integrated architecture, where a type II waveguide source is placed inside a Sagnac interferometer [1]. I was involved in testing different waveguide samples for optimized performance, building and characterizing the source, and analyzing the single photon and entangled photons data.

Evan Meyer-Scott, Nidhin Prasannan, Ish Dhand *et al.* Phys. Rev. Lett. 129, 150501 (2022).

We implemented the temporal source multiplexing approach to demonstrate multiphoton polarization entanglement using a single entangled photon pair source in connection with a quantum buffer through a fast electronic feed-forward system. I was mainly involved in the experimental implementation of such a novel technique. In the first stage, we demonstrated the storage of entanglement and four-photon entanglement from the experimental device. Then I refurbished the experimental setup to lead the demonstration of six and eight-photon entanglement [2].

Nidhin Prasannan, Jan Sperling *et al.* Phys. Rev. Lett. 129, 263601 (2022).

We demonstrated non-linear squeezing in polarization [3]. I have used the Sagnac polarization entanglement source in the multiphoton regime to detect non-linear polarization squeezing by employing photon number resolved detection at the output. I have used the click detector multiplexing theory to detect the non-classical nature of the optical state.

Lisa T. Weinbrenner, Nidhin Prasannan *et al.* Phys. Rev. Lett. 132, 240802 (2024).

Lisa T. Weinbrenner (from Prof. Dr. Otfried Gühne group) proposed a theoretical method to certify the topology of a multi-user quantum network from fidelity measurements of the quantum state shared by the network. For the experimental demonstration, we used our programmable time multiplexed multiphoton entangler to create different photonic-state topologies [4]. I prepared different six photon states to represent different

network topologies and corresponding measurement data were analyzed to verify the state quality and fidelity.

The overall experimental setup is flexible to generate a wide variety of non-classical optical states. We have used this experimental ability to generate different quantum optical states and a series of fundamental quantum optical experiments within and outside our research group.

Nidhin Prasannan, Jan Sperling *et al.* Phys. Rev. A 103, L040402 (2021).

Prof. Jan Sperling proposed the method of testing the entanglement of composite systems within the aspect of real and complex-valued quantum entities [5]. I have taken the polarization tomographic data for a seperable two-photon polarization state to probe the entanglement of the two-rebit state.

Yong Siah Teo *et al.* Phys. Rev. Lett. 133, 050204 (2024).

Prof. Luis. L. Sánchez-Soto and Dr. Yong Siah Teo proposed the idea of the certification of quantum system dimension purely from experimental evidence [6]. This pure mathematical proposal is then experimentally verified for both discrete variable and continuous variable optical states. I provided polarimetric tomographic experimental data for a two-mode squeezed vacuum and multiphoton polarization entangled state to efficiently verify the system dimension with the best precision.

Laura Ares, Nidhin Prasannan *et al.* arXiv:2407.07477 (2024).

We exploit the indistinguishable nature of multiple photons to demonstrate the equivalence of two different quantum manifestations- polarization nonclassicality, and multiphoton entanglement [7]. I have performed the multiphoton interference experiment to experimentally quantify the proposed theoretical concept.

Chapter 4

Introduction

Introduction

Over the last 100 years or more, the physics of the microscopic world has been greatly explained by the laws of quantum mechanics. There were debatable predictions and faithful experimental demonstrations to convince both the scientific and non-scientific communities. Today we have a handful number of choices to probe the quantum nature of physical systems. We are reaching the point of understanding the classical-quantum (or vice-versa) transition behavior of those physical systems by studying various microscopic-macroscopic quantum mechanical systems.

Quantum optics has played a major role in theoretical quantum physics development and was instrumental in its experimental demonstrations. Quantization of optical field (or electromagnetic field in general) gives rise to a single light entity called *photons* [8, 9]. As a microscopic candidate now one can use single or many, identical or non-identical photons to test quantum physics by manipulating its different degrees of freedom such as the amount of quantum (number of photons), polarization, angular momentum, etc. Light as an electromagnetic field, its polarization degree of freedom is widely used to realize the simplest two-dimensional quantum models. A single photon simultaneously in two possible polarization states or two possible paths can be easily prepared with linear optical components, which are the simplest example of quantum superpositions. According to Schrödinger idea, this two-state model is a good example for *quantum cat state* and the existence of *physical reality* is already questioned with no definite polarization attribute to the photon beforehand [10, 11]. The most fundamental quantum effect, single particle quantum interference can be observed by replacing classical light with a single photon in a classical two-path interferometer [12]. From single particle to two or more particle superpositions the concept of quantum entanglement is widely prepared and tested in optical platforms by entangling two or more photons [13, 14]. The notion of two-particle quantum states in the form of entanglement and its experimental investigation with entangled photons were breakthroughs in the history of experimental quantum physics [11, 15]. In fact, most of the fascinating quantum

phenomena were first realized on the optical platform with one or many photons, name a few like single particle interference, two-particle interference, entanglement, tests of Bell's inequality, quantum cryptography, entanglement swapping, quantum teleportation [16–18].

Rather than progressing and testing the fundamental aspects of quantum physics, researchers now turned their attention to bringing the quantum advantage in existing classical technology platforms like metrology, imaging, network-oriented communication, and information processing. The basic methodology is to replace the existing classical hardware resources with quantum resources and replace the governing classical mechanics-based idea with quantum rules. The following quantum schemes are radically different and outperform all classical strategies with the power of quantum superposition and entanglement [19–21]. Quantum optics plays a key role in optics-related quantum innovations for example quantum imaging, quantum communication, and quantum optical metrology [22–25]. Recently the idea of quantum computing is making attention around the scientific community to bring the quantum advantage in computing. Pen-on-paper-drawn proposals on all-optical quantum computing are shown to be promising but primitive demonstrations were lacking scalability and inefficient quantum resources, in the aspects of efficient quantum light sources, optical circuits, and photonic detection. There are different approaches to optical quantum computing, for example, measurement-based protocols, quantum gate approach, and boson sampling [26–28]. But in any case, one needs efficient quantum optical states and detectors.

In this thesis, we can find fair developments and demonstrations on some of the basic resources for the above-mentioned applications, for example. an efficient source for single and entangled photons, a scalable method to generate large-scale photonic polarization entanglement, an all-optical quantum memory device, bright squeezed macroscopic polarization-entangled light states, photon number resolved detection methods, non-linear observables and observation of non-linear squeezing. I will start the thesis format with a basic introduction to nonlinear optical effects and quantum light generation from special materials. Then I will use clever techniques to generate and detect high dimensional quantum optical states and correlations with more number of photons. But before that, I would like to give an overview of the chapters in the following paragraph.

Thesis overview

An efficient source of quantum light is always a prerequisite for all kinds of quantum optical technology. Quantum source's merit requirement may vary from a single photon generation to a few photon light-state or squeezed form of light with the best possible quality. Today photon emitters engineered from semiconductor two-level systems play a key role in acting as a deterministic single photon source with high generation rate and fair single photon state quality, but the main bottleneck is its cryogenic operation. In *Chapter* 1 we introduce a single hybrid bulk-integrated non-linear waveguide source designed to deliver high-quality single, squeezed, and entangled light states simply by controlling the input pump properties and operational mode of the setup [1]. These devices are flexible to use in ambient or cryogenic conditions depending on the purpose of the technology.

For the past few years, non-linear optical techniques have been widely used to generate quantum light, especially with spontaneous parametric down-conversion methods using bulk materials. But nonlinear interaction in waveguide microstructures is not exploited much leaving behind an awful opportunity to generate bright quantum light by consuming remarkably less amount of input pump power (few micro-watts). With this demonstration, we also overcome one of the long-standing limitations in bulk setup, where certain trade-off conditions do not permit simultaneous optimization of brightness and photon collection probability (also called heralding or Klyshko efficiency) from the source. Which is a fundamental limit in bulk nonlinear source posed by Gaussian beam type pump and signal optical interaction within the material. But our waveguide sources, intrinsically designed for single spatial mode operation can simultaneously attain maximum performance in all relevant parameters for a nonlinear quantum light source. Here the maximum brightness and heralding efficiency depend on the coupling efficiency between the fiber mode and nonlinear waveguide mode, which is rather an engineering problem, not a fundamental limitation.

Furthermore, we do spectral engineering on the non-linear interaction process to generate spectrally decorrelated pure photons, which are suitable for multiphoton interference experiments. In a decorrelated source heralding idler photons doesn't reveal any spectral-temporal information about the signal photons making them spectrally pure and indistinguishable, suitable for a wide range of quantum applications. This is the core concept that we use in the next chapter to interfere multiple indistinguishable single photons emitted from a single waveguide source. Subsequently emitted photons are delayed and interfered, to demonstrate multiphoton state manipulation and entanglement. Apart from a photon pair source,

in this chapter, for the first time, we develop a type II phase-matched waveguide sandwiched free space Sagnac interferometer to generate two-photon polarization entanglement. Highly efficient and bright polarization entanglement is experimentally demonstrated with high fidelity.

Chapter 2 is dedicated to a pristine scalable approach in multiphoton entanglement generation. In measurement-based quantum computation entangled states are the key input resources for computation, logical operations are performed on individual entangled photons, and results are feed-forwarded for the next logic operation on the consecutive or entanglement-sharing particle. Practically then one needs scalable methods to generate large entangled photonic states with considerable rates and fidelity. Until now the multiphoton entanglement generation relies on spatial multiplexing and fusion-based post-selection operation with many identical sources. Early boson sampling experiments were also relied on spatial multiplexing for more number of input photons. Source multiplexing in space is always resource-consuming where one needs multiple entangled photon sources and requires the same number of optical elements and single photon detectors for each stage of the multiplexing. This boils down to a resource scalability problem in spatial multiplexing. We decided to tackle this resource scalability limit by introducing temporal source multiplexing and active feed-forward arrangement for multi-photon entanglement generation [2].

Experiments harnessing time multiplexing schemes were demonstrated before, in connection with probabilistic to pseudo-deterministic heralded photon source development. All these time multiplexing protocol uses a *polarization sensitive* quantum memory to store and release photons in a predefined time window. The heralding trigger signals specifically control the store-release memory operations. This method is shown to be efficient for post-selected single-photon preparation with 67% generation or success probability with non-linear type sources, the best available quantum dot source has 57% end-to-end efficiency and promising better values in the future. In our project, we invent a *polarization 'in'sensitive* highly efficient quantum memory designed to store both single-qubit polarization states and two-qubit entangled states. An active optical switch will then add programmable nature to the memory for multi-photon entanglement generation in a time-multiplexed manner with the assistance of a fast feed-forward scheme. We use this programmable memory to store and entangle subsequently emitted polarization-entangled photon pairs from a single quantum light source. Large photonic entanglement can be generated in this manner and the experimental scheme is only limited by the efficiency of the memory. The type of entanglement created with this approach strictly depends on the nature of the unitary operation performed by the active and passive elements within the

memory. We give a specific experimental example for entanglement generation with one active switch inside the memory. However, with additional active or passive elements, one can perform multiple unitary operations and generate different graph states. Our active feed-forward method has shown to be an excellent platform to entangle multiple photons from a single emitter regardless of emitter platform (SPDC source, solid state emitters).

We demonstrate 4-photon and 6-photon polarization entangled photonic states (Greenberger–Horne–Zeilinger (GHZ) states) with high fidelity and count rate. More importantly, our feed-forward added time multiplexing scheme highly benefits from an increased generation rate compared to existing spatial and time multiplexing methods. This comes from the possibility of considering multiple Bell pairs not just from consecutive pump pulses, but with a large number of pump pulses. One can think of obtaining two or three Bell pairs from a probabilistic source in 25 consecutive pump pulses which increases the generation probability dramatically. We experimentally tested this feed-forward advantage most efficiently for individual state size experimental settings meaning, the 4-photon and 6-photon entanglement experimental count rate shows a 9-fold and 35-fold increase in rates for 22 pump pulses multiplexing compared to the nearest multiplexed case. Also, an exponential scale increase in generation rate is predicated for larger entanglement with the same number of source multiplexing and feed-forward. Another supreme advantage is the programmable nature of the memory device, the whole memory protocol depends on a fast field programmable gate array (FPGA) based feed-forward program sequence. The switch operation inside the memory can be programmed in any manner upon users interest, making the device versatile for any kind of multiphoton state manipulation without any change in the experimental setup. We give an experimental demonstration of the device's flexibility by generating different six-photon polarization state topology simply by changing the FPGA program sequence. Moreover, we use this different six-photon topology to test a new quantum network topology certification protocol [4].

In *Chapter* 3, I investigated, what happens if we go beyond two-photon approximation from type II squeezers which are placed inside the Sagnac for two-photon polarization entanglement generation in chapter 1. I specifically look into the details of the measurement strategy, much needed to exploit the full quantum advantage of squeezed light with a higher mean photon number. This is a stimulating topic in Gaussian boson samplers, where one sends multiple phase stabilized bright squeezed modes into a multi-port interferometer network to solve complex sampling problems. In this aspect, our Sagnac setup can constitute a single element in a Gaussian boson sampling type experiment where phase stabilized two Type II bright squeezed light

interfere on a polarization beam splitter and cause multiphoton interference. In a low squeezing regime this setup compromises for two photon polarization entanglement generation but a strong pump regime leaving unexplored. Toward the end of this project, we theoretically simulate and experimentally demonstrate macroscopic polarization entanglement from the Sagnac source combined with non-Gaussian measurements in the form of photon number detection. Experimental data reveals the two-mode non-classical correlation in polarization with high significance and a polarization noise-free light source suitable for quantum metrology. Our key results also involve the first-ever detection of non-linear squeezing (NLS) of light states in polarization degree of freedom [3].

Readily available highly efficient superconducting nano-wire click detectors are multiplexed in time to play the role of photon number resolved detector. Which is a resource-efficient multiplexing scheme that uses only a few fiber splitters and two click detectors. Click detector multiplexing and non-Gaussian measurement approach provide a non-linear functional form for two-mode polarization quantum measurement observables defined in terms of Stokes operators. Corresponding measurement outcomes are expected to be rather different compared to usual linear Stokes operator measurements. Previous approaches towards bright squeezing and macroscopic entanglement involve linear observables and Gaussian measurement strategies where one only deals with total intensity measurement instead of revealing true photon numbers, which is a pure non-Gaussian detection. We construct second-order (variance) and higher-order moments of the non-linear measurement operator to study the two-mode photon number fluctuations and correlation from our light source. We further derive an inequality bound for the moments to differentiate classical-nonclassical light state, based on this inequality squeezing type non-classical signature can be verified. For those non-classical lights, we detect non-linear squeezing and provide experimental evidence of non-linear polarization squeezing with our macroscopic polarization-entangled light source. We point out that such types of polarization noise-free or squeezed light sources are suitable for quantum applications. Also theoretically investigate and prove the noise resilience advantage of non-linear squeezing over linear squeezing.

In the conclusion remarks, I have essentially reshaped the introduction details with some figures of merit which we have demonstrated with our quantum light sources and experimental demonstrations. Possible changes and future project directions are explained in the outlook paragraph. In a broad sense, I am interested in exploring quantum correlation and quantum advantage not just with single or two-photon states but with quantum optical states with more number of photons. This requires efficient bright quantum light sources and detectors which can reveal

the true quantum nature of light by resolving the number of photons in the state. The higher the photon number higher the complexity of the quantum system and useful to solve the same kind of complex problems with quantum supremacy.

Chapter 5

Waveguide-Integrated Bright Quantum Light Source

Contents

5.1 Spontaneous Parametric Down-Conversion and Quantum Light Source Engineering

Parametric fluorescence, or the well-known spontaneous parametric down-conversion effect (SPDC) played an important role in developing several quantum mechanical ideas for its experimental demonstration. Since the first observation of parametric fluorescence [29, 30], extensive studies on its photon statistics, and photon-photon correlation were carried out both in the discrete (photon counting) and continuous variable picture (quadrature or intensity measurements). The quantum nature of the SPDC process makes a specially engineered nonlinear material an ideal candidate for quantum light state generation. Spontaneous decay of a single pump photon causes simultaneous emission of two identical or nonidentical photons from the nonlinear material [31], A process then used to carry out many single and two-particle experiments on the fundamental physics aspects like quantum interference, quantum entanglement, etc. The entangled nature of the two-mode parametric light sources had become a cornerstone for EPR-type experiments and Bell tests [32]. Higher order emission from the SPDC process in the form of many photons can be identified as an epitome of a highly squeezed light source, an optical resource that finds application from metrology to computing in the quantum domain.

Over the years efforts have been made to improve the quality of such sources, especially in terms of on-demand generation, brightness, purity, and collection ef-

ficiencies. In this section, I will explain the basic theory behind the SPDC process and practically implement a heralded single-photon source on a bulk-integrated waveguide platform. Further then benchmark the aforementioned quality criteria for single and two-photon states with best precision. The spectral engineering section describes how pure single-photon states can be prepared through careful engineering of the properties of the non-linear material and pump laser source, such photonic states are essential for multiphoton interference and higher dimensional state preparation. Finally, a demonstration from a pair of identical photons to a bright, highly polarization-entangled two-photon source is made possible by an elegant interferometric approach.

5.1.1 Nonlinear optics

Basic electrodynamics theory says if we apply an electric field to a material, it can distort the orientation of charged particles inside the material according to the material property and applied electric field strength. The presence of oppositely charged dipoles inside the material aligns its direction according to the applied electric field, known by the name electric polarizability, In linear optics we explain this phenomenon with a simple equation,

$$P(t) = \varepsilon_0 \chi^{(1)} E(t), \tag{5.1.1}$$

where $\chi^{(1)}$ is the linear susceptibility of the optical material and ε_0 is the permittivity of free space. However the natural response of certain materials towards electromagnetic fields is non-linear, and the outcomes of nonlinear effects become observable under intense electric fields. The invention of highly coherent lasers, especially pulsed lasers provides an indispensable tool to explore these non-linear optical and electrical effects. To have a basic foundation for this thesis and our device development, some of the well-explained non-linear optical effects and their governing equations are adapted from existing articles and literature's [33].

In nonlinear optics, the dipole moment polarization response can be explained by a power series expansion in terms of applied electric field strength and polarization susceptibility of the material,

$$P(t) \; = \; \varepsilon_0 \Big[\chi^{(1)} E(t) + \chi^{(2)} E^2(t) + \chi^{(3)} E^3(t) + ... \Big]. \tag{5.1.2}$$

We have nonlinear optical susceptibility terms of different order showing up ($\chi^{(2)}$, $\chi^{(3)}$ ...) in Eq. (5.1.2). These coefficients hint that under the assumption of energy and momentum conservation, it's possible to explain and observe higher

harmonic light generation on certain materials when irradiated with strong electromagnetic fields. In this thesis, I mainly focus on the second-order nonlinear polarization effect $\chi^{(2)}$ and material properties for the generation of second harmonic light. One of the key material identifiers for the presence of $\chi^{(2)}$ is its non-centrosymmetry (inversion symmetry). When irradiated, several physical effects in the form of additional output electromagnetic radiation along with the input light can be observed from the material. Even though this behavior is a consequence of nonlinear interaction within the material, the process further depends on the number of input optical fields and has to obey input-output energy and momentum conservation laws. For the simplest case, consider the interaction of $\chi^{(2)}$ material with an electric field of strength E_o and frequency ω. Then solve the second-order nonlinear polarization term for its response,

$$E(t) = E_o e^{-i\omega t} + c.c \ , \tag{5.1.3a}$$

$$P^{(2)}(t) = 2\chi^{(2)} E_o E_o^{*} + \Big(\chi^{(2)} {E_o}^2 e^{-i2\omega t} + c.c\Big). \tag{5.1.3b}$$

The above relation says something special about nonlinear optics, starting from an electromagnetic field of frequency ω, after interacting with the material we have an additional output radiation field mode oscillating with twice the frequency (2ω) of the input field. The process of generation of harmonics of fundamental input field goes with the idea of higher harmonic generation (HHG), in our case its second harmonic generation (SHG) [34]. This technique is now widely used for converting light from one frequency to another for a range of applications.

Instead of a single input excitation field now consider two monochromatic plane waves with frequency of ω_1 and ω_2 interacting with the nonlinear medium,

$$E(t) = E_1 e^{-i\omega_1 t} + E_2 e^{-i\omega_2 t} + c.c \ ,$$

expansion of quadratic electric field term for nonlinear polarization effects gives,

$$\begin{aligned} P^{(2)}(t) = 2\chi^{(2)}\Big[E_1 {E_1}^{*} + E_2 {E_2}^{*}\Big] + \chi^{(2)}\Big[{E_1}^2 e^{-i2\omega_1 t} + {E_2}^2 e^{-i2\omega_2 t} \\ +2E_1 E_2 e^{-i2(\omega_1+\omega_2)t} + 2E_1 E_2 e^{-i2(\omega_1-\omega_2)t} + c.c\Big], \end{aligned} \tag{5.1.4a}$$

this can be rewritten purpose of explanation,

$$\begin{aligned} P^{(2)}(t) = 2\chi^{(2)}[E_1 {E_1}^{*} + E_2 {E_2}^{*}] + \chi^{(2)}\Big[P(2\omega_1) + P(2\omega_2) \\ +P(\omega_1+\omega_2) + P(\omega_1-\omega_2)\Big]. \end{aligned} \tag{5.1.4b}$$

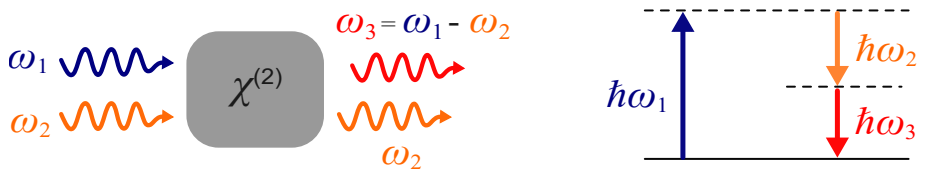

Figure 5.1.1: DFG process: (left) An illustration for the seeded DFG process. (right) Energy level diagram for a vacuum-induced DFG process or SPDC process

Equation (5.1.4b) supports the generation of multiple output radiations, showing multiple harmonics and combinations of input frequencies (ω_i). The term P($2\omega_1$) and P($2\omega_2$) corresponds second harmonics of the input field ω_1 and ω_2. P($\omega_1 + \omega_2$) will lead to the generation of an electromagnetic field that oscillates at the frequency of $\omega_1 + \omega_2$ and the process is called sum frequency generation (SFG). SFG process has been used in many areas of optical physics to generate tunable lasers for a wide variety of applications. At the same time, there is a difference frequency component $\omega_1 - \omega_2$ in the equation, this leads to the process of difference frequency generation (DFG). However, each process needs specific requirements to happen in the given material, hence suppressing the simultaneous occurrence of many output fields. Also, the generated field can be recombined inside the material and constitute less at the conversion process. For an efficient selective conversion process, along with material properties certain phase-matching condition also has to be satisfied. Conservation of energy should be satisfied within the input-output frequency relation.

Here we use the DFG process as an example to convey the energy conservation formalism through a simple energy level diagram approach, under perfect condition (phase matched) an additional output field of $\omega_3 = \omega_1 - \omega_2$ is produced by interacting two dissimilar frequency components (ω_1, ω_2) inside the material. Since ω_1 is greater than ω_2 remaining energy from ω_1 will be emitted as ω_2 ($\omega_3 = \omega_1 - \omega_3$) after the interaction process for energy conservation. This should be viewed as, $\omega_1 \rightarrow (\omega_2, \omega_3)$ decay process stimulated by the input seed field ω_2. For an unseeded case, the energy diagram in Fig. 5.1.1 explains that ω_1 component excites the atoms to the excited state and then returns to the ground state by the emission of two fields with frequency ω_2 and ω_3 mediated by a virtual energy level. We just realized that vacuum seeding also leads to twin field generation from a strong single input pump field (ω_1) under the condition $\omega_3 + \omega_2 = \omega_1$. But in general, this vacuum-induced nonlinear process is very weak and less likely to spontaneously occur in the system. This is a pure quantum mechanical phenomenon and now very familiar with the name spontaneous parametric down-conversion (SPDC), during which a high-energy pump photon spontaneously decays into two low-energy photons (Sig-

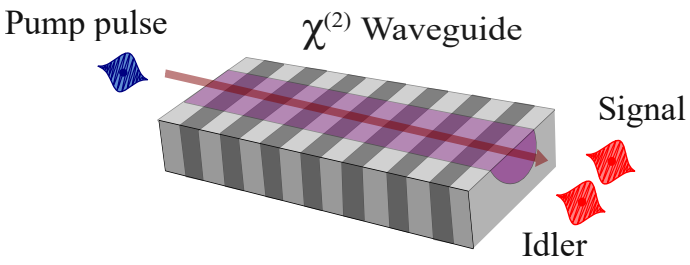

Figure 5.1.2: SPDC process: A pump photon decays spontaneously within the nonlinear medium, emitting a pair of photons with identical (or nonidentical) characteristics.

nal and Idler photons[1]) as a nonlinear interaction outcome. An illustrative figure for SPDC kind two-photon decay is given in Fig. 5.1.2. Such weak twin beams show a strong non-classical correlation between the two output light fields in different degrees of freedom [35, 36]. And you are not surprised why I explicitly took the DFG process to detail in this paragraph. Instead of vacuum, different seeding techniques are demonstrated with PDC sources for nonclassical state preparation, stimulated emission tomography, and metrology applications [37, 38]. Experimental investigations with coherent and thermal light states as a seed for PDC sources proved single photon addition to a classical optical state and quantum commutation relation in practice [39, 40].

5.1.2 Parametric sources for quantum light

We have learned that under certain conditions a DFG process in an engineered nonlinear material can be used as an efficient scheme for the generation of quantum light. But a quantum process needs an equivalent mathematical quantum description to describe the physics behind it. Similar to the quantization of a single-mode harmonic oscillator problem, we follow the field quantization formalism for a three-wave mixing process by considering the complete classical Hamiltonian of the system. Quantizing the process Hamiltonian then provides a more general and necessary description for the generated light in terms of quantum states and quantum operators. Energy contribution for the three-wave mixing process can come from the input pump field and second-order field components of nonlinear polarization, integrating the total field within the nonlinear medium volume gives,

$$\mathbf{H} \propto \int_v \mathbf{P}^{(2)}(t) \cdot \mathbf{E}(t)\, d\boldsymbol{r}. \tag{5.1.5}$$

[1] A nomenclature followed from the literature

By taking into account the strong electromagnetic pump field (ω_p) and the non-linear polarization induced additional interacting fields (ω_1, ω_2), we can rewrite the Hamiltonian with corresponding electric field terms,

$$\mathbf{H} \propto \int_v \chi^{(2)}\, \mathbf{E}(\omega_p, t)\, \mathbf{E}(\omega_1, t)\, \mathbf{E}(\omega_2, t)\, d\boldsymbol{r}\,, \tag{5.1.6}$$

where $\chi^{(2)}$ is dependent on all the three frequencies involved in the process. From the basic postulates, quantization of Hamiltonian necessitates quantization of electromagnetic field involved in the process [41]. Which introduces the corresponding positive and negative electric field operators deduced from filed quantization rules,

$$\hat{E}_j^{(-)}(r,t) = \hat{E}_j^{(+)\dagger}(r,t) \propto \int d\omega_j\, \exp[-ik_j.r + \omega_j t]\; \hat{a}_j^{\dagger}(\omega_j)\,, \tag{5.1.7a}$$

$$\hat{\mathbf{E}}_j = \hat{E}_j^{(-)}(r,t) + \hat{E}_j^{(+)}(r,t). \tag{5.1.7b}$$

Plugging Eq. (5.1.7b) in Eq. (5.1.6) provides quantum operators for all kinds of processes involved in our three-wave mixing process. But we will only consider those parts where the Hamiltonian describes the parametric decay process and is given by,

$$\begin{aligned}\hat{H}_{PDC} = \frac{\epsilon_o}{3}\chi^{(2)} \int_v d\mathbf{r} \left[\hat{E}_p(r,t)^{(+)} \left(\hat{E}_1(r,t)^{(-)}\right)^2 + h.c.\right] \\ + \left[\hat{E}_p(r,t)^{(+)}\, \hat{E}_1(r,t)^{(-)}\, \hat{E}_2(r,t)^{(-)} + h.c.\right].\end{aligned} \tag{5.1.8}$$

Equation (5.1.8) gives two terms to describe two different types of PDC process. In the first case, single pump mode decays into two photons occupied in a single polarization mode constituting the type I PDC process. In this case, PDC photon polarization aligns orthogonal to the pump polarization. In the second term, decayed photons are occupied in two distinct modes which gives type II PDC. Throughout this thesis, we deal with the type II PDC process, where we generate signal and idler photons in orthogonally polarized modes. With the time dependant Hamiltonian in hand, SPDC quantum state $|\Psi_{PDC}\rangle$ can be obtained by the operation of the unitary operator $\hat{U} = \exp\left(-i\hat{H}t/\hbar\right)$, but for the PDC process it's not straight forward. We have to consider the Hamiltonian which takes care of the interaction time of the process and time ordering effects, making the calculations more rigorous (a detailed approach can be found here [42]). For the theses, I will consider the simplified final unitary operator for the state generation,

$$\hat{U} = \exp\left[\frac{-i}{\hbar}\int dt\, \hat{H}_{PDC}(t)\right]. \tag{5.1.9a}$$

Since we are considering the Hamiltonian for the two-mode PDC process we need to consider the same number of modes for our output state. These initial modes can be either occupied with vacuum or well-defined classical or quantum states (seeded PDC sources). For the simplest case, we take vacuum as our input mode,

$$|\Psi_{PDC}\rangle = \hat{U}\,|0,0\rangle = \exp\Big[\frac{-i}{\hbar}\int dt\,\hat{H}_{PDC}(t)\Big]\,|0,0\rangle\,. \tag{5.1.10a}$$

Before writing down the explicit formula for the state we need to consider the nonlinear material geometry of the SPDC process in detail. In general, for bulk nonlinear material, generated photons show a highly multimode nature both in the spectral and spatial degree of freedom. One favorable approach to decouple the spatial and spectral degree of freedom is to adapt waveguide geometry for the nonlinear material. Which supports selective guided spatial modes inside the material, simultaneously favoring high light confinement and nonlinear interaction [43]. For a single spatial mode guided waveguide source possessing a type II PDC process [44], we can rewrite the Hamiltonian as-

$$\hat{H}_{PDC} = \frac{\epsilon_o}{3}\chi^{(2)}\int dz\;\hat{E}_p(z,t)^{(+)}\;\hat{E}_1(z,t)^{(-)}\;\hat{E}_2(z,t)^{(-)}\;+\;h.c. \tag{5.1.11}$$

In Eq. (5.1.11) we consider integration only along the field propagation direction (z) and within the interval limit of the interaction length of the waveguide. The generated state is then free of spatial multimodness, providing a more simplified state representation that involves only the joint spectral details of the system.

$$|\Psi_{PDC}\rangle = \hat{U}\,|0,0\rangle\,,$$
$$|\Psi_{PDC}\rangle = \exp\left[\frac{-i}{\hbar}\left(A\int d\omega_i\int d\omega_s\;f(\omega_s,\omega_i)\;\hat{a}_s^{\dagger}(\omega_s)\;\hat{a}_i^{\dagger}(\omega_i)+h.c.\right)\right]|0,0\rangle\,. \tag{5.1.12a}$$

Absorbing the spatial and other information into the constant factor (A), Eq. (5.1.12a) contains a well-simplified Hamiltonian and the corresponding unitary operator for the state generation [45]. The leftover spectral integration part is devoted to the pure single photon state generation scheme in Sec. 5.1.3. There we will explain more about spectral state engineering for the generation of heralded pure single photons followed by an experimental demonstration.

Photon number description

Similar to the electric field quantization approach there is another route to SPDC Hamiltonian by defining suitable single mode creation/annihilation operators for

the modes involved in the PDC process and squeezing parameter. For a brief photon number basis introduction consider a type II PDC process with three creation operators for three modes $\hat{a^\dagger}$, $\hat{b}^\dagger$, $\hat{c}^\dagger$ where,

$$\begin{aligned} \hat{a}^\dagger |n\rangle &= \sqrt{n+1}\,|n+1\rangle \ , \\ \hat{a}\,|n\rangle &= \sqrt{n}\,|n-1\rangle \, . \end{aligned}$$

Hamiltonian of the process then can be written down involving the free propagating modes and with the interacting modes,

$$\hat{H} = \hbar\omega_s \hat{a}^\dagger \hat{a} + \hbar\omega_i \hat{b}^\dagger \hat{b} + \hbar\omega_p \hat{c}^\dagger \hat{c} + i\hbar\chi^{(2)}(\hat{a}\hat{b}\hat{c}^\dagger - \hat{a}^\dagger \hat{b}^\dagger \hat{c}). \tag{5.1.14}$$

We can treat pump mode as a classical strong coherent light field and assume undepleted, in fact very small number of pump photons are decaying in a PDC process yielding,

$$\hat{H} = \hbar\omega_s \hat{a}^\dagger \hat{a} + \hbar\omega_i \hat{b}^\dagger \hat{b} + i\hbar\left(\zeta^* e^{i\omega_p t}\hat{a}\hat{b} - \zeta e^{-i\omega_p t}\hat{a}^\dagger \hat{b}^\dagger\right). \tag{5.1.15}$$

Here the pump field strength and nonlinear interaction strength terms are absorbed into the ζ. In the interaction picture, under the assumption of pump frequency sum up to the signal-idler frequency desired Hamiltonian can be written as[2],

$$\hat{H} = i\hbar\left(\zeta^* \hat{a}\hat{b} - \zeta \hat{a}^\dagger \hat{b}^\dagger\right). \tag{5.1.16}$$

A unitary evolution operator with this corresponding Hamiltonian gives us,

$$\hat{U} = \exp\left[\frac{-i\hat{H}t}{\hbar}\right] = \exp\left(\zeta^* \hat{a}\hat{b} - \zeta \hat{a}^\dagger \hat{b}^\dagger\right). \tag{5.1.17}$$

The final term in Eq. (5.1.17) is our desired two-mode PDC state generation operator also called the two-mode squeezing operator $\hat{S}(\zeta)$. Complex parameter ζ explains the squeezing strength or the amount of non-classicality which in principle depends on pump strength and nonlinear interaction strength. A two-mode squeezed vaccum (TMSV) state can then be generated by the action of the squeezing operator,

$$|\zeta\rangle = \hat{S}\,|0,0\rangle = \sqrt{1-\lambda^2}\sum_{n=0}^{\infty} \lambda^n\,|n_h, n_v\rangle \quad , \quad \lambda = \tanh(\zeta). \tag{5.1.18}$$

[2]A detailed description of single mode and two-mode Hamiltonian derivation can be found in Quantum optics textbook of C Jerry and P L Knight

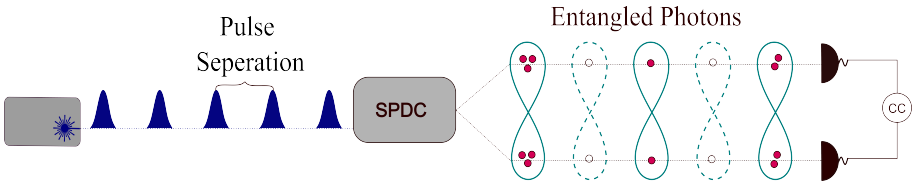

Figure 5.1.3: Schematic of a type II PDC source generating number correlated photons in two spatial/polarization modes. Click events on one of the detectors can be conditioned for the generation of non-Gaussian states of light on the other mode.

Experimental investigations on SPDC-based squeezed light sources brought up the concepts and benefits of quantum optical sensing and imaging [46, 47]. Type II sources are ideal for strong two-mode non-classical correlation probe sources.

Rest of this section we make use of Eq. (5.1.18) to explain photon number state generation from the SPDC process. Also note that the squeezing operator can generate many higher order pairs with nonvanishing probability given by a hyperbolic function of squeezing parameter[3]. In continuous variable picture squeezed light sources can produce highly correlated EPR type states where the correlation can be calculated from quadrature measurements [48]. Two different approaches to the detection of quantum light, photon number, and quadrature (intensity) measurements lucidly render discrete and continuous variable quantum optics measurement strategies in the literature. Throughout this thesis I will use optical state space on a discrete photon number basis and detection is going to be either by click detectors or with cascaded click detectors for photon number resolving capability [see Sec. 7.3.4].

Fig. 5.1.3 depicts a simple model for a heralded generation of photon number state, upon the detection of a single photon on one detector localized single photon state is obtained on the other detector [49]. For a genuine single photon or multi-photon state generation, one needs a perfect photon number resolved detector on both modes, which is then favorable to detect heralded Fock states [50]. A truncated joint probability output distribution for a two-mode squeezed state is given in Fig. 5.1.4 with a squeezing value $r = 1$ (in a lossless scenario). The presence of only the diagonal elements in the click correlation matrix indicates perfect photon number correlation in an ideal two-mode type II SPDC state. It is evident from the click correlation matrix that the generation probability of the conditioned Fock state is limited by the corresponding probability value. For the case of single-photon

[3]Note that we have dropped from complex-valued ζ for real-valued r, we are going to do phase insensitive photon counting measurements in our experiments. In general, there is a photon number-dependent phase term present in the squeezed state representation

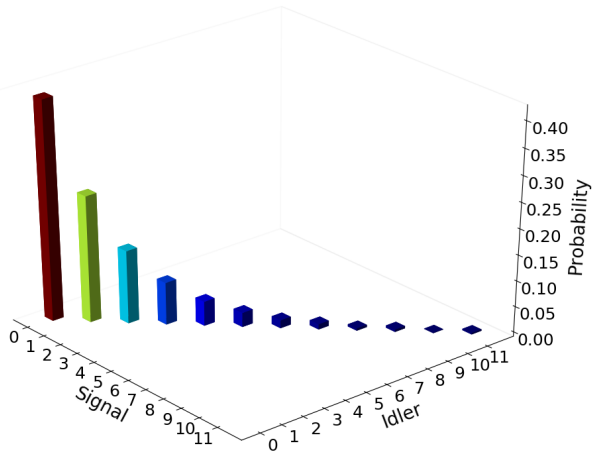

Figure 5.1.4: Two mode correlation click matrix or the expectation value for different photon number contributions for a two-mode squeezed vacuum (TMSV) state. The exponential decrease in the generation probability hints at hard bounds to achieve a higher-order Fock state.

state generation itself, the probability is limited to 25% making the source highly probabilistic. In Sec. 6.2, I will explain how an efficient multiplexing scheme can be implemented to generate single and many photon quantum states in a pseudo-deterministic and resource-efficient manner from probabilistic PDC sources.

5.1.3 Pure single photons

In the previous sections, I briefly introduced the SPDC Hamiltonian for a single spatial mode waveguide system without considering the spectral properties of the PDC photons in detail. We have introduced the squeezed state and squeezing operator in photon number description, for the generation of heralded single-photon Fock states. However, the quality of these single-photon states further depends on spectral correlations and multi-photon contributions, which can cause detrimental effects in quantum interference experiments and quantum optical applications in many ways. Characterizing the spectral properties of the PDC process is of paramount importance in engineering spectrally pure single-photon states and higher dimensional qudit state manipulation using temporal modes of photons [51]. Importantly spectrally pure single photons are an essential resource for multi-photon state manipulation, boson sampling, and multiphoton entanglement generation type experimental platforms, where many indistinguishable photons interfere in a linear optical network [52]. In this section we will look into the details of pump light and waveguide

phasematching conditions to control the spectrum of PDC photons.

Shaping the pump and phasematching

Our PDC photon generation process is driven by ultrafast pulses of light. Frequency bandwidth-rich pump pulses also inherit similar broadband properties for their PDC daughter photons. To elucidate the spectral properties of signal and idler photons, a joint spectral amplitude function has to be disclosed at this point from the PDC Hamiltonian. From Eq. (5.1.11), quantized electric field operators are simplified to get an amplitude function and operator representation given by the form [45],

$$\hat{H}_{PDC}(t) = A \int dt \int_0^L \chi^{(2)} dz \iint d\omega_s d\omega_i \; \alpha(\omega_p) \; \exp\Big[-i(\omega_p - \omega_s - \omega_i)t\Big] \times \exp\Big[i(k_p - k_s - k_i)z\Big] \; \hat{a}^\dagger(\omega_s) \; \hat{a}^\dagger(\omega_i) + h.c. \tag{5.1.19}$$

Where 'A' contains all the constants and other independent parameters followed by the Hamiltonian. In Eq. (5.1.19) susceptibility term is included in the integral, which becomes clear when we do position-dependant $\chi^{(2)}$ modulation over the material in the following section. Frequency-dependent pump function $\alpha(\omega_p)$ entrusted to be a Gaussian function with a central frequency of ω_p. Note that both energy conservation and phase matching conditions ($\Delta k = k_p - k_s - k_i$) are implicit in Eq. (5.1.19). Energy conservation requirement for the pump function $\omega_p = \omega_s + \omega_i$ enforces the function to align exactly $-45°$ in the two-dimensional signal-idler spectral distribution on a Cartesian xy-plane [Fig. 5.1.5(a)]. Since we are in the regime of ultra-short pulses, pump frequency spreads out in the plot with a specified bandwidth contained as the width of the Gaussian distribution. Predefined pump spectral bandwidths play an intricate role in the definition of spectral correlation properties of generated photon pairs. In a real experimental situation adjusting the central frequency is a mere task with a tunable femtosecond laser system and proper bandwidth selection for the pulses can be done with additional linear optical techniques (pump spectral filtering with gratings and slits), which we call pump shaping.

The phase matching function model is not straightforward, choice of the nonlinear material and relevant dispersion engineering techniques are necessary for an efficient PDC process. In Sec. 5.1.1 we insisted that phase matching among the interacting fields (original excitation field and signal/idler generated fields) is necessary for the efficient nonlinear conversion. Meanwhile, the generated field can acquire a position-dependent phase at the time of generation and a propagation-induced

phase within the material. When the two-phase contribution matches, an efficient nonlinear conversion is possible with intensity build-up at the end of the process. In certain materials it is possible to assign different polarization direction combinations for the three interacting fields, therefore polarization-dependent birefringence properties of the material are applicable to control the phases of individual fields and the technique is known as birefringence phasematching. However, not all materials possess enough birefringence strength to compensate for the phase mismatch in the desired wavelength range, which also restricts polarization choice tuples for the fields. Later the technique of quasi-phase matching is re-introduced to engineer the nonlinear coefficient of the material externally in a user-defined manner [53].

Potassium Titanyl Phosphate (KTP) has been a workforce in the past for its phase-matching properties and parametric generation process in the telecommunication wavelength regime (1550 nm). The potential application of quantum light sources in the telecommunication wavelength makes the material ideal to integrate with fiber-based technologies. Throughout this thesis we use *quasi-phase-matching* (QPM) enabled KTP waveguides for type II SPDC process and quantum light generation [54]. QPM is achieved by periodically or aperiodically changing the nonlinear properties of the waveguide over the length of the sample. In a periodic modulation, $\chi^{(2)}$ nonlinearity of the material is periodically inverted with a 50% duty cycle format. A single duty cycle modulation length represents the poling period 'Λ', a parameter that fills the phase mismatch. Practically poling is done by placing an electrode mask on top of the sample like the predefined poling pattern and period. Application of voltage to the electrodes creates a periodic inversion of onlinearity [55]. Fabrication parameters like width and depth of waveguide are important otherwise, spurious effects can destroy the conversion process [56].

We now revisit the PDC Hamiltonian with an additional term in the phase mismatch equation, obtained from the periodic poling condition,

$$\Delta k = k_p - k_s - k_i + \frac{2\pi}{\Lambda}, \tag{5.1.20}$$

$\frac{2\pi}{\Lambda}$ act as a grating vector (k_{QPM}) component and accessible by Λ, to provide phase-matching on the desired wavelength conversion range. Rewriting the Hamiltonian in Eq. (5.1.19) to incorporate phase mismatch compensation gives,

$$\begin{aligned}\hat{H}_{PDC}(t) = A \int dt \int_0^L dz \iint d\omega_s d\omega_i \; \alpha(\omega_p) \; \exp\Big[-i(\omega_p - \omega_s - \omega_i)t\Big] \\ \times \; \exp\left[i\left(k_p - k_s - k_i + \frac{2\pi}{\Lambda}\right)z\right] \; \hat{a}^\dagger(\omega_s) \; \hat{a}^\dagger(\omega_i) + h.c.\end{aligned} \tag{5.1.21}$$

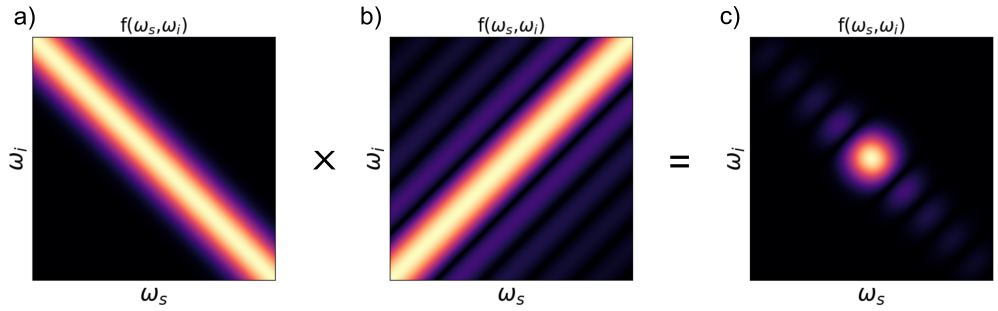

Figure 5.1.5: Joint spectral amplitude for a decorrelated state is plotted (c) for arbitrary values of spectral range and bandwidth. The *sinc* nature of phasematching imparts the same characteristics to the final JSA spectrum with side lobes, affecting the overall purity of the photons.

During the integration, we can consider the length of the crystal as the integration limit for the propagation distance. Also a sinusoidal variation $\left(\chi_0^{(2)} \sin\left(\frac{2\pi}{\Lambda} z\right)\right)$ is approximated for $\chi^{(2)}$ rather than the actual square variation. $\alpha(\omega_p)$ can be replaced to $\alpha(\omega_s+\omega_i)$ by the mathematical identity of a delta function. Periodic oscillation of nonlinearity and sharp waveguide boundaries (specific length 'L') forces the phase-matching function to take the form,

$$\hat{H}_{PDC}(t) = A \iint d\omega_s d\omega_i \;\; \alpha(\omega_s + \omega_i) \;\; \mathrm{sinc}\Big(\Delta k(\omega_s, \omega_i) + \frac{2\pi}{\Lambda}\Big)\, \hat{a}^\dagger(\omega_s)\, \hat{a}^\dagger(\omega_i). \quad (5.1.22)$$

Equation (5.1.22) provides the final expression for the Hamiltonian with a cardinal sine (or *sinc*) shape behavior for the phasematching. Together with a Gaussian approximated pump, joint spectral properties of the state can be described as product function,

$$f(\omega_s, \omega_i) = \alpha(\omega_s + \omega_i) \;\; \times \;\; \mathrm{sinc}\Big(\Delta k(\omega_s, \omega_i) + \frac{2\pi}{\Lambda}\Big). \quad (5.1.23)$$

Following Eq. (5.1.23) a theoretical plot for the joint spectral amplitude (JSA) is given in Fig. 5.1.5. Pump bandwidth and phasematching are adjusted to get a near-ideal circular shape for the product state, which is also the signature shape for a decorrelated state. Later in the experiment, I will show a decorrelated JSA for signal-idler photons through joint spectral intensity measurements.

Spectral engineering

Identifying the spectral correlation between the signal and idler photons is important in the sense of state engineering and corresponding applications. Now the spectral

information can be extracted from the definition of the JSA function formulated above in Eq. (5.1.23), which is encoded as a two-dimensional distribution or in a matrix form. We make use of singular value decomposition method (or Schmidt decomposition) to decompose $f(\omega_s, \omega_i)$ into a product of two orthonormal set of functions (ϕ_k, ψ_k) and can be written as [45, 57],

$$f(\omega_s, \omega_i) = \sum_{k=0}^{\infty} \lambda_k \ \phi_k(\omega_s) \ \psi_k(\omega_i). \tag{5.1.24}$$

Decomposition outcomes, Schmidt modes (ϕ_k, ψ_k) and Schmidt coefficients λ_k ($\lambda_k \geq 0$ and $\lambda_k > \lambda_{k+1}$) are now the quantifiers for spectral correlation within the state. Schmidt decomposition for JSA also brought up a complete quantum mechanical framework for the time-frequency modes of PDC photons [51]. The spectrally broadband nature of photons can be explained by decomposed time-frequency (TF) eigenmodes in a suitable basis set. With the advent of corresponding broadband creation operators PDC state operators can be written as,

$$A \iint d\omega_s d\omega_i \ f(\omega_s, \omega_i) \ \hat{a}^\dagger(\omega_s) \ \hat{a}^\dagger(\omega_i) = A \sum_{k=0}^{\infty} \lambda_k \ \hat{P}_k^\dagger \ \hat{Q}_k^\dagger \ , \tag{5.1.25}$$

where $\hat{P}_k$, $\hat{Q}_k$ form the corresponding broadband TF operator for the eigenmodes given by,

$$\hat{P}_k^\dagger := \int d\omega_s \ \ \phi_k(\omega_s) \ \ \hat{a}^\dagger(\omega_s) \ , \tag{5.1.26a}$$

$$\hat{Q}_k^\dagger := \int d\omega_i \ \ \psi_k(\omega_i) \ \ \hat{a}^\dagger(\omega_i). \tag{5.1.26b}$$

The intrinsic higher dimensional nature of TF degree of freedom was shown to be useful in qudit state engineering, and entanglement generation using TF modes of PDC states. On the measurement aspects engineered nonlinear devices like *Quantum Pulse Gate* (QPG) [58] can perform single or multi eigenmode-selective measurements on TF states; enabling tomographic kind state reconstruction in TF degree of freedom [59, 60].

If we have many spectral modes present in the state, upon detection of an idler photon, signal photon information is revealed because of the strong spectral entanglement from Eq. (5.1.24). This makes the heralded photon spectrally distinguishable and limits its application. A relevant parameter called Schmidt number is introduced to calculate the amount of spectral multimodness in the state,

$$K = \frac{1}{\sum_k \lambda_k^4}. \tag{5.1.27}$$

The presence of many Schmidt modes always gives a value $K > 1$, the higher this value higher the spectral entanglement. But the case of $K = 1$ is special in the sense that there should be only a single pair of Schmidt modes contributing to the state. Equation. (5.1.24) then boils down to a product of two basis sets, producing a spectrally separable state called *decorrelated* state. Detecting a photon on the idler side now projects the signal mode into a completely mixed state, revealing no spectral information about the heralded photon. Therefore heralded spectrally pure single photon state generation is possible in the case of decorrelated JSA with $K = 1$ [61]. In a spectrally multimode situation ($K > 1$), a heralded single photon state is possible at the expense of strong filtering on the heralding side. This will effectively reduce the overall heralding efficiency and brightness of the system [62]. In an ideal case, a decorrelated source avoids spectral filtering and generates a bright spectrally pure single-photon state. Note that no detector can spectrally resolve the photons during the detection, which makes the detectors informationally blind for any type of spectral correlation.

The idea of spectral engineering now can be employed by manipulating material dispersion properties and pump bandwidth structure. Since we already fixed the KTP waveguide as our choice, group velocity dispersion properties of optical fields and corresponding phasematching properties are adjusted in the operational range of 775 nm pump central wavelength and 1550 nm for signal-idler wavelength spectrum. Symmetric group velocity matching technique is used to engineer group velocities of the interacting fields within the selected non-linear material (KTP)[4]. This can be achieved by assigning different polarization to the pump-signal-idler modes, and birefringence properties of KTP then organizing the group velocity of the pump field to stay between the group velocity of the signal and idler field. Consequently, the phasemacthing angle follows near $+59^\circ$ slope (positively oriented) concerning the x-axis of the phasematching spectrum, which essentially bisects the -45° oriented pump to get a nearly decorrelated JSA product state.

Once we fix the phasematching function, adjusting the pump bandwidth can create a JSA spectrum with different characteristics like correlation, anti-correlation, and decorrelation within the state. In Fig. 5.1.5 a decorrelated JSA is derived for our periodically poled waveguide structure. Because of specific periodic poling and sharp boundary conditions phasematching function turns out to be a *sinc* shaped one. It's evident from the final product state that the JSA has contributed from these side-lobs, correspondingly high values of purity are still not achievable directly on such devices. A near-circular shape can be obtained by spectral filtering with

[4]A detailed visualization of dispersion engineering and phasematching angle description on frequency conversion process (also for SPDC) can be found here [63]

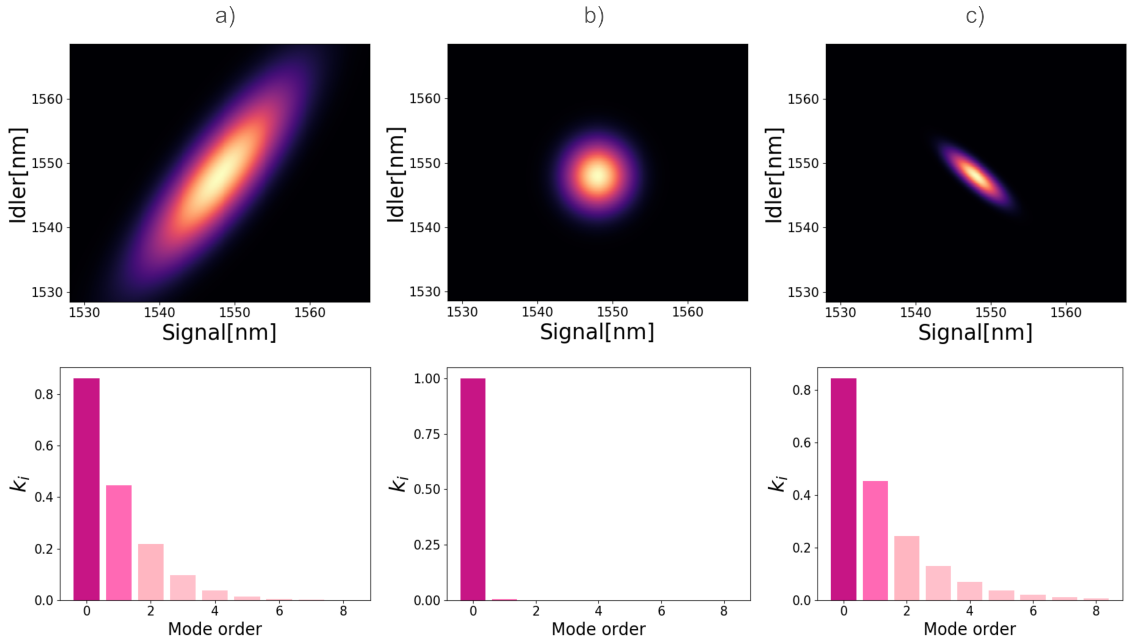

Figure 5.1.6: (top) Two-dimensional plot for JSA function by considering Gaussian profile for both pump and phasematching, with three different pump bandwidth settings [a) broad, b) optimized, c) narrow]. Corresponding Schmidt coefficient values for the mode order are obtained by the singular value decomposition of the respective JSA spectrum (plotted along the bottom line).

proper bandwidth, which discards the *sinc* side lobes and increases overall state purity.

To avoid all kinds of filtering practices, different types of poling patterns have been explored before. Instead of a 50% duty cycle box function type poling pattern, a position-dependent Gaussian poling approach looks ideal for a perfect *decorrelated* state. For a Gaussian phasematching distribution with different pump bandwidth configurations [64], corresponding $f(\omega_s, \omega_i)$ is envisaged in Fig. 5.1.6. A broader pump can generate a positively correlated JSA [fig. (a)] with $K = 1.8$, and a narrower pump [fig. (c)] can give a negatively correlated JSA with $K = 1.68$. Both of them contribute multiple spectral modes and therefore spectral entanglement. Finally, an optimized pump-phasematching bandwidth setting generates a perfect decorrelated state with symmetric Gaussian distribution for both signal-idler spectra, resulting in a Schmidt number $K = 1.00002$ [fig. (b)]. The importance of decorrelated states becomes clear when we start to interfere with two or more photons from two different sources or a single source in a multiplexed manner. Otherwise, multimode nature ($K > 1$) is a resource to engineer higher-dimensional quantum

states using TF modes of a single photon.

The single mode and multimode nature of JSA also have some implications on the photon number statistics of the state. In a multimode situation, the PDC output state also can act as a source of multimode squeezers. Each mode can act as a source of TMSV state. This can be equivalently written as,

$$|\Psi_{PDC}\rangle = \bigotimes_k \operatorname{sech}(r_k) \sum_{n=0}^{\infty} \tanh^n r_k \, |n_h, n_v\rangle \,, \tag{5.1.28}$$

a tensor product of many squeezed states where 'k' denotes a single squeezer identifier. Such multimode nature can give different signal-idler marginal photon statistics and can be probed experimentally [65].

5.1.4 Two photon experiments

We have been following the well-established mathematical descriptions for the *Parametric Generation* process in the last sections. However, the most interesting part is quantifying the predictions with experimental results. In a practical situation losses and decoherence can degrade our predictions. Therefore the observation of quantum effects needs several optimization tasks. We implement an efficient waveguide incorporated twin photon source and benchmark its performance by maximizing different source parameters.

We use commercially available periodically poled KTP (PPKTP) waveguides (from *AdVR Inc*) phasematched for a parametric type II decay process 775 nm $\rightarrow$ 1550 nm + 1550 nm, as our primary source for the SPDC light. Three different waveguide samples are characterized during the development of a single and entanglement source project. We name these waveguides as 1, 2, and 3 for now, waveguide 1 is damaged during the coating process. So partial test data is available for sample 1. More test data are made available for waveguides 2 and 3, on different experimental plots in this section. Finally, we chose a specific waveguide with optimized values for experiments like the Hong-Ou-Mandel test, correlation test, and entanglement source development.

Optical characterization of waveguides is done beforehand and in-house, for both linear and nonlinear effects. For the linear case, optical transmission losses in the waveguides are measured (0.01 dB/cm) by interferometric measurements. On the other hand, the SHG (in line with a reverse PDC process) conversion experimental method is used to characterize nonlinear responses of the poled KTP waveguides. This is done by exciting the waveguide modes with both horizontal and vertical polarized 1550 nm light to generate sum frequency output at 775 nm. Since we use

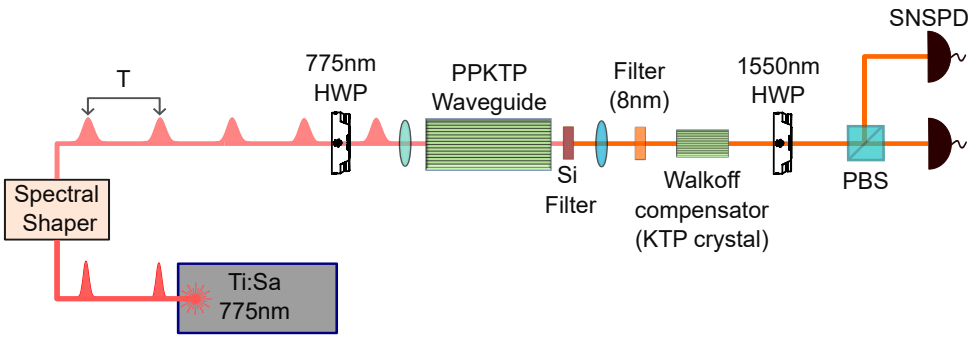

Figure 5.1.7: Experimental model for a twin photon source characterization setup.

tunable input laser light for the SHG process exact phasematch wavelength can be scanned for each waveguide. Corresponding SHG output efficiency is important to understand the quality of waveguides, and also reveals the operational wavelength range (pump and PDC light) of our SPDC process. Waveguide spatial mode behavior is analyzed by coupling light from one side and imaging the beam profile at the exit side for both TE and TM input polarization (actually experiment with both 775 nm and 1550 nm light separately for its spatial propagation behavior).

Setup Description

A mode-locked Titanium-sapphire (Ti-Sa) laser produces pulses of light with a pulse width of 150 fs and a repetition rate of 76 MHz (pulse separation of 13.15 ns). Since femtosecond (fs) pulses are broadband we need to have fine control over the pulse bandwidth for the pump shaping. This can be done by a grating sand-witched 4f line, broadband pulse from the laser is positively chirped upon first reflection from a grating, and an adjustable slit will select the proper spectral range from the chirped output for the experiment. This selected part is then reflected back to the grating for a negative chirp, again creating a short pulse with a specific bandwidth. A short single-mode fiber (PM type, $l = 15$ cm) is placed on the pump path for spatial filtering. The low pump power requirement of our waveguide source (< 1 mW) makes sure that no spurious nonlinear optical processes are happening inside the fiber. Pump light is coupled to the waveguide by an aspheric lens ($f = 6$ mm) system on both ends of the waveguides. Fabrication imperfection can alter the waveguide mode from ideal Gaussian, limiting the pump coupling from single mode fiber to waveguide mode to 40%. Absorption properties of Silicon in the range of 775 nm are used for the maximum pump suppression on the other side of the waveguide, which also benefits high transmission properties in the telecom (1550 nm) range. Addi-

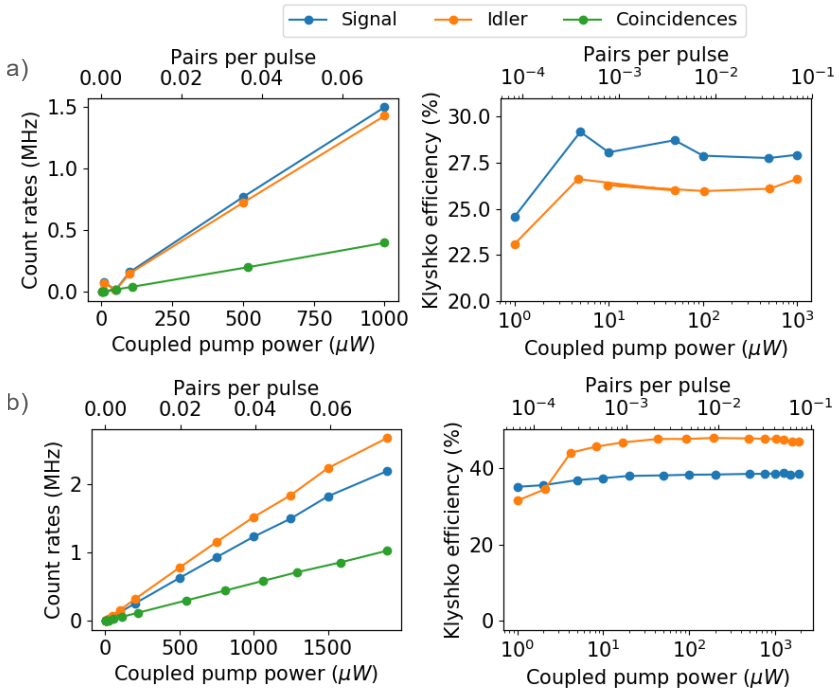

Figure 5.1.8: Photon counts measurement data from two different waveguide sources (waveguide 2 (fig. a) and waveguide 3 (fig. b)) [1]. (left) Single's and coincidence counts for different pump power strengths. (right) Klyshko efficiencies were calculated for the signal and idler arm from raw data for different pump power coupling. For all measurements pump power values are measured after the waveguide.

tional filters of bandwidth 8 nm (and 12 nm) and operational central wavelength 1550 nm are used to avoid side lobes coming from the *sinc* phasematching. Finally, a polarization-dependent beam splitter separates the signal and idler photons and directs them to single-mode fibers with a collection efficiency close to 80%. Superconducting nanowire detectors with an efficiency of 78% are used for detecting these fiber-collected photons.

One of the primary benchmarks for a quantum light source is its overall system efficiency to deliver and detect single photon events, we use the Klyshko method [66] to characterize the source efficiency,

$$\eta_{signal} = \frac{R_{CC}}{S_{idler}} \quad \text{and} \quad \eta_{idler} = \frac{R_{CC}}{S_{signal}} \ . \tag{5.1.29}$$

The efficiency of each arm is calculated by the ratio of coincidence counts (R_{CC}) to single counts (S_{idler}) from the opposite arm; η_{signal}, η_{signal} stands for efficiency of

the individual arm. Losses and fiber-waveguide spatial mode mismatch can severely affect the efficiency of the source. Losses in the optical surfaces and fiber coupling efficiencies can be quickly estimated by sending classical light through the setup. Such estimates are beneficial to compare the observed efficiency with the expected values from the setups. During the pump coupling, we make sure that waveguides are excited in a single spatial mode (775 nm) to avoid multimode PDC effects, which essentially deteriorate pair production efficiency and reduce coincidence rates. We achieved a maximum of $> 50\%$ heralding efficiencies in our measurements. Multiple sets of waveguides show heralding efficiencies in the range of 30% to 50%. The brightness of the order of 3×10^6 pairs/(mode·s·mW) is observed in multiple waveguide channels. On average tested waveguides produce a million counts for a milli-Watt pump power, which makes the source an essential tool for high gain squeezed light generation with high pump strength. But at the moment we run the source in a low pump power regime for single photon state generation. Single and two-photon coincidence rates, Klyshko efficiencies, and brightness for multiple waveguides are given in Fig. 5.1.8.

Spectral properties of the photons are estimated from the joint spectral intensity (JSI) measurements. We make use of a time of flight spectrometer method [67] to measure the JSI. Signal and Idler photons are sent through long dispersive fibers, and the arrival time of photons is then mapped to the corresponding two-dimensional wavelength or frequency spectrum. Theoretically expected JSA (for a 9 mm waveguide sample length with 2.6 nm pump bandwidth) and experimentally observed JSI are given in Fig. 5.1.9. By slightly adjusting the pump bandwidth and tweaking the filter angle a circular JSI is obtained for some efficient selected waveguides. Theoretical predictions show a spectral purity of $\approx 86\%$, while experimental observation shows $> 97\%$ purity for multiple waveguides. This is essentially due to the broadband filters in the signal-idler optical path, increasing the purity by throwing away the side lobes of the actual JSI.

It is important to experimentally observe some genuine quantum or let's say nonclassical behavior for the light state; in our case, from type II PDC light. Practically one can generate a light state with a mean photon number of one or at the few photon level by optical attenuation from readily available sources like lasers or flash lamps. One of the striking difference between those coherent/incoherent classical sources and genuine quantum sources are their self-contained photon statistics properties. Second-order correlation functions in terms of measured classical light intensities provide an explicit platform to test the photon statistics [68]. Quantum

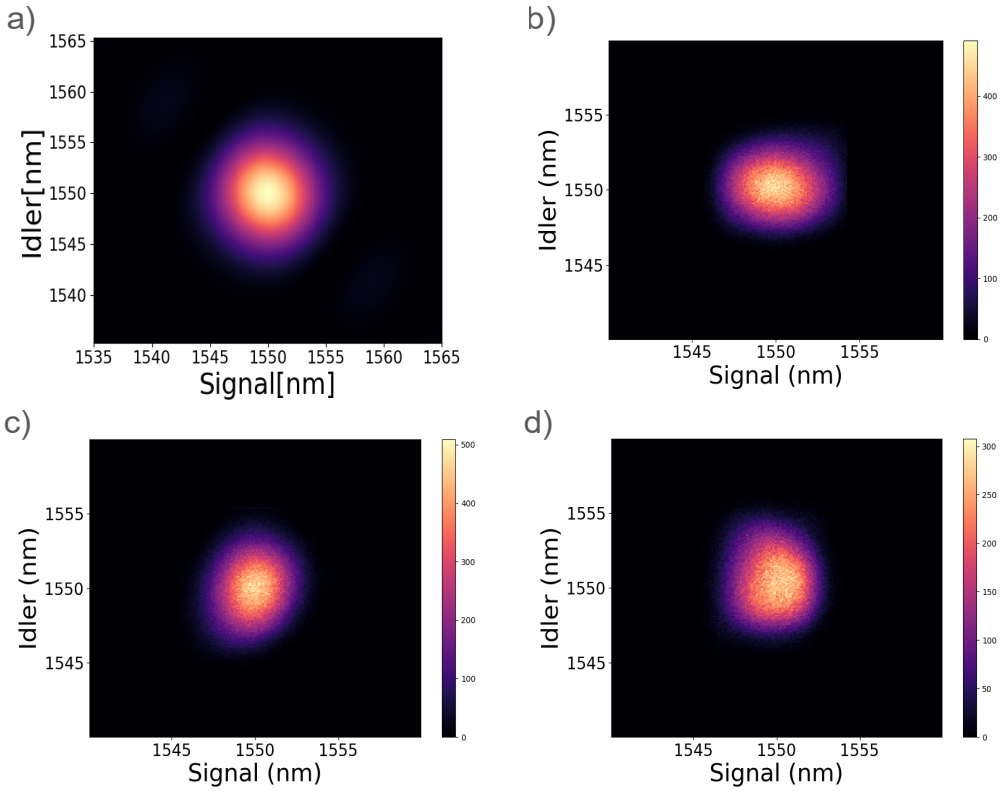

Figure 5.1.9: (a) Absolute value of JSA distribution generated by considering realistic settings (waveguide parameters and pump bandwidth). Plots b, c, d (waveguide #1, #2, #3) show experimentally observed JSI for three different waveguides from three different samples. Each sample has many waveguides in it with different poling periods and waveguide dimensions.

version of second-order coherence correlation function $g^{(2)}(0)$,

$$g^{(2)}(0) = \frac{\langle \hat{a}^\dagger \hat{a}^\dagger \hat{a} \hat{a} \rangle}{\langle \hat{a}^\dagger \hat{a} \rangle^2} \ , \tag{5.1.30a}$$

$$g^{(2)}(0) = 1 + \frac{\langle (\Delta \hat{n})^2 \rangle \ - \ \langle \hat{n} \rangle}{\langle \hat{n} \rangle^2} \ , \tag{5.1.30b}$$

which distinguishes the existence of both classical and nonclassical states of light from corresponding expectation values (Eq. (5.1.30b)) and intensity counts. Experiments essentially involve single and coincidence measurements at the output of a 50:50 splitter, while the input side contains probe light on one mode and vacuum on the other as in the Fig. 5.1.10.

For our type II PDC source running in spatially and spectrally single mode, par-

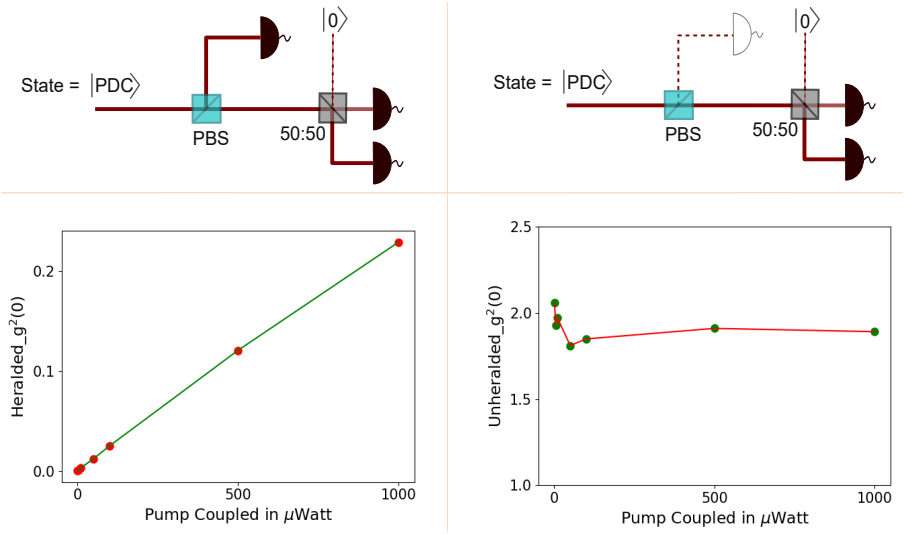

Figure 5.1.10: Data with waveguide #3. On the left three-fold coincidence measurement setup for heralded $g^{(2)}(0)$ measurement. For different pump power settings $g^{(2)}(0)$ shows values less than one, *anti-bunching* property of the non-classical light state, where heralding projects the other mode into a genuine single-photon state. Unheralded $g^{(2)}(0)$ measurements on the right side show values close to two for *bunching* effect from a marginal thermal beam. In both measurements $g^{(2)}(0)$ shows a slight power dependant behaviour.

tial trace operation on one mode (either signal or idler) leaves behind the marginal into a mixed state and follows thermal photon statistics [69]. So a *bunched* light characteristic value of $g^{(2)}(0) = 2$ for the marginals indicates perfect thermal state behavior from the source. A tendency to shift this value towards $g^{(2)}(0) = 1$ indicates the presence of spectral multimodness (Multiple squeezed modes causes the convolution of its corresponding thermal behavior, which converges to a Poissonian statistics [70].) and noise count contributions from other sources, which then attributes Poissonian photon statistics. In low pump strength PDC source, heralding one mode prepares a single photon state on the other mode with *no or reduced* probability of having coincidence clicks at the beam splitter output. Therefore heralded correlation data shows $g^{(2)}(0) < 1$, a nonclassical signature otherwise called *anti-bunching* effect in photon statistics [71]. Even though there is no direct relationship with bunching or anti-bunching, Eq. (5.1.30b) is sometimes useful to explain the *sub-Poissonian* behavior of light. Where the condition $\langle(\Delta\hat{n})^2\rangle < \langle\hat{n}\rangle$ entails a nonclassical behavior for the optical state to overcome the Poissonian (or shot noise) noise limits of coherent light ($\langle(\Delta\hat{n})^2\rangle = \langle\hat{n}\rangle$). Other experimentally viable tests like Mandel's Q_M parameter [72] and binomial Q_B parameter [73] are also useful to test

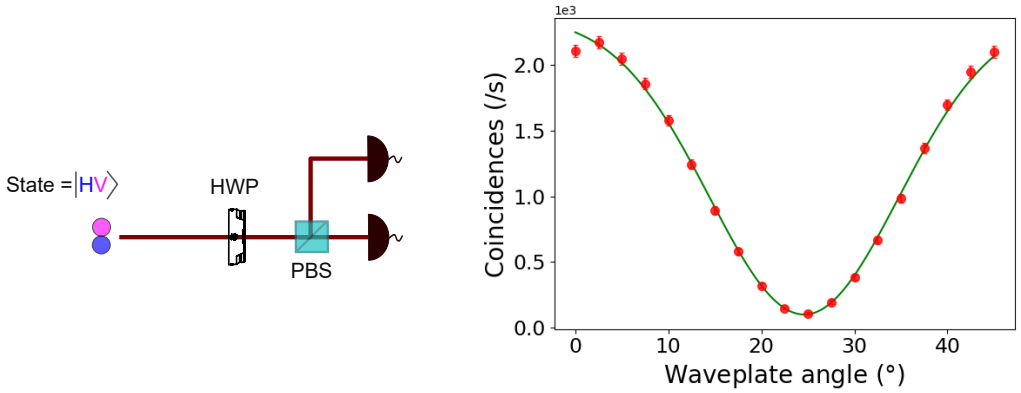

Figure 5.1.11: (left) Polarization-based HOM experimental arrangement for two-photon interference. (right) Experimentally observed HOM dip data set and theoretical curve fit from one of the selected waveguide. HOM visibility of $> 93\%$ is possible with this source (waveguide #3).

the classical-nonclassical deviations, which can also find a direct relationship with second order quantum coherence function $g^{(2)}(0)$. Experimental findings of $g^{(2)}(0)$ for one of our waveguide source can found in Fig. 5.1.10.

The indistinguishable nature of PDC pair photons is tested with the most celebrated Hong-Ou-Mandel experiment (HOM) [16]. In analogy to a beam splitter-based HOM experiment, a PBS-based HOM experiment is envisaged in our setup. Orthogonally polarized collinear signal-idler photons are sent through a combination of HWP and PBS. The optical axis of the HWP is swept from 0° to 45°, changing the two-photon polarization state from distinguishable to indistinguishable concerning the HWP and PBS combination. As a consequence of a pure quantum effect coincidence rate in the output of the PBS falls to a minimum value (depending on the distinguishability of photons), where the two photons always follow the same output mode. HOM interference visibility is then obtained from the corresponding maximum (C_M) - minimum (C_m) coincident counts. A polarization HOM variant experiment has a different expression for visibility value given by,

$$\mathrm{V}_{HOM} = \frac{C_M/2 - C_m}{C_M/2}. \tag{5.1.31}$$

We experimentally observe the visibility of $(93 \pm 2)\%$ for two-photon interference with signal-idler photon pairs. In a perfect case, this means when the photons become completely indistinguishable, HOM visibility should reach 100% with no coincidence at the detectors. But this is not expected in our case for multiple reasons. When the two photons are emitted from the waveguide exit port, except the

polarization degree of freedom we expect perfect indistinguishability for the photons in other degrees of freedom. This is not true, since the birefringence property of KTP material can impart relative time delay between orthogonally polarized photons while on propagation through the waveguide. Within the experimental setup, this relative delay is compensated by placing a bulk KTP crystal on the beam propagation path. We chose the crystal length half the length of our waveguides[5], and placing the crystal in such a way that waveguide and bulk crystal optic axis are 90° off to each other. Then the polarization-dependent temporal delay from the waveguide is compensated upon propagation in a similar material with 90° off-axis. Since our choice of compensation crystal length is not optimum, uncertainty in the crystal length choice and the pair creation point inside the waveguide can affect the interference quality. The provision of a perfect circular JSA spectrum is possible by bisecting the pump function with an ideal 45° phase matching angle. But this does not hold for our KTP waveguides, where it is slightly off. Consequently, signal-idler photons possess slightly different spectral bandwidths in the JSA spectrum, imparting the same amount of distinguishability to diminish visibility. Recently our group started to explore higher-order spatial modes for pump excitation in the KTP waveguide to tune the phase matching angle but keep 1550 nm generation in fundamental mode, which seems to be a promising approach to reaching the near-ideal phasematching angle in the KTP waveguides. There is always a fundamental trade-off in the visibility of a two-photon HOM experiment with a PDC source, where the squeezing operator always contains the higher-order photon number contribution. Optimal operational pump power is crucial to maximize the HOM dip quality. Similar to signal-idler HOM experiments it's possible to test the signal-signal or idler-idler type HOM experiments. Since we have spectrally pure photons generated within the source, it's possible to attain high indistinguishability between two different emitted pairs at two different time bins. We will look more into these details in our time-multiplexed quantum state engineering section.

[5]Choice of this length is under the naive assumption that, on average the PDC photon generation process happens at the center of the waveguide. This seems to be working well in our samples, our new experimental observation having 97% HOM visibility

5.2 Hybrid Bulk-Integrated Entanglement Source

5.2.1 Introduction

Over the years photonic sources of entanglement have played an important role in testing many theoretical quantum models. Ground-breaking experiments like Bell's tests, quantum teleportation, entanglement swapping, and cryptography, were first realized in the lab with photonic sources of entanglement [74–76]. Since then there have been efforts to build efficient and on-demand sources of entangled photons. SPDC process has shown to be an efficient method to engineer entangled states of light in many degrees of freedom and is still an active field of research [77, 78]. For the first time, we introduce a new kind of polarization entanglement source with integrated waveguide structures in a hybrid-bulk experimental setup. We make use of a type II PDC process to generate polarization entangled states of light, by adapting two mode polarization source of light in a suitable linear optic setup geometry. This section will detail the state generation concepts, challenges, and benchmarking performance of our source by evaluating several criteria needed for an efficient entanglement source. Based on the optimized performance for single and two-photon experiments we now fix our waveguide choice to waveguide #3 and continue the experiments on entanglement source development.

5.2.2 Polarization entangled photons

In quantum state formalism, the non-separability of a multipartite system into different subsystems is always an intriguing problem in defining the system in question. Schrödinger coined the term quantum entanglement for this kind of behaviour [79] and entangled states found remarkable nonclassical features later on in different areas of quantum physics. On the aspects of the nature of reality, non-locality, and hidden variable theory eminent people like Einstein, Bohr, Bell, and many others considered the simple theoretical model of a two-particle entangled state to debate the very fundamental nature of quantum mechanics [11, 80]. Then later there were a series of experiments to prove or disprove these conceptual ideas by generating entangled states from two particles to many particles using photons, ions, and atoms [81–83]. Most simplest and well-studied bipartite entanglement states are considered here for the understanding of the topic and the scope of this section.

We consider the polarization degree of light associated with two individual pho-

tons for entanglement creation and write down the state for definition,

$$|\psi_{\pm}\rangle = \frac{1}{\sqrt{2}}(|H_1V_2\rangle \pm e^{i\phi}|V_1H_2\rangle) \ , \tag{5.2.1a}$$

$$|\phi_{\pm}\rangle = \frac{1}{\sqrt{2}}(|H_1H_2\rangle \pm e^{i\phi}|V_1V_2\rangle). \tag{5.2.1b}$$

Equtaion (5.2.1a) and (5.2.1b) represent maximally entangled Bell states for two photons (marked as 1, 2) in two polarization modes. Entangled states in an arbitrary polarization basis can be manipulated by the action of linear optical elements like waveplates. Which makes the photon's polarization degree of freedom an essential choice for entanglement manipulation and measurements.

5.2.3 More on waveguide versus bulk sources

Polarization entanglement was realized in multiple material platforms, especially using bulk nonlinear crystals in low gain, two-level emitters approach on semiconductor quantum dots [84]. Rather than a cryo-cooled semiconductor platform nonlinear crystal-based approach has the advantage of room-temperature operation. On top of that nonlinear sources provide access to higher order heralded Fock states, and bright squeezed light states by cranking up the pump power in the same setup; those state finds application in many complex sampling experiments. Polarization entanglement demonstration exists with SPDC sources, covering all kinds of phase-matching, type I, type II, collinear, and noncollinear in a single pass or double pass pump configuration; a detailed review can be found here [85]. As we faced in the heralded source case [Sec. 5.1.4], the three-way tradeoff between brightness, fiber-coupling efficiency, and spectral purity in bulk source place a major limitation, making the entanglement type source engineering also a challenge. The bulk material theoretical model explains, the fundamental trade-off between collection efficiency and brightness essentially depends on the optical beam focusing parameter (κ) condition [86],

$$\kappa = \frac{L}{k\omega_o^2}, \tag{5.2.2}$$

which depends on sample length (L), Gaussian beam waist ω_o (for signal, idler and pump) and its wave-number (k). Note that stringent condition potentially relates coupling efficiency and brightness in a reciprocal manner: high brightness requires a tight pump focus which concentrates the down-converted light into the spatial modes collected by the fibers. Spatial multimodness can be another limitation when we

deal with the tight focusing condition on bulk crystals, which enforces strong spatial filtering to maximize the pairs. High Klyshko efficiency, however, requires a weak focus that more strongly correlates the spatial modes of signal and idler photons such that if one photon is coupled into the fiber, the other is likely to be coupled too. This trade-off means the fundamental performance limits of bulk sources have largely been saturated. These limitations can be solved by the introduction of spatially and spectrally single-mode waveguides. Single spatial-mode waveguides in particular completely decouple the brightness from the focusing conditions. While the brightness of bulk sources with optimal focusing scales with increasing nonlinear crystal length as $\sqrt{L}$ or constant, the brightness of waveguide sources increases proportionally to L, as well as inversely with the effective area. The fundamental condition of focusing parameters in bulk experiments is now replaced by technical solutions of efficient light coupling *to/from* waveguide. For single spectral mode operation, spectral engineering in bulk source has a certain range of focusing parameters where the spectral purity is maximized. In waveguides, this spectral-spatial coupling is eliminated thanks to the single-spatial-mode propagation, allowing the spectral purity to be independently optimized. This is evident from our spectrally engineered waveguide-based single photon source and JSI measurements. In our new scheme, we replace the bulk crystal approach with an optimized waveguide-based squeezed light source and demonstrate efficient polarization-entangled light state generation. We adapt the idea of single crystal, double pass interferometric configuration for the source architecture, which is a standard arrangement however with an integrated waveguide source inside it.

Sagnac sources

There are realizations of single or double crystal-based interferometers to generate polarization-entangled light, but in the latter case, two identical SPDC sources are required which is a hard task to obtain all the time [87]. The basic idea for an entangled state generation in this kind of setup is to pump the PDC source with two different possibilities and erase the which-way information of the possible photon pair emission for quantum interference. A remarkable source design was proposed and tested in the form of a Sagnac interferometer configuration with bulk PPKTP bulk samples [88]. Unlike the other interferometer approaches Sagnac approach was intrinsically phase stable and used a single nonlinear crystal for the state generation [89]. In a PBS-based Sagnac source, a type II PDC source is placed inside an interferometer mostly in triangular geometry. Bidirectionally pumping the source serves the possibility of having a pair of photons from either of the side. These two

possibilities then interfered in the PBS giving rise to a polarization entangled state at the output of PBS. Since all the beams follow the same path precise spatial mode matching is possible in such a configuration, and spatial mode overlap is important for interference quality. Bulk Sagnac sources reached high-quality entangled state with high state fidelity [90]. The single-mode waveguide and output fiber coupling ensure indistinguishability in the spatial degree of freedom, but extra care must be taken to ensure time-frequency overlap, particularly as spectrally pure photons require relatively broadband pump pulses, especially compared to continuous-wave sources. The Sagnac scheme does not require degenerate signal and idler emission but does require that the clockwise (c) and counter-clockwise (cc) paths remain indistinguishable. Even though both paths encounter the same optical components, they encounter them at different wavelengths and polarizations (e.g. pump versus photon wavelength, signal vs idler polarization). Any uncompensated dispersive or birefringent materials or coatings thereby reduce the polarization entanglement generated by coupling polarization information to the time-frequency degree of freedom.

Sand-witching a Type II PDC source inside a Sagnac source generates a correlated light source in polarization and photon number. The Quantum state which explains the overall output state out of the interferometer is given by,

$$|\psi\rangle = (1 - |\lambda|^2) \sum_{m,n=0}^{\infty} \lambda^m (e^{i\phi}\lambda)^n |m\rangle \otimes |n\rangle \otimes |n\rangle \otimes |m\rangle, \tag{5.2.3}$$

where λ stands for squeezing parameter and ϕ contain the overall phase acquired from the setup. The preliminary experimental task is to test the source performance in the low photon number regime with relatively low pump power. This allows us to characterize the source for the two-photon polarization entangled state. Later in the next chapter, I will explore the full state mentioned in Eq. (5.2.3) for macroscopic polarization entanglement and polarization squeezing effect with large photon number contribution with strong input pump power.

In low gain regime the state in Eq. (5.2.3) is approximated to $|\psi\rangle \sim |H\rangle \otimes |V\rangle + e^{i\phi}|V\rangle \otimes |H\rangle$. Which is the well-known polarization entangled pair, post-selecting from the total photon number subspace of two (i.e. $m + n = 2$). Two of the maximally entangled Bell states $|\psi_\pm\rangle$ can be obtained by tuning phase from 0 to π respectively. By placing another half-wave plate on one of the output arms it's possible to generate other two $|\phi_\pm\rangle$ Bell states. In general, the required state is post-selected from a multi-photon state, so there is always a trade-off between the pumping strength and entanglement quality. The higher the pump strength higher the squeezing, therefore higher order photon number contribution comes out from the source. Together with the setup's asymmetric

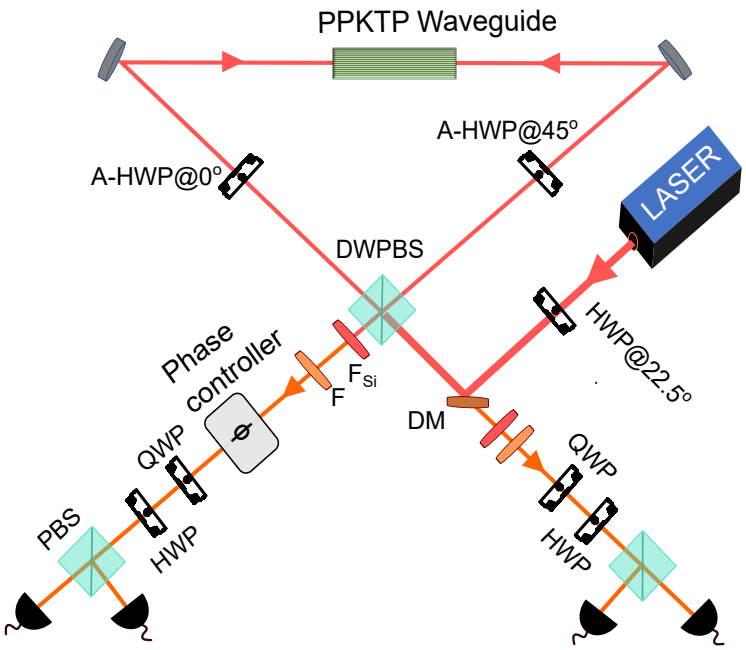

Figure 5.2.1: A hybrid bulk-integrated Sagnac polarisation entangled source [1]. The red and orange lines facilitate the pump and PDC optical path. HWP - half-wave plate, PBS - polarization beam splitter, Phase controller - Soleil-Babinet compensator (SBC), A-HWP works for both 775 nm and 1550 nm light, dual-wavelength Sagnac PBS (DWPBS) also works for both wavelengths. Two achromatic lenses of focal length 6 mm are used for waveguide coupling. A dichroic mirror (DM) reflects the pump light while transmitting the PDC photons to the measurement side. Silicon filters (F_{Si}) are used to suppress the residual pump light on the signal - idler path (but good transmission for telecom photons). Additional broadband filters (F) reject the unwanted PDC spectral sidelobes.

losses, the final output can have false coincidence within the detection window resulting in poor two-photon polarization entanglement visibility and fidelity.

5.2.4 Experimental details

Since we have the perfect settings for the decorrelated two-photon source, Keeping the same pump pulse configuration for the Sagnac source is useful. This gives us a spectrally pure two-photon source for the entanglement generation. Instead of a triangular geometry, we adapted an unfolded geometry as in Fig. 5.2.1. This is due to, multiple beams following a single optical path so additional mirrors in the unfolded setup provide some flexibility during the optical alignment. The main pump

light is set for diagonal polarisation (set by 775 nm HWP in the pump path), DW-PBS splits the pump from the H/V port and then directs them to the waveguide coupling lenses. A pair of achromatic lenses are placed on both sides of the waveguide to couple both pump light and PDC photons. Lens positions and coatings are optimized for efficient collection of PDC light but still maintain 40% pump coupling into the waveguide. Two achr-HWP make sure that only H polarised pump light is coupled to the waveguide from both sides. Only the HWP on the anticlockwise path is fixed to 45° to swap the signal-idler (generated by the clockwise pump) about 90°. This will make sure that signal photon output possibilities always end up to the the same output port of the Sagnac PBS, also the case for the idler photon port. Which helps the interference of clockwise-anticlockwise interference on the PBS within the two-photon subspace. Clockwise HWP at 0° on the other side will compensate for distinguishability from dispersion and phase, which signal-idler can acquire from anti-clockwise HWP. To tune the overall relative phase between H/V polarisation a phase adjusting (SBC) device is placed in one of the paths. This can be used to switch the quantum state by different phase settings, zero or π phase adjustments in the setup can produce two maximally entangled polarisation Bell state ($|\psi_{\pm}\rangle = \frac{1}{\sqrt{2}}(|H\rangle \otimes |V\rangle \pm |V\rangle \otimes |H\rangle)$. By placing another HWP (at 45°) on one of the photon arms we can swap the state to $|\phi_{\pm}\rangle = \frac{1}{\sqrt{2}}(|H\rangle \otimes |H\rangle \pm |V\rangle \otimes |V\rangle)$. Two silicon filters are used in the signal idler path for pump suppression. Broadband 1550/8 and 1550/12 are used to absorb the *sinc* sidelobes. Standard tomographic waveplate (HWP+QWP) combinations are used for different measurement settings, so many measurement settings can be set by automated waveplates for state tomography. The following PBS will then project the state into two spatial modes. Two single-mode fibers (AR coated for 1550 nm) at each PBS output mode collect the measurement outcomes with $\approx$ 85% collection efficiency. Finally, the photons are sent to single photon detectors with a detection efficiency of 72%. Four fast SNSPD detectors with a dead time of 12 ns are used here, which makes the experiment run in full repetition mode of the laser (76 MHz) accounts for high count rates.

5.2.5 Results

Several state verification criteria like entropy, Bell parameter, entanglement measures, and inequalities exist for both entanglement and non-local kind of behavior in bipartite systems. One of the simplest tests to check the polarization entanglement quality is the visibility test. Since the two photons are entangled in polarisation degree of freedom, a strong correlation can be observed at the output of PBS as coincidence measurements. Experimentally this correlation can be probed by col-

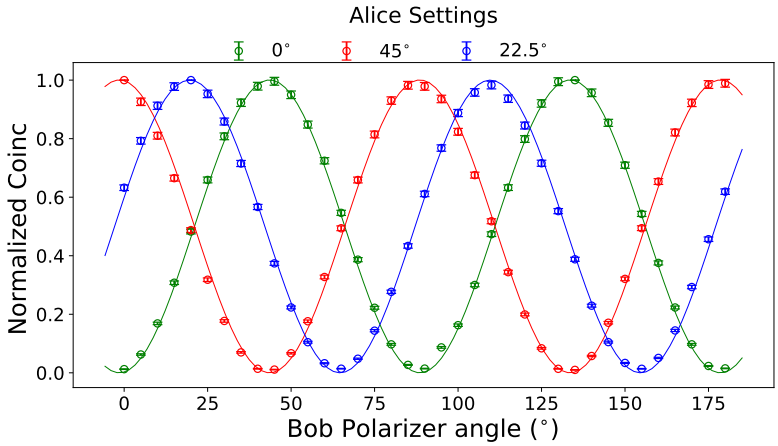

Figure 5.2.2: Entanglement visibility curve for different settings. Alice's side polarisation angle is kept fixed, and Bob's side is rotated for coincidence measurement. Normalized coincidence counts are plotted for the Alice settings H, V, and diagonal basis (Poissonian counting error estimate is included in the plots).

lecting coincidence counts from the two projection PBS output modes for different waveplate settings. Two photons might be correlated or anti-correlated on a polarization basis depending on the overall phase settings and type of Bell state. In a literature sense, two observers (Alice and Bob) keep their respective waveplates at different angles to rotate the polarization state of the photon arriving at their measurement station (tomographic part),

$$|\theta_a\rangle = \cos\theta_a\,|H_a\rangle + \sin\theta_a\,|V_a\rangle \quad , \quad |\theta_b\rangle = \cos\theta_b\,|H_b\rangle + \sin\theta_b\,|V_b\rangle\,. \tag{5.2.4}$$

Now, Alice keeps her waveplate at a fixed position, Bob then sweeps his waveplate to different angles. Coincidence counts $P_{cc}(\theta_a, \theta_b)$ then shows an oscillatory behaviour described by,

$$P_{cc} = \frac{1}{2}\sin^2(\theta_b \pm \theta_a) \quad for \;\; |\psi_\pm\rangle \quad , \quad P_{cc} = \frac{1}{2}\cos^2(\theta_b \pm \theta_a) \quad for \;\; |\phi_\mp\rangle\,. \tag{5.2.5}$$

Finally entanglement visibility can be estimated from maximum (C_M), minimum (C_m) coincidence counts; by evaluating the expression,

$$V = \frac{C_M - C_m}{C_M + C_m}. \tag{5.2.6}$$

Figure 5.2.2 shows the experimentally obtained visibility curve for fixed rectilinear and diagonal measurement settings at one station. Integrated waveguide Sagnac

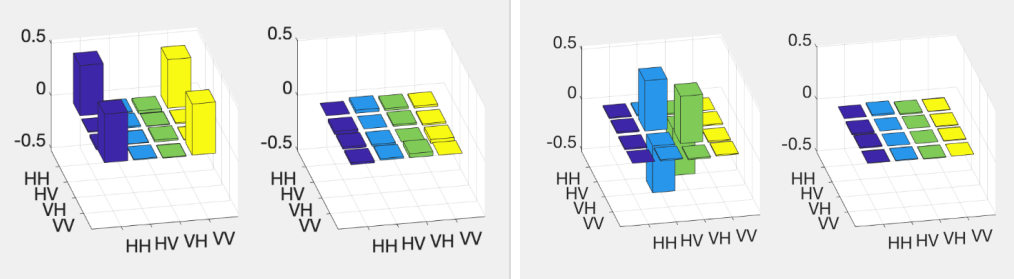

Figure 5.2.3: (left) Reconstructed density matrix for the state $|\phi_+\rangle$. The signature of the positively populated real part confirms the corresponding Bell state. Data shows a near-zero contribution of the imaginary part, asserting that no imaginary phase part is involved in the state formation. (right) Similar values were observed for the state $|\psi_-\rangle$. In both cases more than 94% state fidelity is achieved.

source shows maximum visibility of $(96.0 \pm 0.1)\%$ on the H/V basis and $(94.3 \pm 0.1)\%$ on the diagonal basis. Note that the geometry of the system always produces correlation or anti-correlation on a H/V basis (relative phase is not an issue in the measurements) but an estimate on the diagonal basis is necessary for actual entanglement. Results indicate high-quality polarization-entangled photons from the setup.

In standard quantum mechanics description, to quantify a quantum state we need the full information about the state in the form of a density matrix. Higher dimensional density matrix reconstruction and fidelity estimation require complex calculations, but two-particle state reconstruction is widely studied in literature [91]. An in-depth single-qubit and two-qubit polarization tomographic reconstruction can be found here [92]. Following similar algorithms, a complete Pauli's (σ_x, σ_y, σ_z) measurements are performed on the two-qubit polarization entangled state. This means nine measurement settings are required on each tomographic side, and projection operation from the PBS then provides four different measurement outcomes. Finally, 36 measurement outcomes are collected for the density matrix reconstruction algorithm. Which constitutes an over-complete quantum state tomography with an average coincidence rate of 50000 pairs/s, finding a fidelity of $F = \langle\psi_-|\,\rho\,|\psi_-\rangle = (95.78 \pm 0.04)\%$. Similar measurements are performed for different Bell state settings and observed density matrix components are plotted in Fig. 5.2.3.

Summary

This section started with a brief theoretical introduction to parametric down-conversion and spectral engineering. We then assembled a heralded single-photon source and polarization-entangled two-photon source on an integrated-bulk platform. Periodically poled waveguide approaches find a way around to circumvent the limitations paused by the traditional bulk crystal-based SPDC light sources. Single photon source demonstration simultaneously shows high heralding efficiency ($\approx 50\%$)*, high brightness (count rate* $> 3 \times 10^6/mW$)*, high spectral purity* ($> 97\%$)*. A unique waveguide-based Sagnac source of polarization entanglement is implemented with high-quality entanglement, with two-photon polarization entanglement state fidelity above* 95%*.*

Chapter 6

Time Multiplexing and Multi-Photon Entanglement

6.1 Background

Contents

Quantum states of light having multiple photons are highly desirable in all kinds of quantum-enabled applications. One of the key quantum properties involving many photons in the system is multiphoton entanglement. In which the entanglement is shared by participating photons and can be useful for higher dimensional quantum applications, especially multi-node distributed communication networks with quantum-enhanced performance. Efficient generation of multiphoton entangled states is always a challenge in experimental quantum optics. So far we have discussed the generation of two-photon entanglement but here we are dealing not just with two but more. In this chapter, we introduce a clever source multiplexing technique to efficiently generate many-photon entangled states resource-efficiently and show an exponential increase in production rate when we go to a higher number of entangled photons. Furthermore, we provide experimental proofs and bench-marking data sets for the multiplexing method by generating multi-photon polarization entangled GHZ-type graph states of up to six photons. Then I will explain the details of other protocols, useful to generate different kinds of entangled states or graph states from our proposed device.

The basic idea behind the multiphoton entangled state generation is the fusion process of two maximally entangled polarization Bell states on a PBS followed by

a post-selection strategy. So one needs multiple Bell-type entangled pairs for the above-mentioned entanglement generation protocol. In the past, experimenters were using either a single SPDC crystal in double pass configuration or multi-pair emission possibilities of an SPDC to consider two entangled Bell pairs for three and four-photon entanglement generation [14, 93]. The intrinsic probabilistic nature of these sources limits the efficiency of such a method on system scaling for larger-size photonic entanglement, especially from the resource side. We need many identical Bell pair sources and stitch them together to create multi-photon entanglement, which exponentially increases the overall system requirements. Instead of a spatial approach, another reliable technique for multiphoton entanglement with SPDC source is source multiplexing in time. In this chapter, I will explain the detailed techniques of time multiplexing for many photon entanglement generation and detection. This work has been considered an efficient method to generate large-scale entanglement with a single quantum emitter.

6.2 Source Multiplexing

Multiplexing in general shown to be efficient in photonic source development, photon number detection schemes, and optical network architecture [94, 95]. In this section, we mainly focus on source multiplexing especially in the time domain. On-demand or deterministic single photon and multiphoton sources are still far off the mark. Solid-state emitter systems deliver promising performance in terms of brightness and on-chip integration. Especially micro-cavity coupled quantum dots are fast, bright sources of single photons with 57% end-to-end efficiency [96]. However, there are severe limitations in the form of cryogenic operation, wavelength choice, quality of the photonic state, and light collection strategy. Loosely speaking, the spin-photon interface-mediated large-scale entanglement generation technique faces limitations from the emitter's limited spin coherence time, which solely deteriorates the process of generating chains of entangled photons. Multiple solid-state platforms, fabrication techniques, and collection strategies are now under consideration to overcome most of these limitations. Cavity-based single-atomic systems show higher coherence time with laser trapping methods. A promising way of multiphoton graph state generation up to 15 photons was recently demonstrated with single atom manipulation without any post-selection strategy [97]. But on the other hand system scaling and chip integration is a long-standing issue in quantum atom optics. Non-linear optical sources are still an active candidate for high-quality single, entangled photons and squeezed light generation, especially from the point of gen-

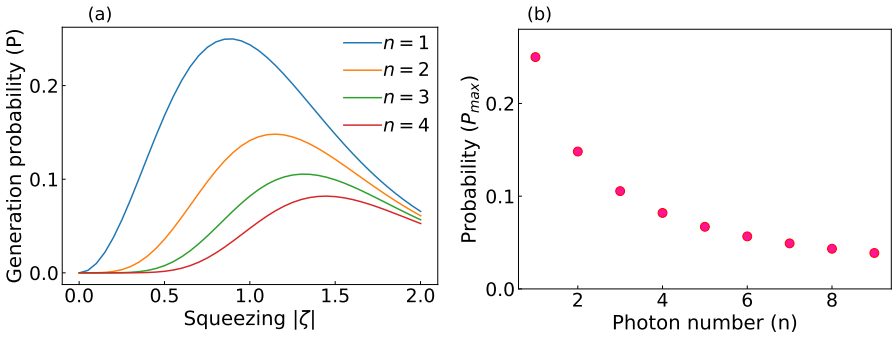

Figure 6.2.1: (a) Colored line shows generation probability for the heralded state $|n\rangle$ for different squeezing strength (ζ) from a single mode TMSV. (b) Maximum generation probability for a specific Fock state out of TMSV state.

erating heralded highly pure single photons, room temperature operation, and ease of integration onto chip scale.

One immediate solution for multiphoton state preparation is the combination of linear optics and source multiplexing. Several identical quantum light emitters can be multiplexed spatially or temporally for efficient provision of as many identical photons. With the help of a linear optical network, it is then straightforward to generate multiphoton entanglement as an outcome of quantum interference, there are existing protocols and demonstrations of multi-photon entanglement generation. We showed that the PDC decay process produces high-quality photons with superior performance in purity ($> 97\%$) and indistinguishability ($> 96\%$). However, the main disadvantage is the probabilistic emission of photon pairs which effectively reduces the overall production rate of the multiphoton state preparation. In a lossless situation, single photon generation probability from a TMSV state can be obtained by,

$$P(n,n) = \Big(1 - \tanh^2(\zeta)\Big) \tanh^{2n}(\zeta) \tag{6.2.1}$$

For single photon state generation, Eq. (6.2.1) is bounded with a maximum probability of 25%. Regardless of the amount of squeezing, this generation probability falls exponentially for higher order Fock state. Fig. 6.2.1 shows generation probability bounds for different photon number states from a single-mode PDC source. Multiplexing schemes leverage a pseudo-deterministic nature for PDC sources for single or higher order Fock state manipulation with increasing generation probability. Possible enhancement on the generation rate of photons from a single PDC source then multiply the probability to have many photons in a multiplexed network of PDC sources. What follows is, a loss-tolerated systematic enhancement is expected on

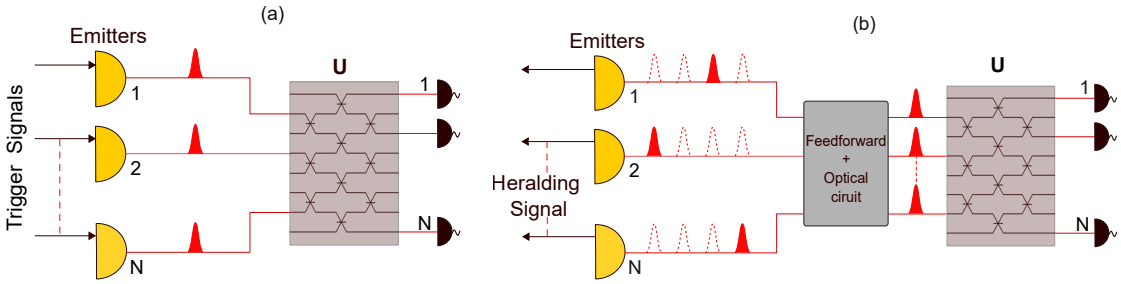

Figure 6.2.2: (a) Multiple deterministic single photon emitters are connected in parallel on the assumption that simultaneous external triggering can initiate single photon emission from each source. (b) Probabilistic sources like heralded single-photon sources (from SPDC) are connected in parallel for many single-photon states and routed with an optical delay to have deterministic photons at specific time bin choice. Finally, in both situations, synchronized single photon states are fed to a linear optical network for multiphoton quantum interference. The outcome of the network operation is detected with multiple on-off detectors for state verification.

quantum correlated multiphoton state preparation using source multiplexing.

6.2.1 Spatial multiplexing

The possibility of source multiplexing stimulates one to consider many identical probabilistic or deterministic single-photon sources synchronized to deliver a single-photon state or multiple single-photon states cleverly. This follows the concept of spatial source multiplexing, and this has been a cornerstone technique in many multiphoton state generation and boson sampling experiments. GHZ type multi-photon polarization entangled graph states up to 12 photons are realized by stitching together six SPDC sources in spatial domain [98]. First-generation boson sampling experiments used either multiple SPDC single photon sources or spatial splitting (multiplexing) of higher order photon number contribution from SPDC as their choice of heralded single-photon inputs for the integrated linear optical network [99]. In an ideal situation, having deterministic sources in hand enables placing multiple sources in parallel for the simultaneous occupation of many photons in different spatial modes. Therefore a large N×N unitary network (photonic processor) inputs can be populated by these spatially multiplexed N source modes and output detection with N photon number detectors. However probabilistic sources have the drawback of randomness in their photon generation time bin. Optical delay circuits and switches can circumvent these issues by proper feed-forward triggering methods. Such spatial and temporal hybrid versions can deliver promising experimental platforms, where a large number of photons in the input/output modes can boost

the real quantum advantage. A schematic representation of spatial multiplexing is given in Fig. 6.2.2. A major resource requirement in spatial multiplexing schemes is the availability of reliable and identical quantum light sources in all spatial source stations. This is a real challenge in the source fabrication and assembling stage. Another bottleneck is the overall resource requirement for larger states. Several resources like light sources, and optical elements increase with the required state size, and the scaling will become exponential when we go to a larger state size or larger network. Spatial multiplexing also has a limited application on the detection side, especially for photon number measurements and quantum state verification. Here number of detection unit requirements also depends on the photon number or detector network multiplexing size. We will look into the details of detector multiplexing in another section.

6.2.2 Time multiplexing

The time multiplexing (TM) technique was theoretically proposed and experimentally demonstrated in many ways to have better performance both in quantum light state generation and detection [100, 101]. The basic idea is to use the time degree of freedom to repeat or iterate a classical or quantum process to have multiple time bins filled with identical state or process outcomes, which can be called time-multiplexed state generation. For example, instead of looking at N single photons from N deterministic sources, one can take one single source and consider N single photon emitting time bins for N photons. Generated state time bins can repeatedly interfere with one another in a time synchronous manner inside an optical loop to perform a specific operation between adjacent or non-adjacent time bin states, which can be called a time multiplexed circuit operation. Free space and fiber-based time multiplexed optical circuits are already in use for classical and quantum random walk experiments, quantum computation, and simulation experiments [102, 103]. Scalability of time-multiplexed circuits allows a large number of step operations in random walk experiments; large scale continues variable entanglement generation and computation made possible in recent experiments [104]. Here we focus on temporal source multiplexing and optical circuit operation to deal with discrete variable quantum states of light. Moreover, we combine time-multiplexing with probabilistic entanglement sources to outperform existing multiphoton entanglement generation strategy. But our proposal is not limited to probabilistic sources, it is equally beneficial for deterministic sources.

Temporal source multiplexing essentially requires a single quantum light emitter and a memory to route the light in a time bin or hybrid (time-spatial) bin mode. The

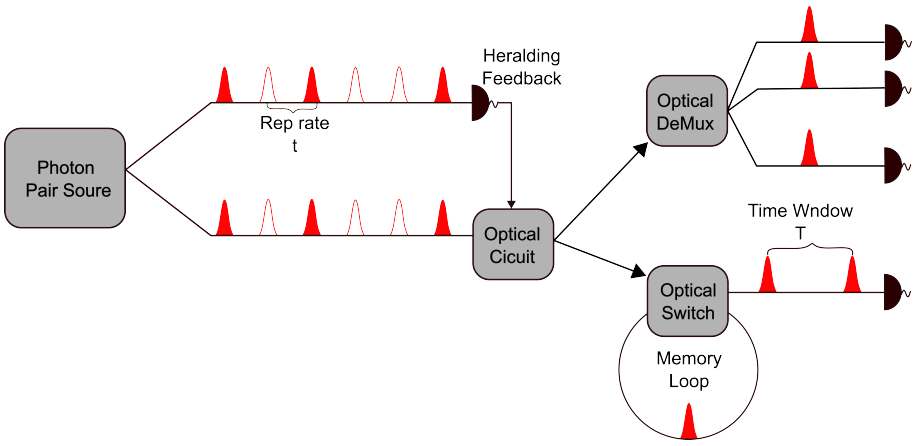

Figure 6.2.3: Temporal source multiplexing model using feed-forward arrangement. An optical demultiplexing scheme can be attached to the heralded photon optical circuit to divert multiple temporal bin photons to many spatial modes. Effectively providing N spatial single photons to N mode quantum circuit from a single source. A single loop, single switch strategy increases the probability of emitting single photons at predefined temporal bins in a single spatial mode.

main motivation behind the TM scheme is to use the heralding information from a PDC photon pair to trigger an optical quantum memory for the storage and release of its partner on-demand or within a predefined time window. Fig. 6.2.3 outlines a basic structure of a parametric source-based temporal source multiplexing scheme. We follow the simplest and most efficient loop-based time bin architecture in this thesis. A click detector on the heralding arm generates a trigger signal, upon detection of a heralding photon, the feedback electronic system then initiates a series of store and release operations to control the optical memory. TM method can be implemented in both continuous and pulse-pumped PDC sources. Source multiplexing enhanced and continous-wave (CW) pumped heralded single-photon source was used in the quantum spectroscopic experiment for better sub-shot noise advantage [105]. A pulsed laser scheme is beneficial in the sense that individual pulse timing information can be marked with a trigger signal derived externally or internally from the laser itself. Combining this information with heralding information avoids unwanted noise feedback to memory.

In a pulsed operation mode, a probabilistic PDC source is pumped with N number of consecutive pump pulses. Within the N pump pulse stream, a single photon pair can be generated with probability $p(n = 1)$. Upon pair generation, the heralded photon will be routed and stored till the last bin of the N pulse bins and release the photon in the following bin. Store-release information to the memory

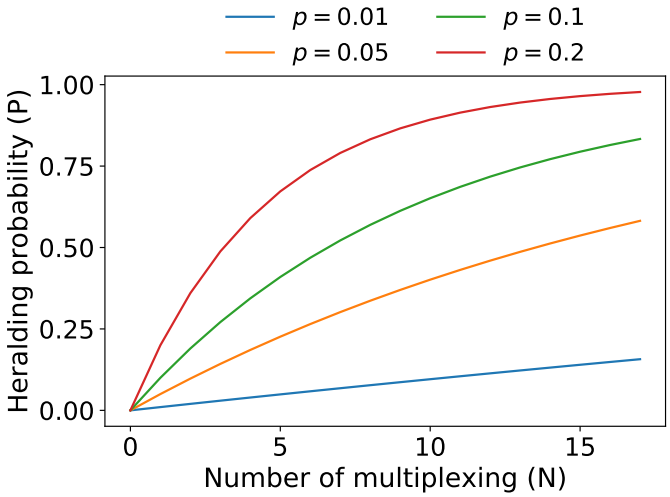

Figure 6.2.4: Theoretically expected heralding probability with multiplexing. Source multiplexing of $N = 17$ is used to increase heralding probability near to unit efficiency for different single photon generation probability (p) from a single mode PDC state.

is feed-forwarded from the heralding side. This technique essentially increases the probability of having a heralded single photon in a predefined time bin. If there is no photon pair event is occurs in the N pulses then the run is discarded and waits for the next N sequence. Since the strength of the pump pulse is kept low to avoid higher-order Fock components, the chances of having more than a single pair event in the N bins pulse stream are very small. But in previous demonstrations, if another photon pair event is generated within the N pulse stream, it will be discarded by the feed-forward and memory. Later in our time multiplexing we tackle this situation with our new memory design and feed-forward to consider all possible photon pair events within the N pump bin for overall rate improvement and entanglement generation.

For the N bin multiplexed scheme (spatial or temporal), single photon heralding probability is given by,

$$P(1, N) = 1 - (1 - p(1))^N. \tag{6.2.2}$$

Equation (6.2.2) supports that, $N \approx 17$ source multiplexing is reasonable towards an on-demand single photon source from the PDC state with maximum generation probability from each source ($p = 0.25$) [106]. For different PDC single photon generation probability (p) multiplexing-enabled enhancement is given in Fig. 6.2.4. With a low gain PDC source, a free space optical memory extension of the TM scheme was experimentally demonstrated in the past bringing the single photon heralding probability to a record value of 67% for $N = 40$ pump pulse time bins [107].

6.3 Quantum Buffer

Quantum memory is fundamentally able to perform storage and retrieval of quantum states without destroying the coherence in the system. Memory-assisted information processing protocol is essential in a network-based quantum computing and communication architecture. In this thesis we mainly focus on an all-optical approach towards a quantum memory, enabling the system to store entangled states of light and extending the TM idea to engineer higher dimensional entangled states of light. Different memory platforms are proposed for the efficient storage and retrieval of photonic states, like optical delay loops, atom clouds, and solid-state systems, where each platform has advantages and disadvantages. Decoherence is a major obstacle in atomic clouds and solid-state memories, Nevertheless, storage efficiency of $\approx 91\%$ and 20 ms of storage time was demonstrated with this platforms [108, 109]. Fiber and free space optical loop-based memories are simple and resource-efficient platforms for classical and quantum light state manipulation especially in telecommunication wavelength.

6.3.1 Loop memory design

All optical storage loops utilizing the polarization degree of optical fields is a standard scheme to delay or store photons for on-demand classical and quantum operations. Here a polarization-dependent passive or active optical device effectively couples and decouples light into a free space loop designed to circulate for a specific round trip time. An active electro-optical element inside the loop then acts as an optical switch to change the polarization state of the light when triggered by an external signal. In fact, the whole device acts as an active memory, allowing the light state to stay inside the loop until the external trigger signal. A Sagnac-based optical loop design is given in Fig. 6.3.1(a). H-polarized light is coupled into the loop through the Sagnac PBS, at the same time switch is activated to rotate the state of light to V polarization, and then the switch goes 'off' for the following round trips. This will keep the light inside the loop for the desired storage time. The switch can be activated once again to change the V-polarized light back to the H-polarized state allowing the light to escape towards the output mode. The design has been chosen in many previous experimental schemes, reduced number of optical elements makes the design more efficient in qubit storage experiments [110, 111]. However, the design is polarization sensitive making the loop operational only for selected input polarization states and thereby limiting its applications.

In this thesis, we propose a new all-optical storage loop extending the con-

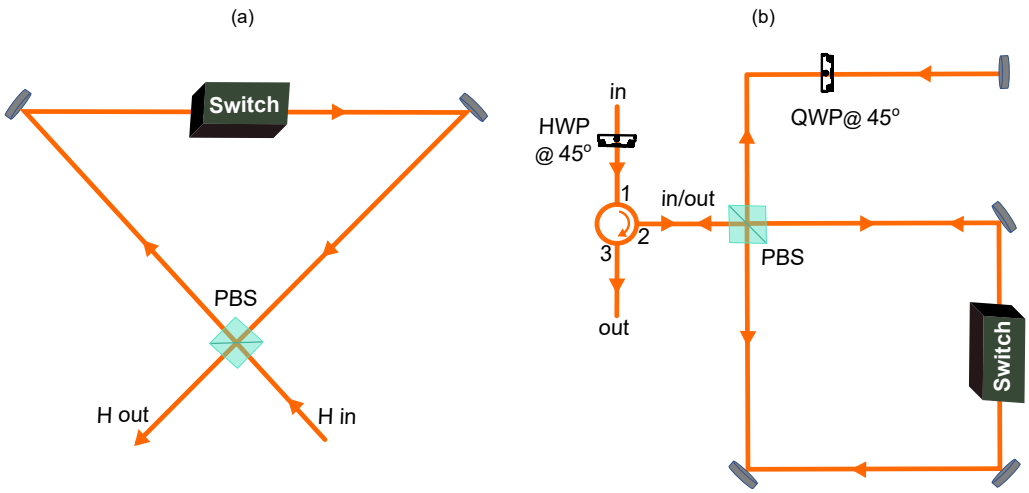

Figure 6.3.1: Loop memory architecture: High bandwidth free space optical loops for delaying and storing photons for a fixed time window. (a) Sagnac loop memory with a single PBS and optical switch. The length of the loop can be adjusted according to the experimental requirements. (b) An unfolded standard Sagnac loop memory is connected to a retro line optical path, allows any input state into the memory, and preserves the state coherence. The length of the loop is designed to match the repetition rate of our laser. QWP inside the retro arm has a 45° setting in double pass configuration, but is open for any rotation operations for different state manipulation.

cept to allow arbitrary polarization light state storage and retrieval, a polarization-insensitive free space optical loop. The design employs an additional delay line to the existing folded or unfolded Sagnac loop and is outlined in Fig. 6.3.1(b). While the switch is off a V/H photon simply covers one round trip and exits the loop with the same polarization state, and we will consider this as a 0^{th} round-trip. For memory operation, the switch should be active for a certain amount of time to keep the photon inside the loop.

Operation Principle. A single port of the PBS is dedicated to coupling the photon in and out of the memory. Through the PBS H/V photon enters and traverses the loop part towards the delay line by keeping the switch in the OFF position. The retro design then sent back the photon to the loop, while this time the switch will be in the ON position. Flipping the polarization then allows the photon to stay inside the memory. For n round trip storage time $2n$ polarization flips are provided to store and release type identity operation[1]

Design Parameters. The efficiency of the memory is important for the sus-

[1] n does not consider the 0^{th} round trip($n = 1, 2, 3..$). Also for n round trips, photons traverse the loop path $n + 1$ times.

tainable performance of the overall system. The total loop length of 3.95 m (13.15 ns delay window) is divided into two sections loop + retro-line, with a 6.5 ns travel time window for each path. The optical switch is a fast electro-optical polarization modulator that works on the principle of nonlinear Pockels effect. This is driven by a high voltage power supply (0 to 3 kV) tunable up to π phase shift depending on the applied voltage, covering a full cycle of polarization rotation from H to V. Normally we fix the voltage for H $\leftrightarrow$ V conversion. EOM driver has a 5 ns rise-fall time which allows switching between the polarization modes sufficiently fast, actually within the half-round trip time, and operates at a switching rate of 100 kHz to 1 MHz. The round-trip loss of the loop is accounted for with the following transmission efficiencies: PBS (98.7%), EOM (99%), HWP (99.6%) specially coated commercial mirrors (99.6%), in-house coated spherical end mirror (99.3%). We have introduced additional mirrors on the folded retro line for space consideration and alignment access. This makes a total single round-trip (13.15 ns pulse separation window) transmission efficiency, $\eta_{RT} = \eta_{PBS}^2 \times \eta_{Mirr}^{10} \times \eta_{EOM} = 91.7\%$ for the total memory line. Fiber circulators separate the input-output light for efficient and perfect routing.

6.3.2 Feed-forward and detection

Performance benchmarking of our *quantum buffer* type loop memory requires an efficient quantum light source and a feedback mechanism. We will now combine our engineered quantum light source developed in chapter 1 with the buffer memory, triggered by a fast feed-forward electronic circuit. An outline of the complete experimental scheme is given in Fig. 6.3.2.

The system has three main parts: a heralded photon source, FPGA-based feedback circuit, and a quantum buffer. In general, the source produces a correlated photon pair under the approximation of low-energy pump strength. Depending on the Sagnac source pumping scheme, the source can produce different types of two-photon states, entangled or non-entangled type photon pairs. One photon from the pair will direct to the heralding arm which is equipped with a tomographic setup and projection PBS will perform polarization resolved output followed by single photon detection at each output mode (V_h, H_h). Partner photon is directed towards the memory through delay fiber and fiber circulator. On the switch OFF condition, the directed photon simply covers the loop once and then exits from memory for tomographic and polarization-resolved measurements. Activation or deactivation of the switch requires a fast input signal from the heralding side.

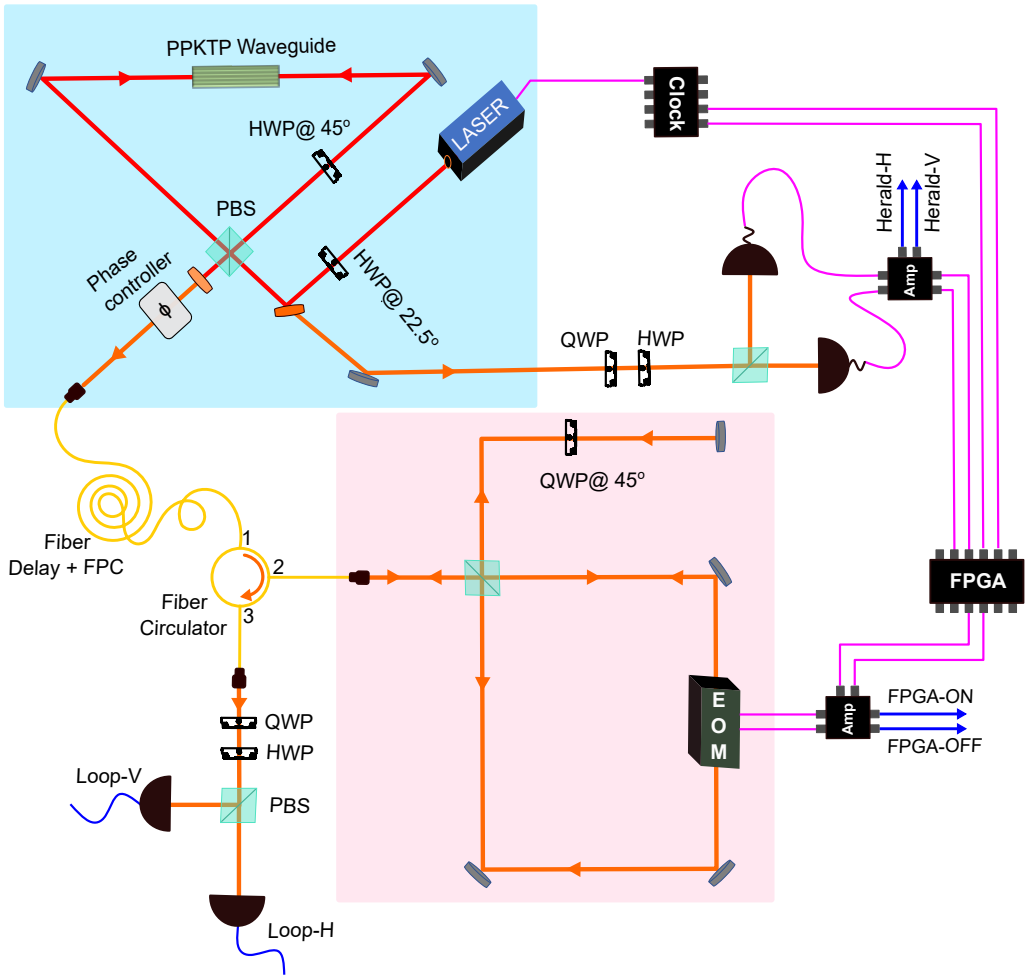

Figure 6.3.2: Programmable time multiplexed optical circuit for quantum state generation and detection: Sagnac source can be configured for different state generation, heralded Fock state, Two-photon entangled state depending on one-sided or two-sided pumping scheme. One of the output modes is coupled to the memory with a Fiber router. A fiber router has three parts: A long fiber delay to load the photons and compensate for the electronic latency beforehand, a Fiber polarization controller (FPC) that adjusts the input polarization of photons, Fiber circulator for in/out-coupling of photons. Experiments run on a 76 MHz repetition rate, 10 to 12 ns detector recovery time of SNSPDs allows the addressing of photons generated in consecutive pump pulse time bins. Four detector signals and two FPGA signals are fed to the time tagger module for gated coincidence measurements. Color codes: Sagnac pump path (red), photon's path (orange), feed-forward controls (magenta), photons click signals for time tagger inputs (blue), fibers (yellow), $2_{in} \times 4_{out}$ amplifiers circuits (black box). The entangled photon source and quantum buffer are boxed in separate colors.

Programming the Switch with Feed-Forward Electronics. We will add a programmable nature to the buffer memory by controlling the switch operation using the signals from the heralding side. This procedure is entirely built on a Field Programmable Gate Array (FPGA) based controlled electronic feed-forward strategy. A separate clock synthesizer circuit upscales the laser trigger signal rate (76 MHz) to 152 MHz and generates a phase-locked clock signal for the feedback FPGA unit with a period of 6.5 ns. This 152 MHz signal then serves as a master clock for the FPGA circuit, which is also crucial for the rise and fall time of the switch operation. Within this 6.5 ns margin, the switch should be able to initiate an ON-OFF sequence when the photon passes through the loop and delay lines, because the two travel paths have similar time windows. So the 6.5 ns clock window is necessary for the FPGA signal processing. A dedicated switch and driver provide ≈ 5 ns rise/fall switching speed, providing enough time to switch the polarization state when passing through the loop or retro path. Besides the input clock signal, FPGA requires an external trigger signal from the heralding side to generate the corresponding control signal for the switch. A $2_{in} \times 4_{out}$ comparator circuit generates four identical herald trigger signals, which use two SNSPD detector signals as inputs (H, V herald detectors), feeding two for the time-tagger and two for the FPGA as the herald trigger. FPGA clock cycle can deliver a 6.5 ns active time window to generate a memory switch trigger signal upon the arrival of the herald signal to the device. Such a long active window time is also useful to place the switch ON-OFF control signal time position to meet the photon, one may want to finely tune the switch position to hit the photon exactly at the right time. This is the reason we generate a 152 MHz (6.5 ns) clock signal for the FPGA overall signal processing. FPGA devices then can be programmed externally to generate trigger sequences for the switch in any flexible manner for different memory operations. The switching time information is also important to efficiently collect the photon in a time bin encoded manner. FPGA output for the switch delivers ON and OFF signal patterns, this can be either copied within the FPGA or with an external comparator circuit to have multiple copies of the triggers for the switch and time tagger. Later we will use the time tagger designated FPGA-ON and FPGA-OFF signal for gating the respective herald and loop photons, collecting them in a time bin encoded manner for efficient state generation and data processing. Since the heralding electronic information reaches rather late to the switch compared to the speed of the heralded photons. The latency of electronic signal transmission has to be compensated to meet the operation intact with the fast-flying photons. An additional fiber spool (500 m) delays the photons between the light source and memory, providing enough time delay (≈ 1.7 μs) to compensate for the latency.

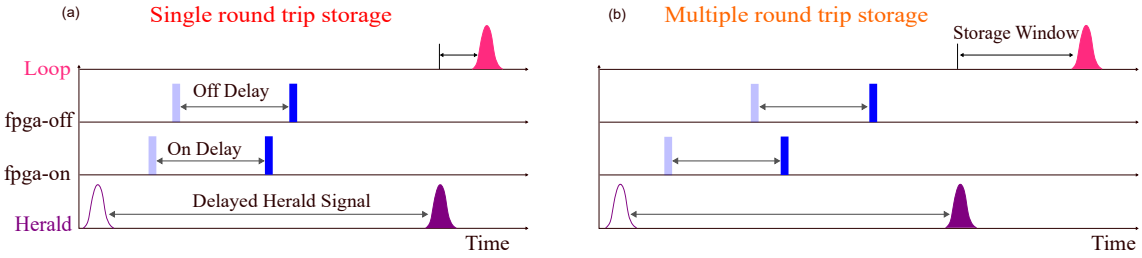

Figure 6.3.3: Delayed time tagging for photon arrival gating. Faded bars and pulse show the actual event position. Bold blue bars and colored pulses represent delayed events in the time axis (a) Single round trip case: Herald photon is delayed to match the timing of loop photon corresponding to a zero round trip situation. Loop photons then come after one cycle in a single round-trip storage experiment. FPGA ON and OFF signals are delayed in such a way that these signals come beforehand on both herald and loop clicks. This helps us to place the gating of signal and loop photons beforehand. (b) Storing for multiple round trips: Where the relative delay between herald and loop, FPGA ON and OFF are changed due to more round trips.

Binning photons. When it comes to time multiplexing keeping track of photon clicks is important to look for actual/expected single and coincidence photon clicks from complete experimental time bin arrays. Since photons are coming in regular time intervals, time bin gating is essential to identify appropriate photon coincidence. Fast-feedforward electronic signals are manipulated for efficient time bin photon counting.

In our time multiplexed scheme an event starts with a single photon detector click on the herald side, registering a click signal in the time tagger herald channel and providing a trigger signal to the FPGA through the comparator circuit. FPGA then creates an ON signal to store the photon and a predefined OFF signal to release the photon. A copy of the ON and OFF signal is also fed to the time tagger to gate the herald and memory photons. Finally, the photon released from the memory delivers another detector click signal to the time tagger. In total, four click signals are going to the time tagger in a qubit storage type single experimental event and repeat over the experimental run time. Since the photon releasing from the memory side possesses a longer time delay, the corresponding output click time bin provides a reference to imply proper time delays for herald and FPGA signals. Time tagger electronics provide inbuilt functions to electronically delay those signals, and permit time bin correlated coincidence recordings for post-processing. Additionally, FPGA ON-OFF signal delays are adjusted in such a way that they will arrive well beforehand concerning herald and loop photon click signals. Time gating bins derived from these early arriving ON and OFF signals are then positioned near to the expected time stamps of herald and loop photons respectively. Fig. 6.3.3 outlines the

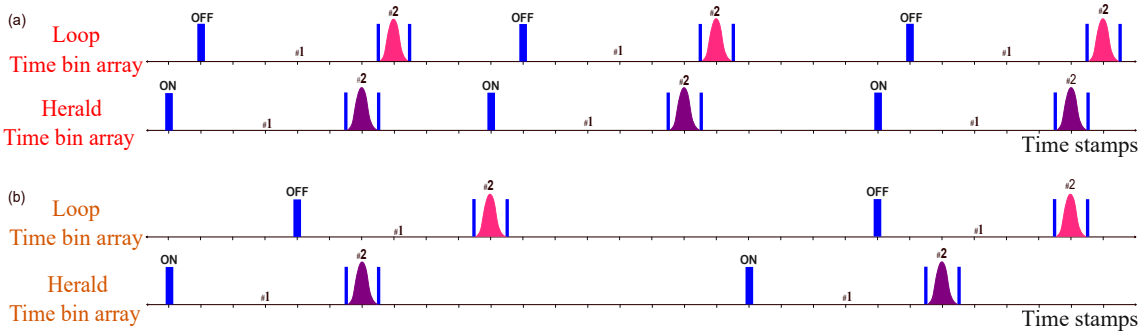

Figure 6.3.4: Time bin click data array generated by the *Combiner* subroutine for the herald and loop channel. (a) Single round trip storage time bin array. The early arrival of ON and OFF signals (thick blue bar) provides gate bins (thin blue bar) to sandwich respective herald and loop photon clicks. The gap between the click bins is numbered for counting purposes. Herald and loop photon clicks are counted from the respective bin positions (let's say #2 position) for singles and coincidences (by comparing herald and loop channels). Large arrays are created by Python scripts to fill the click bins during the experimental run. (b) Time bin array for multiple round trip storage, note that ON-OFF and herald-loop click bin separation is larger in this case.

electronic signal delays applied for individual channels in two different situations, which is for different storage times otherwise different number of round trip options. Timetagger software provides *Combiner* function option to combine multiple time tagger signal channels and make a single array of signal clicks with time stamps obtained from the respective combiner input channel. Fig. 6.3.4 shows the output array pattern after *Combiner* operation, timestamped single bin array containing FPGA clicks, gate bins, and actual photon clicks from both herald and loop sides. Finally *CountBetweenMarkers*[2] (CBM) function is used to count the actual photon clicks from the gated bins from both arrays, making final data for single and coincidence events. These techniques become more relevant when it comes to time bin encoded multiphoton state generation and post-processing for state reconstruction.

[2]Detailed documentation of *Combiner* and *CBM* subroutines are available at *Swabianinstruments* software documentation site

6.3.3 Storing polarization entanglement

We benchmark our buffer memory performance with polarization-based single-qubit and entangled two-qubit storage experiments for different storage times or round trips. Heralded polarization qubits in the form of single photons ($|\psi\rangle = |HV\rangle$) are generated by pumping the source in a single pass configuration from clockwise direction [Fig. 6.3.2]. V-photon is heralded and its partner H photon is directed towards the memory side. The optical circuit is then programmed to store the photons for different time delays, or different numbers of round-trip choices. Tomographic measurements are performed on the retrieved photon from the memory with six different measurement settings (H, V, D, A, R, L). These are the standard measurement settings required for the density matrix reconstruction for a polarisation qubit [92]. For every round trip choice, six different input states (H, V, D, A, R, L) are prepared and stored in the memory. After retrieving from memory, tomographic measurements and fidelity reconstruction were performed for every input polarization state setting. This provides an average single-qubit state fidelity estimate for each round trip choice.

Loop memory-based heralded single and two-photon Fock state qubit storage was also demonstrated in continuous variable picture [110], but an extension to discrete variable polarization entangled qubits is unexplored. This is mainly because of the lack of a polarization-insensitive memory design. We overcome this limit with our new loop design and experimentally demonstrate the storage of polarization entanglement. The basic light source is again the same, pump the Sagnac in double pass configuration so that polarization-entangled photon pairs are emitted into two spatial modes. Out of the entangled pair, one photon is used for heralding and feed-forwarding so that the partner photon will be delayed and stored for a defined time window inside buffer memory. This demonstrates a potential experiment on entanglement storage, stored photons are released on demand, and state fidelities are extracted from tomographic reconstructions as we did in our polarization entanglement experiment in chapter 1.

Experimentally investigated fidelities are shown in Fig. 6.3.5 for both single qubits and polarization-entangled qubits. Standard polarization tomography and state reconstruction tools are used for the fidelity calculations. Data shows corresponding states are stored up to 1 μs enabling the loop memory an ideal platform for buffer type memory towards quantum applications. The Entanglement source is running in 0.001 pair per pulse regime, so when no storage operation is performed the source delivers a polarization-entangled state of maximum fidelity $> 95\%$. Increasing the storage up to 25 round trips (328 ns storage time) drops the fidelity

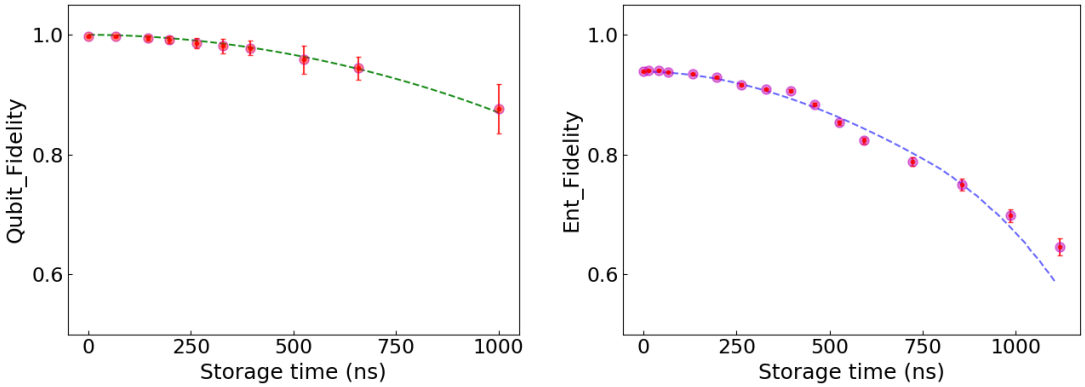

Figure 6.3.5: Fidelity data. Experimentally observed and theoretically fitted quantum state fidelity data sets for single polarization qubits and polarization-entangled two-qubit states for different storage times or round trips. (left) Data for single polarization qubits storage experiment. We went up to 76 round trips which is time equivalent to ≈ 1 µs. Tomography shows corresponding state fidelity ranges from 99% to 88% for the memory retrieved state, showcasing high single qubit fidelity even after 76 round trips. (right) Fidelity data for the polarization-entangled state. Rather than single qubits entangled qubits are prone to imperfections (accidental counts, losses, waveplate errors, and switching contrast) so fidelity drops rather quickly. After 85 round trips(> 1.1 µs) state shows 64% state fidelity, still well above 50%.

only 4%, providing high fidelity Bell state from a time multiplexed point of view.

The efficiency of a quantum memory is an important benchmark, we estimate our memory efficiency with Klyshko methods. From the entanglement storage data set, Klyshko efficiencies are calculated for different measurement settings for each round trip case. Different detector combinations and corresponding singles and coincidence events from each measurement setting, provide an average estimate of Klyshko efficiency for a specific storage time. Finally, memory-only efficiency can be extracted from the relative ratios of initial (no storage) and stored Klyshko efficiency data. Memory-only efficiency does not include the fiber circulator transmission (photon travels this path twice), fiber coupling, and additional round trip losses (1.5 round trip transmission losses during the memory input/output coupling operation). These values are obtained from classical transmission measurements as 92%, 90%, and 91% respectively, and contribute to the final estimate of the total efficiency of the memory. Experimentally measured efficiencies in both cases are given in Fig. 6.3.6 for different round trips. Extracted memory efficiency is close to the classical estimate and 1/e lifetime approaches roughly 131 ns, which is equivalent to 11 round trips, more than enough to consider nearest or non-nearest photon generation possibilities

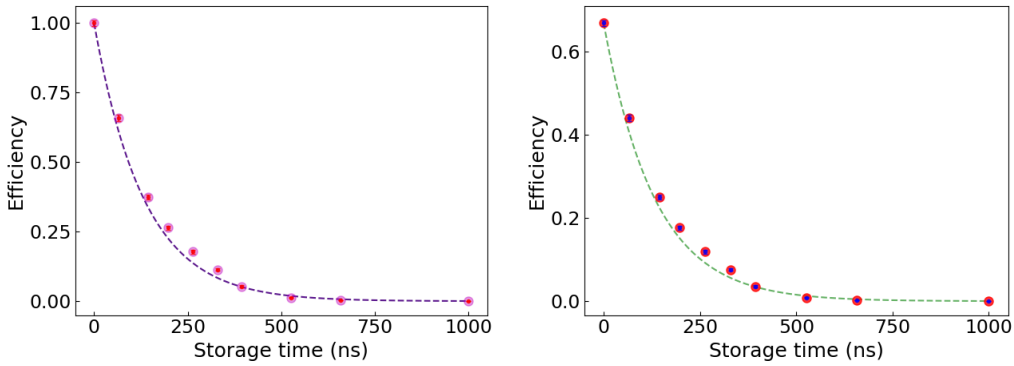

Figure 6.3.6: Memory Efficiencies. (left) Memory-only efficiency extracted by relative Klyshko calculations for different storage time. (right) Total memory efficiency plotted with external loss contribution [loss from the fiber circulator, fiber coupling, extra round trip loss during decoupling]. An exponential fit is given for the decaying behavior on both cases, and memory efficiency 91% extracted from the data sets.

from the source for a time-multiplexed approach. This motivates us to further investigate multiphoton interference experiments by considering subsequent Bell pairs from a single source generated within 10 to 20 number or pump pulse time bins.

6.4 Multi-photon Entanglement

Entanglement in higher dimensions is motivated by its application both in fundamental and applied quantum technology. A higher dimensional quantum entangled state can be constructed either by exploiting higher dimensional Hilbert space of specific degrees of freedom like orbital angular momentum (OAM), spectral and time bin modes of a single system, or with many particles. The most familiar and useful sources of entanglement arise when multiple particles are involved in the entangled degree of freedom, for the simplest case think of many photons entangled in polarization. Depending on the quantum correlation between the photons, the corresponding quantum state can take a different graph structure. Multipartite GHZ and cluster-type graph states are theoretically constructed and experimentally demonstrated to strictly rule out local hidden variable models to quantum computation-like protocols [112, 113]. Direct generation of large-scale entanglement or deterministic sources of multi-particle entanglement is still challenging and experimentally complex. Quantum gate operations on separate indistinguishable photons with ancillary photonic qubits can generate entanglement, which is the well-known

CNOT gate operation for deterministic entanglement. So far probabilistic or post-selection approaches are shown to be the best possible CNOT implementations [114]. Promising routes of single solid-state spin-based entangled emitters are still limited in entanglement size but provide higher rates [115]. Linear optics-based multiphoton interference method plays a glorified role in generating many photon-entangled states by direct post-selection or by conditional detection. But as we see earlier this requires multiple high-quality identical single or entangled sources to perform multiphoton quantum interference. In this section, we will go through the details of multiphoton entangled state generation schemes by interference with many copies of identical single-photon states and entangled bell pairs.

6.4.1 Entanglement multiplexing and multiphoton interference

Quantum interference permits non-classical correlation between two or many indistinguishable photons that have completely different sources of origin [116]. We make use of such nonclassical behavior to generate four-photon entanglement, by interfering two copies of polarization-entangled photon pairs. This specific entanglement generation scheme requires, one photon from each Bell pair allowed to interfere on a PBS, and post-selected output will show a nonclassical correlation between four photons. A theoretical approach for the four-photon state formation can start with the tensor product of two maximally entangled polarization Bell states,

$$|\psi\rangle \;=\; \frac{1}{\sqrt{2}}(|H_1H_2\rangle + |V_1V_2\rangle) \otimes \frac{1}{\sqrt{2}}(|H_3H_4\rangle + |V_3V_4\rangle). \tag{6.4.1}$$

In a practical situation, one mode from source A and one mode from source B are interfered on a PBS as shown in Fig. 6.4.1. Post selected coincidence events from four output modes (two from PBS output and two other modes) projects the state into $|GHZ^{\otimes 4}\rangle$; re-normalizing the state after post selection gives,

$$|\Psi\rangle \;=\; \frac{1}{\sqrt{2}}(|H_1H_2H_3H_4\rangle + |V_1V_2V_3V_4\rangle). \tag{6.4.2}$$

and represents one of the multiphoton type graph states called GHZ state. We have used a type I based fusion scheme between two input modes to generate entanglement [117], and implicitly assume that the photons in the PBS input paths are indistinguishable in all degrees of freedom to guarantee perfect interference outcome. The fidelity of the output state solely depends on the quality of the input Bell state and perfect phase settings in the complete linear optical arrangement. In

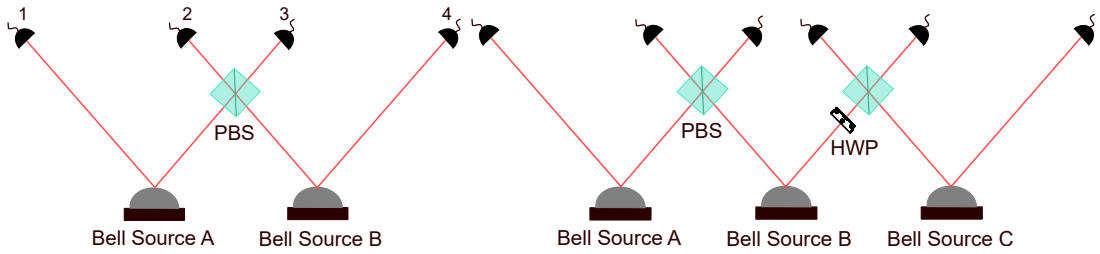

Figure 6.4.1: Graph state generation scheme in a spatial multiplexing platform. Each source emits a single maximally entangled polarization Bell pair. PBS network-based type I fusion process is used to generate multi-photon entanglement. Four and Six fold coincidences indicate specific polarization entanglement on respective arrangement.

a spatial multiplexing sense, stitching together two Bell pair sources can generate a four-photon entangled state. So in general one requires N identical Bell sources for 2N photon entanglement generation.

Many other graph states can be synthesized from multiple Bell sources by applying unitary rotations locally on individual photons before the PBS fusion process. A separate example is given in Fig. 6.4.1 with three Bell state sources but with a Hadamard (HWP at 45°) rotation applied on one of the photons in mode 3. This will generate an H-shaped graph state (which is a specific six-photon cluster state) upon six-fold coincidence at the output detector combination. An equivalent tensor product notation for the initial four-photon state with a two-photon Bell state is given here.

$$|\psi\rangle = \frac{1}{\sqrt{2}}(|H_1H_2H_3D_4\rangle + |V_1V_2V_3A_4\rangle) \otimes \frac{1}{\sqrt{2}}(|H_5H_6\rangle + |V_5V_6\rangle). \tag{6.4.3}$$

Post-selected six-fold coincidence measurement projects the state into,

$$|\Psi\rangle = \tfrac{1}{2}(|H_1H_2H_3H_4H_5H_6\rangle + |H_1H_2H_3V_4V_5V_6\rangle + |V_1V_2V_3H_4H_5H_6\rangle - |V_1V_2V_3V_4V_5V_6\rangle). \tag{6.4.4}$$

On the other hand HWP at zero angle position, a six-fold coincidence provides a six-photon GHZ state. Previous fusion-based experimental demonstrations used three to six SPDC sources to demonstrate multiphoton entanglement from six to twelve photons [98, 118–120]. Which involved bulk high-quality SPDC sources and large-scale linear optical interferometers for fusion operations. A handful amount of multiphoton entanglement-assisted theoretical proposals and experimental quantum advantage demonstrations then demand more and more photons entangled to provide a larger system dimension. Therefore scalability of the existing platform becomes more and more difficult.

6.4.2 An Entanglement assembly line

A new strategy for the efficient generation of multiphoton entangled state either by using deterministic or probabilistic photon pair source then becomes highly desirable for large-scale entanglement. Whatever is proposed, the realistic platform has to deliver a high-fidelity multiphoton state with a high count rate. For the above requirement, we introduce the single emitter-based time multiplexed heralded single-photon source approach to polarization-entangled photon pair source, expecting a similar advantage in overall generation probability and fidelity towards multiphoton state preparation (note that the entanglement generation protocol still relies on post-selection).

For the first time, we combine a bright waveguide-based polarization entanglement source with a new polarization-insensitive memory device to have a time-multiplexed programmable optical circuit. A block diagram of the full experimental implementation can be found in Fig. 6.3.2 and a toy model of the time multiplexing circuit is given in Fig. 6.4.2. We have already realized the basic components for such an experimental design in previous sections. Active and passive devices inside the quantum buffer memory render different unitary operations locally on individual photons to manipulate different graph states. A single pulsed entangled photon source can probabilistically emit Bell pairs from a set of subsequent pump pulse time bins, all optical memory can perform storage and interference operations between subsequent Bell pairs from different time bins. Since all the photons are coming out of a spectrally decorrelated PDC source, indistinguishable photons interfere with high interference visibility even though they are created by pump pulses at different time bins. Therefore the potential of our engineered SPDC source becomes influential in this new time multiplexing architecture by generating many spectrally pure photons at different time bins.

So far we have discussed the storage operation from the quantum buffer. Apart from simple quantum state storage operation, unfolding the features of the buffer memory is now essential for the follow-up details of multi-photon graph state generation. Here we describe three main functions that the loop setup can perform in general. This includes: (i.) the read-in, read-out function or swap operation, in which an incoming photon enters the storage loop and any photon that resides in the memory simply exits the loop, (ii.) the storage function, in which a photon in the storage loop stays inside and any incoming photon leaves the loop immediately unchanged and (iii.) the PBS interference function, in which the incoming photon and the stored photon interfere at a PBS-like interaction. We can name the device as a fast feed-forward loop memory or fast PBS but follow the same operation, and

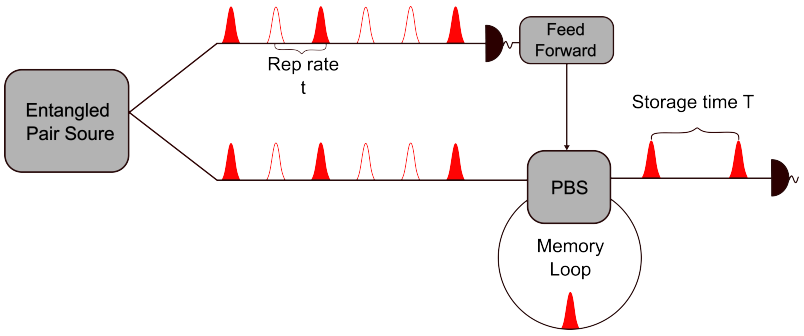

Figure 6.4.2: Single entangled emitter-based graph state generation circuit. Upon detection of a photon on the heralding side, the feed-forward circuit initiates storage operation on its partner photon in the buffer. A second herald click decides what operation has to be done within the buffer circuit between the stored photon and the newly incoming photon. This facilitates a programmable nature to our buffer memory. Entanglement generation can be possible if we allow interference between the photons within the circuit. Users can define the number of waiting times (round trip) or how many pump pulses have to be considered for two Bell pair possibilities in a stream of pump pulses. The number of Bell pairs and number of multiplexed pump pulses are flexible choices, which depend on the entanglement size and efficiency of the loop.

can be equivalently unfolded in the schematic diagram depicted in Fig. 6.4.3 (a). It comprises two key components: a re-configurable Sagnac loop and a delay line. Out of the four PBS ports, two input ports are labeled 'in' and '$from$' representing the physical input, which is typically connected to a quantum state source and the mode arriving from the delay line respectively. Likewise, the two output ports are labeled 'out' and 'to' respectively, for the physical output and the port leading towards the delay line. Counter-propagating paths around the Sagnac loop have been spatially separated for clarity. In other words, although the figure depicts two spatially separated paths for the clockwise (cw) and anti-clockwise cycling (ccw) light and the two EOMs acting on the spatially separated paths, in the implementation these two paths coincide. So $eom1$ and $eom2$ refer to the same physical device, a single fast-switching electro-optic modulator, which is capable of performing (potentially) different actions at the different arrival times of the cw and the ccw components. Similarly, the half-wave plate $W2$ in the schematic diagram represents the double passage through the quarter-wave plate at 45° in the physical setup. The half-wave plate $W1$ accounts for the polarization flip of the qubit during the read-in in the original setup. For clarity, the setup principle is unraveled into the equivalent circuit depicted in Fig. 6.4.3(b), in which the left to right motion represents the passage of time mapping the input ports in and $from$ to the output ports out and to. Both half-wave plates are fixed at 45°, which swaps the polarization modes but leaves the

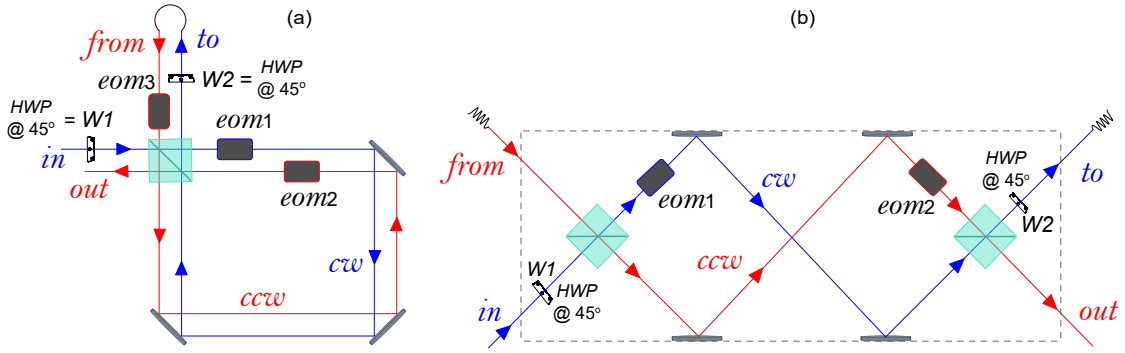

Figure 6.4.3: Decomposing the optical circuit for details: (a) The single optical path is split into two to better understand, how the incoming and outgoing photons follow individual paths and meet individual devices during the trip. (b) Unfolding the memory Sagnac to separate *cw* and *ccw* paths.

light otherwise unchanged.

Different settings of the *EOM*, toggle different operating functions of the loop. We are interested in the following three functions of the loop; The first one is the

*eom*1	*eom*2	Operation
on	off	Interfere (PBS)
on	on	Storage (Identity)
off	off	Swap (Read in/out)

Table 6.1: Here we list the *EOM* status for different circuit operations on the photonic state. *cw* and *ccw* propagating photons demand different *on*, *off* settings and corresponding photonic polarization states to implement the desired operation.

read-in/out function, wherein light from the input ports of the fast PBS is swapped into the output ports without any change in the polarization.

$$|H_{in}\rangle \rightarrow |H_{to}\rangle \ , \ |H_{from}\rangle \rightarrow |H_{out}\rangle \ ,$$
$$|V_{in}\rangle \rightarrow |V_{to}\rangle \ , \ |V_{from}\rangle \rightarrow |V_{out}\rangle \ .$$

To perform this action both *EOM*s are switched OFF. Consequently, the light stored in the loop is released and the input light enters the loop.

(ii.) If both the *EOM*'s are turned ON to perform polarization swaps, then the loop effects an identity transformation between the input and the output modes. In other words, the light from the delay line is directed back to the delay line, and the

light from the physical input is emitted "unchanged" from the output:

$$|H_{in}\rangle \rightarrow |H_{out}\rangle \ , |H_{from}\rangle \rightarrow |H_{to}\rangle \, ,$$
$$|V_{in}\rangle \rightarrow |V_{out}\rangle \ , |V_{from}\rangle \rightarrow |V_{to}\rangle \, .$$

This is the storage function, wherein light that is in the delay line cycles in the loop, i.e., through the fast PBS and back into the delay line. This means that both stored and input light components are effectively isolated from each other.

(iii.) If $eom1$ is turned on to act as a half-wave plate at 45°, performing a polarization swap, but $eom2$ is turned OFF, then loop effects a PBS transformation between the incoming light ('in') and the stored light coming from the delay line ('$from$'). Specifically, the horizontal and vertical polarization's see the different transformations:

$$|H_{in}\rangle \rightarrow |H_{to}\rangle \ , |H_{from}\rangle \rightarrow |H_{out}\rangle \, ,$$
$$|V_{in}\rangle \rightarrow |V_{out}\rangle \ , |V_{from}\rangle \rightarrow |V_{to}\rangle \, .$$

This is the 'PBS interfere' function inside the loop. Table 6.1 summarizes these three functions of the loop circuit. The EOM's (remember both $eom1$ and $eom2$ constitute a single physical device, timely switching operation distinguish $eom1$ and $eom2$) toggling is programmed on the feed-forward FPGA device, and a set of toggling that contains all three different functions creates different types of correlation between photons. This can create either entangled or nonentangled multiphoton states [see Sec. 6.5]. The number of toggling sequences depends on the number of pump pulses or Bell states, which are involved in the total state generation.

GHZ state generation

Here we give a specific example of graph state generation using the new optical circuit and time multiplexing scheme. The basic idea is to make use of our quantum memory both to store and interfere with entangled partner photons of multiple Bell pairs from a single entangled photon pair source. A timeline of the GHZ state generation experiment is given in Fig. 6.4.4. In our experiment, the Sagnac source (blue bar) is pumped with a train of pump pulses (gray dashed lines), which defines the number of trials M for the generation of two-photon state, $|\phi_+\rangle = \frac{1}{\sqrt{2}}\Big(|H_1H_2\rangle + |V_1V_2\rangle\Big)$. Successful generation of Bell pairs from M trials attains a $2N$ photon entangled state out of N entangled pairs. Upon a successful pair-generation event (blue star), we first detect one of the photons as a herald. Similar to our storage experiment,

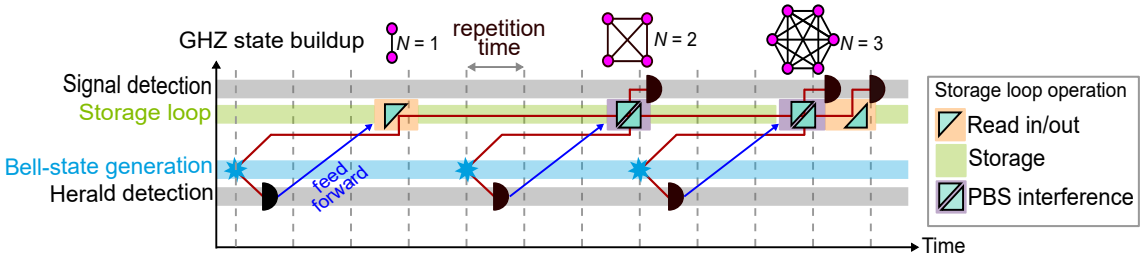

Figure 6.4.4: GHZ state generation timeline. Three Bell pairs are generated sequentially. The detection of one photon triggers the feed-forward including a field programmable gate array (FPGA), which in turn controls the operation mode of an all-optical storage loop. Possible operation modes are "read in and read out" (orange), "Storage" (green), or "PBS interference" (purple) selected by an appropriate switching of the electro-optic modulator (EOM). At each operational stage, the corresponding graph state formation is given on top of it (2, 4, 6 photon GHZ states).

herald detection triggers a feed-forward signal (blue lines) that initiates a read operation (orange square) and then stored (green bar) until the next Bell state is generated. Note that, here the heralded photons also form a part of the final entangled state. Polarization-resolved detection at the herald state initiates a feed-forward signal from either of the detectors at a time. Regardless of the polarization, a single click event from the herald side generates the feed-forward signal for the memory operations. Until another photon is detected in the heralding mode, the loop is set to the storage function by switching on both EOM's. Upon detection of the second herald photon from the next subsequent entangled pair, the storage loop is set to act as a PBS (purple square), such that the newly generated partner photon and the previously stored photon interfere ($eom1$ is 'on' and $eom2$ is 'off'). We again consider the inner product of two Bell states generated at two different time bins to start the four-photon state generation process,[3]

$$\left|\Psi^{\otimes 4}\right\rangle = \frac{1}{\sqrt{2}}\Big(|H_1H_2\rangle + |V_1V_2\rangle\Big) \otimes \frac{1}{\sqrt{2}}\Big(|H_3V_4\rangle + |V_3H_4\rangle\Big)\ , \tag{6.4.8}$$

the stored light that comes from the delay line at the '$from$' port of the PBS interferes with the time bin mode of the newly generated photon pair arriving simultaneously at the 'in' port. Note that because of W_1 operation second bell pair is changed to the 'ψ_+' state. PBS fusion operation expands to,

$$\left|\Psi^{\otimes 4}\right\rangle \sim\ |H_1H_3H_2V_4\rangle + |H_1V_3H_2H_4\rangle + |V_1H_3V_2V_4\rangle + |V_1V_3V_2H_4\rangle\,. \tag{6.4.9}$$

[3]Subscripts are used to convey the corresponding time bins, odd and even time bins numbers corresponds to herald and loop side photons respectively.

This operation maps the above-mentioned spatial PBS fusion scheme to the temporal domain. The circuit's PBS interference operation then changes the state into,

$$\left|\Psi^{\otimes 4}\right\rangle \sim |H_1H_3H_2H_4\rangle + |H_1V_3H_2V_2\rangle + |V_1H_3V_4H_4\rangle + |V_1V_3V_2V_4\rangle\,. \tag{6.4.10}$$

In Eq. (6.4.10), the first two photons represent the heralding photons (odd subscript) and later two from loop side temporal modes (even subscript). On Eq. (6.4.9), the interference operation transforms loop photon pairs with different polarization having their photons emitted into different ports (one into '*out*' and the other into '*to*') of the loop PBS. Also, pairs with the same polarization are emitted into the same output time bin, that is, either both leave via port '*out*' or both via port '*to*'. Finally, only those events are post-selected in which one photon is detected in consecutive time bins. Therefore only those two terms in the product state, in which all photons have identical polarization survive and the resulting state is a four-photon GHZ state,

$$|\Psi_{ghz}\rangle = \frac{1}{\sqrt{2}}\Big(|H_1H_3H_2H_4\rangle + |V_1V_3V_2V_4\rangle\Big). \tag{6.4.11}$$

This time-multiplexed operation repeats until the desired state size [for the case of Fig. 6.4.4, a six-photon GHZ state generated from three Bell states] is achieved, upon which the remaining photon inside the storage loop is actively read out (orange square) and detected.

Cluster state generation

To build up different graph state geometry one may think of applying arbitrary rotations on subsequent photons before the buffer interference operation. This is equivalent to applying local unitary operations (polarization rotation) on individual photons before interfering them on the PBS. For the simplest case, interfering two diagonally polarized single photon states on a PBS can produce a maximally entangled Bell state with 50% of the time. Extending the fusion for three photons generates a linear cluster state. a straightforward implementation of this scheme requires the setup to have an extra EOM to act as a half-wave plate at 22.5°, when there is a photon incoming, and to switch off when the loop is to act as a storage. A two-photon source emitting polarization state $|HH\rangle$ is used in a heralded manner for a stream of single photons. On the first time bin Heralded photon H_1 is rotated to $|D_1\rangle = \frac{1}{\sqrt{2}}(|H_1\rangle + |V_1\rangle)$ by W_1 and arrives at the PBS. Also upon the first heralding signal, the memory operation is toggled to interference operation allowing only the H-polarized mode into the memory with 50% storage success probability,

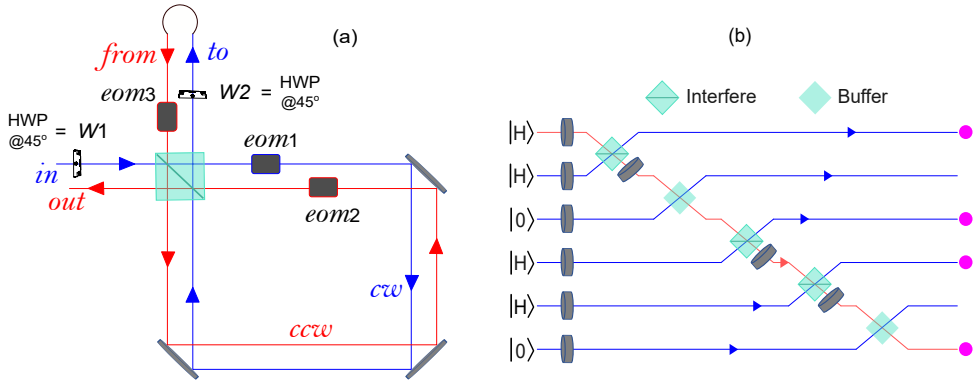

Figure 6.4.5: Cluster state generation circuit details: (a) Loop circuit with an additional modulator *eom*3 inside the delay line. (b) Operational timeline: The dashed green boxes represent the repeated action of the fast PBS and the grey discs represent the extra *EOM* at 22.5° and half-wave voltage placed at the '*from*' port of the loop. The ordering of the fast PBS ports (clockwise starting from top left) is '*from*', '*out*', '*to*', and '*in*'. At those temporal modes when a photon $|H\rangle$ is incident, the loop is switched to the PBS function and the *EOM* is on. For the remaining temporal modes, the *EOM* is switched off and the loop acts as a storage (depicted as a green box without a horizontal line). The red curve represents the mode that is cycling in the loop. The magenta circles at the output represent the desired linear cluster state and the empty modes are discarded.

the reflected mode is discarded because of interference operation mode. Toggling to store operation keeps the first heralded photon for the next herald. As soon as the next herald is detected, the loop is toggled to the interference mode, and the *eom*3 is switched on to its half-wave voltage at 22.5°. Photons $|H_1\rangle$ and $|H_2\rangle$ meet at the PBS as $|D_1\rangle$, $|D_2\rangle$,

$$\left|\Phi^{\otimes 2}\right\rangle = \frac{1}{2}\Big(|H_1H_2\rangle + |H_1V_2\rangle + |V_1H_2\rangle + |V_1V_2\rangle\Big). \tag{6.4.12}$$

After the PBS interference action the state changes to,

$$\left|\Phi^{\otimes 2}\right\rangle = \frac{1}{2}\Big(|H_1H_2\rangle + |H_2V_2\rangle + |H_1V_1\rangle + |V_1V_2\rangle\Big). \tag{6.4.13}$$

As we choose states in which only one photon is emitted in each time bin mode, we need only consider post selected and normalized state $|\phi_+\rangle = \frac{1}{\sqrt{2}}\Big(|H_1H_2\rangle + |V_1V_2\rangle\Big)$. After the interference, the loop is switched back to the storage mode and *eom*3 is turned off till the next detection event. The first qubit is emitted from the system and the second is stored till the next $|H_3\rangle$ qubit arrives. Just before the arrival of the third qubit, the polarization rotation of *eom*3 at the output of mode 2 converts

the state into a two-qubit cluster state and interferes with third qubit $|D_3\rangle$,

$$\left|\Phi^{\otimes 2}\right\rangle \times |D_3\rangle = \frac{1}{2}\Big(|H_1H_2\rangle + |H_1V_2\rangle + |V_1H_2\rangle - |V_1V_2\rangle\Big) \otimes \frac{1}{\sqrt{2}}\Big(|H_3\rangle + |V_3\rangle\Big) \ , \quad (6.4.14)$$

which after the action of the PBS and post-selection turns to

$$\left|\Phi^{\otimes 3}\right\rangle = \frac{1}{2}\Big(|H_1H_2H_3\rangle + |H_1V_2V_3\rangle + |V_1H_2H_3\rangle - |V_1V_2V_3\rangle\Big). \quad (6.4.15)$$

Once the third mode is acted upon by a polarization rotation, the state becomes,

$$|\Phi_{clust}\rangle = \frac{1}{2\sqrt{2}}\Big(|H_1H_2H_3\rangle + |H_1H_2V_3\rangle + |H_1V_2H_3\rangle - |H_1V_2V_3\rangle + |V_1H_2H_3\rangle + |V_1H_2V_3\rangle - |V_1V_2H_3\rangle + |V_1V_2V_3\rangle\Big) \ ,$$

which is exactly the three-qubit cluster state. The circuit block essentially forms a PBS followed by a half-wave plate at 22.5°, and this building block has the action of a controlled-phase gate on the $|D_iD_{i+1}\rangle$ qubits after post selection.

Source multiplexing theory

A benchmark in terms of success probability and generation rate is necessary to compare both spatial and temporal multiphoton state generation schemes. We also compare other time-multiplexed experimental schemes, which have no feed-forward mechanism [121]. A successful $2N$ photon state generation is quantified by the success rate of N photon pairs from the multiplexed scheme, we model a rate equation of type,

$$R_{success} = \frac{f_{rr}P_{success}}{\langle t_{run}\rangle} \ , \quad (6.4.16)$$

which takes into account a reduction of the experimental repetition rate f_{rr} by (potentially) longer waiting times due to the storage of states described by the average run time $\langle t_{run}\rangle$ (in units of pulses, not seconds). This effective experimental repetition rate is then multiplied by the success probability of one run $P_{success}$. In spatial case, a single laser pulse after splitting it up into N spatial modes can pump all sources simultaneously [Fig. 6.4.6(a)]. Consequently, there is no reduction in the actual repetition rate of the experiment, following $\langle t^{sp}_{run}\rangle = 1$. If we say p as the photon pair generation probability for a single source, the probability to fire simultaneous pairs from N sources is $P^{sp}_{success} = p^N$. Then the successful events for the spatial case are,

$$R^{sp}_{success} = f_{rr}p^N. \quad (6.4.17)$$

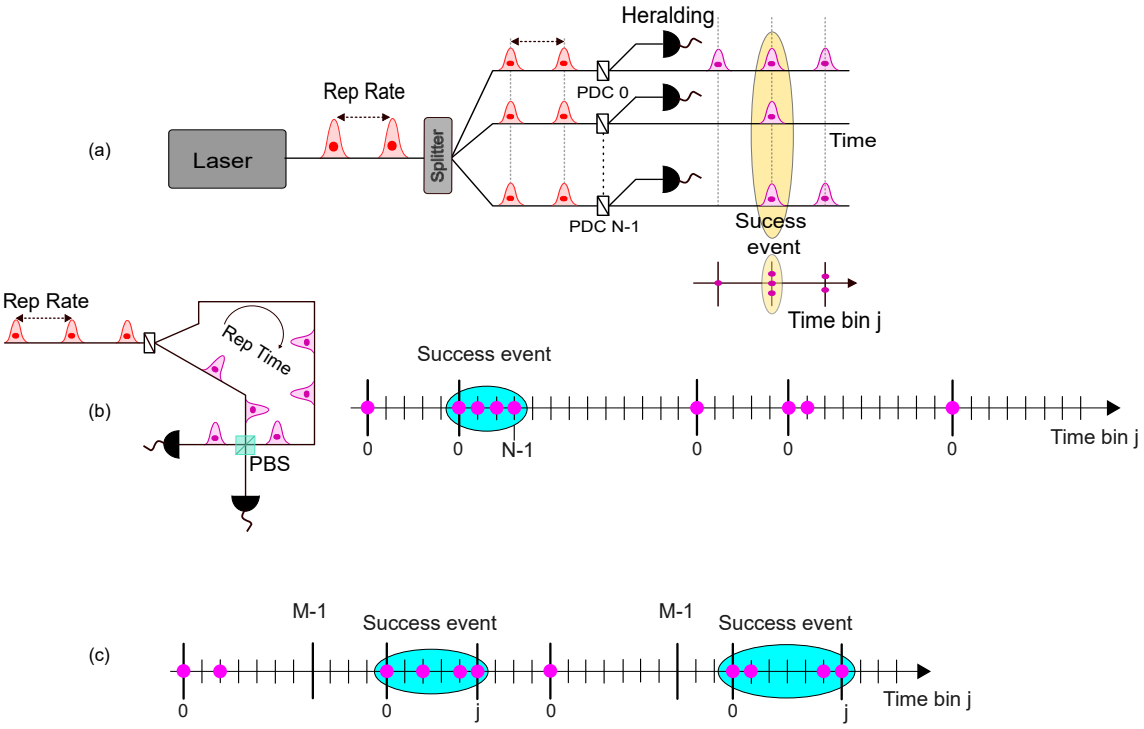

Figure 6.4.6: Different schemes to generate N number of photon pairs: (a) Spatial arrangement of N sources. The firing of all N herald detectors simultaneously announces successful generation events of N photon pairs. (b) Time-multiplexing setup adapted from [121]. One single source is pumped with a repetition rate of f_{rr}. One photon of a generated photon pair is directly sent to the polarising beam splitter (PBS), while its partner is delayed in a loop by f_{rr}^{-1} and arrives synchronously with the first photon of the subsequent pair (if generated) at the PBS where they interfere. The timeline of the time-multiplexed approach is also shown in (b). Its effective repetition rate is reduced by $\langle t_{run}^{TM} \rangle$ to allow for enough roundtrips in the TM loop. Only cases in which photon pairs are generated in N consecutive time bins are success events. (c) Time-multiplexing with feed-forward action as used in our setup, again for $N = 4$. The first pair generation event starts the j counter which stops either with the N^{th} pair created (success event) or after $M - 1$ subsequent time bins.

Time-multiplexing without feed-forward

In order to obtain a $2N$ photon state from a time-multiplexed source, one needs to consider N subsequent pump pulses exciting the source. State generation protocol is successful only when all the nearest pulses contribute pair-wise photons. Therefore we first have to calculate the average waiting time for N subsequent pair generation events, which will then define the average run time and thereby the achievable repetition rate. The first photon starts the time bin counter at $j = 0$ and a successful event includes one photon in each of the subsequent $N-1$ time bins [Fig. 6.4.6(b)], all other events will be discarded as in the spatial setting. Again we find a success probability of $P^{TM}_{success} = p^N$. The average run time is,

$$\langle t^{TM}_{run} \rangle = \frac{p^n N + \sum_{q=1}^{N} p^{q-1} q(1-p)}{p^n + \sum_{q=1}^{N} p^{q-1}(1-p)} \ , \tag{6.4.18}$$

which describes the (probability-weighted time) to get all N pairs plus the (probability-weighted time) to get $N-1$ pairs ($q = N$ term in the sum) and then vacuum plus $N-2$ pairs ($q = N-2$ term) and then vacuum and so on to the time to get no pair at all ($q = 1$ term). The overall success rate is then,

$$R^{TM}_{success} = \frac{f_{rr} p^N}{\langle t^{TM}_{run} \rangle}. \tag{6.4.19}$$

With small p, most attempts end immediately in failure, making $\langle t^{TM}_{run} \rangle \approx 1$, and thus making the rate very close to the spatially multiplexed version. For $N = 10$ and $p = 0.01$ and average run time of $\langle t^{TM}_{run} \rangle = 1.01$.

Time Multiplexing with Feed-Forward

Click information and the feedforward allow the photons to wait not just for subsequent but multiple pump pulse time bins for another successful click event within a predefined number of pump pulse streams. This makes the feed-forward scheme attractive for both rate enhancement and state generation. In practice we wait for the first click, define this as ($j = 0$), and then collect the subsequent clicks until either $(N-1)$ additional pairs are detected or -if this has not happened within the subsequent $(M-1)$ time bins- the run is discarded. After this, we have to wait for the next first click, see Fig. 6.4.6(c). In a successful case, the experimental run ends with the N^{th} generated pair (this defines time bin j) and the remaining $(N-2)$ events were distributed among the remaining $(j-1)$ free bins between bin $j = 0$

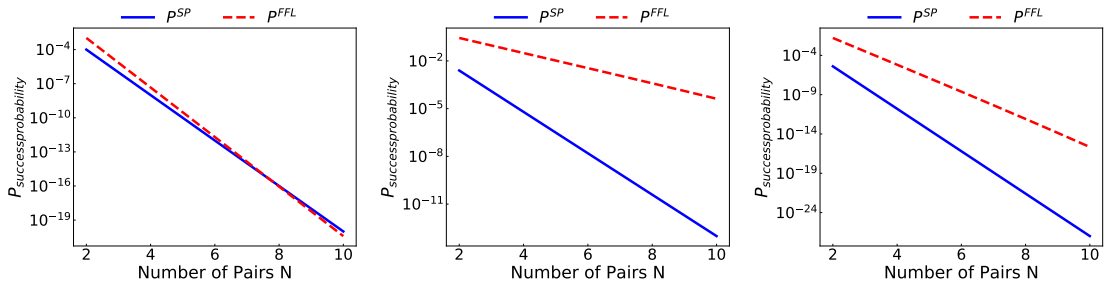

Figure 6.4.7: Success probabilities $P^{FFL}_{success}$ and $P^{SP}_{success}$ for different parameters p and η with increasing state sizes N and optimized M. The first example for low $\eta = 0.4$ (left subplot) only shows an advantage for the FFL scheme for $N < 7$, pair generation probability ($p = 0.01$). For memory efficiency of $\eta = 0.91$, data shows performance scaling when we go to larger entangled states. Real experimental settings $p = 0.05$ (center) from [98] and $p = 0.002$ (right) from [2] are used for the simulations.

and bin $j = j$, leading to an extra binomial factor $\binom{j-1}{N-2}$.

$$\langle t^{FFL} \rangle = \sum_{j=N-1}^{\infty} j p^{N-1} (1-p)^{j-N+1} \binom{j-1}{N-2} = \frac{N-1}{p}. \tag{6.4.20}$$

By adding the waiting time to get the first photon pair ($1/p$), the average waiting time for N pairs then linearly scales to $\frac{N}{p}$. Note, that our typical numbers for the multiplexed sources M are smaller than $\langle t^{FFL} \rangle$ due to finite memory efficiency and fidelity. As a free experimental parameter, the best M can be easily found by optimizing the success probabilities or rates for a given state size. The success rate of obtaining $N-1$ pairs after the first detected one in the subsequent $j = 1, ..., M-1$ time bins is thus described by,

$$P^{FFL,\eta}_{success} = \sum_{j=N-1}^{M-1} p^{N-1} j^{j-(N-1)} \eta^{j+2} \binom{j-1}{N-2}. \tag{6.4.21}$$

Also note that in a successful N photon event, one photon is always cycling in the loop for the j previous roundtrips. Considering the coupling in and the interference (both with an extra roundtrip), the loop efficiency η factor is also included in Eq. (6.4.21) for the success probability.

The average run time of one experiment thus consists of the following; the first one takes into account the average time to produce the first pair, i.e. $\frac{1}{p}$. The second term models the expected time for a successful generation of the remaining $N-1$

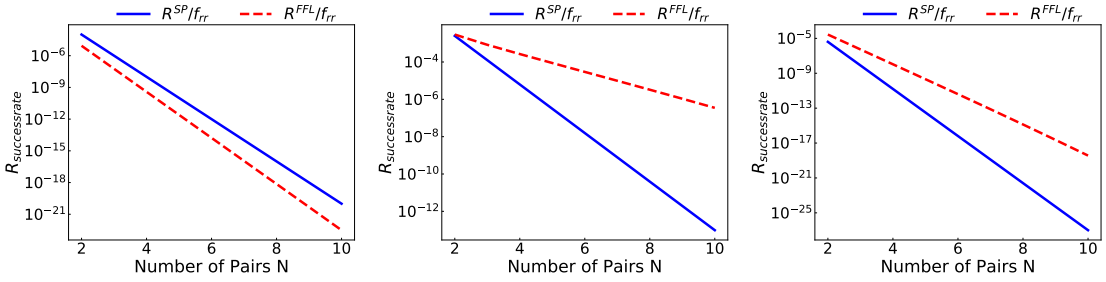

Figure 6.4.8: Success rates $R^{FFL}_{success}$ and $R^{SP}_{success}$ for the same parameters p and η as in Fig. 6.4.7 with increasing state sizes N and optimized M. Note that for $\eta = 0.4$ the advantage in $P^{FFL}_{success}$ cancels out in rate performance when also taking into account the increase of the average runtime in the success rates.

pairs in the subsequent $M-1$ time bins. Finally, the third term takes into account those runs, that were unsuccessful and discarded,

$$\langle t^{FFL,\eta}_{run} \rangle = \frac{1}{p} + \sum_{j=N-1}^{M-1} j p^{N-1} j^{j-(N-1)} \eta^{j+2} \binom{j-1}{N-2} + M(1 - P^{FFL,\eta}_{success}). \qquad (6.4.22)$$

The choice of multiple experimental parameters in these expressions provides a wide range of optimization procedures for the fine-tuning of the system performance. Numerical simulations are performed for success probabilities and rate enhancements, corresponding outcomes are provided in Fig. 6.4.7 and Fig. 6.4.8. Both of them show a very strong dependency on the loop efficiency η of whether the FFL scheme provides an advantage over the spatial scheme or not. A highly efficient quantum memory-enabled TM-feedforward approach observes significant enhancement factors in $P_{success}$ and $R_{success}$ when the state size (or N) becomes larger.

Figure 6.4.9 shows finally the ratio of the success rates $R^{FFL}_{success}/R^{SP}_{success}$ in a two-dimensional parameter plot, again with optimized M parameter for increasing state size. One can find a large region of experimental parameters (p, η) where the FFL arrangement outperforms the spatial scheme. Data again validate that the experimental efficiency achieved in our buffer memory with optimized optical components, above 90% is feasible to observe a strong increase of the enhancement factors with increasing N. In fact with moderate efficiency, when η in the range of 50% to 60% is already providing an advantage for the FFL scheme starting from $N = 2$. It is also important to mention that instead of improving the rate for a constant pair generation probability p using our scheme, it would be possible to improve the entanglement visibility by reducing p, while keeping the $2N$-photon

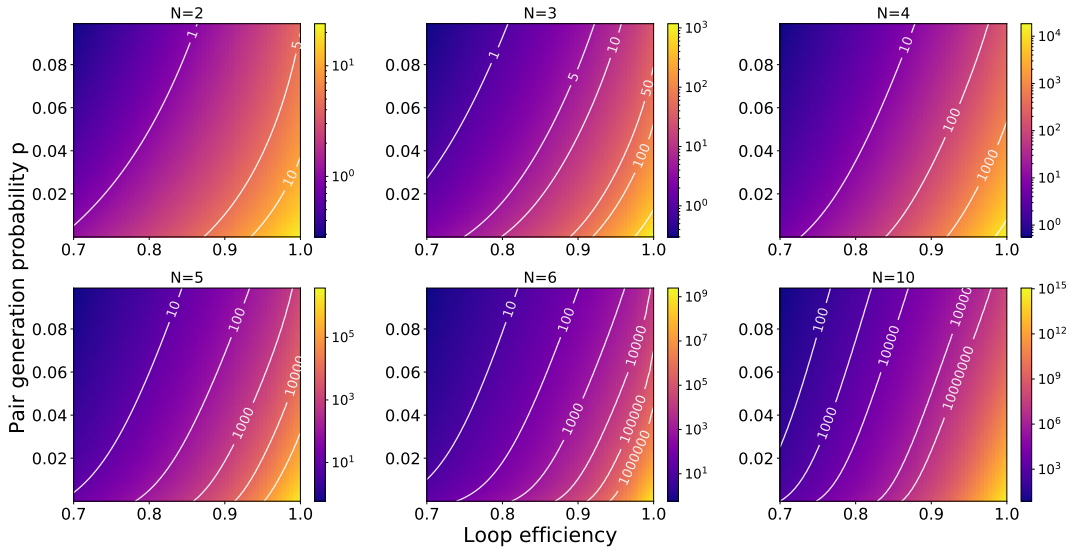

Figure 6.4.9: $2N$ fold coincidence rate enhancement as a function of the Bell pair production probability and the memory efficiency for N Bell pairs ($N = 2, 3, 4, 5, 6, 10$). Larger states are predicted by the same theory to experience stronger enhancement, up to 9 orders of magnitude for $N = 6$, that is, 12-photon GHZ states, the actual state of the art [98].

rate enhancement constant.

A numerical estimation for the state-of-the-art spatial scheme (12-photon GHZ experiment [98]), reveals that- the same experimental parameter settings on our TM-feedforward scheme can produce three orders of magnitude increase in rates in a resource-efficient manner. Increasing the loop efficiency to 99% would even yield an enhancement factor of $\approx$ 170000. Fig. 6.4.10 shows with the increasing size of the produced GHZ state, the advantage of using a feed-forward loop over parallel sources increases significantly. For a 12-photon GHZ state, the feedforward method can deliver up to 1 detected 12-photon state per second, three orders of magnitude increase over the current state-of-the-art spatial arrangement with the same experimental efficiency.

So far we have developed relevant hardware systems and theoretical investigations for a time multiplexing circuit to efficiently generate non-entangled or entangled single or multiphoton states. Optimal parameters are obtained for several system design modules and numerical simulations are performed with different input parameters. The following sections will be devoted to the experimental investigations of temporal source multiplexed multiphoton state generation and measurement strategies to benchmark the output state quality.

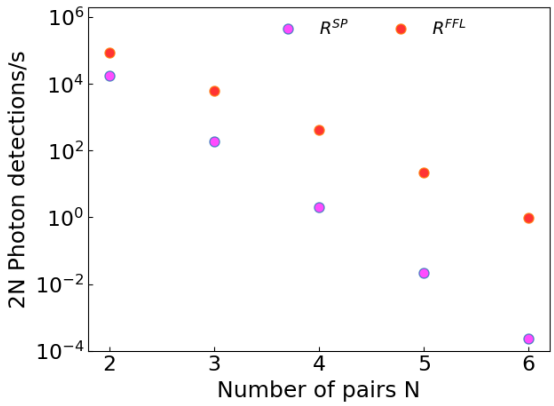

Figure 6.4.10: Expected GHZ state count rates for spatial (R^{SP}) and TM-feedforward (R^{FFL}) arrangement with realistic experimental parameters taken from [98]. When the system size increases absolute rate advantage also increases in R^{FFL} compared to R^{SP}.

6.4.3 Two photon interference

Many indistinguishable photons, which are the key requirement for perfect multi-photon quantum interference now available from a single SPDC source in a time-multiplexed manner. Spectrally engineered source guarantees, single and identical spectral mode behavior for the subsequently emitted photons. The spectral purity of these photons is experimentally estimated from Fig. 5.1.9 and shows a high value ($> 97\%$) because of decorrelated joint spectral amplitude. Now the source emits pure, degenerate, pair photons in a *probabilistic* manner, but we can add source multiplexing to improve the generation probability of photon pairs.

Even though the source generates type II phase-matched orthogonal polarization photons, which are indistinguishable from the action of waveplate rotation on either of the partner photons. The indistinguishable nature of (spatial, temporal, and spectral) signal-idler photon pair was already tested with a HOM interference experiment and reveals high visibility [see data at Fig. 5.1.11]. Next, our proposed FFL approach demands a HOM interference test between signal-signal or idler-idler, which also enables a test to validate the spectral purity of photons emitted at different time bins. Which is also a standard requirement to prove the indistinguishable nature of subsequently emitted photons. Moreover, high two-photon interference visibility in the realm of indistinguishability is essential for validating the multiphoton entangled state generation protocol. An experimental HOM test is then performed with two subsequent heralded single photon events from the same source, by delaying the early arriving (first-time bin) photon inside the loop memory. Even though

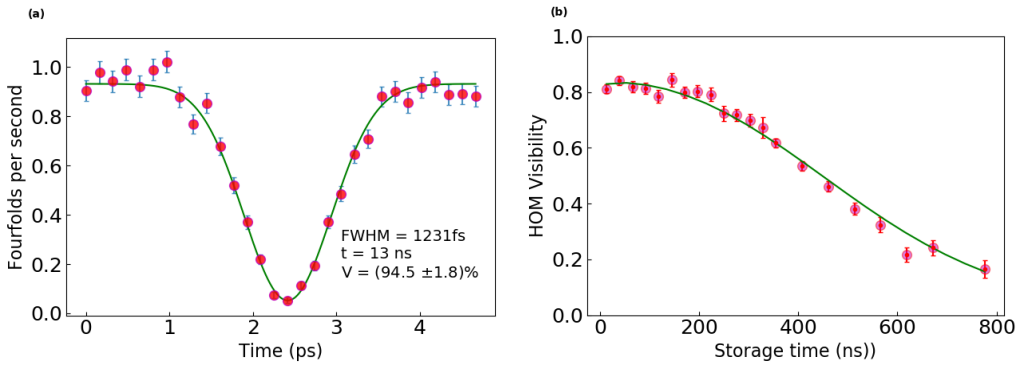

Figure 6.4.11: Hong-Ou-Mandel interference: (a) Normalised HOM visibility plot at low pump power, showing the indistinguishability of the $signal - signal$ photon pairs from subsequent pump pulses. The translation stage position is converted into a timescale to calculate the temporal bandwidth of interfering photons. The corresponding full-width half-maximum of the HOM dip, the storage time of the first photon, and the dip visibility are listed in the plot. (b) Experimental and theoretical observation of HOM dip visibility for several roundtrip/storage times. An optimized pump power (from the previous two-photon entanglement experiment) is used for the entire HOM experimental tests.

the memory loop is designed to match the repetition rate of the laser there can be temporal distortions because of various reasons, implying temporal distinguishability between photons arriving at the PBS inside the loop. To finely adjust the time delay, the retro mirror is made to be placed in a piezo-controlled translational stage. Sweeping the stage for a finely tuned distance range provides a temporal HOM dip. The source is first operated in a low pump power to avoid multiphoton components, consequently, high-quality single photon states are prepared. HOM visibility of 94% is obtained on these settings between the two nearest generated photons (13 ns storage window). The nearest case signal-signal HOM interference data is plotted in Fig.6.4.11(a).

Since we need to store the photon for many round trips to improve the multi-photon state generation probability, HOM experiments are repeated from the two nearest photon pairs to the non-nearest pump pulse time bin. Essentially a source multiplexed HOM experiment is performed between two pairs, which are time bin separated up to 59 pump pulses. On timescale which constitutes the storage of early time bin photon up to 800 ns time. The data is made available in Fig. 6.4.11(b). A relatively higher pump power choice is made for the characterization of multiple round-trip HOM experiments, validating the performance of both source and memory for further experimental needs. The data shows, Interference visibility of 81%

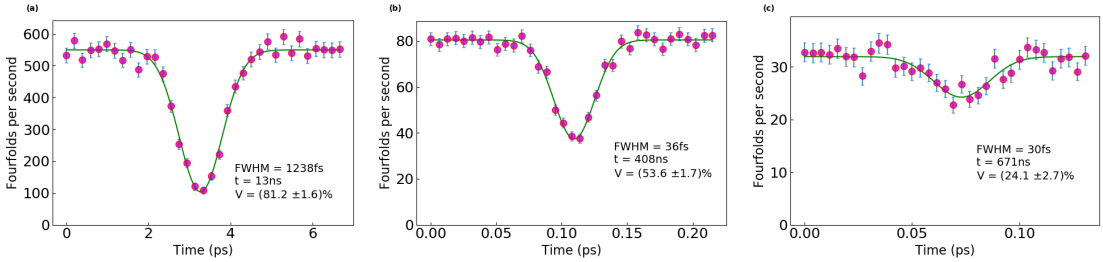

Figure 6.4.12: Example HOM dips at higher power for faster data collection, showing degradation as storage time is increased from 13 ns to 671 ns. The FWHM of the dip also decreases proportionally to the storage time, as the mirror that is scanned to measure the dip is the end mirror of the loop, meaning the translation is effectively multiplied by the number of storage roundtrips.

for the nearest case and drops below the classical limit (50%) from 30 roundtrips onward. But this already provides an advantage to store the photons for 10 to 20 round trips with high visibility. HOM dip visibility plots for three different storage intervals are given in Fig. 6.4.12.

Experiment: The Sagnac source is pumped from one side to generate an orthogonally polarized two-photon state. Two pump pulses are multiplexed to bring consecutive signal photons to the loop side. Upon detection of the second herald, the initially stored first photon is interfered with the freshly generated nearest or non-nearest second photon depending on the storage time. A different switching pattern is adapted for a two-photon interference experiment rather than a qubit storage experiment. Here the idea is to store the first photon in a specific polarization state ($|H_1\rangle$) and wait for the next heralded photon ($|V_2\rangle$). Upon detection of the second herald photon, the loop is programmed to release the stored photon together with the fresh second photon in a final state $|H_1V_2\rangle$. At the output side, a HWP is set at 22.5° to make the photons indistinguishable. Over the coincidence measurement time, the translational stage inside the loop is scanned within a distance range to observe the HOM dip. Finally, four-fold coincidence events (two heralds + two loop events) are counted for HOM visibility calculations. The repetition rate of the pump laser is passively locked to an external precise oscillator to keep the pulse separation intact for better interference quality. From the technical side, HOM performance is mainly affected by the *EOM* switching quality, the angle of the QWP in the loop arm, and the stability of the overall setup. A slight misalignment in the waveplate angle causes considerable degradation in the visibility since the photon passes multiple times through the waveplate in a non-nearest situation.

6.4.4 Four photon polarization entanglement

Multiphoton state generation

High indistinguishability between the subsequent photon pairs now ensures high-fidelity multiphoton state generation. In the first attempt we interfere two Bell states to create a four-photon entanglement and the feed-forward protocol allows more than two pump pulses for two Bell states generation possibility. Since we do the PBS interference operation from two polarization entangled Bell state inputs, initial individual Bell state entanglement fidelity is also highly sensitive for the multiphoton output state quality. Four photon GHZ experiment requires two consecutive Bell pairs from the engineered source and maximal four-photon fidelity is bounded by the product of Bell state fidelity ($F_{GHZ} \leq (F_{Bell})^N, N$ is the number of Bell pairs involved in the experiment). The aim is to generate a four-photon polarization-entangled state in the form of,

$$|\Psi_{ghz}\rangle = \frac{1}{\sqrt{2}}\Big(|HHHH\rangle + |VVVV\rangle\Big). \tag{6.4.23}$$

creating four photons GHZ states with non-local polarization correlations. Also, keep in mind that photons are coming in different time bins.

Sagnac is now pumped from both directions to generate specific polarization entangled Bell state $|\psi_+\rangle$, pump power is adjusted to keep moderate entanglement visibility ($> 93\%$) for each pair from the source (0.01 pair per pulse). A total detection efficiency (Klyshko) of $\approx 38\%$ is observed in the heralding arm, while on the loop side $\approx 23\%$ without any storage operation. Nearest and non-nearest two Bell pairs are then interfered on the loop PBS and fusion-based protocol permits post-selected GHZ states [described in Sec. 6.4.2]. While running the GHZ experiment we keep the delay line retro mirror at the HOM dip minimum position to ensure maximum temporal indistinguishability as to maximum two-photon interference. Fourfold events are accumulated in a gated manner based on feed-forwarded FPGA signals [data collection methods are given in B.0.1]. For different numbers of multiplexing stages and pump power choices, fourfold coincidence are collected and corresponding data sets are provided in Fig. 6.4.13. 21 pump pulses ($M = 21$ from theory) are multiplexed in the demonstration, which means the probability of getting two entangled pairs ($N = 2$) in 21 consecutive pump pulses is considered to test the proposed rate enhancement. The following four-fold events show a 9.2-fold increase in rates/sec compared to the nearest pump pulse multiplexed case. The low dead-time of SNSPD (12 ns) allows the experiments to run at the full repetition rate of the laser, therefore one can expect higher rates/sec for data processing. A

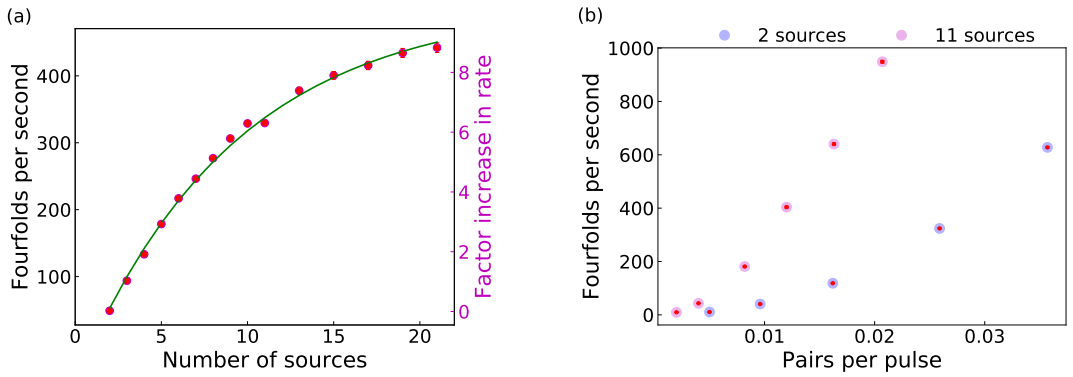

Figure 6.4.13: Experimental four-photon GHZ rates. (a) Experimentally observed four-fold events to the number multiplexing sources, more than 9-fold increase in rates. Experimental data perfectly matches with theoretical estimation plot (green). (b) The scaling of four-fold events to different pump power settings is given in this plot. The pump power value is converted into pair-per-pulse form. A higher number of four folds is expected for larger multiplexing and brighter sources, this is clear from the power dependence of 2 and 11 source multiplexed situations. However, higher squeezing will reduce the quality of state since our click detectors are blind to photon numbers.

total of > 500 four-fold events/s are observed with $M = 21$ multiplexed sources and for a specific pump power (0.001 pair per pulse) setting. Higher rates can be anticipated with more pump power but this can reduce the fidelity of the state because of TMSV higher-order components. However, the experimental observations promise an ideal platform to implement multiphoton generation protocol with realistic near-deterministic Bell sources.

Fidelity Measurements

Quantum state fidelity estimation is a relatively hard task in terms of the number of measurements required for the density matrix reconstruction, which scales exponentially with the size of the Hilbert space. We have used readily available, optimized quantum state reconstruction tools to estimate two-photon entanglement fidelity [Fig. 5.2.3], but an extension of the same protocol to a higher number of photons is not possible. On the other hand, *entanglement witness* operators are developed to detect genuine multipartite entanglement within an N-qubit system, in a manner to differentiate separable and non-separable higher dimensional systems [122]. For relatively larger quantum systems like clouds of ions and atoms spin squeezing technique has shown to be a valuable tool to identify entanglement and nonclassical behaviour [123]. In both cases, the essential idea is to violate cer-

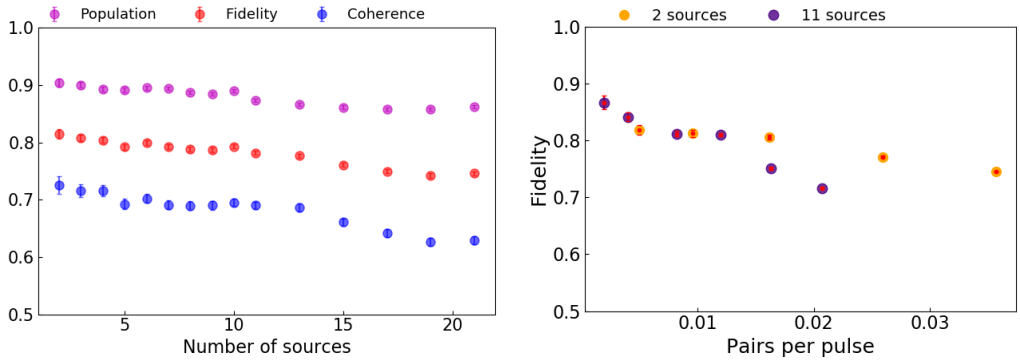

Figure 6.4.14: State fidelities and power dependence. A set of fidelity values for a four-photon GHZ state with a different number of source multiplexing scenarios is presented. Also for a choice of cases, 2 and 11 source multiplexed situation power dependence of fidelity is given in the second plot. (left) Expectation values for H/V measurement ($\mathcal{D}_N$ = populations) and anti-diagonal measurement ($\mathcal{A}_N$ = coherence) together with corresponding fidelity estimates are plotted in a single window. As expected M goes higher fidelity also decreases but performs well above 50% for 21 roundtrips. (right) Unavoidable multiphoton components on higher squeezing always deteriorate fidelity which is shown here for a fixed source multiplexing fidelity goes down for higher pump power. This effect becomes more sensitive for higher number of multiplexing since unwanted higher order photons started to create false binning in post selection.

tain maximal-minimal bounds to differentiate classical and nonclassical states. We use entanglement witness criteria developed here [124] for multipartite state fidelity estimate.

For an N-qubit GHZ state, density matrix decomposition in pure state form gives,

$$|GHZ_N\rangle\langle GHZ_N| = \frac{1}{2}\Big(|H\rangle\langle H|^{\otimes N} + |V\rangle\langle V|^{\otimes N} + |H\rangle\langle V|^{\otimes N} + |V\rangle\langle H|^{\otimes N}\Big)\,, \tag{6.4.24a}$$

$$|GHZ_N\rangle\langle GHZ_N| = \frac{1}{2}(\mathcal{D}_N + \mathcal{A}_N). \tag{6.4.24b}$$

Where the Diagonal elements $\mathcal{D}_N = |H\rangle\langle H|^{\otimes N} + |V\rangle\langle V|^{\otimes N}$ are obtained from Pauli $\sigma_z^{\otimes N}$ measurements locally on the N individual photons. Similarly, Pauli's operator-based transformations are derived for Anti-diagonal elements $\mathcal{A}_N$,

$$\mathcal{A}_N = \frac{1}{N}\sum_{k=0}^{N-1}(-1)^k \mathcal{M}_k^{\otimes N}\,. \tag{6.4.25}$$

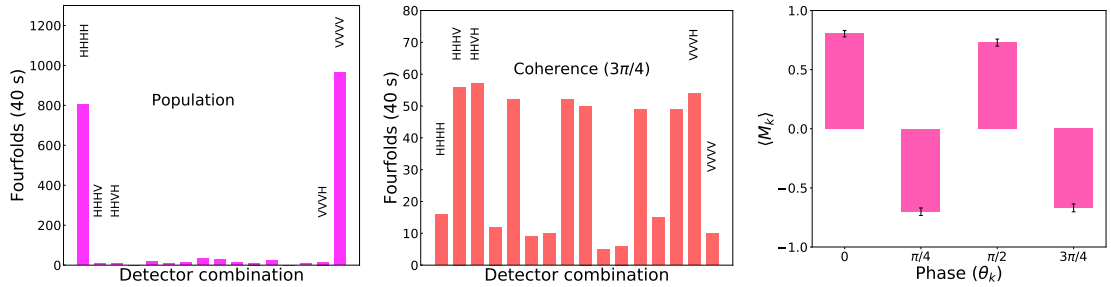

Figure 6.4.15: Diagonal ($\mathcal{D}_N$), Anti-diagonal ($\mathcal{A}_N$) and $\mathcal{M}_k^{\otimes N}$ measurements: 2^N different combinations of expected four fold events for $\sigma_z^{\otimes N}$ and $\mathcal{M}_{k=3}^{\otimes N}$ are shown the first two plots. (left) Click populations only on the HHHH and VVVV combination confirms that the post-selection protocol works well in our experiments and contributes to the diagonal terms. (center) Anti-diagonal measurement output combination for a specific basis choice ($\mathcal{M}_{k=3}^{\otimes N}$) is plotted here. (right) Finally expectation values for $\mathcal{M}_k^{\otimes N}$ for different phase settings. Visibility of $> 70\%$ for the off-diagonal terms implies reasonable phase stability in the setup, even though we show high contrast for the H/V basis ($> 90\%$). But the state certainly shows genuine multiphoton entanglement.

While $\mathcal{M}_k^{\otimes N}$ can be obtained from,

$$\mathcal{M}_k^{\otimes N} = \left[\cos\left(\frac{k\pi}{N}\right)\hat{\sigma}_x + \sin\left(\frac{k\pi}{N}\right)\hat{\sigma}_y\right]^{\otimes N} \quad , \quad k = 1, 2...N. \tag{6.4.26}$$

Equation 6.4.26 essentially means a set of measurements in the xy-plane on the Bloch sphere, again this can be done locally on the individual qubits. The fidelity of the GHZ state is now possible to probe experimentally with $N + 1$ measurement settings using a waveplate-based tomographic arrangement. Note that fidelity estimation depends on the number of qubits, but for a 4-photon case only five measurements are required. Also, the choice of $\mathcal{A}_N$ decomposition is not unique certainly several classes of measurement bases in the xy-plane exist for $\mathcal{A}_N$. This proves several fidelity value estimations simultaneously possible for the same state in question.

We then estimate the experimental fidelity of the four-photon GHZ state as $F = \frac{1}{2}(\langle \mathcal{D}_N \rangle + \langle \mathcal{A}_N \rangle)$. Measurement basis for $\mathcal{M}_k$ operator are derived in the form of $\frac{(|H\rangle \pm e^{i\theta}|V\rangle)}{\sqrt{2}}$ [119, 120], where $\theta = \frac{2\pi}{k}$ for $k = 0, 1, 2, 3$. Each setting can be manipulated by HWP and QWP combinations. Expectation values in the form of four-fold click probabilities are then evaluated for each measurement setting in different multiplexing situations and given in Fig. 6.4.14. Data shows above 81% state fidelity for a 4-photon GHZ state for the best possible two nearest multiplexed Bell pair case. Multiplexing of 21 sources still shows high state fidelity above 60%

from raw coincidence click probabilities. Since the Fidelity values are well above the 50% limit, generated states certify genuine multipartite entanglement for the GHZ state through the entanglement witness operator approach. Click probability pattern from the measurement outcome of $\mathcal{D}_N$ and for a specific choice of $\mathcal{M}_k^{\otimes N}$ is given in Fig. 6.4.15, additionally experimental values of all the four coherence terms are added here.

Finite system efficiency especially from the memory side and entanglement source limitations (fidelity) are the major concerns to run the experiment for a particular choice of multiplexing number M, 21 sources (21 pump pulses) for this experiment. If we crank up the pump for more rates, the squeezers naturally start to contribute higher-order photon numbers into the protocol which leads to a reduction in state quality. Moreover keeping the photon inside the memory for more roundtrips ends up in losses, this would be identified from the saturation of four-photon coincidence rates towards higher numbers of M in the experimental data. In practice one can easily attach any reliable, efficient two-photon polarization entanglement source to our buffer memory for larger state generation, there is no technical limitation to replace the source.

6.4.5 Six and Eight photon polarization entanglement

In a spatial situation going from a four to six-photon state requires an additional Bell state source, interferometric setup, and detectors in line with an existing four-photon arrangement. With the same optical and electronic hardware circuit we further investigated larger entangled states like six and eight-photon experiments, which shows the prime advantage of our method in system scalability. The fusion process requires three, and four Bell pairs for six and eight photon experiments, this can be readily attained from a multiplexing of 21 pump pulses. The only change in the state generation protocol is the number of switching and the format of switching, this is straightforward through the user-defined FPGA programming. This essentially means in a four-photon experiment the two interfered photons are released one after the other following a successful PBS interference operation. For six photon state generation, we have to keep one photon inside the memory after the first interference and wait for the third photon pair. This can be repeated for eight photon experiments with four Bell pairs.

The high fidelity of a four-photon experiment guarantees reasonable fidelity for a six-photon test. We kept the possible numbers of source multiplexing 'M' for the six-photon experiment too and carried over six-fold coincidence measurements on H/V basis. This is legitimate to test the post-selection success and verification

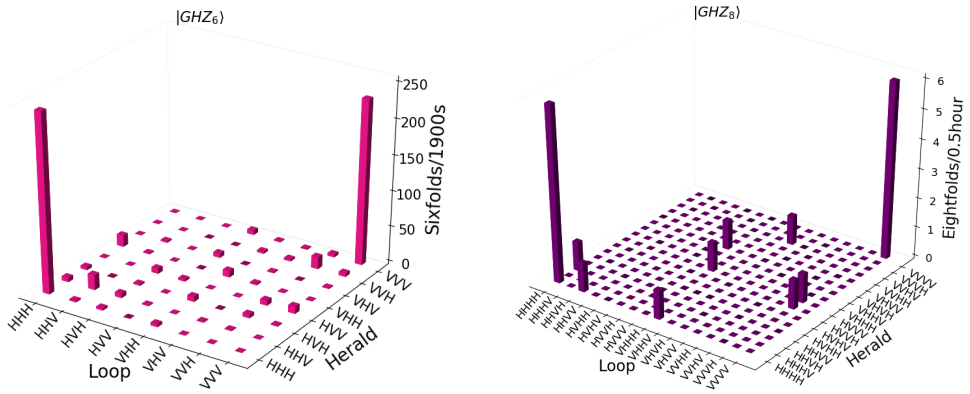

Figure 6.4.16: Six and Eight photon experiment: Experimental expectation values for the diagonal ($\mathcal{D}_6$, $\mathcal{D}_8$) elements from Eq. (6.4.24b), which is the click population in H/V measurement basis. (left) Six photon output distributions for a multiplexed experiment (number of pump pulses $M = 4$) with 0.012 pair per pulse estimation from the pump power. (right) Eight photon click patterns were observed on H/V basis. Which shows 60% H/V visibility and 20 eight-fold events for 30 minutes of data acquisition. $M = 14$ pump pulses are multiplexed for this test data with a pair per pulse contribution of 0.01.

towards a state format $|\psi\rangle = \frac{1}{\sqrt{2}}\Big(|H^{\otimes 6}\rangle + |V^{\otimes 6}\rangle\Big)$. It is clear from Fig. 6.4.16, where click population in computational (H/V) basis confirms a six and eight-photon GHZ state outcomes after reprogramming the memory device for more number of photons. A maximum H/V visibility of $\approx 77\%$ is reached with pump power settings of 0.012 pairs per pulse regime, a slight reduction of the pump power also shows higher visibility $\approx 80\%$ for a six photon GHZ test. This visibility is based on the ratio of expected outcome $(|HHHHHH\rangle, |VVVVVV\rangle)$ to the total number of output combinations.

Relatively large rates of six-fold trials benefit bench-marking the FFL entanglement generation scheme and further characterization of the generated quantum state. Six photon GHZ experiments with 22 pump pulse multiplexing show 35-fold enhancement in a six-fold coincidence rate compared to the nearest possible multiplexing. Observed rate enhancement underpins our theoretical prediction that larger states have better rate scaling on the feedforward platform. On the same pump power settings (0.012 pair per pulse) we detected 1.5/sec six-fold events with a maximum multiplexing of 22 pump pulses. Experimental observation of six photon rates for different multiplexing settings and corresponding scaling factors are given in Fig.6.4.17.

Fidelity estimation requires diagonal and anti-diagonal elements defined for six

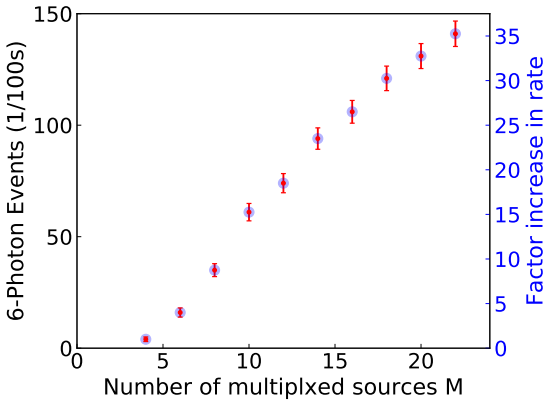

Figure 6.4.17: Six photon rates. A complete data set for six photon events from nearest possible source multiplexing to non-nearest pump pulses up to $M = 22$. For the maximum number of multiplexing ($M = 22$), we could observe a six-photon event every second, limited by the pump power and entanglement quality trade-off. Six photon rates show a 35-fold increase from the nearest to non-nearest ($M = 22$) experimental events.

photon case, which means simply increasing the dimension $N = 6$ for the $\mathcal{A}_N$ and $\mathcal{M}_k^{\otimes N}$,

$$\mathcal{A}_6 = \frac{1}{6}\sum_{k=0}^{5}(-1)^k \mathcal{M}_k^{\otimes 6} \,, \tag{6.4.27a}$$

$$\mathcal{M}_k^{\otimes 6} = \left[\cos\left(\frac{k\pi}{6}\right)\hat{\sigma}_x + \sin\left(\frac{k\pi}{6}\right)\hat{\sigma}_y\right]^{\otimes 6} \,, \quad \text{for} \quad k = 0, 1, 2, 3, 4, 5. \tag{6.4.27b}$$

Corresponding experimental expectation values show $\approx 60\%$ coherence value in each anti-diagonal measurement setting. Thereby the generated GHZ state always shows fidelity of above 60%, paving the condition for genuine six-qubit multiphoton entanglement. Experimental fidelity estimation numbers can be found in Fig. 6.4.18 for different multiplexing settings. A more or less flat response of the fidelity values is an interesting observation for the multiplexed six-photon experiment. We would expect this might be an effect of low pump power, especially false coincidence probability becomes more and more irrelevant when go to higher number of Bell pairs and larger entanglement size. So going beyond a six-photon experiment is an interesting avenue to understanding the device performance but then losses and Bell source have to be improved. We are eager to see a high rate, near deterministic two-photon entanglement source with feed-forward memory to explore even higher state and overall performance.

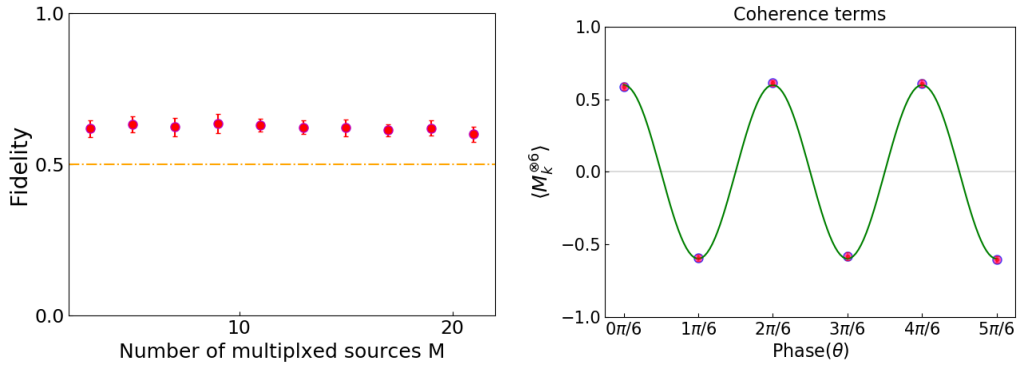

Figure 6.4.18: Fidelity and Coherence: Fidelity values of up to 22 source multiplexed 6-photon GHZ state, Coherence measurements outcome $\mathcal{M}_k^{\otimes 6}$ are plotted here. (left) State fidelities for the corresponding number of multiplexing stages show a flat response. Above 50% fidelity shows genuine multiphoton entanglement for the generated state. (right) Experimentally observed expectation values for $\mathcal{M}_k^{\otimes 6}$ for six different bases for a specific source multiplexing number (M). A scaled theoretical fit perfectly matches with experimental data.

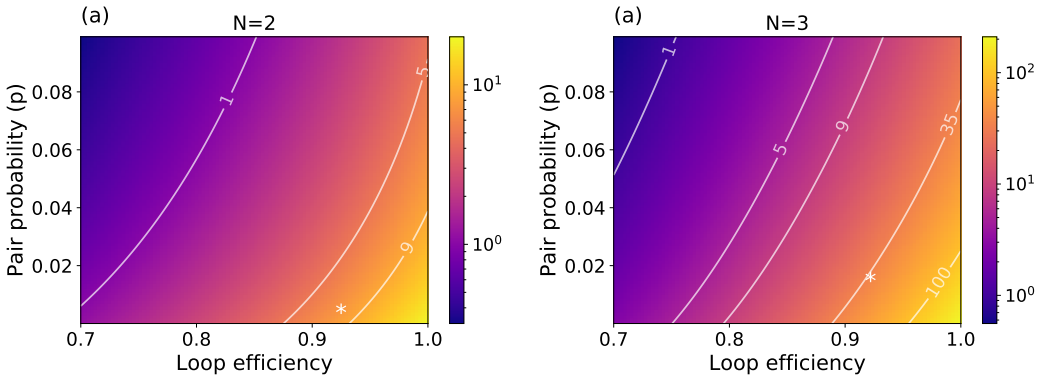

Figure 6.4.19: Enhancement factors $R_{success}^{FFL}/R_{success}^{SP}$ in a logarithmic colour scale for $N = 2$ (a), and $N = 3$ (b) with $M = 21$ and $M = 22$, respectively. White crosses in the plot mark the experimental parameters.

Using the realistic and observed experimental parameters, now it's possible to compare the rate scaling with our theoretical model. A number of source multiplexing $M = 21$ and $M = 22$ are used for the 4-photon and 6-photon experiments respectively. On average loop efficiency value of 92% is measured in the setup, with a fluctuation of $\pm 1\%$ over the experimental period. On the theory side, 7 and 34 fold enhancement is predicted with the proposed model, showing a close resemblance

with the experimental observations. Fig. 6.4.19 displays the rate enhancement factor for the feedforward TM scheme compared to the spatial scheme with loop efficiency and pair generation probability as free parameters for fixed M and N. Expected rate scaling for the experimental settings, efficiency η, and generation probability p are marked in the plots.

In addition, by considering four Bell pairs an eight-photon experiment is initiated for future considerations. But only a few counts are received for H/V measurements even with multiplexing, $|GHZ_8\rangle$ in Fig. 6.4.16. Preliminary data persistently shows 60% visibility in H/V measurements basis, which is good but not promising in the point of anti-diagonal measurements where phases play a relevant role. Therefore we expect state fidelity close to 50% bound, but full state characterization takes a considerable amount of time in terms of 9 measurement settings with enough 8-fold events. Overall system efficiency and Bell state quality have to be increased to reach an efficient 8 to 10-photon experiment.

6.5 Programmable Memory for Multi-photon State Breeding

6.5.1 Quantum network topology certification

Entanglement is a key resource in network-oriented quantum information processing implementations [125]. Entangled photonic flying qubits play an important role in realizing these network architecture and protocol implementations [126]. In a free-space or fiber-distributed situation, entanglement-enabled quantum networking protocol requires an efficient multiphoton entanglement source, where single or multiple photons are shared by many network nodes. Also, a reliable entanglement distribution with trusted nodes is essential for efficient network operation. This demands a characterization/benchmark algorithm of such networks by considering all aspects of distributed quantum networks. So far this was done by studying the optimal performance of the choice of the quantum state and entanglement verification on the established network [127–129]. A more general approach, certifying the topology of the network can well explain how or in which manner entanglement is distributed in the network. This approach becomes relevant when one wants to ensure the security of the network or participating network users want to know the distribution of quantum resources. In detail, there might be a situation, where an intricate network source provider delivers entangled photons to each node by guaranteeing maximal entanglement properties. While the interconnected parties may then be interested to know, how the entanglement topology is established in the network with minimum effort. There might be incidence, where a potential malicious party can take part and spoil the network security, so one wants to avoid sharing entanglement with a malicious party by identifying the topology.

This situation can be well explained by an example given in Fig. 6.5.1 with two different topology or entanglement distributions in an eight-party network. In Fig (a) entanglement is distributed by two tripartite sources and one Bell pair source, whereas in Fig (b) distribution contains two Bell pair sources and one four-photon entanglement. Then the concerned question is how can the eight parties identify the es-

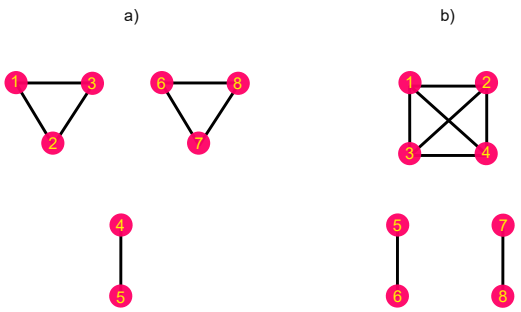

Figure 6.5.1: Two different network topology.

tablished topology of the network. How can then such network users positively identify node-to-node shared entanglement details? How can one identify which type of source is used? how many qubits are entangled to its node, and between which of their qubits entanglement has successfully been generated?.

Lisa Weinbrenner *et al.*[4] proposed a protocol to certify the underlying topology of a quantum network based on a set of hypothesis tests, which root from a set of fidelity measurements on the network state and corresponding statistical figures [4]. The proposed network model contains N nodes that share N qubits with specific topology generated by the source provider. Within this working model the protocol assumes that physical sources deliver GHZ states of size $m < N$, which essentially reduces the number of possible combinations to look for separable or non-separable qubit properties and fidelities. Consequently, a resource-efficient topology certification scheme is made available for multipartite quantum networks.

Hypothesis test protocol requires a set of fidelities $\{F_I\}$ for the subsystem set I, for example, this could be {1,2,3,4}, {5,6}, {7,8} as in fig (b). The advantage of the GHZ state fidelity estimation method we used in Sec. 6.4.4 is that it is possible to simultaneously estimate the fidelity of the subsystem $m < n$ from the same set of measurements on n qubits. If an n-qubit system has high fidelity then the subset m qubits has also a nonvanishing fidelity with a GHZ state; where we can expect $F_m > F_n/2$ because of the common entries on the diagonal. Therefore Similar to our 4 and 6 photon GHZ state measurements a set of measurements $\langle M_k^{\otimes N}\rangle$ and $\sigma_z^{\otimes N}$ on the network are enough to generate the F_I set for different topology list. A necessary requirement is that the working source generate GHZ state fidelity $F > \frac{1}{2}$. Any topology T is characterized by a set of fidelities $\{F_I^T\}$ of the included GHZ states. The hypothesis corresponding to T is then given by a set of conditions of the type

$$F_I^T - \max_{G\supset I}\left\{F_G^T\right\} > \frac{1}{2}, \tag{6.5.1}$$

where $G \supset I$ denotes the relevant supersets of the qubits in the n-qubit set I. For instance, in order to distinguish the distinct topologies in Fig. 6.5.1, the hypothesis for configuration (a) should contain the conditions $F_{\{1,2,3\}} - F_{\{1,2,3,4\}} > 1/2$, $F_{\{4,5\}} > 1/2$ and $F_{\{6,7,8\}} > 1/2$, and the hypothesis for (b) the conditions $F_{\{1,2,3,4\}} > 1/2$, $F_{\{5,6\}} > 1/2$ and $F_{\{7,8\}} - F_{\{6,7,8\}} > 1/2$, rendering these hypotheses mutually exclusive. Taking the differences of the fidelities, e.g., $F_{\{7,8\}} - F_{\{6,7,8\}} > 1/2$, is necessary to distinguish between tripartite entanglement on $\{6,7,8\}$, which leads to high fi-

[4]This theory is entirely developed by the group of Prof. Otfried Gühne from University Siegen. We were responsible for the experimental realization of multiphoton quantum state light source and measurement implementations to test the theory

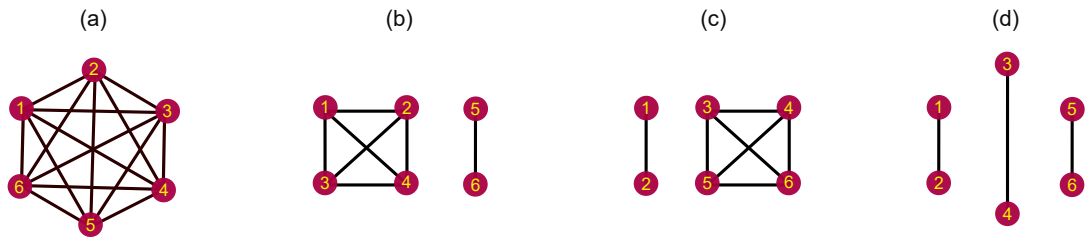

Figure 6.5.2: Different six photon entanglement topologies which are either completely entangled or partially entangled, depending on the graph structure. Black lines between nodes represent the sharing of entanglement. Those states can be generated by the combined memory operations of SWAP+INTEREFERE+STORE in different aspects. Four different states (a) $|GHZ_6\rangle$ (b) $|GHZ_4\rangle \otimes |GHZ_2\rangle$ (c) $|GHZ_2\rangle \otimes |GHZ_4\rangle$ (d) $|GHZ_2\rangle \otimes |GHZ_2\rangle \otimes |GHZ_2\rangle$ graph models are plotted respectively.

delities $F_{\{7,8\}}$ *and* $F_{\{6,7,8\}}$, and bipartite entanglement on $\{7, 8\}$, which only results in a high fidelity $F_{\{7,8\}}$. Finally, one always has to consider the null hypothesis, where the fidelities are small, making it impossible to certify the network structure.

6.5.2 Experimental implementation

In order to experimentally demonstrate the certification of distinct network topology, we program our time multiplexed loop circuit to generate different six photon entanglement topologies on polarization basis. Fig. 6.5.2 shows different topologies that we can create from our GHZ setup. This demonstrates the flexibility of our system to generate different types of six-photon states by changing the feed-forward sequence inside the memory, without any physical changes in the experimental setup in practice. Sec. 6.4.2 explains different memory operations between multiple Bell pairs which can generate either entangled or separable multiphoton state from the emitter+memory feed-forward sequence. Which actually corresponds to the programming of qubit memory feed-forward operations like SWAP and INTERFERE in a different order based on the multiphoton state topology model. We are motivated to test this protocol in a realistic photonic experimental platform involving six network users.

An example six-photon state in the form, $|GHZ_4\rangle \otimes |GHZ_2\rangle$ can be generated as follows. Upon detection of a photon from the first Bell pair, its partner is stored in the memory employing a SWAP operation. It then interferes with a photon from the successive Bell pair to generate a $|GHZ_4\rangle$ state using the INTERFERE operation. The stored photon is then exchanged for a photon from the third Bell pair via another SWAP operation. Note that we did not depict a final SWAP operation, which serves

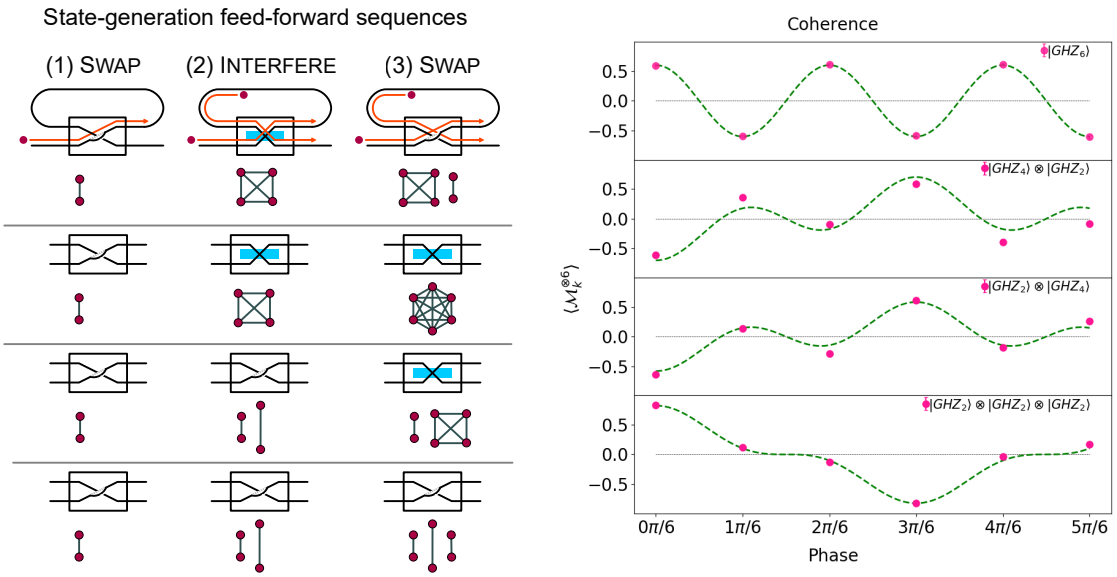

Figure 6.5.3: (left) Circuit type representation of different memory operations on arriving photons. Depending on the desired state type feed-forward sequences SWAP and INTERFERE are interchanged on the respective lines. (right) Measured average coherence terms $\langle \mathcal{M}_k^{\otimes 6} \rangle$ for the four different network topologies. Where the solid circles represent observed experimental data for the four different states, and dotted lines are theoretical expectation values fitted for experimental settings.

to read out the final photon from the memory. Two consecutive INTERFERE operations generate a $|GHZ_6\rangle$ state, while a SWAP operation followed by an INTERFERE operation generates the state $|GHZ_2\rangle \otimes |GHZ_4\rangle$. Finally, two SWAP operations yield the state $|GHZ_2\rangle \otimes |GHZ_2\rangle \otimes |GHZ_2\rangle$, where photons from each Bell pair only share entanglement with each other. Corresponding circuit operation models are given in Fig. 6.5.3. Note that in our setup we fix the phase for a six-photon GHZ state as $|GHZ_6\rangle = (|0\rangle^{\otimes 6} + |1\rangle^{\otimes 6})/\sqrt{2}$, which implicitly fixes the phase of the four-photon state to $\left|GHZ_4^-\right\rangle = (|0\rangle^{\otimes 4} - |1\rangle^{\otimes 4})/\sqrt{2}$, so the hypotheses formulation is based on this four-photon source.

As we saw, the source generates Bell states with entanglement visibility exceeding 93%. In total, we multiplexed up to seven pump pulses to create the three Bell states required for this work, which correspond to $M = 7$ and $N = 3$. This yields a final six-photon event rate of approximately 0.3 Hz. Note that higher rates can be achieved by multiplexing more pump pulses. This, however, comes at the cost of decreased state fidelity. As described above, for any network topology fidelity estimate we perform the Pauli measurement $\sigma_z^{\otimes 6}$ as well as the measurements of the

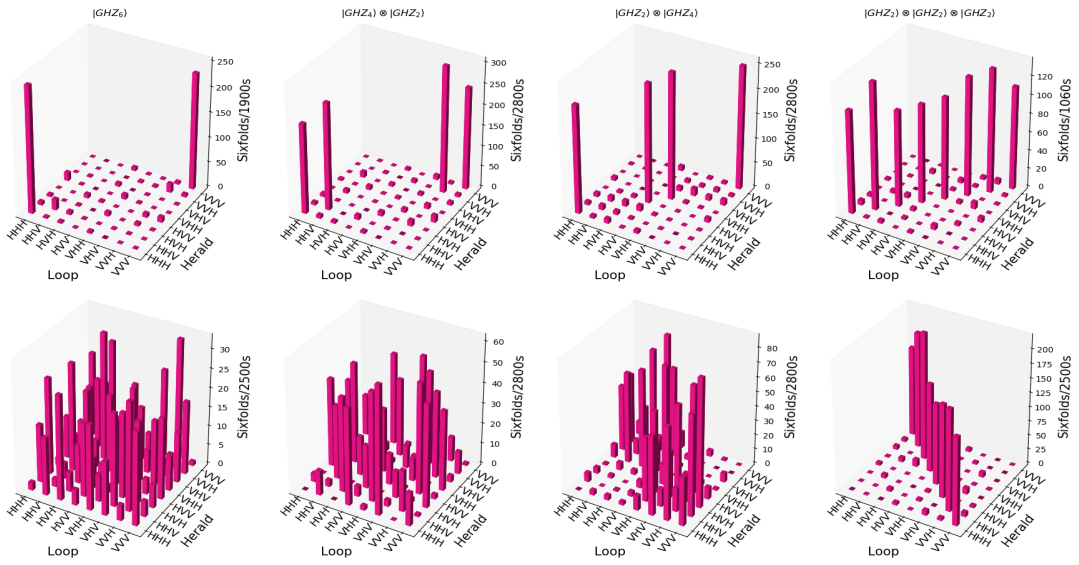

Figure 6.5.4: (Top row) Population of six-fold clicks for the four different topologies (as named in the figure) measured in the $\sigma_z^{\otimes 6}$ basis. Direct population analysis shows $\mathcal{D}_N$ values of $(74 \pm 1.7)\%$, $(83.7 \pm 1.1)\%$, $(82.3 \pm 1.1)\%$, and $(92.6 \pm 0.8)\%$, respectively, for the states from left to right. A Poissonian error on the counts is included in the data analysis. As expected, fidelities decrease for larger-size GHZ states. (Bottom row) Six-fold click probabilities are measured in a specific coherence term ($\langle \mathcal{M}_3^{\otimes 6} \rangle$) setting.

$\mathcal{M}_k^{\otimes 6}$ on the qubits. For the latter, we set the corresponding wave plate angles in front of the detection. We record around 1000 successful six-fold events for every measurement setting to ensure good statistics. Our data yields H/V populations of $\mathcal{D}_6 = (74 \pm 1.7)\%$ and a total coherence value of $\mathcal{A}_6 = (60 \pm 0.9)\%$, resulting in a total fidelity of $F_6 = (67 \pm 0.01)\%$ for the $|GHZ_6\rangle$ state. Similar measurements are carried out on the remaining states and a set of measurement outcomes for $\sigma_z^{\otimes 6}$, $\mathcal{M}_3^{\otimes 6}$ are given in Fig. 6.5.4 as raw click matrix. High visibility values are obtained for each state, from the measurement setting $\sigma_z^{\otimes 6}$ and corresponding click probabilities. A plot of coherence measurement terms ($\langle \mathcal{M}_k^{\otimes 6} \rangle$) for four different topologies are shown in Fig. 6.5.3.

Having different network topologies in hand with high fidelity, naturally motivates us to test the hypotheses test on these states. The main requirement to have a GHZ state fidelity $F > \frac{1}{2}$ is guaranteed here with $F_6 = (67 \pm 0.01)\%$ for $|GHZ_6\rangle$. Successful detection of multipartite entanglement satisfies the first hypothesis requirement $H_1 : F_{\{1,2,3,4,5,6\}} > 1/2$. Additionally, for other states, we construct the

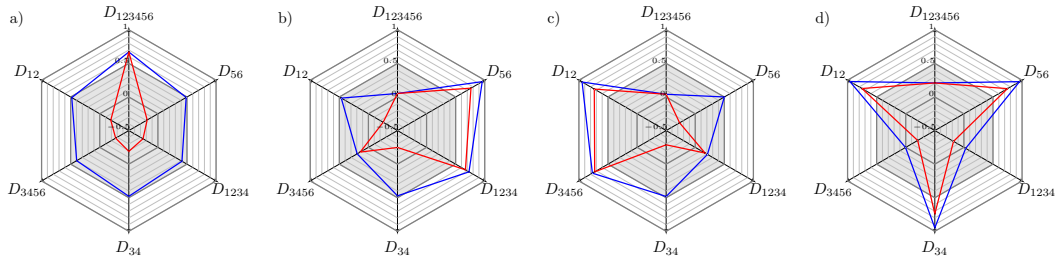

Figure 6.5.5: Graphical depiction of the fidelities (blue curves) and the differences of the fidelities considered in the hypotheses (red curves) for the four different measured datasets. The different directions D_I denote either the fidelity F_I (blue) or the difference $F_I - \max_{G\supset I} F_G$ (red). The differences allow for a clear separation between the states in the sense that only the desired terms are larger than 1/2 (outside the dark area). The hypothesis test leads to the following results: dataset a) belongs to the state $|GHZ_6\rangle$, b) to $|GHZ_4\rangle \otimes |GHZ_2\rangle$, c) to $|GHZ_2\rangle \otimes |GHZ_4\rangle$ and d) to $|GHZ_2\rangle \otimes |GHZ_2\rangle \otimes |GHZ_2\rangle$. Plots are taken from Lisa Weinbrenner *et al.* [4].

following hypothesis requirements,

$$H_1 \ : \ F_{123456} > 1/2; \tag{6.5.2a}$$

$$H_2 \ : \ \begin{cases} h_{21} & : \ F_{1234} - F_{123456} > 1/2 \quad \text{and} \\ h_{22} & : \ F_{56} - \max\{F_{3456}, F_{123456}\} > 1/2; \end{cases} \tag{6.5.2b}$$

$$H_3 \ : \ \begin{cases} h_{31} & : \ F_{12} - \max\{F_{1234}, F_{123456}\} > 1/2 \quad \text{and} \\ h_{32} & : \ F_{3456} - F_{123456} > 1/2; \end{cases} \tag{6.5.2c}$$

$$H_4 \ : \ \begin{cases} h_{41} & : \ F_{12} - \max\{F_{1234}, F_{123456}\} > 1/2, \\ h_{42} & : \ F_{34} - \max\{F_{1234}, F_{3456}, F_{123456}\} > 1/2 \quad \text{and} \\ h_{43} & : \ F_{56} - \max\{F_{3456}, F_{123456}\} > 1/2, \end{cases} \tag{6.5.2d}$$

$$H_\emptyset \ : \ \text{otherwise}, \tag{6.5.2e}$$

where H_2, H_3, and H_4 are hypotheses models for $|GHZ_4\rangle \otimes |GHZ_2\rangle$, $|GHZ_2\rangle \otimes |GHZ_4\rangle$ and $|GHZ_2\rangle \otimes |GHZ_2\rangle \otimes |GHZ_2\rangle$ respectively . Finally, $H_\emptyset$ stands for null hypotheses test. As described in the model, experimentally obtained data sets $(\mathcal{A}_6, \mathcal{D}_6)$ for each state are used to construct fidelities for the choice of qubit subsets from each state for hypothesis testing. Fig. 6.5.5 shows how the protocol succeeds in differentiating the states from fidelity estimates of the subsystem. D_I's are actually fidelity values obtained from F_I or difference of fidelity $F_I - \max_{G\supset I} F_G$ and corresponding values $D_I > \frac{1}{2}$ distinctly identify the state topology. A rigorous statistical modeling and fidelity estimation details can be found in [4].

Summary

A resource-efficient scheme for multiphoton polarization entangled state generation is proposed and realized efficiently. A flexible and programmable quantum memory is introduced to entangle many photons in a sequential manner. Then entanglement multiplexing in time is introduced for large-scale photonic entanglement, experimentally demonstrating four and six-photon entanglement with a single emitter. We theoretically predicted and experimentally demonstrated scaling on multiphoton state generation rate with a time multiplexing scheme compared to other generation methods. Finally, genuine entanglement properties are detected on the generated state with high fidelity.

Chapter 7

Nonlinear Polarization Squeezing

7.1 Macroscopic Polarization Entanglement and Polarization Squeezed Light

Contents

In the previous chapter, we discussed the multiphoton entangled state, where multiple single photons are entangled and distributed in different spatial or temporal modes. This has been found important applications in multi-user-based quantum network applications and fundamental quantum physics experiments. However the paradigm of having an entangled photonic state, where each entangled mode with many photons is not considered yet. Which are otherwise called macroscopic entangled states in photon number basis, and are not explored much in literature. At the same time, there are experimental demonstrations in CV pictures in the form of a macroscopic entangled state with a coherent state of light containing large mean photon numbers [130, 131]. However, in DV aspects, the number resolved photon counting approach is a promising direction to exploit distinct macroscopic entanglement and nonclassical behavior within the light states. On this perspective, the simplest type of NOON states $\left(|\psi\rangle = \frac{1}{\sqrt{2}}\left(|N\,0\rangle + |0\,N\rangle\right)\right)$ are well studied in theory and exper-

iment for its generation and supremacy in quantum metrological applications [132, 133]. However, the production of a higher-order NOON state is not straightforward with a linear optical scheme. A two-photon NOON state is a direct outcome of the HOM experiment but higher order NOON state always relies on post selection. In this chapter, we will show a specific example of a macroscopic light source by exploiting our Sagnac entanglement in a high-gain PDC regime. Photon number resolved measurements are essential for the quantification of these states. A resource-efficient detector multiplexing scheme together with photon counting theory then reveals the nonclassical nature of our entanglement source in polarization and photon number degree of freedom. Moreover, the quantumness in the state is described with a new operational approach, which provides a new nonlinear functional form for the measurement operator to quantify the quantum characteristics. The measurements further verify, the observation of polarization squeezing and photon number state nonclassicality from our entanglement source output. This work has been conducted as a novel scheme to probe nonlinear squeezing effects in optical states and quantum metrology applications.

7.2 Squeezing in Polarization

Measurements are important in the sense of acquiring maximum information about a physical system. In a realistic situation measurements often produce a noisy data set. There can be various reasons for the fluctuations, measurement noise reduction has paramount importance in precision metrology devices. When it comes to quantum systems, measurements become even more sensitive, the real state of the system is unpredictable before the measurements because of superposition and observations on the system change the state of the system under the credit of *collapse model*. However quantum expectation values and variances of a measurement operator are useful to measure fluctuations. 'Seminal work on quantum noise' behavior on an optical interferometer laid the foundation, to explore the advantage of quantum entities in measurement noise reduction possibilities [23, 24]. A fundamental limit to the measurement noise can be bound by the quantum mechanical properties of the system, which proves that ultimate precision can be achieved with quantum probes. Squeezed light states are nonclassical light states, which come with exceptional quantum properties with associated measurement operators, and provide a quantum advantage when used as a probing source.

Squeezing holds the synonym of noise reduction in quantum physical systems, quantum operator-based measurement uncertainties can exemplify this. In quan-

tum statistics formalism, measurements mean the ensemble average of a quantum operator. For optical state measurements- suitable dimensionless operators in terms of quadrature operators are introduced to understand the outcomes of optical detection (from intensity measurements),

$$\begin{aligned} \hat{X}_1 &= \frac{1}{2}(\hat{a} + \hat{a}^\dagger) \ , \\ \hat{X}_2 &= \frac{1}{2i}(\hat{a} - \hat{a}^\dagger) \ , \end{aligned} \tag{7.2.1}$$

which do not obey commutation relation ($[\hat{X}_1, \hat{X}_2] = \frac{1}{2}$), hence follow Heisenberg's uncertainty relation,

$$\langle (\Delta \hat{X}_1)^2 \rangle \, \langle (\Delta \hat{X}_2)^2 \rangle \ \geq \ \frac{1}{4}. \tag{7.2.2}$$

Equation (7.2.2) do not permits simultaneous quadrature measurements $\hat{X}_1$, $\hat{X}_2$, with at most precision. In this sense, second-order moments of an operator are ideal to describe the measurement uncertainty. There can be states with reduced uncertainty on one quadrature at the expense of another, bounded by Eq. (7.2.2). These are generally called squeezed light states, while the squeezing allowed only in one quadrature either $\hat{X}_1$ or $\hat{X}_2$). Squeezed light often compares with coherent light state uncertainty limit ($\langle (\Delta \hat{X}_1)^2 \rangle = \langle (\Delta \hat{X}_2)^2 \rangle = \frac{1}{4}$) to set a classical-nonclassical bound to test the advantage of quantum light probe. In an optical probe-based measurement strategy, squeezed light sources outperform classical states, while considering the squeezing properties of the measurement operator. Many groundbreaking optical experiments were performed for the demonstration of squeezing and squeezing enabled advantage [134–137]. Apart from optical platforms different physical systems have been exploited for squeezing effects like single ion or atomic ensembles [138, 139], mechanical oscillators [140], superconducting cavity [141]; which shows the very fundamental nature of Eq. (7.2.2).

In general quadrature operators and measurements are phase-dependent, and precise phase information is necessary for state reconstruction, squeezing measurements, and quantum advantage demonstration. In optical measurements, this requires a homodyne-like measurement scheme, where the generated quantum state interferes with the coherent state (also called local oscillator) on a beam splitter by keeping a common phase relationship beforehand [142]. A more comprehensive quantum optical state reconstruction requires homodyne measurement followed by photon number measurement [143], but later we show that the nonclassical nature of our specific light state can be probed directly by photon number measurements. For which, similar to electric field quadrature, we look into other degrees of freedom of light (photon number, polarization) for squeezing behavior.

7.2.1 Photon number squeezing

Probing the light state in terms of the number of photons contained in light field mode is important to explore the particle nature of light in detail. Perfect photon number resolved detectors (PNR) are unavoidable for such measurements. In theory, the action of the photon number operator yields the actual number of photons present in the state and can be expressed as,

$$\langle\psi|\,\hat{n}\,|\psi\rangle = \langle n\rangle \ , \tag{7.2.3}$$

where $\hat{n}$ plays the role of photon number operator. For an ideal classical choice, coherent states of light in photon number basis can be expressed as (with complex amplitude α),

$$|\alpha\rangle \ = \ e^{-\frac{|\alpha|^2}{2}} \sum_{n=0}^{\infty} \frac{\alpha^n}{\sqrt{n!}} \, |n\rangle \, . \tag{7.2.4}$$

For the state in Eq. (7.2.4) photon number probability distribution and photon number variance can be obtained directly,

$$\begin{aligned} P(n) \ = \ |\langle n|\alpha\rangle|^2 \ = \ e^{-|\alpha|^2} \frac{|\alpha|^{2n}}{n!} \quad , \\ \langle(\Delta\hat{n})^2\rangle \ = \ \langle\hat{n}\rangle \ = \ |\alpha|^2 \ . \end{aligned} \tag{7.2.5}$$

Poissonian nature of photon statistics, or shot noise limit of coherent states of light are clear in Eq. (7.2.5). Since coherent state light sources play an important role in applied technology, states of light which has subPoissonian photon statistics will have priority and can be observed in quantum light [47, 144]. Following the formalism of quadrature squeezing, light states that show photon number operator variance below the coherent state limit are alluded to *photon number squeezed*[1]. Fock states ($|n\rangle$) are ideal number squeezed states with zero uncertainty in photon number. Based on the binomial probabilistic counting nature (from click or no-click information) heralded single-photon Fock states (from SPDC) are used for sub-shotnoise spectroscopy experiments [105, 145].

For a fixed mean photon number both coherent state and Fock state photon number distribution are plotted in Fig. 7.2.1. In an ideal situation, the Fock state will be populated with a definite photon number and can be quantified with a *perfect* PNR detector. Nevertheless, a pseudo photon number resolving detector and click counting theory approach [146] still proves that the Fock state has a narrower spread than

[1]There are various synonyms in this regard like subPoissonian, sub-shot noise, nonclassical light state. Most of the time it's related to beating the coherent state limit

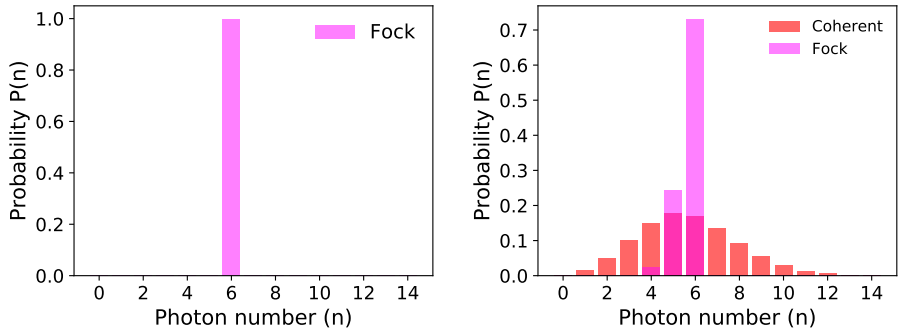

Figure 7.2.1: (left) An ideal Fock state photon number distribution for $|n\rangle = 6$. (right) Photon number reconstruction for a coherent state and Fock state with a mean photon number of 6. Pseudo photon number resolving capability and click counting theoretical approach are used for the photon number distribution estimation [146].

a coherent state and satisfies the condition for subPoissonian statistics. Different types of test parameters are proposed for the meaningful discrimination/definition of optical state based on expectation values of photon number operator, for example, Mandel formula,

$$Q_M = \frac{\langle(\Delta n)^2\rangle}{\langle n\rangle} - 1. \tag{7.2.6}$$

Mandel Q_M parameter in Eq. (7.2.6) will take a negative value if the variance is less than the mean value, signature condition for nonclassical light states [72]. A more general optical state characterization approach, which considers underlying photon numbers with multiple click detectors is introduced to test the sub-binomial nature of light. This attempt brought up the Q_B parameter which considers the number resolved photon statistics from c number of 'photon clicks' and N number of On-Off click detectors, given by the formula [73],

$$Q_B = N\frac{\langle(\Delta c)^2\rangle}{\langle c\rangle(N - \langle c\rangle)} - 1. \tag{7.2.7}$$

A negative value of Q_B implies a sub-binomial nature for the state, demonstrated experimentally with detector multiplexing [147]. Later we show that the theory and methods of multiplexed click detection become an efficient scheme to characterize the squeezing effect from an entanglement source or non-linear squeezers.

7.2.2 Polarization squeezing

The fundamental relation between the polarization property of light with its photon number in the form of the Stokes operator motivates the idea of squeezing in polarization. Polarization properties of light are a better choice to explore squeezing because of its two-dimensional Hilbert space and ease of manipulation. Since the light is in squeezed form, a polarization noise-free light source is an important candidate for polarimetric probing technology [148].

Geometrical optics and electromagnetic theory introduced intrinsic two-component transverse electric field oscillation properties of light with the name of polarization. For an electric field propagating in the z-direction and transverse field oscillation lying in the xy-plane take the field real components, $E_x = a\cos(wt-kz+\delta_1)$ and $E_y = b\cos(wt-kz+\delta_2)$ (locus point of corresponding electric fields,). Using this relation a general polarization description for the light state can be derived in the form of ellipse [149],

$$\left(\frac{E_x}{a}\right)^2 + \left(\frac{E_y}{b}\right)^2 - 2\frac{E_x}{a}\frac{E_y}{b}\cos(\delta) = \sin^2\delta. \tag{7.2.8}$$

Now different polarization settings can be generated by adjusting the common phase ($\delta = \delta_2 - \delta_1$) relation between the two field components. For $\delta = m\pi$ and $\delta = m\frac{\pi}{2}$, Eq. (7.2.8) reduces to,

$$\frac{E_y}{E_x} = (-1)^m\frac{b}{a}\ , \tag{7.2.9a}$$

$$E_x^2 + E_y^2 = a^2\ , \tag{7.2.9b}$$

and $m = 0, \pm1, \pm2...$ for Eq. (7.2.9a) produce linearly polarized light. In the case of both fields having equal field amplitude ($a = b$) and $m = \pm1, \pm2, \pm3...$, Eq. (7.2.9b) produces circularly polarized light (sign of δ also matters to define the state of light, e.g. left or right).

While studying the polarization properties, Stokes introduced a three-component vector to define the polarization state of light. To construct the vector, we have to consider an arbitrary plane-polarized light in the xy-plane and having retarding component (ϵ) between the field components. Corresponding electric field term and intensity formulation takes the form,

$$E = E_x\cos\theta + e^{i\epsilon}E_y\sin\theta\ , \tag{7.2.10a}$$

$$I = E_xE_x^*\cos^2\theta + E_yE_y^*\sin^2\theta + E_xE_y^*e^{-i\epsilon}\cos\theta\sin\theta + E_yE_x^*e^{i\epsilon}\cos\theta\sin\theta. \tag{7.2.10b}$$

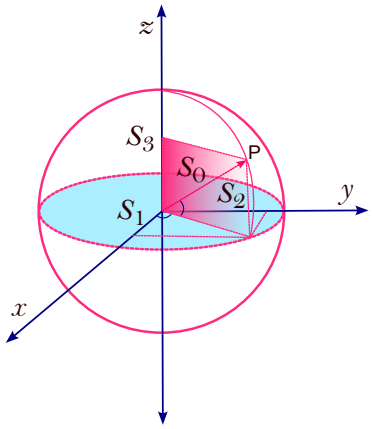

Figure 7.2.2: Representation of an arbitrary classical polarization state on a Poincaré sphere, where the three Stokes components which form the vector P are marked as S_1, S_2 and S_3.

A suitable matrix notation in the name of coherence matrix then introduced with field amplitude terms as the elements of the matrix,

$$J = \begin{bmatrix} \langle a^2 \rangle & \langle ab^* e^{i\delta} \rangle \\ \langle ba^* e^{-i\delta} \rangle & \langle b^2 \rangle \end{bmatrix}. \tag{7.2.11}$$

Using the coherence matrix elements, four Stokes vector components are defined as,

$$\begin{aligned} S_0 &= \langle a^2 \rangle + \langle b^2 \rangle, \\ S_1 &= \langle a^2 \rangle - \langle b^2 \rangle, \\ S_2 &= \langle abe^{i\delta} \rangle + \langle bae^{-i\delta} \rangle, \\ S_3 &= i(\langle bae^{-i\delta} \rangle - \langle abe^{i\delta} \rangle), \end{aligned} \tag{7.2.12}$$

An in-depth derivation and details of Stokes vector formalism can be found in *Principles of Optics by Born and Wolf* [149]. Elements of J matrix and Stokes vectors components in Eq. (7.2.12) are defined in terms of field modes a, b for E_x, E_y respectively, to show the similarity with quantum operators later on. A convenient geometric visualization for a general Stokes vector and individual Stokes vector components is given in Fig. 7.2.2. Any polarization state of a monochromatic plane wave can be represented as a point on the surface of the sphere. Therefore the length of an arbitrary polarization vector on the sphere is obtained from the vector formula,

$$S_0^2 = S_1^2 + S_2^2 + S_3^2. \tag{7.2.13}$$

The definition of S_0 in Eq. (7.2.12) relates the length of the classical polarization vector to the total intensity of the light field. Measurements of Stokes components

can be performed with the help of a polarizer and a retarding element in the beam path. The polarizer angle and the retarding elements can be set by the choice of angle in Eq. (7.2.10b), each element in the coherence matrix can be accessed by this choice.

For the quantum description of light polarization, one needs to recast the field quantization method introduced before, to Stokes vectors. This can be done by defining the corresponding creation and annihilation operator for the electric field polarization modes a and b. For obvious reasons, we can call these modes horizontal and vertical polarization modes of light. Operators $\hat{a}$ and $\hat{b}$ play the role of generation of single-mode field excitations in definite polarization degree of freedom,

$$\begin{aligned} \hat{a}^\dagger \otimes \hat{I} \;\; |0\rangle\,|0\rangle &= |H\rangle\,|0\rangle\,, \\ \hat{I} \otimes \hat{b}^\dagger \;\; |0\rangle\,|0\rangle &= |0\rangle\,|V\rangle\,, \end{aligned} \tag{7.2.14}$$

where $|H\rangle$ and $|V\rangle$ represents single photons in horizontal and vertical polarization modes. Using the field operator we can directly write down the corresponding quantum Stokes operators for full polarization state manipulation,

$$\begin{aligned} \hat{S}_0 &= \hat{a}^\dagger\hat{a} \;+\; \hat{b}^\dagger\hat{b}, \\ \hat{S}_1 &= \hat{a}^\dagger\hat{a} \;-\; \hat{b}^\dagger\hat{b}, \\ \hat{S}_2 &= \hat{a}^\dagger\hat{b} \;+\; \hat{b}^\dagger\hat{a}, \\ \hat{S}_3 &= i\;(\hat{b}^\dagger\hat{a} \;-\; \hat{a}^\dagger\hat{b}), \end{aligned} \tag{7.2.15}$$

In the particle picture, $\hat{S}_0$ gives the total number of photons ($\hat{n} = \hat{n}_h + \hat{n}_v$) in two polarization modes, equivalent to intensity measurement in classical Stokes vector picture. Commutation relation among the Stokes operators can be derived by the same commutation algebra of $\hat{a}$ and $\hat{a}^\dagger$,

$$[\hat{S}_0\,,\;\hat{S}_i] = 0\;, \tag{7.2.16a}$$

$$[\hat{S}_i\,,\;\hat{S}_j] = 2i\sum_{k=1}^{3}\epsilon_{ijk}\,\hat{S}_k\;, \tag{7.2.16b}$$

where ϵ_{ijk} stands for Levi-Civita symbol and takes permutations of 1,2,3 for Stokes operators. This tells us that the Stokes operator follows the commutation relation of SU(2) Lie algebra, like orbital angular momentum states. The non-commutative nature of Stokes operators in Eq. (7.2.16b) reminds us of the impossibility of measurement simultaneity of these operators, demanding the validity of Heisenberg's uncertainty condition here too,

$$\langle(\Delta\hat{S}_i)^2\rangle\,\langle\Delta\hat{S}_j^2\rangle \;\geq\; |\langle\hat{S}_k\rangle|^2. \tag{7.2.17}$$

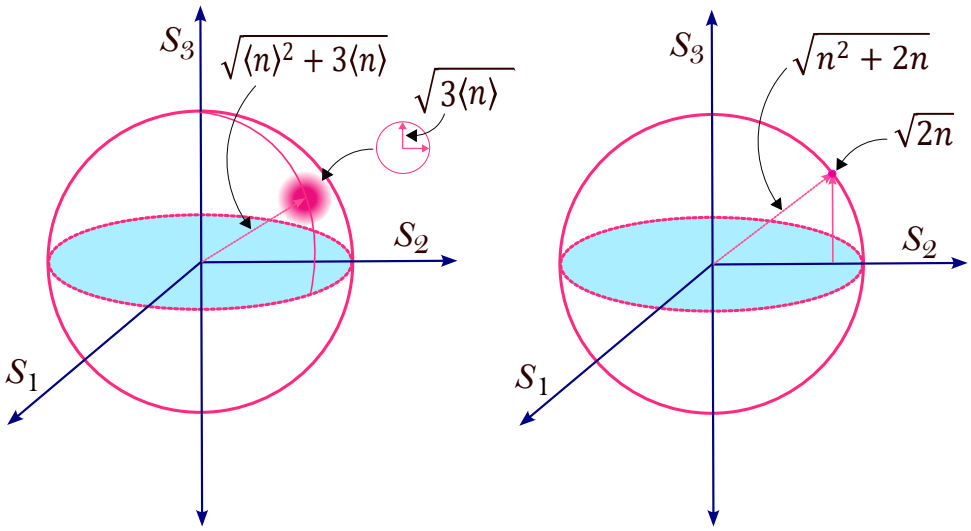

Figure 7.2.3: Poincaré sphere representation for coherent state and photon number state [150]. Non-zero variance for the coherent state shows up as a spread-ed point in the sphere (left), rather a sharp single point (right) represents a photon number state.

Quantum three-component Stokes vector length is then calculated by the squared sum of individuals,

$$\hat{S}_1^2 + \hat{S}_2^2 + \hat{S}_3^2 = \hat{S}_0^2 + 2\hat{S}_0. \tag{7.2.18}$$

Unlike the classical vector length in Eq. (7.2.13) there is an additional operator term here. This radius operator dynamics over a sphere form a quantum Poincaré sphere to define arbitrary quantum Stokes superpositions. The average or mean length of the radius can be obtained from expectation values of Eq. (7.2.18) in square root.

Since we have constructed the quantum descriptions of light polarization operators, it's meaningful to test the action of these quantum operators on different light states. As we chose a coherent state as a start for photon number properties, here a two-mode (H, V polarization) coherent state is an ideal choice to start with,

$$|\Psi_{coh}\rangle = |\alpha_h\rangle\,|\alpha_v\rangle \ , \tag{7.2.19a}$$

$$\langle \hat{S}_0\rangle \ = \ \langle \hat{a}^\dagger \hat{a}\rangle \ + \ \langle \hat{b}^\dagger \hat{b}\rangle \ = \ \langle \hat{n}\rangle \ = \ |\alpha_h|^2 \ + \ |\alpha_v|^2. \tag{7.2.19b}$$

Equivalent to the coherent state photo number average, the expectation value of $\hat{S}_0$ Stokes operator gives the total photon number average from a two-mode coherent state. Fluctuations in polarization measurements can be understood by variances

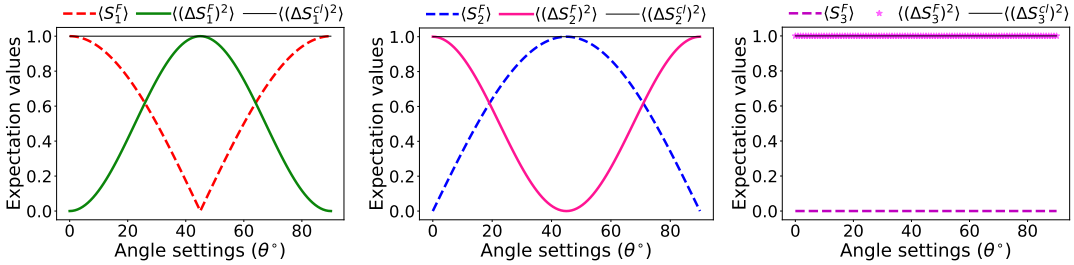

Figure 7.2.4: Variance properties of Stokes observable $\hat{S}_1$, $\hat{S}_2$, $\hat{S}_3$ for a general single photon state in Eq. (7.2.22) parameterized by angle θ. In all three cases, the black line stands for Stokes observable variance calculated for a two-mode coherent state $|\alpha_h\rangle\,|\alpha_v\rangle$ with mean photon number of $|\alpha_h|^2 + |\alpha_v|^2 \approx 1$.

of the Stokes operator,

$$\langle(\Delta\hat{S}_i)^2\rangle = \langle\hat{S}_i^2\rangle - \langle\hat{S}_i\rangle^2 , \tag{7.2.20a}$$

$$= \langle\hat{n}_h\rangle + \langle\hat{n}_v\rangle = |\alpha_h|^2 + |\alpha_v|^2. \tag{7.2.20b}$$

Equality of Eq. (7.2.19b) and Eq. (7.2.20b) reveals that two-mode polarization coherent state Stokes operator measurements statistics has a similar structure to coherent state photon number measurement statistics as in Sec. 7.2.1. The length behavior of the state vector in Poincaré sphere is given by,

$$\langle\hat{S}_1^2 + \hat{S}_2^2 + \hat{S}_3^2\rangle = \langle\hat{S}_0^2 + 2\hat{S}_0\rangle, \tag{7.2.21a}$$

$$\langle\hat{S}_0^2 + 2\hat{S}_0\rangle = \langle\hat{n}^2 + 2\hat{n}\rangle = \langle\hat{n}^2 - \hat{n} + 3\hat{n}\rangle = \langle\hat{n}\rangle^2 + 3\langle\hat{n}\rangle. \tag{7.2.21b}$$

Combining Eq. (7.2.19b) and Eq. (7.2.21b) variance of the radius shows a non-zero value and its Poincaré plot representation becomes uncertain. Any light is said to be *polarization squeezed* if one of its Stokes operators shows variance below the variance of coherent light [151, 152], where the definition of polarization fluctuations/variance is in Eq. (7.2.20a). Polarization-sensitive measurement strategy with classical light probes can be replaced with so-called polarization-squeezed light for quantum-enhanced performance, especially in sensing and metrology fields.

Before going into the realm of intricate polarization squeezed states, we will check how a single photon state deals with Stokes operators,

$$|1\rangle = \cos\theta\,|H\rangle\,|0\rangle + \sin\theta\,|0\rangle\,|V\rangle \ , \tag{7.2.22}$$

here a single photon can be occupied in any of the two polarization modes. The state is also a single photon entangled state in polarization when $\theta = 45^o$. For $\theta = 0$

the state becomes a H polarized single photon state also an example for polarized photon number state $|n_h\rangle|0\rangle$ with $n = 1$ corresponding Stokes values are,

$$\langle \hat{S}_0 \rangle = \langle \hat{S}_1 \rangle = 1 \ , \ \langle \hat{S}_2 \rangle = \langle \hat{S}_3 \rangle = 0 \ , \tag{7.2.23a}$$

$$\langle \hat{S}_0^2 \rangle = \langle \hat{S}_1^2 \rangle = \langle \hat{S}_2^2 \rangle = \langle \hat{S}_3^2 \rangle = 1 \ , \tag{7.2.23b}$$

$$\langle \Delta \hat{S}_0{}^2 \rangle = \langle \Delta \hat{S}_1{}^2 \rangle = 0 \ , \ \langle \Delta \hat{S}_2{}^2 \rangle = \langle \Delta \hat{S}_3{}^2 \rangle = 1. \tag{7.2.23c}$$

From Eq. (7.2.23a) and Eq. (7.2.23c), it conclude that single photon state $|H\rangle|0\rangle$ is polarization squeezed in $\hat{S}_1$. Similar Stokes values can be obtained for a V-polarized single-photon state. Polarization properties for an arbitrary polarization state (from Eq. (7.2.22)) are plotted in Fig. 7.2.2 for different state settings. Squeezing in polarization can be observed for a range of parameter (θ) settings and corresponding polarization states. Stokes operator $\hat{S}_1$ and $\hat{S}_2$ for single photon state settings shows a clear deviation from a coherent state of similar amplitude. Rather differently $\hat{S}_3$ shows similar characteristics for both states. But polarization squeezing condition is already satisfied in the other two Stokes operator variance cases.

7.3 Click Counting Theory

7.3.1 Detecting few photon states

So far we have discussed the classical and nonclassical properties of light states containing either single or multiple photons. As discussed before, such light sources are realized with nonlinear optical effects in our experiment. We have not yet discussed in detail about the detection mechanism of these faint quantum photonic states. Quantum light source properties arguably demand a quantum perspective for the detection scheme. Individual *quanta* sensitive detectors otherwise called single photon detectors play an important role in the quantum technology platform. A perfect single photon or photon number resolving (PNR) detector or detection scheme is still an active research topic. Quantum light detection modules in the limit of single photon sensitive are now available with $> 93\%$ detection efficiency [153]. Integrated detection modules both in semiconducting and superconducting-based technologies provide a wide variety of detectors covering a broad range of electromagnetic spectrum.

In all experiments, we make use of high efficient single photon sensitive detector based on superconducting nano-wire strips (SNSPD) as the light-sensitive material [154]. Which contains a few centimeters long superconducting wire (NbN) kept at a cryogenic temperature of 0.8 K, the material becomes superconductive and

persists current without any resistance. When a quantum of light with enough energy ($h\nu$) falls on the superconducting material a phase transition occurs, the wire becomes resistive and the corresponding voltage across the wire can be read out as an electronic signal. The signal usually manifests as a photon 'click' information. Such detectors simply provide a click or no click information upon light/photon fall or not fall on the detector with an efficiency of more than 90%. But at the same time not possible to reveal the number of photons present in the light state, limiting further classification of light in the photon number regime. Efficient PNR detectors like transition edge sensors (TES) are at the early stage of mass production, because of complex cryogenic system requirements. On the other side detector multiplexing with readily available single-photon detectors is a promising approach for PNR capabilities. On-chip detector multiplexing requires many detector pixels connected in series or parallel combinations for the efficient discrimination of multiphoton pulse [155, 156]. A recent scheme promotes a single superconducting nano-wire detector for PNR detection by looking at the underlying voltage response curve of the superconducting detection process, but this is too limited in terms of the number of photons and post-processing reliability [157]. The most simple cost and resource-efficient scheme may be the off-chip multiplexing strategy, which involves chopping of the input light pulse with linear optical elements into many temporal bins (or spatial but not resource-efficient). In a temporal scheme number of resolved photons are distributed in many temporal bins, which can be detected with a single click detector but spatial case requires many detectors. All multiplexing strategies are still limited in the sense of detection range, if the number of photons within the pulse exceeds the multiplexing or PNR range then the scheme becomes futile. For the above reasons detector multiplexing schemes are said to be pseudo photon number resolving detectors and useful for resolving few photon optical states.

7.3.2 Theory for multiplexed click detection

Measurement outcomes of a single click detector can be described by its corresponding positive operator valued measures (POVM) with on-off information. For this, a useful click counting operator in the form of the normally ordered operator can be found here [158] and written as,

$$\hat{p}_{noclick} = |0\rangle\langle 0| =: \exp(-\hat{n}) : \quad , \quad \hat{p}_{click} = \hat{1} - |0\rangle\langle 0| =: \hat{1} - \exp(-\hat{n}) : . \tag{7.3.1}$$

The description of POVM in Eq. (7.3.1) holds for a single click detector (provides information about the existence or absence of input light, below the detector threshold intensity but no information about the photon number content). Multi-photon

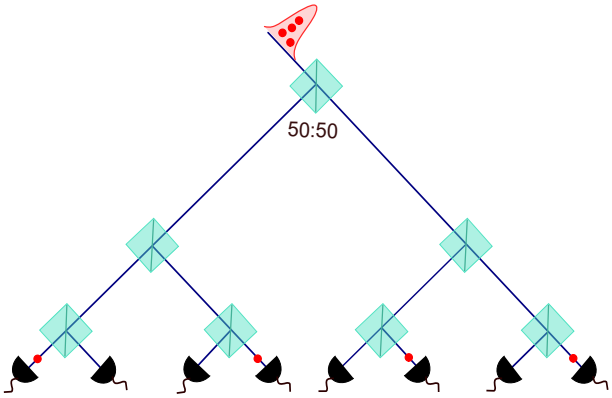

Figure 7.3.1: Detector spatial detection multiplexing scheme with 50:50 beam splitter network. Also demands as many click detectors.

light states and noise-convoluted photon sources need multiple on-off detectors in cascaded format to reveal the actual photon statistics of the optical state. In the absence of a true PNR detector, we take detector multiplexing schemes as an efficient route for proper photon statistics and state characterization.

For a brief construction of detector multiplexing, one can think of spatial multiplexing as in Fig. 7.3.1. Here the input light is split into N spatial modes with a network of 50:50 beam splitter, and corresponding N output station modes are provided with N click detectors. Splitting of multiphoton pulse and distribution of photons to individual click detectors happens probabilistically. While on theory a formulation that combines a single click detector POVM with multiplexing provides a joint normally ordered operator with a binomial distribution factor. Such an operator describes the probability to fire k number of clicks out of N detectors, given by the formula [158],

$$\hat{p}_{click} = \hat{\pi} = \hat{1} - : \exp\left(\frac{\eta\hat{n}}{N}\right) :, \tag{7.3.2a}$$

$$\hat{p}_{noclick} = \hat{1} - \hat{\pi} =: \exp\left(\frac{\eta\hat{n}}{N}\right) :, \tag{7.3.2b}$$

$$\hat{\Pi}_k =: \binom{N}{k} \hat{\pi}^k \left(\hat{1} - \hat{\pi}\right)^{N-k} : . \tag{7.3.2c}$$

For a single-mode light field containing multiple photons, $\hat{\Pi}_k$ reconstructs the photon number distribution with utmost precision depending on the number of multiplexing stages. Background noise counts and efficiency of a realistic click detector

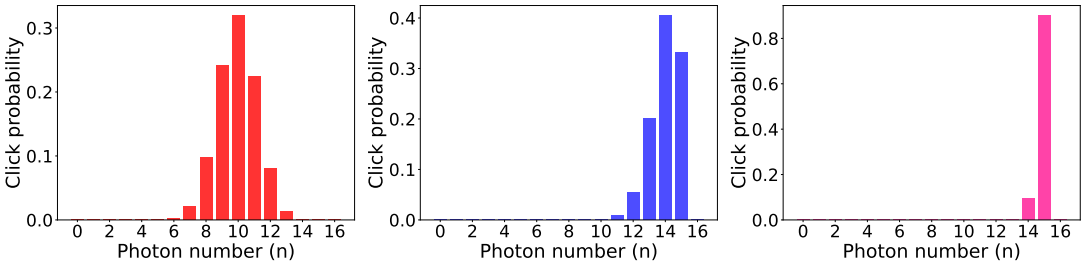

Figure 7.3.2: Fock state $|n\rangle = 15$ is considered to test the counting statistics of click operator $\hat{\Pi}_k$. Each detector in the network is modeled for $\eta = 1$ without any detector noise. Counting statistics for detector multiplexing stages of $N = 16$ (red), $N = 100$ (blue), $N = 1000$ (pink) are plotted here. The higher number of multiplexing results in perfect photon counting statistics and approaches an ideal measurement result.

can also be included in Eq. (7.3.2) for perfect state simulation and reconstruction from the experimental outcome. An overall system efficiency parameter η is already included in the above expression, which can be considered as the combined transmission and detection efficiency of the system. An arbitrary Fock state click probability distribution using the click counting operator is given in Fig. 7.3.2 with a different number of detectors (N) in multiplexing.

A generalization of click counting theory is introduced to handle multi-mode and correlated/uncorrelated light fields [146]. For two-mode light states like TMSV, such generalization permits correlated photon counting statistics reconstruction. Click counting operator for a two-mode case can be readily written by using Eq. (7.3.2) in a tensor product manner,

$$\hat{\Pi}_{k_a k_b} = : \binom{N_a}{k_a} \hat{\pi}^{k_a} \left(\hat{1}_a - \hat{\pi}_a\right)^{N_a - k_a} \binom{N_b}{k_b} \hat{\pi}^{k_b} \left(\hat{1}_b - \hat{\pi}_b\right)^{N_b - k_b} : . \tag{7.3.3}$$

Equation (7.3.3) jointly acts on the two polarization modes a, b of TMSV. Photon number truncated TMSV state click counting photon statistics reconstruction model is given in Fig. 7.3.3. In contrast to Fig. 5.1.4 from Sec. 5.1.2 non-diagonal elements are populated here for the same state even with perfect click detectors. This can be expected from the multiplexing scheme that there is a non-zero probability for more than one photon to fall into the same detector, because of the probabilistic splitting of light. This asserts the requirement of a larger multiplexing network for perfect state reconstruction, which has a high mean photon number.

The statistical significance of moments of a random variable is important to understand the related physical phenomena. We know that fluctuations especially

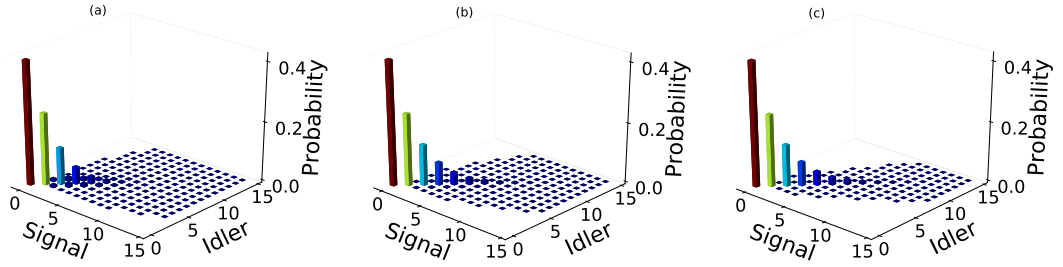

Figure 7.3.3: Click counting based photon statistics reconstruction for a TMSV state with a squeezing value of 1 and with detection efficiency $\eta = 1$. a) $N = 15$, b) $N = 100$, c) $N = 1000$ detectors are multiplexed for the same state photon number probability reconstruction. A higher number of multiplexing reduces the "false binning" problem in multiplexing schemes. Consequently, a more correlated TMSV state is reaching (c) with less contribution from off-diagonal elements.

in the sense of first and second-order moments (mean and variance) of random variables in classical physics are important to understand measurement statistics. In fact, in Sec. 7.2 we have used second-order moments of a quantum operator to define squeezing effects related to different degrees of freedom. In this manner, moments of click counting operator are useful to construct relevant criteria to discriminate light state in the test. A direct relation between photon counting probability and click moment can be constructed in the case of multiplexing with N detector, which takes the form [146],

$$\langle : \hat{\pi}^m : \rangle \; = \; \frac{(N-m)!}{m!} \sum_{k=0}^{N} k\,(k-1)\,...\,(k-m+1)\,c_k \;, \tag{7.3.4}$$

click probability c_k for k number of clicks can be calculated from the expectation values of $\hat{\Pi}_k$ in Eq. (7.3.2). Rendering the possibility to calculate the click moments from experimental click probability directly. Furthermore, a functional involving higher-order moments is constructed in a matrix form to test the positive semi-definite property.

$$\mathbf{M} = \begin{pmatrix} \langle : \hat{\pi}^0 : \rangle & \langle : \hat{\pi}^1 : \rangle & \langle : \hat{\pi}^2 : \rangle & \dots & \langle : \hat{\pi}^N : \rangle \\ \langle : \hat{\pi}^1 : \rangle & \langle : \hat{\pi}^2 : \rangle & \ddots & \ddots & \vdots \\ \langle : \hat{\pi}^2 : \rangle & \ddots & \langle : \hat{\pi}^4 : \rangle & \ddots & \vdots \\ \vdots & \ddots & \ddots & \ddots & \vdots \\ \langle : \hat{\pi}^N : \rangle & \dots & \dots & \dots & \langle : \hat{\pi}^{2N} : \rangle \end{pmatrix} . \tag{7.3.5}$$

Principle minors of the $\mathbf{M}$ matrix follow positive semi-definite property and can

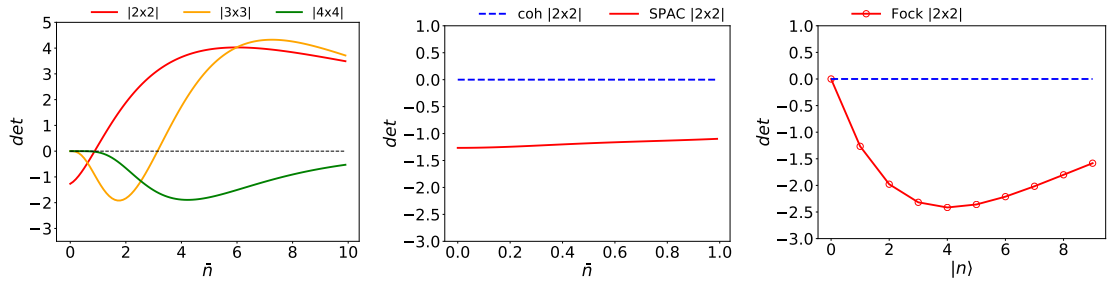

Figure 7.3.4: Non-classicality test for selected single-mode optical states. Numerical simulations are based on a truncated Fock basis (for SPAC and SPAT) for up to 15 photons. Detector multiplexing $N = 8$ with an efficiency of $\eta = 0.9$ is used to reconstruct the click distribution and moments. (left) Different principal minors ($|2 \times 2|$, $|3 \times 3|$, $|4 \times 4|$) of M matrix for SPAT state are plotted here for different thermal state mean photon number $\bar{n}$ [reproduced from [159]]. Each minors are scaled with different multiplying factors $|2\times2|$ ($\times10^2$), $|3\times3|$ ($\times10^5$) and $|4\times4|$ ($\times10^8$). It's clear that higher-order moments are useful for probing the nonclassicality when lower-order moments cannot. (center) SPAC state nonclassicality is revealed with $|2 \times 2|$ ($\times10^2$) principal minor for different $\bar{n}$, where $\bar{n}$ is for weak coherent state. Also, the dashed line plot close to zero demonstrates the $|2 \times 2|$ ($\times10^2$) minor for a weak coherent state for the same mean value, which fails the nonclassicality criteria. (right) Finally, different Fock states have opted to test the criteria and demonstrate the sub-binomial nature for every choice of $|n\rangle$.

be used to test the nonclassical photon statistics. The variance of click counting statistics can be readily obtained from the first 2×2 principal minor of $\mathbf{M}$,

$$det \begin{vmatrix} \langle : \hat{\pi}^0 : \rangle & \langle : \hat{\pi}^1 : \rangle \\ \langle : \hat{\pi}^1 : \rangle & \langle : \hat{\pi}^2 : \rangle \end{vmatrix} = \langle : (\Delta\hat{\pi})^2 : \rangle. \tag{7.3.6}$$

A negative value for Eq. (7.3.6) underpins sub-binomial photon statistics, therefore sub-binomial light detection with click counting method. Violation of positive semi-definite of $\mathbf{M}$ matrix then implies direct probing of the nonclassical nature of optical states. Fig. 7.3.4 depicts click moment-based nonclassical estimates for single photon added thermal state (SPAT), single photon added coherent state (SPAC), and Fock state. Construction of higher order moments is beneficial if second or lower order moments fail to observe non-classicality, but with higher order moments succeeds the test [see for example SPAT simulation].

7.3.3 Nonlinear polarization squeezing

After the detailed inspection of multiplexed click counting, we come back to optical state synthesis again to combine click counting theory with quantum state engi-

neering for our specific choice of degree of freedom (DOF). In a discrete variable picture, measurement of the Stokes operator involves photon number resolved measurements. We use the above-mentioned click counting operator and moment-based approach to probe Stokes measurements with multiplexed detection schemes.

To characterize the polarization properties of light one can use photon number difference measurements from two polarization (h, v) modes, $\hat{a}^\dagger\hat{a} - \hat{b}^\dagger\hat{b}$,

$$\langle\alpha, \beta| \left(\hat{a}^\dagger\hat{a} - \hat{b}^\dagger\hat{b}\right) |\alpha, \beta\rangle \,. \tag{7.3.7}$$

If the measurements are carried out in a rotated mode $|\alpha, \beta\rangle \mapsto |\alpha', \beta'\rangle$, in the Heisenberg picture we can instead rotate the measurement operator and act on the initial state. For arbitrary Stokes measurements, Eq. (7.3.7) then takes the form,

$$\langle\alpha, \beta| \, \mathbf{e}.\hat{\mathbf{S}} \, |\alpha, \beta\rangle \,. \tag{7.3.8}$$

Therein, arbitrary Stokes observable $\mathbf{e}.\hat{\mathbf{S}}$ corresponds to the measurement projection direction on the Poincaré sphere. Where $\hat{\mathbf{S}} = (\hat{a}^\dagger\hat{b} + \hat{b}^\dagger\hat{a}, -i\hat{a}^\dagger\hat{b} + i\hat{b}^\dagger\hat{b}, \hat{a}^\dagger\hat{a} - \hat{b}^\dagger\hat{b})$ and vector $\mathbf{e}$ has components $\mathbf{e} = (\sin\theta\cos\phi, \sin\theta\sin\phi, \cos\theta)$ with θ and ϕ as polar and azimuthal angle from Poincaré sphere . Photon number operator for two polarization modes now can be rewritten by combining $\hat{S}_0$ and $\mathbf{e}.\hat{\mathbf{S}}$.

$$\hat{n}_h = \hat{a}^\dagger\hat{a} = \frac{\hat{S}_0 + \mathbf{e}.\hat{\mathbf{S}}}{2} \quad , \quad \hat{n}_v = \hat{b}^\dagger\hat{b} = \frac{\hat{S}_0 - \mathbf{e}.\hat{\mathbf{S}}}{2}. \tag{7.3.9}$$

Second order polarization measurement uncertainty can be obtained from $\langle: \left(\Delta\mathbf{e}.\hat{\mathbf{S}}\right)^2 :\rangle$,

$$\begin{aligned} \langle: \left(\Delta\mathbf{e}.\hat{\mathbf{S}}\right)^2 :\rangle &= \langle: \left(\Delta(\hat{n}_h - \hat{n}_v)\right)^2 :\rangle \,, \\ \langle: \left(\Delta\mathbf{e}.\hat{\mathbf{S}}\right)^2 :\rangle &= \langle: \hat{n}_h^2 :\rangle - 2\langle: \hat{n}_h\hat{n}_v :\rangle + \langle: n_v^2 :\rangle - (\langle: \hat{n}_h :\rangle - \langle: \hat{n}_v :\rangle)^2. \end{aligned} \tag{7.3.10a}$$

Classical light state then satisfy a normally ordered variance condition $\langle: \left(\Delta\mathbf{e}.\hat{\mathbf{S}}\right)^2 : \rangle > 0$. Violation of this condition assigns nonclassical polarization properties to the light states. In continuous variable picture Eq. (7.3.10a) can be probed by intensity difference measurements between two polarization modes and violation of Eq. (7.3.10a) demonstrate nonclassical nature which we call it as *linear polarization squeezing*.

In the DV picture, true PNR detectors are required for photon number difference measurements as in Eq. (7.3.10a). For now a pseudo-PNR device and click counting theory can be an alternative to probe Stokes measurement in photon number

regime. Photon number click probability can be implemented with click operator in Eq. (7.3.3) for the case of two modes (A, B)[2],

$$\hat{\pi}_A = \hat{1} - : \exp\left(\frac{-\eta \hat{n}_h}{N}\right) : \quad = \hat{1} - : \exp\left(\frac{-\eta(\hat{S}_0 + \mathbf{e}.\hat{\mathbf{S}})}{2N}\right), \tag{7.3.11a}$$

$$\hat{\pi}_B = \hat{1} - : \exp\left(\frac{-\eta \hat{n}_v}{N}\right) : \quad = \hat{1} - : \exp\left(\frac{-\eta(\hat{S}_0 - \mathbf{e}.\hat{\mathbf{S}})}{2N}\right). \tag{7.3.11b}$$

Mean click number from each mode are obtained from $\langle N\hat{\pi}_A \rangle$, $\langle N\hat{\pi}_B \rangle$. For Polarization measurements (otherwise Stokes measurements), again consider the mean difference in click number,

$$\hat{S}_{NL} = N\hat{\pi}_A - N\hat{\pi}_B = 2N : \exp\Big(-\frac{\eta}{2N}\hat{S}_0\Big) \sinh\Big(\frac{\eta}{2N}\mathbf{e}.\hat{\mathbf{S}}\Big) : \ . \tag{7.3.12}$$

Importantly, the operator in Eq. (7.3.12) is a nonlinear function of Stokes operators which includes a hyperbolic sine of the sought-after projection $\mathbf{e}.\hat{\mathbf{S}}$ and which also includes an exponential scaling with the total photon number $\hat{S}_0$, accounting for detector saturation. This nonlinear nature is an intrinsic feature when combining modern click-counting theory with angular-momentum algebra. Similar to the linear counterpart part a squeezing-type inequality for the nonlinear Stokes operator is inevitable for polarization measurements. Normally ordered variance of $\hat{S}_{NL}$ then follows $\langle : (\Delta \hat{S}_{NL})^2 : \rangle \geq 0$ for classical light states. This motivates the quest for nonlinear squeezing effects in light states together with a click-counting scheme. Furthermore, the measurement outcome analogy between the linear and nonlinear functional of a quantum operator is important for a better understanding of the approach and the quantum state. Similar to the mean click number difference, the total click number operator from the two polarization modes represents a nonlinear operator of the form,

$$\hat{S}_{0,NL} = N\hat{\pi}_A + N\hat{\pi}_B = 2N\Big[\hat{I} - : \exp\big(-\frac{\eta}{2N}\hat{S}_0\big) \cosh\big(\frac{\eta}{2N}\mathbf{e}.\hat{\mathbf{S}}\big) :\Big], \tag{7.3.13}$$

and total photon number shown to be measurement direction ($\mathbf{e}.\hat{\mathbf{S}}$) dependant. With the absence of such restrictions, linear operator $\hat{S}_0$ contradicts with nonlinear operator $\hat{S}_{0,NL}$. In our experimental scheme and data analysis, we will evaluate higher order moment of click statistics which essentially take care of both mean click difference and total click number for the complete moment-based description of the state.

[2]Here two modes are taken as A and B for general introduction, but it is useful to connect with the following experimental scheme where measurements are done on two different spatial modes.

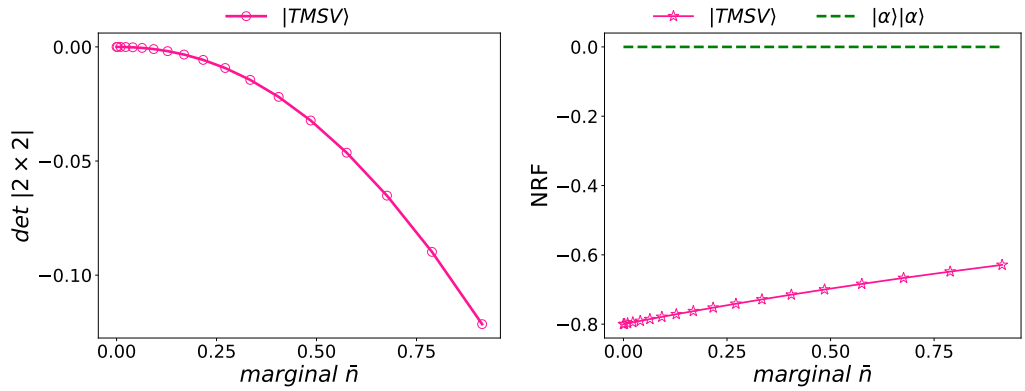

Figure 7.3.5: Numerically detecting non-classicality for the two-mode light state. $N = 8$ detectors with an efficiency of $\eta = 0.8$ are used for the simulation. (left) Principal minor $|2 \times 2|$ of M matrix for a TMSV state shows negative values (scaled with 10^3) [159], which is plotted for different squeezing strength up to a marginal mean photon number range $\bar{n} = 1$. (right) Noise reduction factor simulation for two-mode coherent state and TMSV state, obtained from the relation $\frac{\langle:(\Delta\hat{S}_{NL})^2:\rangle}{N\langle:\hat{\pi}_A^1:\rangle + N\langle:\hat{\pi}_B^1:\rangle}$. Which is a useful quantity to detect correlation/nonclassicality in two mode light beams.

Since measurements of Stokes observable involve photon numbers from two modes, the matrix of moments needs to be adapted for more than a single mode. Similar to a single mode click moment operator in Eq. (7.3.4), moments for a two-mode click counting operator were derived while studying multi-mode light photon statistics and correlation [159], taking a normally ordered form,

$$\langle:\hat{\pi}_A^{m_A}\hat{\pi}_B^{m_B}:\rangle = \sum_{k_A=m_A}^{N}\sum_{k_B=m_B}^{N} c_{k_Ak_B}\binom{k_A}{m_A}\binom{k_B}{m_B}\binom{N}{m_A}^{-1}\binom{N}{m_B}^{-1}, \tag{7.3.14}$$

which makes multimode moments directly calculated from joint click counting probability $c_{k_Ak_B}$. The covariance click matrix obtained from the experimental data set or an ideal two-mode optical state in the form of $c_{k_Ak_B}$ is then used to construct the moment matrix of the form,

$$\mathbf{M} = \begin{pmatrix} \langle:\hat{\pi}^0:\rangle & \langle:\hat{\pi}_A:\rangle & \langle:\hat{\pi}_B:\rangle & \langle:\hat{\pi}_A^2:\rangle & \langle:\hat{\pi}_A\hat{\pi}_B:\rangle & \langle:\hat{\pi}_B^2:\rangle & \dots \\ \langle:\hat{\pi}_A:\rangle & \langle:\hat{\pi}_A^2:\rangle & \langle:\hat{\pi}_A\hat{\pi}_B:\rangle & \langle:\hat{\pi}_A^3:\rangle & \langle:\hat{\pi}_A^2\hat{\pi}_B:\rangle & \langle:\hat{\pi}_A\hat{\pi}_B^2:\rangle & \dots \\ \langle:\hat{\pi}_B:\rangle & \langle:\hat{\pi}_A\hat{\pi}_B:\rangle & \langle:\hat{\pi}_B^2:\rangle & \langle:\hat{\pi}_A^2\hat{\pi}_B:\rangle & \langle:\hat{\pi}_A\hat{\pi}_B^2:\rangle & \langle:\hat{\pi}_B^3:\rangle & \dots \\ \vdots & \vdots & \vdots & \vdots & \vdots & \vdots & \ddots \end{pmatrix}, \tag{7.3.15}$$

resulting matrix $\mathbf{M}$ includes moments up to the N^{th} order for a two-mode scenario and is positive semi-definite for classical light bounded by the condition $\mathbf{M} \geq 0$.

Violation of the bound shows a nonclassical correlation between the modes in the test. Every single element at the moment matrix can be accessed by Eq. (7.3.14), for example, joint first-order click moment from two modes,

$$\langle : \hat{\pi}_A \hat{\pi}_B : \rangle \;=\; \frac{1}{N_A N_B} \sum_{k_1=0}^{N_A} \sum_{k_2=0}^{N_B} k_1 k_2 c_{k_1,k_2} \;, \tag{7.3.16}$$

where two modes are detected by N_A and N_B number of detector modules. Principal minors of the sub-matrix are again useful to detect nonclassicality in two mode click statistics for different orders of nonclassicality. As a direct consequence, second-order nonlinear polarization squeezing criteria can be derived from the second-order elements of $\mathbf{M}$,

$$\begin{aligned} \langle : \left(\Delta \hat{S}_{NL}\right)^2 : \rangle \;=\; & N^2 \Big(\langle : \hat{\pi}_A^2 \hat{\pi}_B^0 : \rangle \;-\; 2 \langle : \hat{\pi}_A^1 \hat{\pi}_B^1 : \rangle \;+\; \langle : \hat{\pi}_A^0 \hat{\pi}_B^2 : \rangle \Big) \\ & - N^2 \Big(\langle : \hat{\pi}_A^1 \hat{\pi}_B^0 : \rangle \;-\; \langle : \hat{\pi}_A^0 \hat{\pi}_B^1 : \rangle \Big)^2 . \end{aligned} \tag{7.3.17a}$$

Equation (7.3.17a) and principal minor 2×2 from Eq. (7.3.15) are used to detect nonclassical behavior for a two-mode light state (TMSV), and shown in Fig. 7.3.5.

Eigenvalue decomposition of $\mathbf{M}$ is one straight approach to identify non-classicality in the system, this returns all the eigenvalues (e) and eigenvectors ($\vec{v}$) for the moment matrix. Obtaining negative eigenvalues for the moment matrix implies a nonclassical signature for the physical system. Therefore computation of the minimal eigenvalue (e_m) and associated minimum eigenvector ($\vec{v}_m$) in the realm of positive semi-definite is important and bounded by $e \geq 0$ for a matrix describing the classical system. Providing the system hails some quantum characteristics, then the negativity ($\mathcal{N}$) for the matrix for nonclassical behavior takes the form,

$$\mathcal{N} = \vec{v}_m^{\dagger}\, \mathbf{M}\, \vec{v}_m . \tag{7.3.18}$$

An expression that is useful to calculate the higher order non-classicality with respect to the dimension of detection bins (N_A, N_B). Later in our experimental observations moments and correlation up to 8^{th} order will be demonstrated with $\mathcal{N}$ in Eq. (7.3.18).

7.3.4 Time multiplexed detection

When the system or state dimension becomes large (for example states with high mean photon number), the spatial detector multiplexing scheme [e.g in Fig. 7.3.1] starts to demand more resources to efficiently quantify the state. Effectively the

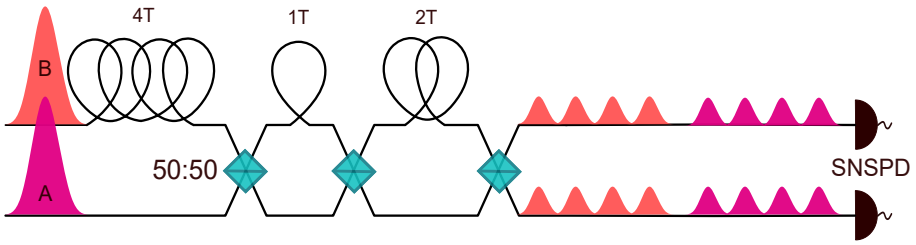

Figure 7.3.6: Time multiplexed PNR detection scheme: Two light pulses (A and B) mimic a few photon optical states and are sent through a TMD network. Three-stage fiber splitter network can resolve eight photons from each pulse distributed as pairs of four bins at the output mode. Light pulse B is delayed from the input fiber side (4T equivalent time for fiber delay length 4L) to avoid cross-talk with pulse-A photons. A total of 16 time-bins are time synchronized with a global gate trigger for efficient data collection and post-processing.

resource requirements scale exponentially with state dimension, and experimental implementation becomes more challenging, this situation is similar to what we see in the case of spatial source multiplexing. Time bin multiplexed detectors (TMDs) are shown to be an efficient scheme for photon number statistics measurements and nonclassical correlation experiments[95, 160]. Since we are in the telecommunication wavelength regime low loss optical fibers and fiber beam splitters do an efficient job in TMD experiments.

In the TMD scheme optical pulses with large photon numbers are sent through a network of fiber splitters connected with fiber delays (T) to split and separate photons in different time bin modes. In the end, only two detectors are needed to record the time-separated clicks. If the temporal separation between the individual time bin photons is large enough compared to the detector dead time, it's possible to address every single resolved photon from the input pulse. The number of multiplexing stages ('n' beam splitters) decides how many bins or photons can be resolved in a TMD detection system. An n-stage beam splitter can resolve 2^n photons by the detector. A layout diagram for 8-bin TMD is given in Fig. 7.3.6 with three fiber splitting stages. Bin separation between the pulses is adjusted by a suitable choice of fiber delay length ('L', depending on the dead time of the detector), which fixes the bin separation between two consecutive bins of one output mode. After each beam splitting stage fiber delay length has to be adjusted in such a way that, twice the length of the previous stage (L, 2L, 4L, ...) to have equal spacing between the train of bin pulses at the final output. By adding additional delays in one of the input modes it's possible to use both input ports for PNR measurements from two different input light modes. Input temporal delay is to avoid the mixing of resolved photons from two input choices, and delay length can be fixed based on the

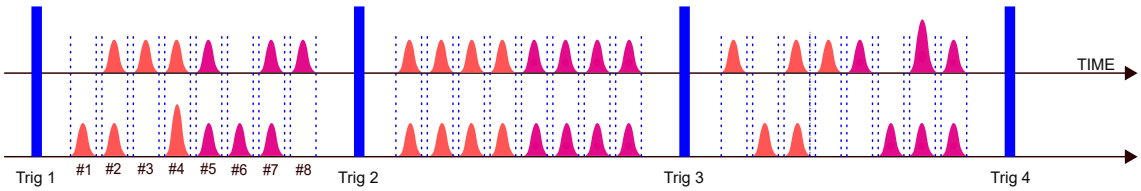

Figure 7.3.7: Collecting photons from an 8-bin TMD output. Figure is adapted for a situation where both inputs (A and B) are used for PNR measurements. The blue bar denotes the trigger signal corresponding to a pump pulse. For each blue bar, a set of gate bins is generated as dotted blue bars. The number of resolved photons is then occupied in between these gate bins for counting purposes. Note that the probability of filling multiphoton events in a specific bin is represented as bigger pulses. The total number of photons from the first two sets (four from top four from bottom, magenta) depicts the number of photons for the first input pulse A. Remaining photons (orange) set account for input B which is time separated by the input delay. Coincidence measurements can be done by comparing counts from two channels for each trigger signal.

fiber length choice of the last stage multiplexing of the TMD (2L here). For 8bin TMD, this delay length corresponds to 4L and provides a total of 16 bin output bin streams with equal bin separation. Time bins of the size, 128 bins are demonstrated before for bench-marking photonics experiments with larger photonic states [161]. A variable beam splitter attached to a single fiber loop geometry has shown to be an efficient method to characterize bright light pulse with high dynamic range, also with a single detector [162].

A dedicated data collection program[3] is used to collect singles/coincidences click data for long-time experimental measurements. The data acquisition method is designed as follows. A trigger signal is derived from the pump laser system for each pulse. Based on every trigger signal (so for each pump pulse), the time tagger circuit generates multiple gate signals and places them according to the expected photon arrival time positions. For each photon bin position two gate bins are assigned to hold the actual photon click bin in between the gate window. Photon clicks arrival time and bin positions can be identified beforehand by using a built-in histogram program from the time tagger. A single trigger signal then provides a stream of gate windows to hold photon clicks as shown in Fig. 7.3.7. The scheme is beneficial for counting the total number of photons from a specific input pulse and bin-bin correlation measurements from two input pulses.

[3]For time-gated photon counting an efficient subroutine has been developed and updated for many years in our group. With some additional Python program modules the core code is then adapted for current experimental schemes

7.4 A Source for Entanglement and Squeezing in Polarization

We have developed a qualitative theory for polarization squeezing both in the linear and nonlinear regimes. Previous experimental investigations on polarization squeezing are mainly devoted to continuous variable regimes with EPR-type correlated beams and by evaluating linear Stokes measurements. This motivates us to probe nonlinear squeezing in polarization by adapting photon number measurement on a bright quantum light source. We have studied the two-photon polarization correlation emitted by a type II squeezer inserted in a Sagnac geometry. Here we

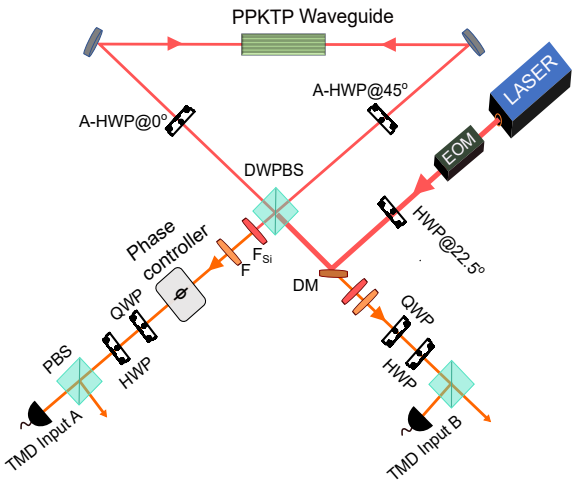

Figure 7.4.1: Polarization squeezing experimental setup: A pulse picker unit (EOM) is introduced in the pump laser path of the entanglement setup. A and B are photon collection modes, connected to the two input ports of the TMD unit for PNR measurement from the respective modes.

deliberately run the system in a low gain regime to emit two photons at a time for high-quality two-qubit polarization entanglement. Now, we would like to ask what kind of correlation exists in a high gain regime with many photons or the regime of macroscopic polarization entanglement. Extending the entanglement structure to a higher dimension (polarization and Fock space) is nontrivial in the sense of state generation and tomographic reconstruction perspective. Interestingly measurement of the underlying photon number correlation for the same state now seems to be accessible with PNR detectors, previous CV implementation backs our DV approach for observable squeezing effects [163]. This renders us to probe the nonlinear functional of polarization observable and higher order moments for an entanglement

source operated in high gain regime.

For an experimental quantification of our nonlinear approach, the entanglement scheme developed for the two-photon case is upgraded for TMD-based PNR measurements and the source is operated in a high gain regime to have multi-photon events from the squeezers. To understand the photon statistics and expectation values of Stokes observable an efficient modeling of the experimental scheme is carried out. The source modeling involves the generation and detection of high mean photon number polarization entangled state parameterized by the squeezing strength ($|\lambda| < 1$) of SPDC.

Bidirectional pumping of the source can individually contribute to the generation of TMSV light state from two sides and mixing them on the Sagnac PBS finally enables quantum interference and different amount photon number occupation at the four different output PBS modes. Overall state generation from the experimental scheme can be equivalently written in a density operator form,

$$\hat{\rho} \;=\; (1-\lambda^2)^2 \sum_{m_1,n_1,m_2,n_2=0}^{\infty} \lambda^{m_1}\lambda^{*n_1}(\lambda e^{i\phi})^{m_2}(\lambda e^{i\phi})^{*n_2} \times |m_1, m_2, m_2, m_1\rangle \langle n_1.n_2, n_2, n_1| \,, \tag{7.4.1a}$$

where the total phase setting ϕ and squeezing strength λ are contained in Eq. (7.4.1)a. Since the state is in a pure form, a state vector notation can be assigned as in Eq. (5.2.3), which takes the form,

$$|\psi\rangle \;=\; (1-|\lambda|^2) \sum_{m,n=0}^{\infty} \lambda^m(\lambda e^{i\phi})^n \,|m, n, n, m\rangle \,, \tag{7.4.2}$$

and define a well desirable *macroscopic Bell state* [164]. The above-specified state in Eq. (7.4.2) is conveniently generated by the action of an exponential operator of the type,

$$|\psi\rangle \;=\; (1-\lambda^2)\, \exp\big(\lambda \hat{a}^\dagger \hat{d}^\dagger \;+\; \lambda e^{i\phi} \hat{b}^\dagger \hat{c}^\dagger\big)\; |0,0,0,0\rangle \,. \tag{7.4.3}$$

On the detection side, N-bin time multiplexed detectors are used to collect the click probabilities. For number resolved correlation/squeezing measurements, we consider a normally ordered operator model from click theory model,

$$\hat{\mathbf{O}} \;=: \exp\big(-X_a\, \hat{a}^\dagger \hat{a} - X_b\, \hat{b}^\dagger \hat{b} - X_c\, \hat{c}^\dagger \hat{c} - X_d\, \hat{d}^\dagger \hat{d}\;\big) : \,, \tag{7.4.4}$$

where $\mathrm{X}_i \in \frac{\eta m_i}{N_i}$, constant factor which carries over information like the order of the click operator moment (m), system efficiency (η), number of click detectors at each

mode(N). For nonlinear polarization correlation(in particular nonlinear squeezing part) we perform photon number measurement at the two output mode as shown in Fig. 7.4.1, boils down the expectation value of click operator on the state, $|\psi\rangle = (1-|\lambda|^2)\sum_{m,n=0}^{\infty}\lambda^m(\lambda e^{i\phi})^n\,|m,n,n,m\rangle$,

$$\langle\psi|\,\hat{\mathbf{O}}\,|\psi\rangle \;=\; \big\langle :\, \exp\!\big(-\frac{\eta m_A}{N_A}\hat{n}_A - \frac{\eta m_B}{N_B}\hat{n}_B\big)\, :\big\rangle. \tag{7.4.5}$$

Photon number correlation on a rotated state or light state's polarization basis change ($|\psi\rangle \to |\psi'\rangle$) can be manipulated by the act of tomographic arrangement. On the measurement aspects expectation value transforms to $\langle\psi'|\,\hat{\mathbf{O}}\,|\psi'\rangle$ or equivalently $\langle\psi|\,U^{\dagger}\hat{\mathbf{O}}U\,|\psi\rangle$. Where the tomographic waveplate's unitary matrix is given by,

$$\begin{bmatrix}\tau_{qwp} & \rho_{qwp}\\ \tau^*_{qwp} & \rho^*_{qwp}\end{bmatrix} = \begin{bmatrix}\frac{1-i\cos 2\theta}{\sqrt{2}} & \frac{-i\sin 2\theta}{\sqrt{2}}\\ \frac{i\sin 2\theta}{\sqrt{2}} & \frac{1+i\cos 2\theta}{\sqrt{2}}\end{bmatrix} \quad , \quad \begin{bmatrix}\tau_{hwp} & \rho_{hwp}\\ \tau^*_{hwp} & \rho^*_{hwp}\end{bmatrix} = \begin{bmatrix}-i\cos 2\theta & -i\sin 2\theta\\ i\sin 2\theta & i\cos 2\theta\end{bmatrix}. \tag{7.4.6}$$

Click correlation measurement outcome in terms of moments can be constructed by combining Eq. (7.4.5) and Eq. (7.4.6) for the desired state (detailed calculation is available in appendix C.0.1),

$$\langle :\hat{\mathbf{O}}: \rangle \;=\; \frac{N^2(1-|\lambda|^2)^2\,(N-\eta m_A)(N-\eta m_B)}{\begin{bmatrix} N-|\rho|^2\eta m_A & \rho\tau^*\eta m_A & 0 & \lambda'\\ \rho^*\tau\eta m_A & N-|\tau|^2\eta m_A & \pm\lambda' & 0\\ 0 & \pm\lambda'^* & N-|\tau|^2\eta m_B & -\rho^*\tau\eta m_B\\ \lambda'^* & 0 & -\rho\tau^*\eta m_B & N-|\rho|^2\eta m_B\end{bmatrix}}\;, \tag{7.4.7}$$

where $\pm\lambda' = e^{i\phi}\sqrt{(N-\eta m_A)(N-\eta m_B)}\lambda$ and the sign depends on $e^{i\phi} = \pm 1$ setting on the experiment. Therefore several parameter choices are available in Eq. (7.4.7) to learn or tune the system behavior. Since the type II source is designed to generate Bell state of type $|\psi\rangle$ (in low gain regime $|\psi\rangle = \frac{1}{\sqrt{2}}(|H,V\rangle + e^{i\phi}\,|V,H\rangle\,)$, corresponding phase settings in high gain regime indicate macroscopic Bell state transition from $|\psi_+\rangle \leftrightarrow |\psi_-\rangle$. Finally, Eq. (7.4.7) provides a complete description to simulate the experimental scenario in Fig. 7.4.1 with the click counting approach. For different squeezing strength λ and polarization measurement choices, a theoretical evaluation of second order moment $\langle :\,(\Delta\hat{S}_{NL})^2\,:\rangle$ in terms of Eq. (7.3.17a) is given in Fig. 7.4.2. This is possible by selecting suitable m_A, m_B values to obtain corresponding π_A, π_B terms in $\langle :\,(\Delta\hat{S}_{NL})^2\,:\rangle$. Certainly, the source shows nonclassical statistics and signature-probing of nonlinear polarization squeezing is made possible.

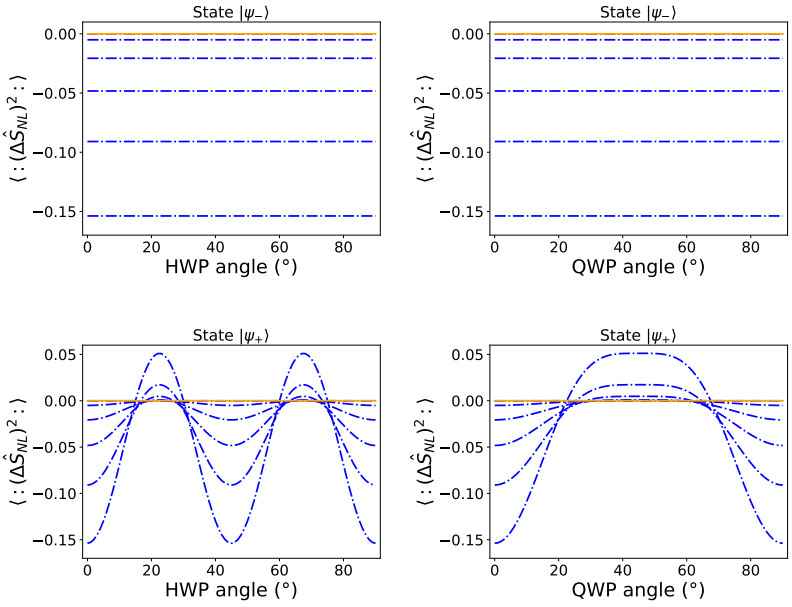

Figure 7.4.2: Second-order moment or variance, numerically obtained from the employed click counting method on macroscopic polarization state and demonstration of nonlinear polarization squeezing. N=8 detector multiplexing and overall system efficiency of $\eta = 0.5$ are applied for the simulation. On the top side, plots for the state $|\psi_-\rangle$ are considered to evaluate $\langle : (\Delta \hat{S}_{NL})^2 : \rangle$ for different HWP and QWP angle settings respectively from left to right. Multiple dashed blue line stands for $\langle : (\Delta \hat{S}_{NL})^2 : \rangle$ for different squeezing strength $\lambda = 0.01,\ 0.1,\ 0.2,\ 0.3,\ 0.4,\ 0.5$, where higher the squeezing higher the negativity (otherwise nonclassical). On the bottom, $|\psi_+\rangle$ state details are plotted for similar settings. Rather than $|\psi_-\rangle$ state $|\psi_+\rangle$ squeezing property is basis dependant which is clear from the oscillatory plot. But $|\psi_-\rangle$ is special by which the state is a perfect example for basis independent nonclassical effect for all polarization observable and polarization noise free light [163].

7.5 Experiments and Results

In contrast to pair photon polarization entanglement, a key difference in the experimental scheme is the mode of operation. Instead of low gain PDC high gain operation operation of the source predicts moderately high mean photon number polarization entanglement from the source. A moderate pump power of 100 μW (with $\approx$ 1 MHz rep-rate) is coupled from each side, which is equivalent to 0.1 nJ per pulse and produces sixfold coincidence events on the computational basis waveplate setting. From the technical side, the TMD detector design demands a reduction in the repetition rate of the experiment. Since we are resolving photon numbers

in time, enough number of time bin and large time bin separation is needed from the detection side. ≈ 80 ns dead time of the SNSPD detector makes bin separation ≈ 100 ns between individual output photon click bins. For each pump pulse, signal-idler output photon number bin separation requires more than 1 μs total time delay, demanding similar time separation between pump pulses. This enforces a considerable reduction in the experimental repetition rate of the laser, scaling down from 76 MHz to 1 MHz rate. Currently faster TMDs are under development with SNSPD detectors having dead time in the range of 12 ns but for our squeezing experiments we make use of our off-the-shelf TMD with 100 ns bin separation 8-bin TMD with a total transmission efficiency in the range of 72%. Two SNSPD click detectors with a detection efficiency of 81% are placed at the TMD end for detecting time bin resolved photons. Laser repetition rate down-scaling is done by placing a pulse picker unit in front of the pump laser. Which is essentially an electro-optic polarization modulator, that rotates/flips polarization depending on the applied voltage and trigger rate (1 MHz for the experiment). With a PBS in combination pulse picking unit then only by pass polarization flipped pulse towards the waveguide with the same rep-rate. Triggering of the modulator is time synchronized with the pump laser and time tagging unit. An FPGA-based clock synthesizer is used to create a phase-locked copy of the laser trigger signal for both the pulse-picking unit and time tagger (for synchronized data collection), making every single picked pulse-generated polarization squeezed state to account for the output click collection. The time tagger trigger signal derived from the FPGA unit serves the same blue trigger pulse described in Fig. 7.3.7.

All possible click combinations from the two collection modes (A and B in Fig. 7.4.1) are post-processed and saved in the form of a matrix to obtain single and coincidence click probabilities. Each channel has nine click possibilities (0 to 9 number of photons) and possesses 81 coincidence possibilities from two channels. An example data set of a 9×9 matrix measured in the computational basis (or 0° angle setting) is given in Fig. 7.5.1.

Experimentally obtained these click matrix elements are now useful to recast the individual click probability $c_{k_A k_B}$ for moment matrix reconstruction. For an arbitrary polarization basis projection ($\mathbf{e}$) raw coincidence clicks from two modes are obtained as a matrix $\mathbf{C}$,

$$\mathbf{C} = \begin{pmatrix} C_{0,0} & \dots & C_{0,8} \\ \vdots & \ddots & \vdots \\ C_{8,0} & \dots & C_{8,8} \end{pmatrix}, \tag{7.5.1}$$

where subscripts stand for corresponding photon number coincidence. Individual

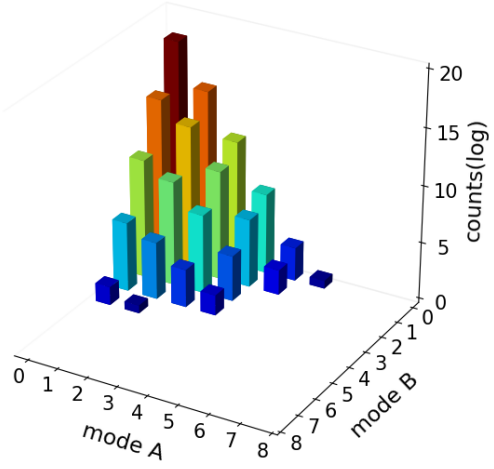

Figure 7.5.1: Click matrix: Counts registered from the two modes are plotted in a matrix format which includes all possible coincidences and marginal singles. Higher order pairs up to six folds are populated on the chosen plot basis. Since we collect a large amount of click information counts are plotted in a log scale.

click probabilities ($c_{k_A k_B}$) are computed from Eq. (7.5.1) by averaging over the total number of events in the matrix,

$$C = \sum_{k_A=0}^{N} \sum_{k_B=0}^{N} C_{k_A,k_B} \ , \tag{7.5.2a}$$

$$c_{k_A,K_B} = C_{k_A,K_B}/C \ , \tag{7.5.2b}$$

click probability equivalent experimental moment matrix reconstruction is then possible by using Eq. (7.3.14), which is actually in a matrix product format. Where the Binomial multiplier coefficient can be reformulated in the form of a sampling matrix,

$$\mathbf{T} = \left(\frac{\binom{k}{m}}{\binom{N}{m}} \right)_{m,k \in (0,..N)} , \tag{7.5.3a}$$

$$\mu = \begin{pmatrix} \langle : \hat{\pi}_A^0 \hat{\pi}_B^0 : \rangle & \dots & \langle : \hat{\pi}_A^0 \hat{\pi}_B^8 : \rangle \\ \vdots & \ddots & \vdots \\ \langle : \hat{\pi}_A^8 \hat{\pi}_B^0 : \rangle & \dots & \langle : \hat{\pi}_A^8 \hat{\pi}_B^8 : \rangle \end{pmatrix} = \frac{1}{C} \mathbf{T} \mathbf{C} \mathbf{T}^T . \tag{7.5.3b}$$

Now it's straightforward to compute second-order moment for every measurement

bases $\mathbf{e}.\hat{\mathbf{S}}$ from the respective click matrix and moment matrix, which is done by opting associated moment elements ($\mu_{i,j}$) from μ matrix and placing in Eq. (7.3.17a). Error estimation in the form of second-order uncertainties for each moment element is important to test experimental precision for every data set. The moment uncertainty matrix is given by the following expressions,

$$\mu^{(2)} = \frac{1}{C}(\mathbf{T}*\mathbf{T})\mathbf{C}(\mathbf{T}*\mathbf{T})^T, \tag{7.5.4a}$$

$$\sigma(\mu) = \frac{1}{\sqrt{C-1}}\sqrt{\mu^{(2)} - \mu * \mu}\ , \tag{7.5.4b}$$

and $\sigma(\mu)$ stands for the uncertainty matrix[4]. Similar to variance evaluation respective error elements are placed in Eq. (7.3.17a) for the error estimate.

Maximally entangled macroscopic type Bell states are generated by strong pumping of the source. Similar to the two-photon case the phase in the setup ($e^{i\phi}$) is set to ± 1 using the Soleil-Babinet, generates $|\psi_-\rangle$ and $|\psi_+\rangle$ state with higher order photon number contribution. The provision of tomographic waveplates (HWP and QWP) on both sides enabled two-mode polarization tomographic measurements with a sampling of 10°. For every setting, measurements are carried out for 1300 sec and collected 10^8 events for all possible coincidence (k_A, k_B) from modes A and B. Moreover this yields join click count statistics c_{k_A,k_B} for all bases settings and corresponding state setting $|\psi_\pm\rangle$.

Experimental plots on the complete data sets of non-linear operator's second order moment are given in Fig. 7.5.2. For the two different Bell states, coincidence clicks are collected for different settings on the half-wave, and quarter-wave waveplates (note that on both sides A and B, the same waveplate settings are used). For the measurement scheme whenever HWP rotates QWP is kept at zero and vice versa, in general, it's possible to access all the Stokes observable $\hat{S}_i$ from these measurement settings. Symmetric state $|\psi_-\rangle$ is special that shows a basis independent nonclassical behavior and possesses negativity regardless of measurement direction. In contrast, $|\psi_+\rangle$ nonclassicality strongly basis dependant, showing an oscillatory character over the measurement angles. Two features that are exactly predicted in theoretical plots in Fig. 7.4.2 are demonstrated with high precision. To extract the experimental parameters, a theoretical fit is applied to the data based on the same click theory expressions. A single set of fit parameters was shown to be well works

[4]Different multiplication rules are used in these equations,(7.5.3b), (7.5.4). For A*B matrix multiplication, element-wise multiplication is ruled between A and B elements. AB or (AB)C stands for the standard matrix multiplication between matrices. Square roots are acting on each element of the matrix

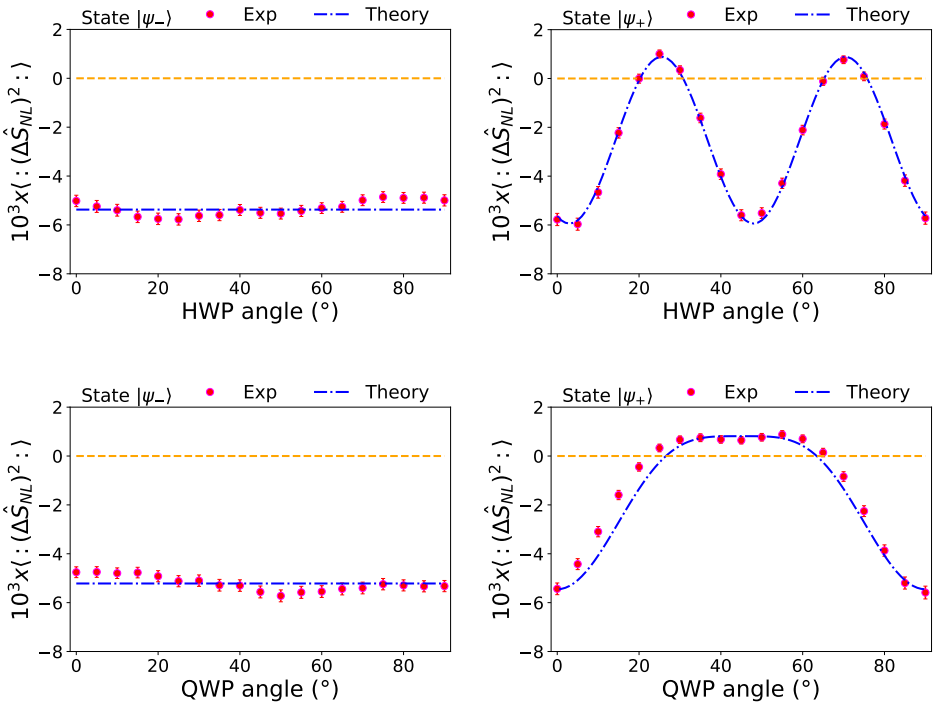

Figure 7.5.2: Experimental observation of nonlinear polarization squeezing in the form of second order moment of Stokes observable. The left column shows nonlinear polarization non-classicality depicted as negativity for the symmetric macroscopic Bell state $|\psi_-\rangle$ with phase setting $\phi = 0$. Measurements are taken for different settings on HWP for fixed QWP at 0° and vice versa. Similar measurements are carried out for the phase settings $\phi = \pi$ providing anti-symmetric state $|\psi_+\rangle$. Based on the theoretical simulation (blue curve) we tried to fit the experimental observation by adjusting a single set of fit parameters for squeezing strength $\lambda = 0.36$ and overall system efficiency $\eta = 13.6\%$.

for the experimental data set, yielding a squeezing value $\lambda = 0.36$ and overall system efficiency $\eta = 13.6\%$ from the fits. From the same measurement data quadrature equivalent squeezing of 3.3 dB is extracted for our squeezed light source, which can be improved by reducing the losses in the setup and with highly efficient PNR detectors. Slight deviations from the theoretical-experimental fit are expected for the following reasons, long measurement runs can cause perturbations in the setups and can affect the couplings at various points in the setups. This may cause irregularities in the input pump power or photon collection side. Deviations from the exact measurement angle (waveplate settings) can show up as a slight shift in the oscillation behavior of the model and experiment. But still with the current experimental effi-

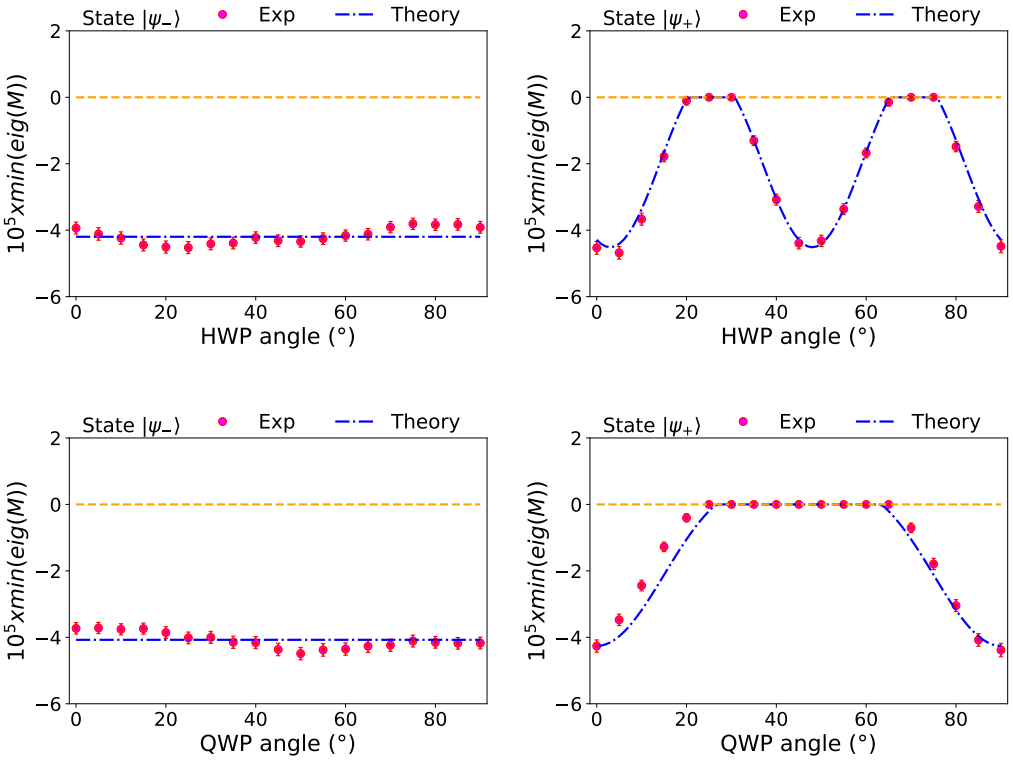

Figure 7.5.3: Higher order moment reconstruction: Left column shows eighth order moment for the Bell state $|\psi_-\rangle$, right side is for $|\psi_+\rangle$. Similar to the variance case, the choice of theoretical fit parameter matches with the eighth-order moment.

ciency we are at a point to demonstrate nonlinear squeezing in polarization degree of freedom.

The same data set is then used to calculate higher-order moments to benchmark the properties of optical states in test and nonlinear squeezing operators. This is done by the minimum eigenvalue method defined in Eq. (7.3.18). Furthermore, to extract maximum information from the statistics we construct moments that include both click difference and total photon number nonlinear operators from Eq. (7.3.12) and Eq. (7.3.13). Click operator relates the nonlinear Stokes operator by, $\hat{\pi}_A = (\hat{S}_{0,NL} + \hat{S}_{NL})/N$ and $\hat{\pi}_B = (\hat{S}_{0,NL} - \hat{S}_{NL})/N$. Consequently a moment matrix $\mathbf{M}$ which exploits all the possible moments of $\hat{S}_{0,NL}, \hat{S}_{NL}$ constructed as,

$$\mathbf{M} = \left(\mu_{m_A+m'_A, m_B+m'_B}\right)_{(m_A,m_B),(m'_A,m'_B)\in(0,..,N/2)\times\in(0,..,N/2)}. \tag{7.5.5}$$

The $\mathbf{M}$ matrix rows and columns are defined by two mode moment ordered pairs (m_A, m_B), $(m_A^{'}, m_B^{'})$, respectively. Minimum negative eigenvalues obtained for the experimental $\mathbf{M}$ matrix $(mineig(M))$ are plotted in Fig. 7.5.3, depicts nonlinear polarization nonclassicality of $\hat{S}_{0,NL}$, $\hat{S}_{NL}$ upto eighth order. Being detected with an 8-bin detector resulting data constitutes maximum information extractable from measurement outcomes. Beyond variance-based squeezing criteria, we can thereby explore nonclassical signatures in the skewness (third order), kurtosis (fourth order), etc. of nonlinear Stokes operators. Also, access to higher moments via more detection bins (N) generally allows for an improved classical-nonclassical state quantification. Error estimate $\sigma(\mathcal{N})$[5] can be calculated by the method provided in Eq. (7.5.4),

$$\sigma(\mathcal{N}) \;=\; |\vec{v}|^{\dagger}\, \sigma(\mathbf{M})\, |\vec{v}|. \tag{7.5.6}$$

In comparison with the second-order approach, however, the higher-order moments never rise above the boundary at zero.

7.6 Noise Resilience Model

In previous methods, we used quantum light resources for better statistics and showed these sources outperform classical resources, especially in the shot noise or Poissonian limit strategy. However the performance of both classical and quantum resources in the presence of noise (or mixed with noise) is equally important and not yet considered. In this regime, two-mode correlated twin beam light states showed superior performance in imaging and sensing schemes and proved to be an ideal light source with high signal-to-noise (SNR) performance [165, 166]. Here the sample probing light will be flooded with background noise and after the interaction, quantum correlation between the signal and idler modes is used to throw away noise contributions from the measurement data. A technique well established in many quantum imaging and sensing experiments [167]. Also, many information-hiding schemes are proposed and realized to explore noise effects in the quantum probes.

We are interested in investigating noise effects on light sources with linear and nonlinear measurement schemes presented in this chapter. Therefore polarization states and measurements are convoluted with thermal background and considered as noise test models. A Gaussian phase space distribution function of the form, $(\pi\bar{n})^{-2} e^{-(|\alpha|^2+|\beta|^2)/\bar{n}}$ with mean photon $\bar{n}$ suits the definition of thermal noise. Noise models also transform operators involved in the measurements. Transformed photo

[5]Note that vector modulus operation on $|\vec{v}|$ is vector element-wise modulus not the same as normal vector modulus operation

number operators in the form of generating functions are useful to construct other measurement observables (like polarization),

$$\langle: \hat{n}^k :\rangle_{\bar{n}} \;=\; \sum_{j=0}^{k} \binom{k}{j} \frac{k!}{(k-j)!} \bar{n}^j \langle: \hat{n}^{k-j} :\rangle, \tag{7.6.1a}$$

$$\langle: e^{-z\hat{n}} :\rangle_{\bar{n}} \;=\; \frac{1}{1+\bar{n}z} \langle: e^{-z\hat{n}/(1+\bar{n}z)} :\rangle. \tag{7.6.1b}$$

Then Eq. (7.6.1a) and Eq. (7.6.1b) in single mode description can be extended to the two-mode case to have equivalent expressions for Stokes operators. First and second-order exponents of linear Stokes operators are constructed within the noise model,

$$\langle: \hat{S}_L :\rangle_{\bar{n}} \;=\; \langle \hat{a}^\dagger \hat{a} \rangle \;-\; \langle \hat{b}^\dagger \hat{b} \rangle, \tag{7.6.2a}$$

$$\langle: \hat{S}_L^2 :\rangle_{\bar{n}} \;=\; \langle (\hat{a}^\dagger \hat{a})^2 \rangle \;- 2\langle \hat{a}^\dagger \hat{b} \hat{a}^\dagger \hat{b} \rangle + \langle (\hat{b}^\dagger \hat{b})^2 \rangle + (2\bar{n}-1)\left(\langle \hat{a}^\dagger \hat{a} + \hat{b}^\dagger \hat{b} \rangle\right) + 2\bar{n}^2, \tag{7.6.2b}$$

and $\bar{n}$ sub-scripted expectation values define noise convoluted measurement outcome. Similar approaches provide expressions for the nonlinear Stokes operator,

$$\langle :\hat{S}_{NL}:\rangle_{\bar{n}} = \tfrac{N}{1+\bar{n}/N} \left\langle \left[\tfrac{N+\bar{n}-1}{N+\bar{n}}\right]^{\hat{b}^\dagger \hat{b}} \right\rangle - \tfrac{N}{1+\bar{n}/N} \left\langle \left[\tfrac{N+\bar{n}-1}{N+\bar{n}}\right]^{\hat{a}^\dagger \hat{a}} \right\rangle, \tag{7.6.3a}$$

$$\langle :\hat{S}_{NL}^2:\rangle_{\bar{n}} = \tfrac{N^2}{1+2\bar{n}/N} \left\langle \left[\tfrac{N+2\bar{n}-2}{N+2\bar{n}}\right]^{\hat{b}^\dagger \hat{b}} \right\rangle - \tfrac{2N^2}{(1+\bar{n}/N)^2} \left\langle \left[\tfrac{N+\bar{n}-1}{N+\bar{n}}\right]^{\hat{a}^\dagger \hat{a} + \hat{b}^\dagger \hat{b}} \right\rangle + \tfrac{N^2}{1+2\bar{n}/N} \left\langle \left[\tfrac{N+2\bar{n}-2}{N+2\bar{n}}\right]^{\hat{a}^\dagger \hat{a}} \right\rangle. \tag{7.6.3b}$$

As we did for the previous cases, first and second-order exponents of the Stokes operator and their expectation values are used here to obtain first-order and second-order moments for statistical benchmark, also squeezing effects under the same noise contribution will be explored. To test this, most simplest case of a polarization state in the form of single-photon polarization is used,

$$|\psi\rangle \;=\; \cos\theta\, |1\rangle \otimes |0\rangle \;+\; e^{i\phi} \sin\theta\, |0\rangle \otimes |1\rangle\,. \tag{7.6.4}$$

An arbitrary single-photon polarization state with θ parameter is beneficial in the sense of manipulating any polarization state on the Poincaré sphere. In shorthand, the application of linear and nonlinear squeezing operators within the noise model provides simplified expressions for expectation values for the single photon state,

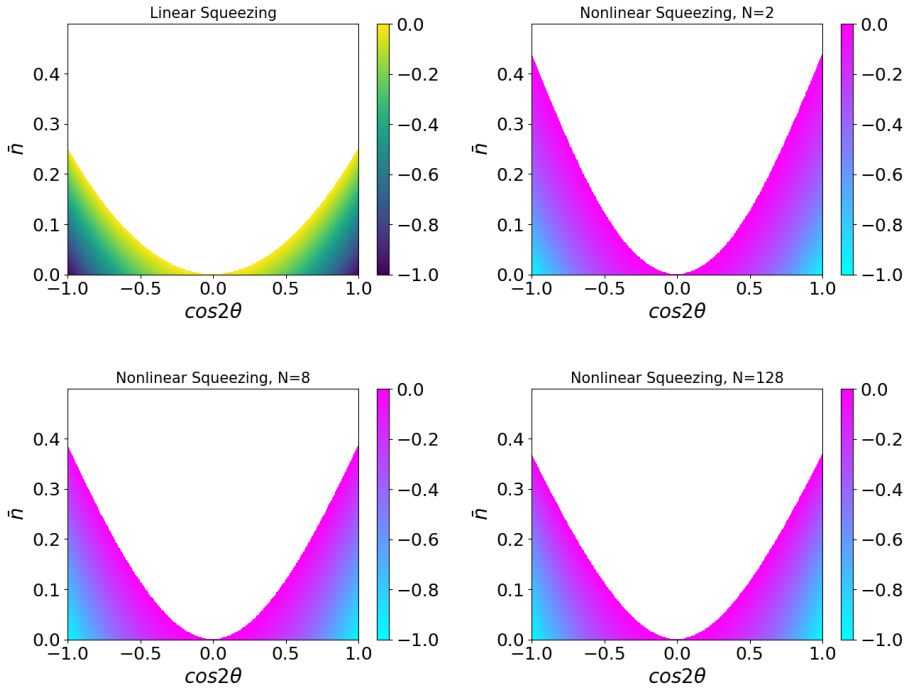

Figure 7.6.1: Certifying linear and nonlinear squeezing in the form of negativity for the second-order moments of the corresponding operator for a single photon polarization state. A two-dimensional plot for the variance is parameterized by thermal noise with mean photon number $\bar{n}$ and $\cos 2\theta$. Note that only negativity of variances is plotted in all cases to highlight the bounds with respect to the parameters. In the linear case, noise resilience is bounded at $\bar{n} = 0.25$. Nonlinear measurement schemes for different detection bins ($N = 2$, $N = 8$, $N = 128$) accommodate more noise in the system but still promise non-classical probing.

and directly writes down the form here,

$$\langle : \hat{S}_L : \rangle_{\bar{n}} = \cos 2\theta \quad , \quad \langle : \hat{S}_L^2 : \rangle_{\bar{n}} = 4\bar{n} \ , \tag{7.6.5a}$$

$$\langle : \hat{S}_{NL} : \rangle_{\bar{n}} = \frac{\cos 2\theta}{(1 + \bar{n}/N)^2} \quad , \tag{7.6.5b}$$

$$\langle : \hat{S}_{NL}^2 : \rangle_{\bar{n}} = \frac{2N(N + 2\bar{n} - 1)}{(1 + 2\bar{n}/N)^2} - \frac{2N(N + \bar{n} - 1)}{(1 + \bar{n}/N)^3} \ , \tag{7.6.5c}$$

normally ordered second order moment of linear Stokes operator $\langle : (\Delta \hat{S}_L)^2 : \rangle = 4\bar{n} - \cos^2\theta$ shows negativities when $\bar{n} < (\cos^2 2\theta)/4$, a signatures for linear squeezing. In contrast, the variance of the nonlinear operator depends on both $\cos^2 2\theta$ and the number of click detectors from Eq. (7.6.5b) and Eq. (7.6.5c). Variances for two

schemes are then extracted for different noise backgrounds and $\cos 2\theta$ values and plotted in Fig. 7.6.1.

In theory, we compared linear and nonlinear scheme squeezing performance with different noise contributions. Nonlinear squeezing persists for higher noise contributions $\bar{n}$ than possible for its linear counterpart, excluding $\cos 2\theta = 0$. For the case, $\cos 2\theta = \pm 1$, the noise level is bounded by $\bar{n} = 0.25$ for the linear case while the threshold is at ≈ 0.385 for the nonlinear scenario. This shows an improvement of more than 54% for the depicted N = 8 click detection bins. The effect is then further examined for $N = 2$ and $N = 128$ detection bins, resulting in 75% and 47% increased noise robustness for the respective multiplexing schemes. More than 50% improvements in detecting squeezing even with a small number of multiplexing bins, make the nonlinear approach a promising route to extract signal information from noise. From the above example, it is interesting to notice that the measurement strategy for a single photon state with specific noise ($\bar{n}$) background is more lean to observe nonlinear squeezing rather than linear squeezing. In the realm of nonlinear squeezing operators, it would be interesting to investigate squeezing effects on other types of quantum light states and different degrees of freedom further. This specifically motivates one to apply the nonlinear squeezing effects to the benefits of quantum metrology applications.

Summary

The idea of "beyond two-photon correlation from a polarization entangled Bell source" is realized here with an engineered PDC source. High mean photon number output state from these sources demands "a genuine quantum detector featuring photon number resolving capabilities" for state characterization. With the help of a time multiplexed on-off detector system and binomial click counting theory, we formulate a nonlinear measurement operator for Stokes observables. Experiments show that nonclassical correlation can be detected with the best precision with this nonlinear operator, demonstrating direct observation of nonlinear polarization squeezing from a bright squeezer sandwiched Sagnac source. Moreover, we insist that photon number resolved measurements are ideal for an in-depth classification of the few photon optical states and their applications.

Chapter 8

Conclusion and Outlook

8.1 Conclusion

The motivation to introduce time-multiplexing methods on non-classical light generation and detection with a special focus on multiphoton entanglement and quantum squeezing are experimentally investigated and interesting results are detailed in the thesis. Light emission as a true quantum effect, spontaneous parametric fluorescence properties of a second order nonlinear waveguide material is engineered by adjusting waveguide properties and optical excitation field. Consequently, quantum light generation and detection in the form of a pair of photons and heralded single photons are demonstrated with high quality. Next, a type II phase-matched integrated waveguide source is placed inside a Sagnac interferometer for generating polarization-entangled photon pairs, the first-ever demonstration of its kind. Our source then swiftly tackled the long-standing fundamental efficiency trade-off limits of its bulk-crystal-type entangled setups.

The idea of source multiplexing is then implemented to address multiple entangled photon pairs in time from a single source. A quantum memory allows storage of entanglement and quantum interference between these consecutive time bins addressed entangled pairs for higher-order photonic entanglement generation. Multi-photon polarization-entangled states are experimentally generated, detected, and characterized for a high count rate with high-quality entanglement. We further studied the multiphoton effect on the Sagnac entanglement source by exploiting the bright squeezed nature of waveguide SPDC in the strong pump regime with photon number resolved measurements. This experiment is motivated and supported by the theory of click counting and detector multiplexing. We used click moments to detect non-classicality in our bright Sagnac source. The corresponding photon number measurement operator takes the form of a nonlinear functional form of quantum observable and an experimental observation of nonlinear squeezing is reported with high precision. We report that our non-linear operators surpass linear measurement strategy when we have considerable noise in the background of the quantum signal that we are interested in. In the following para-

graphs, I will give a glimpse of experimental figures of merits from different projects.

Single photon source to entangled photon pair source

A single-device platform for single and multiphoton quantum light is envisaged by exploiting type II SPDC on a periodically poled KTP waveguide structure. Strong light confinement in this single spatial mode micro-structure offers efficient nonlinear interaction and shows bright correlated light emissions in two polarization modes. Photon click events on the two modes are recorded with highly efficient superconducting nano-wire detectors for an actual count rate of above 1 MHz with 1 mW coupled pump power. On average 40% of the time coincidence events are recorded from the source, which contributes to heralded single photon state generation and, consequently the detection of genuine non-Gaussian state of light. The much demanding spectrally pure single-photon states are prepared by engineering the pump spectral properties and phase-matching properties of the nonlinear material. Theoretical simulations are performed on the available waveguide parameters and pump width selection, predicting above 80% spectral purity for the photonic state, which is verified in our time of flight spectrometer experiment with $> 97.5\%$ purity. The discrepancy in the purity values or the relatively high experimental spectral purity is credited to the broadband spectral filtering part in the experiment, where the unwanted *sinc* phasematching side-lobes are removed without any disturbance on the central spectrum and overall quantum light brightness. Therefore our nonlinear waveguide incorporated light source generates a highly pure spectrally decorrelated heralded single photon state. Non-classical photon statistics nature of the light source are manifested by quantum correlation, $g^2(0)$ measurements. We observe heralded $g^2(0) < 1$ value well below the classical bound, indicating the non-classical signature effect of *anti-bunching*. Hong-Ou-Mandel effect, a celebrated two-photon interference experiment reveals that a pair of photons emitted from the waveguide source are highly degenerate. The indistinguishable nature of signal and idler photons delivers 93% quantum interference visibility in the HOM experiment.

We have tested many waveguides at the early stages of the project and found reproducible results for spectrally decorrelated, quantum light sources on multiple waveguides. We chose the best waveguide SPDC sample to devise an entanglement source, by sandwiching the same type II SPDC waveguide source inside the Sagnac model interferometer. Our unique integrated waveguide source overcomes the *fundamental* limitations imposed by the traditional bulk crystal-based single or entanglement source, onto a pure *technical* limitation. Traditional SPDC sources have the problem of brightness versus Klyshko efficiency tradeoff governed by the tight or weak optical beam focusing conditions inside the bulk crystal structure.

But in a waveguide source brightness and Klyshko efficiencies technically depend on the free-space or fiber coupling efficiencies from the pump side and signal/idler collection modes respectively. Maximizing the coupling efficiencies maximizes the overall performance of our unique source. We went on assembling the Sagnac source for generating a polarization-entangled photon pair source by considering only the first-order photon pair generation probability component from the SPDC Hamiltonian. The final device produced good quality maximally entangled photonic state in polarization, $|\psi\rangle = \frac{1}{\sqrt{2}}\big(|H_1V_2\rangle + e^{i\phi}\,|V_1H_2\rangle\big)$. Phase ($e^{i\phi}$) in the setup can be tuned to swap the state between two maximally entangled states $|\psi_\pm\rangle = \frac{1}{\sqrt{2}}\big(|H_1V_2\rangle \pm |V_1H_2\rangle\big)$. Source characterization was done with over 60000/s entangled photon coincidence events followed by an entanglement visibility test and quantum state fidelity estimation. Standard entanglement visibility measurements on the rectilinear and diagonal bases reveal interference visibility of $> 95\%$, which ensures genuine entanglement from the source. Finally state density matrix $\hat{\rho}$ is obtained from complete two-qubit polarization tomographic measurements and maximum likelihood reconstruction methods. Observed experimental data and estimate shows state fidelity of $F = \langle\psi_-|\,\hat{\rho}\,|\psi_-\rangle = (95.78 \pm 0.04)\%$ and tangle value 0.842 ± 0.1. In this project, we report a new type of highly efficient entangled photon source and also observed genuine two-qubit polarization entanglement with the best available precision.

Two photons entangled to too many photons entangled

In the second chapter, we try to exploit the time bin degree of freedom to entangle multiple photons originating from a single source in a resource-efficient manner. Instead of having multiple photon sources, we chose many photons emitted from a single source in multiple time bins. Our quest for time-multiplexed multiphoton entanglement generation protocol requires spectrally decorrelated photons and a single efficient Bell state source. Both requirements are achieved in the first chapter of this thesis. From the hardware side, additionally, I need a quantum memory to store and interfere multiple photons emitted back to back from the single emitter. We realized an all-optical polarization insensitive memory to address consecutive Bell pairs from a single source using the feed-forward technique. Quantum memory is capable of storing single or entangled qubits (also quantum superposition) and keeping the state coherence for long storage time for any kind of quantum operations. Together with a fast electro-optic polarization switch, quantum memory is capable of implementing interference operation between two more photons. We combine these two operations (store and interfere) in different sequences and demonstrate the entanglement of up to six photons with a high count rate. In principle, different

graph states or entangled states can be prepared using our proposed device, which depends on the type of unitary operation inside the memory. As a demonstration, we performed GHZ-type multiphoton graph state implementation with a single active optical switch within the memory.

All optical memory is realized as a free space optical loop with linear optical elements and one high-speed active polarization switch to implement high-speed unitary operations on photons. The loop is designed to match the repetition rate of the laser so that subsequent entangled photons can be interfered with in a timely manner. Loop has a total transmission efficiency of $\approx 92\%$, enabling the storage of polarization superposition states for more than 1 μs with considerable quantum coherence. The single qubit storage experiment shows the incredible stability of our setup to keep the polarization qubit with fidelity of above 82% for more than 1 μs of time. The more decoherence-prone entanglement storage is reported for the first time up to 1 μs, where the retrieved state shows above 60% fidelity. Importantly only 330 ns is required to consider 25 pump pulses from the pump laser, which means during 25 pump pulses we can look for the required number of Bell states for multiphoton state generation using feed-forward. For 330 ns storage time retrieved Bell state fidelity drops only 4% from 95% to 91%, promising high-quality multi-photon photon entanglement after interference. The actual power of multiplexing opens up when we consider N number of Bell pairs from M pump pulses with $M >> N$. In this regime, we theoretically showed that the feedforward-based time multiplexing approach surpasses all existing multiphoton generation protocols with exponential advantage. On experimental demonstration, we chose $N = 2,\ 3$ Bell pairs, and M pump pulses for four-photon ($M = 21$) and six-photon ($M = 22$) GHZ entanglement generation. To understand the rate scaling behavior we repeated the experiment from the lowest possible multiplexing to a maximum of $M = 22$ pump pulse sequence. This shows a 9-fold increase in the four-photon GHZ rate and a 35-fold rate increase in the six-photon GHZ experiment, underpinning our theoretical prediction with close resemblance. For a specific pump power choice the four-photon experiment delivered more than 1000 four-folds per second and 1.5 six-fold events per second with the multiplexing setting $M = 22$. Furthermore, on every multiplexing case ($M = 2$ to 22) corresponding state fidelities are also reported for both GHZ states. In all cases generated multi-photon state shows above 50% state fidelity, signature bound for genuine multiphoton entanglement. We obtained a maximum fidelity of 81% for the four-photon GHZ state on the nearest case multiplexing and above 60% fidelity for the largest non-nearest pump pulse case ($N = 21$). Six photon GHZ nearest case source multiplexing shows a maximum of 65% fidelity and for all other higher numbers of multiplexing (up to $N = 22$)

our system delivered above 60% state fidelity. As an application, we used our device to test a new proposal on quantum network topology certification protocol, where network participants can identify the topology of the network from fidelity estimates without any prior information about the network model or distributed state. In our experiment, different separable and non-separable six-photon states or instances of different topology are prepared by simply programming the quantum memory sequence. Finally, these different topologies are efficiently identified by the network participants by analyzing the fidelity measurement data without any prior information revealed to those participants.

Non-linear operator to Non-linear squeezing

The motivation to investigate multiphoton emission effects from a Sagnac polarization entanglement source brought up the direct observation of non-linear squeezing in our experimental setup and the results are reported in the final chapter. We intentionally pump the Sagnac source to generate bright squeezed light from both directions and evaluate higher-order multiphoton interference contribution out of the source. In this pump regime, Sagnac will generate macroscopic polarization entanglement expecting more than a two-photon contribution to the output state. Photon number resolved measurements are implemented on the final output state to detect non-classical correlations from the same source. Which uses a resource-efficient time multiplexed photon number detection unit built from low-loss fibers in combination with beam splitters.

Since our measurements involve polarization and photon number statistics, detector multiplexing-based photon counting theory is developed to analyze any bright optical state with a high mean photon number. Our theory results in a nonlinear functional of the relevant Stokes measurement operator, which incorporates photon number correlation from two polarization modes. Expectation values of moments of nonlinear operators validate non-negative values for classical optical states and negative values for nonclassical states. We carried out non-Gaussian measurements on our experimental scheme and detected the first-ever nonlinear squeezing effect from a light source. High gain polarization entanglement source shows multiphoton coincidence up to six-folds and quadrature squeezing of around 3.3 dB. A resource-efficient time multiplexed detector unit is used to measure photon numbers up to eight photons. Non-linear Stokes measurement was carried out on different macroscopic Bell state settings ($|\psi_{\pm}\rangle$, and corresponding nonclassical moments are reconstructed for different measurement basis settings. Non-classical negativities from the measurements are reported with the best precision ($\pm 15\sigma$ error margin), fitting the experimental data with theoretical predictions. The ability to resolve eight photons

from the detector also renders reconstruction of higher order moment up to 8^{th} order and corresponding negativity up to 8^{th} order is obtained from the experimental data. We then further investigated the effect of background noise on nonclassicality detection both in the linear and nonlinear operator approach. This reveals that our nonlinear Stokes-operator formalism has a significantly increased robustness against noise, rendering it possible to detect nonlinear polarization squeezing even when linear squeezing fails.

8.2 Outlook

Until now we were discussing engineering quantum light sources to generate multiphoton correlations and detection. Now I will discuss more about what we can do or achieve beyond the current status. I certainly want to improve the quality and efficiency of the experimental approach to reach better figures of merits both on the setup and results. Apart from this, I would like to point out some potential applications of our implementations. Furthermore, the importance of applying new quantum light sources, detection schemes, and theoretical methods in fundamental tests.

Spectrally engineered decorrelated sources are prime candidates for optical quantum computing applications where indistinguishable photons are interfered on larger scale unitary networks. Our PPKTP-based high-purity quantum source is certainly the best fit for Gaussian boson sampling type experiments where one wants to interfere bright squeezed light on a photonic circuit. We already demonstrated above 97% spectral purity for our photons this can be pushed to 99% or near ideal case with careful engineering of the source parameters. Demonstration of the waveguide approach outperformed the bulk approach with high nonlinear confinement and bright quantum light will reduce the experimental run time by providing more count rate in a short time interval. Currently, we are using broad-band spectral filtering to select only the central lobe of the *sinc* joint spectral amplitude. Even though it won't affect much on the source brightness part of the nonlinear conversion is still distributed on the side-lobes also affecting the spectral purity. This problem can be circumvented by special poling patterns to possess different phase-matching shapes, for example, a Gaussian profile type poling can provide a perfect circular joint spectral distribution for our pump bandwidth choice and, consequently ideal purity without filtering. The discrepancy in the signal-idler indistinguishability, therefore moderately less two-photon interference visibility (95%) is essentially an outcome of the non-ideal phasematching angle in the JSA. This requires an in-

depth analysis of the phase-matching properties of the crystal and one route to reach near-optimal phase-matching angle is by shaping the pump spatial profile within the waveguide structure. The more the signal-idler states are indistinguishable the more their interference quality is for different applications like generation of single-mode squeezed light from TMSV, multiphoton interference experiments, entangled photon generation, etc.

Every bit of increase in spectral purity also improves our time multiplexed entanglement generation experiment. Since it specifically depends on two-photon interference of the consecutive time bin photons, it's possible to attain a higher interference value when the photons acquire higher spectral purity and distinguishability. Consequently, more and more photons can be interfered to generate larger entangled states. For system scalability, another main concern is optical losses in the system. Currently, we are limited to 40% heralding efficiency from the source. This can be improved by efficient fiber coupling (currently 80%), one can also find even better optical components and also reduction of optical elements in the setup to reduce the transmission losses. Any improvement from coupling and transmission losses will have a striking difference in overall 'x-fold' events and entanglement size. With these modifications, we foresee a near-time experiment to demonstrate ten-photon GHZ entanglement. One of the key proposals is the replacement of a probabilistic photon pair source with a deterministic one, with our current loop efficiency we believe that it's possible to entangle up to 20 photons without any changes on the loop side. Synchronizing multiple sources with a single loop memory is another possible direction but this requires valuable effort from the technical and electronic side. We are also thinking of advancing the loop-based multiplexing with multiple active switches, so that one can generate different entangled graph states, for eg. cluster states for optical quantum computing experiments. This protocol requires switches that can do arbitrary unitary operations on the incoming or stored photons to reach the desired graph structure. In future loop memory can be actively stabilized for compensating environmental disturbances, and timing jitters which can improve interference visibility and overall entanglement state fidelity. With all these modifications we expect more number of photons, different types of graph states, better rates, and state fidelity from a time-multiplexed approach. An interesting application, quantum network certification is already demonstrated in this thesis by demonstrating the device's flexibility to generate different optical states without any change in the experimental setup. We further planning to implement time multiplexed sources in quantum cryptographic protocol experiments to bring advantage in number of participating network users and bit rate. The ability to generate quantum light in the telecom range is a major advantage to connect the

same source with the existing classical network.

I have demonstrated an efficient polarization squeezed light source and a new nonlinear measurement approach with bright squeezed light in the last chapter. This brings up the idea of applying similar sources and techniques in quantum metrology applications. Subshot-noise-type non-classical behavior can be brought up with these sources for polarization-sensitive and photon number-sensitive measurements. This will find major application in imaging, spectroscopy, and other precision measurement required areas where one will use few photons or bright squeezed light as the quantum probe. I already mentioned efficient two-mode squeezers are an important resource for Gaussian boson samplers, especially with a good amount of squeezing. As an immediate application, we are trying to apply the same source and measurement strategy on a spectroscopic experimental scheme to demonstrate quantum advantage. At the moment we are dealing with low squeezing specifically because of losses and less pump coupling. Efforts are going on to reduce the losses in the setup and couple more pump power into the waveguide which can produce higher squeezing. Higher squeezing can increase the signal-to-noise ratio in metrology experiments, consequently promising quantum advantage for a realistic application. The non-linear operator-based measurement approach is more general and applicable to any wavelength and experimental platform. Moreover, we want to experimentally demonstrate its noise resilience capability against linear quantum measurement strategy, which is a theoretical finding we reported in this thesis. From the detection side TMD bin size can be scaled for a larger photonic state (number of photons >100), to count more photons with highly efficient telecom resources. The ability to resolve higher photon numbers finds its application to genuinely distinguish macroscopic classical-quantum light boundary and transition with very high mean photon numbers.

Chapter 9

Acknowledgements

Finally, I would like to thank all the great people who supported me in doing research in such an amazing scientific environment.

First of all, I would like to thank Prof. Christine Silberhorn for giving me the opportunity to work in her research group and lab facilities, 'honestly, I enjoyed working under your guidance'. She gave me enough freedom to do different projects and motivated me with friendly great discussion sessions. As a person who runs a research group of more than fifty pupils, I admire her scientific ability and time management.

Thanks to two amazing persons, Evan and Jan, I have immense gratitude for both of you.
Dr. Evan Meyer-scott a brilliant physicist, introduced me to the group and the research topic. He always helped me to survive in a complex experimental physics platform, thanks for the great discussions.

Prof. Jan Sperling patiently listens to my stupid 'quantum' doubts and corrects me with in-depth details. Our discussions always end up with new project ideas- always an inspiration for me to ask more and more questions. I always want to catch him in his 'coffee time' to discuss more quantum physics ideas.

Many thanks to our wonderful research collaborators and intriguing projects. I had a great opportunity to interact with some of the pioneers of theoretical quantum physics, Prof. Otfried Gühne and University of Siegen theoretical quantum information group members (Lisa, Sophia, and Kiara), Prof. Martin B Plenio and Dr. Ish Dhand from Ulm University, Prof. Luis Lorenzo Sanchez-Soto from Universidad Complutense de Madrid and Dr. Yong Siah Teo from Seoul National University, Dr. Laura Ares from Paderborn University.

Thanks to all my IQO members, for your support and help. I have had a chance to share time with a great deal of smart minds at IQO. Thank you, Benni,

for your expert opinions. Thank you, Laura, Michael, and Christof for all the group events and friendly get-together arrangements.
I had the privilege to share lab activities with a bunch of great researchers, Evan, Johannes, Syam, Melanie, Lennart, Sonja, Thomas, Federico, Philip, Patrick, Abhinandhan, and Jonas. Thanks to the quantum network team (Laura, Fabian, Franz, Jano, and Dana) for the amazing physics discussions and chit-chats. Thanks to Kai, Abhinadhan, and René for our little chats on the P8 corridors. Thank you, Sebastian, Ankita, Werner, Matteo, Felix, and Vahid for sharing the office space and helping me with little scientific and nonscientific things. Thanks to the Technology team (Christof, Viktor, and Raimund) for all the optical coating work on the samples.

My delayed responses always made the IQO administration team to send multiple reminder emails on administration-related matters. I would like to thank Rita, Petra, and Nadine for their immense help in resolving all the academic and non-academic paperwork.

Once again thank you Evan and Jan for doing a quick thesis proofreading.

I thank the European Union (QuPoPCoRN) and the University of Paderborn for funding my research activities.

I would like to thank my family and friends for their support in doing science.

Finally but foremost, I would like to sincerely thank my wonderful wife Raghna for her support and love. Your criticisms and motivations were influential in finishing this write-up.

Appendix A

List of Scientific Contributions

A.1 Publications

(1) **High-performance source of spectrally pure, polarization entangled photon pairs based on hybrid integrated-bulk optics**
Evan Meyer-Scott, Nidhin Prasannan, Christof Eigner, Viktor Quiring, John M. Donohue, Sonja Barkhofen, and Christine Silberhorn
Optics Express Vol. 26, Issue 25, pp. 32475-32490 (2018).

(2) **Experimental entanglement characterization of two-rebit states**
Nidhin Prasannan, Syamsundar De, Sonja Barkhofen, Benjamin Brecht, Christine Silberhorn, and Jan Sperling
Phys. Rev. A 103, L040402 (2021).

(3) **Scalable Generation of Multiphoton Entangled States by Active Feed-Forward and Multiplexing**
Evan Meyer-Scott, Nidhin Prasannan, Ish Dhand, Christof Eigner, Viktor Quiring, Sonja Barkhofen, Benjamin Brecht, Martin B. Plenio, and Christine Silberhorn
Phys. Rev. Lett. 129, 150501 (2022)

(4) **Direct Measurement of Higher-Order Nonlinear Polarization Squeezing**
Nidhin Prasannan, Jan Sperling, Benjamin Brecht, and Christine Silberhorn
Phys. Rev. Lett. 129, 263601 (2022)

(5) **Certifying the Topology of Quantum Networks: Theory and Experiment**
Lisa T. Weinbrenner, Nidhin Prasannan, Kiara Hansenne, Sophia Denker, Jan Sperling, Benjamin Brecht, Christine Silberhorn, and Otfried Gühne
Phys. Rev. Lett. 132, 240802 (2024)

(6) **Evidence-Based Certification of Quantum Dimensions**
Y.S. Teo, S.U. Shringarpure, H. Jeong, N. Prasannan, B. Brecht, C. Silberhorn,

M. Evans, D. Mogilevtsev, and L.L. Sánchez-Soto
Phys. Rev. Lett. 133, 050204 (2024)

(7) **Photonic Entanglement and Polarization Nonclassicality: Two Manifestations, One Nature**
Laura Ares, Nidhin Prasannan, Elizabeth Agudelo, Alfredo Luis, Benjamin Brecht, Christine Silberhorn, Jan Sperling
arXiv:2407.07477 (2024)

(8) **Direct reconstruction of polarization phase space of quantum light**
Nidhin Prasannan, Syamsundar De, Benjamin Brecht, Christine Silberhorn, and Jan Sperling
manuscript in preparation

A.2 Conferences

(1) **Multi-photon Entanglement via Quantum Interference Buffering**
Nidhin Prasannan, Evan Meyer-Scott, Ish Dhand, Christof Eigner, Viktor Quiring, Sonja Barkhofen, Benjamin Brecht, Martin B Plenio, and Christine Silberhorn
DPG Fall meeting Freiburg (2019)

(2) **Scalable Generation of Multiphoton Entanglement**
Nidhin Prasannan, Evan Meyer-Scott, Ish Dhand, Christof Eigner, Viktor Quiring, Sonja Barkhofen, Benjamin Brecht, Martin B Plenio, and Christine Silberhorn
GDR IQFA Colloquium Paris (2022)

Appendix B

Handling time bin clicks - GHZ experiment

B.0.1 GHZ Time bin detection

The feed-forward approach is a golden scheme to implement 'signal gating' techniques to avoid false 'photon clicks' and provide experimental data with minimal errors. This has been already demonstrated in our previous single qubit, entangled qubit, and HOM dip experiments. As explained, the key benefit is the ability to generate multiple FPGA signals from the herald click information, which simultaneously controls memory operation and time tagger-based data collection. But in any case, state generation (GHZ experiment) or state detection (polarization squeezing), one of the most intriguing tasks in a time bin multiplexed experimental platform is implementing efficient data collection and processing subroutines or algorithms. In a spatial situation, N photons are distributed to N detectors, coincidences from N detectors are a straightforward task for commercial time tagging modules. In contrast, the TM scheme allows state-size independent click detection with a fixed number of detectors. In the squeezed light source experiment we were interested in resolving the number of photons from a single pulse, but in the GHZ experiment the situation is slightly different because its source multiplexing instead of photon number. To be precise we want to address every entangled 'photon pairs' at different time bins.

GHZ experiment uses four detectors, two for polarization resolved heralding unit and two for polarization resolved loop side. Which makes them a complete unit for polarization tomographic measurements with waveplate settings. But the same four detectors collect subsequent photon pair clicks after the multiphoton state generation protocol by the storage loop. So 4, 6, and 8-photon experiments use the same number of detectors. Therefore an efficient coincidence counting function to count consecutive time bin photons is necessary. To do this, once again FPGA 'ON-OFF' signals are used as gate signals for both herald and loop photons. For a photon experimental situation an 'ON' signal is generated upon the detection of the first herald and an 'OFF' signal is generated for the second herald. Moreover, in the

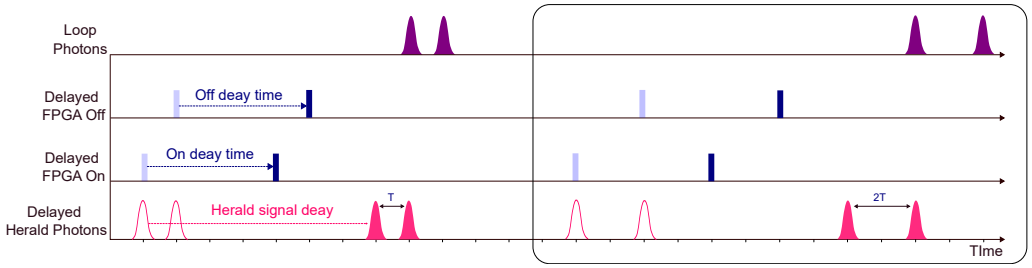

Figure B.0.1: Illustrating the delay channels in the time tagger for photon clicks and FPGA signals with arbitrary time stamps. Blank pulse modes and dim bars represent the actual arrival time of the heralds and FPGA signals. But these signals are then delayed to bring FPGA signals in first hand followed by photon clicks. The unboxed part shows the example of a four-photon click pattern for the two nearest entangled pairs while the boxed part is for the non-nearest case. It's important to mention that While making these delay adjustments one should take care of both source multiplexing time size ($M \times rep - time$) and delay time length to avoid mixing of signal bins.

state generation part, the second herald signal initiates the interference operation followed by the release of two buffer photons one after the other in consecutive time bins. This motivates us to use the OFF signal to gate the two loop photons, both ON and OFF triggers for the herald photons gating. Rest is done by the dedicated time tagger built-in functions. Which post-process the gated bins to count the clicks for corresponding n-fold events. The basic idea is again to construct delayed virtual channels on the time tagger to accommodate user-defined delays to compensate time difference between different signals (herald and loop photon click signals). Also, delays for FPGA signals are adjusted in such a way that ON and OFF signals arrive earlier than photon click signals. This is important because gating signals are generated from FPGA signals. An example signal pattern style is given in Fig. B.0.1.

For a four-photon experiment, two herald signals are generated from two entangled photon pairs. First herald clicks generate an ON signal from FPGA to store the partner in the loop, second herald initiates a four-photon GHZ state generation process. But note that the second herald signal is dynamically distributed between '$M-1$' source bins (referring to Fig. 6.4.6) making that actual click bin position probabilistic. FPGA OFF signal derived from the second herald is then useful to place gates around both loop photons. Because this initiates interference and consecutive release of both photons one after the other. To gate the herald clicks one needs both ON and OFF signals. Addressing each four-photon event requires efficient click bin data array processing. This is done by time-synchronized subroutines

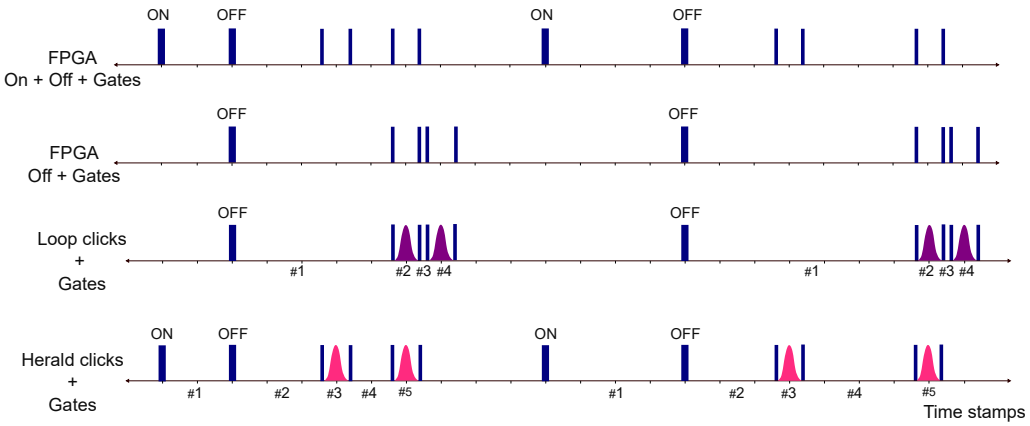

Figure B.0.2: Gated time bin array model for herald and loop photons. In this example, the time bin array of two four-photon events is specified for explanatory reasons. If we consider the marks on the axis line as pump pulse intervals then two non-nearest Bell pairs are generated at different times. On the top two timelines (bin array) FPGA signals and derived gate bins are placed at respective positions. In an ideal case combining the second timeline axis with the loop photon click channel provides complete loop photon events for the whole experimental run time. Similarly combining the first timeline axis with the herald signal channel gives us herald clicks. These two combined channels are provided in 3^{rd} and 4^{th} as time bin arrays. But losses in the system and failed INTERFERENCE operation can result in partially filled or empty bins in between the runs. This will be accounted for in the repeated CBM counting procedure, only those events where four-photon clicks occurred will constitute a GHZ state, rest is discarded or useful to study loss effects on multipartite entanglement generation.

available in the time-tagger software package. which are COMBINER and COUNTBETWEENMARKERS(CBM) operations. A combiner operation combines multiple virtual channels and provides a single array of click data at respective time stamps and CBM functions are useful to count particular events in an array of data in a user-specified manner. We then combine the Off signal channel and loop click channel from the time-tagger to get a single array of FPGA OFF + loop photon clicks. Similarly, FPGA ON + FPGA OFF + herald photon clicks array to address the herald photons. While generating an FPGA signal array we additionally create gating window bins on the actual signal photon click's expected positions using a custom-built python script. These (expected) click positions can be identified beforehand using time-tagger-based histogram measurements[1]. The combined final time bin data array for both herald and loop photon case is given in Fig. B.0.2. CountBe-

[1]this is only to identify the click position through histograms, but histogram itself is not a good method for direct time bin multiplexed data collection. A dynamic, continuous, long-term GHZ data acquisition requires gating and processing

tweenMarker subroutine from the time tagger is then called for counting the clicks only from the gated window with start-stop fashion and repeatedly count from a single long bin array which we generated through long measurement time. Note that in Fig. B.0.2 herald or loop photons fall in the repeated bin interval number. Specifying the window number on the CBM function parameters picks only events from this particular window repeatedly and accounts for four-fold coincidence over the accumulation time. For six photons and above this procedure becomes iterative. Where multiple ON-OFF signal contributions are used to collect the six or eightfold events. Every herald generates feed-forward electronic FPGA signals, but not all of them contribute GHZ state. If we already consider the intrinsic 50% post-selection probability, interference operation failure and losses in the system can attribute unfilled gate windows within the array. Which will be simply discarded during the counting subroutine and does not produce a GHZ event.

Appendix C

Non-linear polarization squeezing - Theoretical modeling

C.0.1 Phase space model for TMSV and Sagnac source

Two-mode squeezed states in terms of photon number can be expressed as,

$$|\lambda\rangle \;=\; \sqrt{1-|\lambda|^2}\sum_{n=0}^{\infty}\lambda^n\,|n,n\rangle\,. \tag{C.0.1}$$

We use Glauber–Sudarshan quasi probabilistic P-function formalism to deal with phase space modeling of our light source. Therefore it's convenient to represent Fock states in a coherent state basis.

$$\begin{aligned} |n\rangle &= \frac{\hat{a}^{\dagger n}}{\sqrt{n!}}\,|0\rangle\,, \\ \text{also}\quad \hat{a}^{\dagger n}\,|\alpha\rangle \;&=\; e^{-\frac{|\alpha|^2}{2}}\partial_\alpha^n\Big(e^{\frac{|\alpha|^2}{2}}\,|\alpha\rangle\Big). \end{aligned} \tag{C.0.2}$$

Equation C.0.2 is useful to switch between Fock to coherent state basis and vice-versa by assuming $\alpha = 0$. Which is also useful to construct density matrix form for TMSV in C.0.1.

$$|m\rangle\langle n| = \frac{1}{\sqrt{m!n!}}\,e^{-|\alpha|^2}\,\partial_\alpha^m\,\partial_{\alpha^*}^n\,\Big(e^{|\alpha|^2}\,|\alpha\rangle\langle\alpha|\Big)\Big|_{\alpha=0}, \tag{C.0.3}$$

$$|\lambda\rangle\langle\lambda| = \sum_{m,n=0}^{\infty}\int \mathrm{d}^2\alpha\;\mathrm{d}^2\beta\;(1-|\lambda|^2)\,\lambda^m\,\lambda^{*n}\,\delta(\alpha)\,\delta(\beta)$$

$$\times\,\frac{e^{-|\alpha|^2-|\beta|^2}}{m!n!}\partial_\alpha^m\partial_{\alpha*}^n\partial_\beta^m\partial_{\beta*}^n\Big(e^{|\alpha|^2+|\beta|^2}\,|\alpha,\beta\rangle\langle\alpha,\beta|\Big), \tag{C.0.4a}$$

$$|\lambda\rangle\langle\lambda| = \int \mathrm{d}^2\alpha\;\mathrm{d}^2\beta\;P_\lambda(\alpha,\beta)\;|\alpha,\beta\rangle\langle\alpha,\beta|\,, \tag{C.0.4b}$$

where $P_\lambda(\alpha,\beta) = e^{|\alpha|^2+|\beta|^2}\ \exp[\lambda\partial_\alpha\partial_\beta + \lambda^*\partial_{\alpha^*}\partial_{\beta^*}] \times e^{-|\alpha|^2-|\beta|^2}\ \delta(\alpha)\ \delta(\beta)$. We use this semi-classical picture to explain the optical light modes emitting from the Sagnac arrangement. Let $|\alpha,\beta,\gamma,\delta\rangle$ represent four modes (coming from the two TMSV modes) produced by the bidirectional pumping of the source. Clockwise pump generate $|\alpha,\beta\rangle$ modes with α as horizontal(signal) polarization and β as vertical(idler) polarization. Where γ and δ respective signal-H and idler-V modes for anti-clockwise pump generated fields. We use Fig. 7.4.1 as the reference for propagation modes and directions. Signal and idler modes generated by the clockwise pump are polarization swapped by the HWP in the path leading to $|\alpha,\beta,\delta,\gamma\rangle$. Sagnac PBS then shuffles the polarization from different propagation modes making the state $|\alpha,\gamma,\delta,\beta\rangle$. Finally, the first and last two modes are directed towards the A and B detection side. Phase controller in arm A imparts relative phase to the state and becomes $\left|\alpha,\gamma e^{i\phi},\delta,\beta\right\rangle$. The optical state out of the Sagnac then can be written as,

$$\hat{\rho} = \int \mathrm{d}^2\alpha\,\mathrm{d}^2\beta\,\mathrm{d}^2\gamma\,\mathrm{d}^2\delta\ P_\lambda(\alpha,\beta)\,P_\lambda(\gamma,\delta)\ \left|\alpha,\gamma e^{i\phi},\delta,\beta\right\rangle\left\langle\alpha,\gamma e^{i\phi},\delta,\beta\right|, \tag{C.0.5a}$$

$$= \int \mathrm{d}^2\alpha'\,\mathrm{d}^2\beta'\,\mathrm{d}^2\gamma'\,\mathrm{d}^2\delta'\ P_\lambda(\alpha',\delta')\,P_\lambda(\beta' e^{-i\phi},\gamma')\,|\alpha',\beta',\gamma',\delta'\rangle\,\langle\alpha',\beta',\gamma',\delta'|\,, \tag{C.0.5b}$$

$$= (1-|\lambda|^2)^2 \sum_{m_1,n_1,m_2,n_2=0}^{\infty} \lambda^{m_1}\lambda^{*n_1}(\lambda e^{i\phi})^{m_2}(\lambda e^{i\phi})^{*n_2}\,|m_1,m_2,m_2,n_1\rangle\,\langle n_1,n_2,n_2,n_1|\,. \tag{C.0.5c}$$

In our squeezing chapter, we have directly written the pure state form of the above equation,

$$|\psi\rangle = (1-|\lambda|^2)\sum_{m,n=0}^{\infty}\lambda^m(\lambda e^{i\phi})^n\,|m,n,n,m\rangle\,. \tag{C.0.6}$$

C.0.2 Click counting on macroscopic Bell state

In a multimode click scenario, the joint click moment is given by the expression,

$$\hat{O} =: \exp\Big(-X_a\hat{a}^\dagger\hat{a} - X_b\hat{b}^\dagger\hat{b} - X_c\hat{c}^\dagger\hat{c} - X_d\hat{d}^\dagger\hat{d}\Big):\,, \tag{C.0.7}$$

An equivalent operator in coherent state basis takes the form,

$$\begin{aligned}\hat{O} = \int \frac{\mathrm{d}^2\alpha\,\mathrm{d}^2\beta\,\mathrm{d}^2\gamma\,\mathrm{d}^2\delta}{\pi^4(1-X_a)(1-X_b)(1-X_c)(1-X_d)} \\ \times\ \exp\Big(-\frac{X_a|\alpha|^2}{1-X_a} - \frac{X_b|\beta|^2}{1-X_b} - \frac{X_c|\gamma|^2}{1-X_c} - \frac{X_d|\delta|^2}{1-X_d}\Big) \\ \times\ |\alpha,\beta,\gamma,\delta\rangle\,\langle\alpha,\beta,\gamma,\delta|\,,\end{aligned} \tag{C.0.8}$$

where we make use the following identity (for $\bar{n} > 0$),

$$\frac{:\exp\left(\frac{-\hat{a}^\dagger \hat{a}}{[\bar{n}+1]}\right):}{(\bar{n}+1)} = \frac{1}{\bar{n}\pi}\int \mathrm{d}^2\alpha\, e^{\frac{-|\alpha^2|}{\bar{n}}}\,|\alpha\rangle\langle\alpha|\,, \tag{C.0.9}$$

which bring Eq. (C.0.7) to Eq. (C.0.8). Since we do measurements only at modes A and B, we can set $X_b = 0$ and $X_c = 0$. Furthermore, unitary operations on the measurement side can alter the amplitudes of coherent state modes. Therefore final measurement operator becomes,

$$\begin{aligned}\hat{O} = &\int \frac{\mathrm{d}^2\alpha\,\mathrm{d}^2\beta\,\mathrm{d}^2\gamma\,\mathrm{d}^2\delta}{\pi^4(1-X_a)(1-X_d)} \\ &\times \exp\Big(-\frac{X_a|\tau\alpha+\rho\beta|^2}{1-X_a} - \frac{X_d|-\rho^*\gamma-\tau^*\delta|^2}{1-X_d}\Big) \\ &\times \quad |\alpha,\beta,\gamma,\delta\rangle\langle\alpha,\beta,\gamma,\delta|\,,\end{aligned} \tag{C.0.10}$$

where ρ and τ are matrix elements of the unitary (waveplate) operator. Using Eq. (C.0.10) we can now find the expectation value $\langle\hat{O}\rangle$ on state $|\psi\rangle$ in Eq. (C.0.6),

$$\langle\psi|\,\hat{O}\,|\psi\rangle = \frac{(1-|\lambda|^2)^2}{\pi^4(1-X_a)(1-X_d)}\int \mathrm{d}^{2.4}\vec{\alpha}\,\exp\Big(-\vec{\alpha}^\dagger Y\vec{\alpha} + \vec{\alpha}^T Z\vec{\alpha} + \vec{\alpha}^\dagger Z^*\vec{\alpha}^*\Big), \tag{C.0.11}$$

where α in vector form is matrix representation of four modes $\vec{\alpha} = \begin{bmatrix}\alpha\\ \beta\\ \gamma\\ \delta\end{bmatrix}$, additionally $Y = Y^\dagger$ and $Z = Z^*$. Matrices Y and Z^* are given by,

$$\begin{aligned} 2Z^* &= \lambda\begin{bmatrix}0&0&0&1\\0&0&e^{i\phi}&0\\0&e^{i\phi}&0&0\\1&0&0&0\end{bmatrix} \quad , \quad Y = \begin{bmatrix}Y_{11}&Y_{12}\\Y_{21}&Y_{22}\end{bmatrix} \\ Y_{11} &= \begin{bmatrix}\frac{1-|\rho|^2X_a}{1-X_a} & \frac{\tau^*\rho X_a}{1-X_a}\\ \frac{\tau\rho^*X_a}{1-X_a} & \frac{1-|\tau|^2X_a}{1-X_a}\end{bmatrix} \quad , \quad Y_{22} = \begin{bmatrix}\frac{1-|\tau|^2X_d}{1-X_d} & \frac{-\tau^*\rho X_d}{1-X_d}\\ \frac{-\tau\rho^*X_d}{1-X_d} & \frac{1-|\rho|^2X_d}{1-X_d}\end{bmatrix}, \\ Y_{12} &= Y_{21} = \begin{bmatrix}0&0\\0&0\end{bmatrix}. \end{aligned} \tag{C.0.12}$$

Using the above relation we can transform the integral function in Eq. (C.0.11) to matrix form. For this, we can make use of an identity,

$$\int_{\mathbb{C}} \mathrm{d}^{2.n}\vec{\alpha}\, \exp\Big(-\vec{\alpha}^{\dagger} Y \vec{\alpha} + \vec{\alpha}^{T} Z \vec{\alpha} + \vec{\alpha}^{\dagger} Z^{*} \vec{\alpha}^{*}\Big) = \pi^{n} \left(\det \begin{bmatrix} Y & 2Z^{*} \\ 2Z & Y^{*} \end{bmatrix}\right)^{-1/2}. \quad \text{(C.0.13)}$$

Combining Eq. (C.0.12) and Eq. (C.0.13) and applying the relations into Eq. (C.0.11) gives an expression to calculate expectation values on any rotated basis.

$$\langle\psi|\,\hat{O}\,|\psi\rangle \;=\; \frac{(1-|\lambda|^{2})^{2}(1-X_{a})(1-X_{d})}{det\begin{bmatrix} 1-|\rho|^{2}X_{a} & \tau^{*}\rho X_{a} & 0 & \tilde{\lambda} \\ \tau\rho^{*}X_{a} & 1-|\tau|^{2}X_{a} & \tilde{\lambda}e^{i\phi} & 0 \\ 0 & \tilde{\lambda}^{*}e^{-i\phi} & 1-|\tau|^{2}X_{d} & -\rho^{*}\tau X_{d} \\ \tilde{\lambda}^{*} & 0 & -\tau^{*}\rho X_{d} & 1-|\rho|^{2}X_{d} \end{bmatrix}}, \quad \text{(C.0.14)}$$

here $\tilde{\lambda} = \sqrt{(1-X_a)(1-X_d)}\lambda$. Expressions for the unitary operator and corresponding ρ,τ elements are given in the main part Eq. (7.4.6). Finally if we consider exact moment operator by replacing X_a and X_d with, $\mathrm{X}_i \in \frac{\eta m_i}{N_i}$ transform Eq. (C.0.14) into,

$$\langle\psi|\,\hat{O}\,|\psi\rangle \;= \big\langle :\, \exp\big(-\frac{\eta m_A}{N_A}\hat{n}_A - \frac{\eta m_B}{N_B}\hat{n}_B\big)\, : \big\rangle$$

$$\langle\hat{O}\rangle = \frac{N^{2}(1-|\lambda|^{2})^{2}\,(N-\eta m_A)(N-\eta m_B)}{\begin{bmatrix} N-|\rho|^{2}\eta m_A & \rho\tau^{*}\eta m_A & 0 & \lambda' \\ \rho^{*}\tau\eta m_A & N-|\tau|^{2}\eta m_A & \pm\lambda' & 0 \\ 0 & \pm\lambda'^{*} & N-|\tau|^{2}\eta m_B & -\rho^{*}\tau\eta m_B \\ \lambda'^{*} & 0 & -\rho\tau^{*}\eta m_B & N-|\rho|^{2}\eta m_B \end{bmatrix}}. \quad \text{(C.0.15)}$$

This is what is exactly derived in Eq. (7.4.7) and used for theoretical simulation.

References

[1]E. Meyer-Scott, N. Prasannan, C. Eigner, V. Quiring, J. M. Donohue, S. Barkhofen, and C. Silberhorn, "High-performance source of spectrally pure, polarization entangled photon pairs based on hybrid integrated-bulk optics.", Opt. Express. **26**, 32475–32490 (2018).

[2]E. Meyer-Scott, N. Prasannan, I. Dhand, C. Eigner, V. Quiring, S. Barkhofen, B. Brecht, M. B. Plenio, and C. Silberhorn, "Scalable generation of multiphoton entangled states by active feed-forward and multiplexing.", Phys. Rev. Lett. **129**, 150501 (2022).

[3]N. Prasannan, J. Sperling, B. Brecht, and C. Silberhorn, "Direct measurement of higher-order nonlinear polarization squeezing", Phys. Rev. Lett. **129**, 263601 (2022).

[4]L. T. Weinbrenner, N. Prasannan, K. Hansenne, S. Denker, J. Sperling, B. Brecht, C. Silberhorn, and O. Gühne, "Certifying the topology of quantum networks: theory and experiment.", Phys. Rev. Lett. **132**, 240802 (2024).

[5]N. Prasannan, S. De, S. Barkhofen, B. Brecht, C. Silberhorn, and J. Sperling, "Experimental entanglement characterization of two-rebit states.", Phys. Rev. A **103**, L040402 (2021).

[6]Y. Teo, S. Shringarpure, H. Jeong, N. Prasannan, B. Brecht, C. Silberhorn, M. Evans, D. Mogilevtsev, and L. Sánchez-Soto, "Evidence-based certification of quantum dimensions.", Phys. Rev. Lett. **133**, 050204 (2024).

[7]L. Ares, N. Prasannan, E. Agudelo, A. Luis, B. Brecht, C. Silberhorn, and J. Sperling, "Photonic entanglement and polarization nonclassicality: two manifestations, one nature.", arXiv **2407.07477** (2024).

[8]M. Plank, "Ueber irreversible strahlungsvorgänge.", Annalen der Physik **306**, 69–122 (1900).

[9]G.Lewis, "The conservation of photons.", Nature **118**, 874–875 (1926).

[10]E. Schrödinger, "Die gegenwärtige situation in der quantenmechanik.", Naturwissenschaften. **23**, 807–812 (1935).

[11]A. Einstein, B. Podolsky, and N. Rosen, "Can quantum-mechanical description of physical reality be considered complete?", Phys. Rev. **47**, 777 (1935).

[12]P.Grangier et al., "Experimental evidence for a photon anticorrelation effect on a beam splitter: a new light on single-photon interferences.", EPL **1**, 173 (1986).

[13]C. A. Kocher and E. D. Commins, "Polarization correlation of photons emitted in an atomic cascade.", Phys. Rev. Lett. **18**, 575 (1967).

[14]D. Bouwmeester, J. W. Pan, M. Daniell, H. Weinfurter, and A. Zeilinger, "Observation of three-photon greenberger-horne-zeilinger entanglement.", Phys. Rev. Lett. **82**, 1345 (1999).

[15]S. J. Freedman and J. F. Clauser, "Experimental test of local hidden-variable theories.", Phys. Rev. Lett. **28**, 938 (1972).

[16]C. K. Hong, Z. Y. Ou, and L. Mandel, "Measurement of subpicosecond time intervals between two photons by interference", Phys. Rev. Lett. **59**, 2044 (1987).

[17]C. H. Bennett and G. Brassard, "Quantum cryptography: public key distribution and coin tossing.", Theoretical Computer Science **560**, 7–11 (1984).

[18]C. H. Bennett, G. Brassard, C. Crépeau, R. Jozsa, A. Peres, and W. K. Wootters, "Teleporting an unknown quantum state via dual classical and einstein-podolsky-rosen channel.", Phys. Rev. Lett. **70**, 1895 (1993).

[19]V. Giovannetti et al., "Quantum-enhanced measurements: beating the standard quantum limit", Science **306**, 1330–1336 (2004).

[20]A. K. Ekert, "Quantum cryptography based on bell's theorem.", Phys. Rev. Lett. **67**, 661 (1991).

[21]R. P. Feynman, "Simulating physics with computers.", Int J Theor Phys. **21**, 467–488 (1982).

[22]E. Brambilla, L. Caspani, O. Jedrkiewicz, L. A. Lugiato, and A. Gatti, "High-sensitivity imaging with multi-mode twin beams.", Phys. Rev. A **77**, 053807 (2008).

[23]C. M. Caves, "Quantum-mechanical noise in an interferometer.", Phys. Rev. D **23**, 1693 (1981).

[24]C. M. Caves, "Quantum limits on noise in linear amplifiers.", Phys. Rev. D **26**, 1817 (1982).

[25]C. H. Bennett, F. Bessette, G. Brassard, et al., "Experimental quantum cryptography.", J. Cryptology. **5**, 3–28 (1992).

[26]R. Raussendorf, D. E. Browne, and H. J. Briegel, "Measurement-based quantum computation on cluster states.", Phys. Rev. A **68**, 022312 (2003).

[27]E. Knill, R. Laflamme, and G. Milburn, "A scheme for efficient quantum computation with linear optics.", Nature. **409**, 46–52 (2001).

[28]S. Aaronson and A. Arkhipov, "The computational complexity of linear optics.", Theory of Computing. **9**, 143–252 (2013).

[29]S. E. Harris, M. K. Oshman, and R. L. Byer, "Observation of tunable optical parametric fluorescence", Phys. Rev. Lett. **18**, 732 (1967).

[30]D. Magde and H. Mahr, "Study in ammonium dihydrogen phosphate of spontaneous parametric interaction tunable from 4400 to 16 000 $\mathring{A}$", Phys. Rev. Lett. **18**, 905 (1967).

[31]D. C. Burnham and D. L. Weinberg, "Observation of simultaneity in parametric production of optical photon pairs", Phys. Rev. Lett. **25**, 84 (1970).

[32]L. K. Shalm et al., "Strong loophole-free test of local realism", Phys. Rev. Lett. **115**, 250402 (2015).

[33]R. W. Boyd, *Nonlinear optics* (Elsevier, 2020).

[34]P. A. Franken, A. E. Hill, C. W. Peters, and G. Weinreich, "Generation of optical harmonics", Phys. Rev. Lett. **7**, 118 (1961).

[35]P. G. Kwiat et al., "New high-intensity source of polarization-entangled photon pairs.", Phys. Rev. Lett. **75**, 4337 (1995).

[36]A. Mair, A. Vaziri, G. Weihs, et al., "Entanglement of the orbital angular momentum states of photons.", Nature **412**, 313–316 (2001).

[37]A. Zavatta, V. Parigi, and M. Bellini, "Experimental nonclassicality of single-photon-added thermal light states", Phys. Rev. A. **75**, 052106 (2007).

[38]M. Liscidini and J. E. Sipe, "Stimulated emission tomography", Phys. Rev. Lett. **111**, 193602 (2013).

[39]A. Zavatta. et al., "Quantum-to-classical transition with single-photon-added coherent states of light", Science **306**, 660–662 (2004).

[40]V. Parigi et al., "Probing quantum commutation rules by addition and subtraction of single photons to/from a light field", Science **317**, 1890–1893 (2007).

[41]P. Dirac, *The principles of quantum mechanics* (Oxford University Press, 1930).

[42]A. Christ, B. Brecht, W. Mauerer, and C. Silberhorn, "Theory of quantum frequency conversion and type-ii parametric down-conversion in the high-gain regime", New Journal of Physics **15**, 053038 (2013).

[43]S. Tanzilli, H. D. Riedmatten, H. Zbinden, et al., "Highly efficient photon-pair source using periodically poled lithium niobate waveguide", Electronics Letters **37**, 26–28 (2001).

[44]A. Christ, K. Laiho, A. Eckstein, T. Lauckner, P. J. Mosley, and C. Silberhorn, "Spatial modes in waveguided parametric down-conversion", Phys. Rev. A. **80**, 033829 (2009).

[45]W. P. Grice and I. A. Walmsley, "Spectral information and distinguishability in type-ii down-conversion with a broadband pump", Phys. Rev. A. **56**, 1627 (1997).

[46]L.-A. Wu, H. J. Kimble, J. L. Hall, and H. Wu, "Generation of squeezed states by parametric down conversion", Phys. Rev. Lett. **57**, 2520 (1986).

[47]J. Rarity, P. Tapster, and E. Jakeman, "Observation of sub-poissonian light in parametric downconversion", Optics Communications **62**, 201–206 (1987).

[48]Z. Y. Ou, S. F. Pereira, H. J. Kimble, and K. C. Peng, "Realization of the einstein-podolsky-rosen paradox for continuous variables", Phys. Rev. Lett. **68**, 3663 (1992).

[49]C. K. Hong and L. Mandel, "Experimental realization of a localized one-photon state", Phys. Rev. Lett. **56**, 58 (1986).

[50]M. Cooper, L. J. Wright, C. Söller, and B. J. Smith, "Experimental generation of multi-photon fock states", Optics Express. **21**, 5309–5317 (2013).

[51]B. Brecht, D. V. Reddy, C. Silberhorn, and M. G. Raymer, "Photon temporal modes: a complete framework for quantum information science", Phys. Rev. X **5**, 041017 (2015).

[52]B. J. Metcalf et al., "Multiphoton quantum interference in a multiport integrated photonic device", Nature Communications **4**, 1356 (2013).

[53]J. A. Armstrong, N. Bloembergen, J. Ducuing, and P. S. Pershan, "Interactions between light waves in a nonlinear dielectric.", Phys. Rev. A. **127**, 1918 (1962).

[54]A. Eckstein, A. Christ, et al., "Highly efficient single-pass source of pulsed single-mode twin beams of light.", Phys. Rev. Lett. **106**, 013603 (2011).

[55]M. Yamada, N. Nada, M. Saitoh, and K. Watanabe, "First-order quasi-phase matched linbo3 waveguide periodically poled by applying an external field for efficient blue second-harmonic generation.", Appl. Phys. Lett. **62**, 435–436 (1993).

[56]M. Santandrea et al., "Fabrication limits of waveguides in nonlinear crystals and their impact on quantum optics applications.", New Journal of Physics **21**, 033038 (2019).

[57]J. Eberly, "Schmidt analysis of pure-state entanglement.", Laser Phys. **16**, 921–926 (2006).

[58]A. Eckstein, B. Brecht, and C. Silberhorn, "A quantum pulse gate based on spectrally engineered sum frequency generation .", Optics Express. **15**, 13770–13778 (2011).

[59]V.Ansari, J. M. Donohue, et al., "Tomography and purification of the temporal-mode structure of quantum light.", Phys. Rev. Lett. **120**, 213601 (2018).

[60]L. Serino et al., "Realization of a multi-output quantum pulse gate for decoding high-dimensional temporal modes of single-photon states.", PRX Quantum **4**, 020306 (2023).

[61]P. J. Mosley et al., "Heralded generation of ultrafast single photons in pure quantum states.", Phys. Rev. Lett. **100**, 133601 (2008).

[62]E. Meyer-Scott et al., "Limits on the heralding efficiencies and spectral purities of spectrally filtered single photons from photon-pair sources.", Phys. Rev. A **95**, 061803(R) (2017).

[63]B. Brecht, "Engineering ultrafast quantum frequency conversion.", Ph.D Thesis (2014).

[64]A. M. Brańczyk, A. Fedrizzi, et al., "Engineered optical nonlinearity for quantum light sources", Optics Express. **19**, 55–65 (2011).

[65]A. Christ, K. Laiho, A. Eckstein, K. N. Cassemiro, and C. Silberhorn, "Probing multimode squeezing with correlation functions.", New Journal of Physics **13**, 033027 (2011).

[66]B. Y. Zel'Dovich and D. N. Klyshko, "Field statistics in parametric luminescence", ZhETF Pis ma Redaktsiiu **9**, 69 (1969).

[67]M. Avenhaus, A. Eckstein, P. J. Mosley, and C. Silberhorn, "Fiber-assisted single-photon spectrograph", Optics Letters. **34**, 2873–2875 (2009).

[68]R. J. Glauber, "The quantum theory of optical coherence.", Phys. Rev. Lett. **130**, 2529 (1963).

[69]A. Eckstein et al., "Realistic $g^{(2)}$ measurement of a pdc source with single photon detectors in the presence of background.", Phys. Status Solidi C **8**, 1216–1219 (2011).

[70]W. Mauerer et al., "How colors influence numbers: photon statistics of parametric down-conversion.", Phys. Rev. A. **80**, 053815 (2009).

[71]H. J. Kimble, M. Dagenais, and L. Mandel, "Photon antibunching in resonance fluorescence", Phys. Rev. Lett. **39**, 691 (1977).

[72]L. Mandel, "Sub-poissonian photon statistics in resonance fluorescence", Optics Letters. **7**, 205–207 (1979).

[73]J. Sperling, W. Vogel, and G. S. Agarwal, "Sub-binomial light", Phys. Rev. Lett. **109**, 093601 (2012).

[74]D. Bouwmeester, J. W. Pan, K. Mattle, et al., "Experimental quantum teleportation", Nature **390**, 575–579 (1997).

[75]J. W. Pan, H. W. D. Bouwmeester, and A. Zeilinger, "Experimental entanglement swapping: entangling photons that never interacted", Phys. Rev. Lett. **80**, 3891 (1998).

[76]T. Jennewein, C. Simon, G. Weihs, H. Weinfurter, and A. Zeilinger, "Quantum cryptography with entangled photons", Phys. Rev. Lett. **84**, 4729 (2000).

[77]A. Mair, A. Vaziri, G. Weihs, et al., "Entanglement of the orbital angular momentum states of photons", Nature **412**, 313–316 (2001).

[78]M. Avenhaus, M. V. Chekhova, L. A. Krivitsky, G. Leuchs, and C. Silberhorn, "Experimental verification of high spectral entanglement for pulsed waveguided spontaneous parametric down-conversion", Phys. Rev. A. **79**, 043836 (2009).

[79]E. Schrödinger, "Discussion of probability relations between separated systems", Mathematical Proceedings of the Cambridge Philosophical Society **31**, 555 (1935).

[80]J. S. Bell, "On the einstein podolsky rosen paradox", Physics Physique Fizika **1**, 195 (1964).

[81]Q. A. Turchette, C. S. Wood, B. E. King, et al., "Deterministic entanglement of two trapped ions.", Phys. Rev. Lett. **81**, 3631 (1998).

[82]D. N. Matsukevich et al., "Bell inequality violation with two remote atomic qubits.", Phys. Rev. Lett. **100**, 150404 (2008).

[83]C. Sackett, D. Kielpinski, B. King, et al., "Experimental entanglement of four particles.", Nature **404**, 256–259 (2000).

[84]A. Dousse, J. Suffczyński, A. Beveratos, et al., "Ultrabright source of entangled photon pairs", Nature **466**, 217–220 (2010).

[85]A. Anwar, C. Perumangatt, F. Steinlechnera, T. Jennewein, and A. Ling, "Entangled photon-pair sources based on three-wave mixing in bulk crystals", Rev. Sci. Instrum. **92**, 041101 (2021).

[86]R. S. Bennink, "Optimal collinear gaussian beams for spontaneous parametric down-conversion", Phys. Rev. A. **81**, 053805 (2010).

[87]Y. H. Kim, M. V. Chekhova, S. P. Kulik, M. H. Rubin, and Y. Shih, "Interferometric bell-state preparation using femtosecond-pulse-pumped spontaneous parametric down-conversion", Phys. Rev. A. **63**, 062301 (2001).

[88]B. S. Shi and A. Tomita, "Generation of a pulsed polarization entangled photon pair using a sagnac interferometer", Phys. Rev. A. **69**, 013803 (2004).

[89]T. Kim, M. Fiorentino, and F. N. C. Wong, "Phase-stable source of polarization-entangled photons using a polarization sagnac interferometer", Phys. Rev. A. **73**, 012316 (2006).

[90]M. M. Weston and all, "Efficient and pure femtosecond-pulse-length source of polarization-entangled photons", Optics Express **24**, 10869–10879 (2016).

[91]D. F. V. James, P. G. Kwiat, W. J. Munro, and A. G. White, "Measurement of qubits", Phys. Rev. A. **64**, 052312 (2001).

[92]J. Altepeter, E. Jeffrey, and P. Kwiat, "Photonic state tomography.", Advances In Atomic, Molecular, and Optical Physics. **52**, 105–159 (2005).

[93]J. W. Pan, M. Daniell, S. Gasparoni, G. Weihs, and A. Zeilinger, "Experimental demonstration of four-photon entanglement and high-fidelity teleportation.", Phys. Rev. Lett. **86**, 4435 (2001).

[94]E. Meyer-Scott et al., "Single-photon sources: approaching the ideal through multiplexing.", Rev. Sci. Instrum. **91**, 041101 (2020).

[95]M. J. Fitch, B. C. Jacobs, T. B. Pittman, and J. D. Franson, "Photon-number resolution using time-multiplexed single-photon detectors.", Phys. Rev. A **68**, 043814 (2003).

[96]N. Tomm, A. Javadi, N. Antoniadis, et al., "A bright and fast source of coherent single photons.", Nat. Nanotechnol **16**, 399–403 (2021).

[97]P. Thomas, L. Ruscio, O. Morin, et al., "Efficient generation of entangled multiphoton graph states from a single atom.", Nature **608**, 677–681 (2022).

[98]H.-S. Zhong et al., "12-photon entanglement and scalable scattershot boson sampling with optimal entangled-photon pairs from parametric down-conversion.", Phys. Rev. Lett. **121**, 250505 (2018).

[99]J. B. Spring et al., "Boson sampling on a photonic chip.", Science **339**, 798–801 (2012).

[100]J. Clausen, H. Hansen, L. Knöll, et al., "Conditional quantum-state engineering in repeated 2-photon down-conversion.", Appl Phys B **72**, 43–50 (2001).

[101]T. B. Pittman, B. C. Jacobs, and J. D. Franson, "Single photons on pseudodemand from stored parametric down-conversion.", Phys. Rev. A **66**, 042303 (2002).

[102]A. Schreiber et al., "Photons walking the line: a quantum walk with adjustable coin operations.", Phys. Rev. Lett. **104**, 050502 (2010).

[103]A. Regensburger, . Bersch, M. A. Miri, et al., "Parity–time synthetic photonic lattices.", Nature **488**, 167–171 (2012).

[104]W. Asavanant et al., "Generation of time-domain-multiplexed two-dimensional cluster state.", Science **366**, 373–376 (2019).

[105]J. Sabines-Chesterking et al., "Sub-shot-noise transmission measurement enabled by active feed-forward of heralded single photons.", Phys. Rev. Applied **8**, 014016 (2017).

[106]A. Christ and C. Silberhorn, "Limits on the deterministic creation of pure single-photon states using parametric down-conversion.", Phys. Rev. A **85**, 023829 (2012).

[107]F. Kaneda and P. G. Kwiat, "High-efficiency single-photon generation via large-scale active time multiplexing.", Sci. Adv. **5**, eaaw8586 (2019).

[108]M. Cao et al., "Efficient reversible entanglement transfer between light and quantum memories.", Optica **7**, 1440–1444 (2020).

[109]A. Ortu, A. Holzäpfel, J. Etesse, et al., "Storage of photonic time-bin qubits for up to 20ms in a rare-earth doped crystal.", npj Quantum Inf **8**, 29 (2022).

[110]M. B. amd G. Boucher, J. F. Ortas, B. Pointard, and R. Tualle-Brouri, "Quantum storage of single-photon and two-photon fock states with an all-optical quantum memory.", Phys. Rev. Lett. **122**, 210501 (2019).

[111]P. Steindl et al., "Artificial coherent states of light by multiphoton interference in a single-photon stream.", Phys. Rev. Lett. **126**, 143601 (2021).

[112]J. W. Pan, D. Bouwmeester, M. Daniell, et al., "Experimental test of quantum nonlocality in three-photon greenberger–horne–zeilinger entanglement.", Nature **403**, 515–519 (2000).

[113]P. Walther, K. Resch, T. Rudolph, et al., "Experimental one-way quantum computing.", Nature **434**, 169–176 (2005).

[114]J. O'Brien, G. Pryde, A. White, et al., "Demonstration of an all-optical quantum controlled-not gate.", Nature **426**, 264–267 (2003).

[115]N. Coste, D. A. Fioretto, N. Belabas, et al., "High-rate entanglement between a semiconductor spin and indistinguishable photons.", Nat. Photon **17**, 582–587 (2023).

[116]H. de Riedmatten, I. Marcikic, W. Tittel, H. Zbinden, and N. Gisin, "Quantum interference with photon pairs created in spatially separated sources.", Phys. Rev. A **67**, 022301 (2003).

[117]D. E. Browne and T. Rudolph, "Resource-efficient linear optical quantum computation.", Phys. Rev. Lett. **95**, 010501 (2005).

[118]C. Y. Lu, X. Q. Zhou, O. Gühne, et al., "Experimental entanglement of six photons in graph states.", Nature Phys **3**, 91–95 (2007).

[119]X. C. Yao, T. X. Wang, P. Xu, et al., "Observation of eight-photon entanglement.", Nature Photon **6**, 225–228 (2012).

[120]X. L. Wang et al., "Experimental ten-photon entanglement.", Phys. Rev. Lett. **117**, 210502 (2016).

[121]Y. Pilnyak, N. Aharon, D. Istrati, E. Megidish, A. Retzker, and H. S. Eisenberg, "Simple source for large linear cluster photonic states.", Phys. Rev. A **95**, 022304 (2017).

[122]O. Gühne and G. Tóth, "Entanglement detection.", Physics Reports **474**, 1–75 (2009).

[123]G. Tóth, C. Knapp, O. Gühne, and H. J. Briegel, "Spin squeezing and entanglement.", Phys. Rev. A **79**, 042334 (2009).

[124]O. Gühne, C. Y. Lu, W. B. Gao, and J. W. Pan, "Toolbox for entanglement detection and fidelity estimation.", Phys. Rev. A **76**, 030305(R) (2007).

[125]S. Wehner et al., "Quantum internet: a vision for the road ahead.", Science **362**, eaam9288 (2018).

[126]M. Pompili et al., "Realization of a multinode quantum network of remote solid-state qubits.", Science **372**, 259–264 (2021).

[127]A. Pappa, A. Chailloux, S. Wehner, E. Diamanti, and I. Kerenidis, "Multipartite entanglement verification resistant against dishonest parties.", Phys. Rev. Lett. **108**, 260502 (2012).

[128]M. Navascués, E. Wolfe, D. Rosset, and A. Pozas-Kerstjens, "Genuine network multipartite entanglement.", Phys. Rev. Lett. **125**, 240505 (2020).

[129]W. McCutcheon, A. Pappa, B. Bell, et al., "Experimental verification of multipartite entanglement in quantum networks.", Nat Commun **7**, 13251 (2016).

[130]P. Sekatski et al., "Proposal for exploring macroscopic entanglement with a single photon and coherent states.", Phys. Rev. A **86**, 060301(R) (2012).

[131]A. Lvovsky, R. Ghobadi, A. Chandra, et al., "Observation of micro–macro entanglement of light.", Nature Phys **9**, 541–544 (2013).

[132]M. Mitchell, J. Lundeen, and A. Steinberg, "Super-resolving phase measurements with a multiphoton entangled state.", Nature **429**, 161–164 (2004).

[133]I. Afek et al., "High-noon states by mixing quantum and classical light.", Science **328**, 879–881 (2010).

[134]R. E. Slusher, L. W. Hollberg, B. Yurke, J. C. Mertz, and J. F. Valley, "Observation of squeezed states generated by four-wave mixing in an optical cavity.", Phys. Rev. Lett. **55**, 2409 (1985).

[135]L. A. Wu, H. J. Kimble, J. L. Hall, and H. Wu, "Generation of squeezed states by parametric down conversion.", Phys. Rev. Lett. **57**, 520 (1986).

[136]A. Heidmann, R. J. Horowicz, S. Reynaud, E. Giacobino, C. Fabre, and G. Camy, "Observation of quantum noise reduction on twin laser beams.", Phys. Rev. Lett. **59**, 2555 (1987).

[137]J. Aasi, J. Abadie, B. Abbott, et al., "Enhanced sensitivity of the ligo gravitational wave detector by using squeezed states of light.", Nature Photon **7**, 613–619 (2013).

[138]D. M. Meekhof, C. Monroe, B. E. King, W. M. Itano, and D. J. Wineland, "Generation of nonclassical motional states of a trapped atom.", Phys. Rev. Lett. **76**, 1796 (1995).

[139]J. Hald, J. L. Sørensen, C. Schori, and E. S. Polzik, "Spin squeezed atoms: a macroscopic entangled ensemble created by light.", Phys. Rev. Lett. **83**, 1319 (1999).

[140]E. E. Wollman et al., "Quantum squeezing of motion in a mechanical resonator.", Science **349**, 952–955 (2015).

[141]B. Yurke, P. G. Kaminsky, R. E. Miller, E. A. Whittaker, A. D. Smith, A. H. Silver, and R. W. Simon, "Observation of 4.2-k equilibrium-noise squeezing via a josephson-parametric amplifier.", Phys. Rev. Lett. **60**, 764 (1988).

[142]U. Leonhardt and H. Paul, "Measuring the quantum state of light.", Progress in Quantum Electronics **19**, 89–130 (1995).

[143]J. Sperling et al., "Balanced homodyne detection with on-off detector systems: observable nonclassicality criteria.", Europhysics Letters **109**, 34001 (2015).

[144]G. Brida, M. Genovese, and I. R. Berchera, "Experimental realization of sub-shot-noise quantum imaging.", Nature Photon. **4**, 227–230 (2010).

[145]R. Whittaker et al., "Absorption spectroscopy at the ultimate quantum limit from single-photon states.", New J. Phys. **19**, 023013 (2017).

[146]J. Sperling, W. Vogel, and G. S. Agarwal, "Quantum state engineering by click counting.", Phys. Rev. A **89**, 043829 (2014).

[147]T. J. Bartley et al., "Direct observation of sub-binomial light.", Phys. Rev. Lett. **110**, 173602 (2013).

[148]A. Rothen, "The ellipsometer, an apparatus to measure thicknesses of thin surface films.", Rev. Sci. Instrum. **16**, 26–30 (1945).

[149]M. Born and E. Wolf, *Principles of optics,* 6^{th}*ed.*. 1984.

[150]N. Korolkova, G. Leuchs, R. Loudon, T. C. Ralph, and C. Silberhorn, "Polarization squeezing and continuous-variable polarization entanglement.", Phys. Rev. A **65**, 052306 (2002).

[151]A. S. Chirkin et al., "Quantum theory of two-mode interactions in optically anisotropic media with cubic nonlinearities: generation of quadrature- and polarization-squeezed light.", Quantum Electron. **23**, 870 (1993).

[152]A. S. Chirkin, "Polarization-squeezed light and quantum degree of polarization (a review).", Opt. Spectrosc. **119**, 371–376 (2015).

[153]F. Marsili et al., "Detecting single infrared photons with system efficiency.", Nature Photon **7**, 210–214 (2013).

[154]A. D. Semenov, G. N. Goltsman, and A. A. Korneev, "Quantum detection by current carrying superconducting film.", Physica C: Superconductivity. **351**, 349–356 (2001).

[155]J. Tiedau et al., "Single-channel electronic readout of a multipixel superconducting nanowire single photon detector.", Optics Express. **28**, 5528–5537 (2020).

[156]T. Zhang et al., "Superconducting single-photon detector with a speed of 5ghz and a photon number resolution of 61.", Photon. Res. **12**, 1328–1333 (2024).

[157]C. Cahall et al., "Multi-photon detection using a conventional superconducting nanowire single-photon detector.", Optica **4**, 1534–1535 (2017).

[158]J. Sperling, W. Vogel, and G. S. Agarwal, "True photocounting statistics of multiple on-off detectors.", Phys. Rev. A **85**, 023820 (2012).

[159]J. Sperling, W. Vogel, and G. S. Agarwal, "Correlation measurements with on-off detectors.", Phys. Rev. A **88**, 043821 (2013).

[160]D. Achilles et al., "Photon-number-resolving detection using time-multiplexing.", Journal of Modern Optics **51(9–10)**, 1499–1515 (2003).

[161]J. Tiedau, M. Engelkemeier, B. Brecht, J. Sperling, and C. Silberhorn, "Statistical benchmarking of scalable photonic quantum systems.", Phys. Rev. Lett. **126**, 023601 (2021).

[162]J. Tiedau et al., "A high dynamic range optical detector for measuring single photons and bright light.", Opt. Express **27**, 1–15 (2019).

[163]T. S. Iskhakov, M. V. Chekhova, G. O. Rytikov, and G. Leuchs, "Macroscopic pure state of light free of polarization noise.", Phys. Rev. Lett. **106**, 113602 (2011).

[164]T. S. Iskhakov, I. N. Agafonov, M. V. Chekhova, and G. Leuchs, "Polarization-entangled light pulses of 10^5 photons.", Phys. Rev. Lett. **109**, 150502 (2012).

[165]H. Defienne et al., "Quantum image distillation.", Sci. Adv. **5**, eaax0307 (2019).

[166]S. Johnson, A. McMillan, S. Frick, J. Rarity, and M. Padgett, "Hiding images in noise.", Optics Express. **31**, 5290–5296 (2023).

[167]T. Gregory et al., "Imaging through noise with quantum illumination.", Sci. Adv. **6**, eaay2652 (2020).